Theoretical development and experimental validation of a method to reconstruct forces on the TBM structure during operation

Zur Erlangung des akademischen Grades

Doktor der Ingenieurwissenschaften

der Fakultät für Maschinenbau

Karlsruher Institut für Technologie (KIT)

genehmigte

Dissertation

von

Dipl.-Ing. Christian Zeile

Tag der mündlichen Prüfung: 13. Juli 2015

Hauptreferent: Prof. Dr.-Ing. Robert Stieglitz

Korreferent: Prof. Dr.-Ing. Alexander Fidlin

Abstract

The blanket systems in a fusion reactor are subjected to high mechanical and thermal loads. During the entire operating scenario, a main contribution to the high mechanical loads is related to static and transient electromagnetic effects. In the experimental campaign in ITER (International Thermonuclear Experimental Reactor), the Test Blanket Module (TBM) will experience similar electromagnetic loads. Especially with regard to the development of blanket systems for a future Demonstration fusion reactor (DEMO), it is of importance to develop the engineering models and codes to a high degree of confidence and to check the accuracy of theoretically calculated effects of the environmental conditions on the blanket systems. For this reason, a force reconstruction method that is able to estimate the electromagnetic forces on the TBM in ITER is an essential part of the development of these models and codes. Therefore, a system and method that are applicable in ITER based on an arrangement of sensors that is able to cope with the environmental conditions in a fusion reactor has been developed in this work. This is supported by the development of an experimental setup and corresponding mock-ups in order to demonstrate the applicability of the force reconstruction method to the TBM in ITER.

The investigation of different force reconstruction methods shows that methods suitable for the application to the TBM have to be based on a modal model of the system in order to reconstruct the distributed forces. Furthermore, they have to incorporate a stochastic element that continuously adapts the states of the model in order to be more robust against modelling errors.

An already existing force reconstruction method that fulfills these criteria is the Augmented Kalman Filter (AKF), a deterministic-stochastic approach. Hence, this algorithm was selected as possible candidate and extended to be able to reconstruct the distributed three-dimensional forces. Nevertheless, the AKF is a predictor-corrector algorithm and therefore not able to consider future measurement signals for the reconstruction.

In order to overcome this drawback, an algorithm able to include future measurement signals has been proposed as second candidate. The algorithm combines an optimization algorithm, which takes into account future values for the optimization, and a state observer based on Kalman filter techniques for the adaption of the states of the model. This algorithm used in a similar implementation as model predictive controller (MPC) has been proposed for force reconstruction for the first time.

The two algorithms, AKF and MPC, have been implemented and their application to the reconstruction of electromagnetic forces on the TBM has been experimentally validated by a dedicated experimental setup with a basic mock-up, namely the simple pipe mock-up. It has been demonstrated that the mock-up represents well the modal characteristics of the TBM.

The study of different sensor types and technologies shows that strain sensors based on optical fibers are most suitable for the application as they are immune to electromagnetic interference, able to withstand high temperatures and several sensing points can be introduced in one fiber reducing the necessary number of signal wires. In addition, a genetic algorithm has been developed that is able to optimize the sensor placement for a given number of sensors.

In order to investigate the influence of modelling errors on the force reconstruction algorithms, a study based on simulated strain data with the simple pipe mock-up has been conducted. For the evaluation of the impact of errors in the identified eigenfrequencies and eigenvectors as well as the number of sensors, an error measure based on the root mean squared error (RSME) has been defined, which is well suited for the characteristics of the applied forces. It was shown that the RSME with an error in the eigenvectors of 30% is about 14 times higher if 6 sensors are used instead of 16 sensors. In contrast, the influence of the number of sensors for a perfectly matching model turned out to be negligible. The impact of the error in the eigenfrequencies also proved to be relatively small compared to the error in the eigenvectors.

The overall comparison of the RSME of the AKF (with compensation of the time delay) and the MPC has shown no significant difference leading to the conclusion that the RSME is mainly influenced by modelling errors. Based on these results and depending on the available space, a total number of sensors between 10 and 16 sensors is required to compensate modelling errors and to also consider the failure of single sensors.

The results of the experiments with the simple pipe mock-up and 16 electrical strain sensors have shown that for ITER relevant durations of the excitation forces the algorithms are able to achieve an accuracy in the reconstruction of forces suitable for the validation of engineering models and codes. According to a new accuracy definition based on the relative linearity error, the forces can be estimated with an accuracy of about 10 % and the moments in the range of 20 %.

Zusammenfassung

Die Blanket Systeme in einem Fusionreaktor erfahren große mechanische und thermische Lasten. Dabei sind während des gesamten Betriebsszenarios hauptsächlich statische und transiente elektro-magnetisch Effekte für die großen mechanischen Lasten verantwortlich. Das Test Blanket Module (TBM) wird während der Versuchsreihen in ITER (International Thermonuclear Experimental Reactor) vergleichbaren elektro-magnetischen Kräften ausgesetzt sein. Insbesondere im Hinblick auf die Entwicklung von Blanket Systemen für einen zukünftigen Demonstrationsreaktor (DEMO) ist es von großer Bedeutung, die verwendeten theoretischen Modelle und Codes zu einem hohen Maß an Zuverlässigkeit weiterzuentwickeln und die Genauigkeit der theoretische berechneten Effekte der Umgebungsbedingungen auf das Blanket System zu überprüfen. Aus diesem Grund ist eine Methode zur Rekonstruktion der elektro-magnetischen Kräfte, die auf das TBM in ITER einwirken, ein wesentlicher Beitrag zur Entwicklung dieser Modelle und Codes. Daher wurden im Rahmen dieser Arbeit ein System und eine Methode entwickelt, die in ITER anwendbar sind, und auf einem Sensorsystem basieren, das unter den Umgebungsbedingungen in einem Fusionsreaktor eingesetzt werden kann. Dies wird unterstützt durch die Entwicklung eines experimentellen Versuchsaufbaus mit dazugehörigen Versuchsmodellen, um die Anwendbarkeit der Kraftrekonstruktionsmethode auf das TBM in ITER zu demonstrieren.

Die Untersuchung verschiedener Methoden zur Kraftrekonstruktion hat gezeigt, dass auf das TBM anwendbare Methoden auf einem modalen Modell des Systems basieren muss, um verteilte Kräfte rekonstruieren zu können. Zusätzlich müssen sie ein stochastisches Element enthalten, das kontinuierlich die Zustände des Modells anpasst und dadurch robuster gegenüber Fehlern bei der Modellbildung ist.

Ein bereits existierende Kraftrekonstruktionsmethode, die diese Kriterien erfüllt, ist der Augmented Kalman Filter (AKF), ein deterministisch-stochastischer Ansatz. Daher wurde dieser Algorithmus als möglicher Kandidat ausgewählt und erweitert, um verteilte dreidimensionale Kräfte rekonstruieren zu können. Da der AKF allerdings ein Prädiktor-Korrektor Algorithmus ist, ist er nicht fähig zukünftige Messsignale zu berücksichtigen.

Um diesen Nachteil zu umgehen, wurde ein Algorithmus, der zukünftige Messsignale in die Lösung mit einschließt, als zweiter Kandidat vorgeschlagen. Der Algorithmus kombiniert einen Optimierungsalgorithmus, der zukünftige Messsignale bei der Optimierung berücksichtigt, und einen Zustandsbeobachter basierend auf einem Kalman Filter, um die Zustände des Modells anzupassen. Dieser Algorithmus, der in einer ähnlichen Implementierung als model predicitive controller (MPC) verwendet wird, wurde erstmals zur Kraftrekonstruktion vorgeschlagen.

Die zwei Algorithmen, AKF und MPC; wurden implementiert und die Anwendung zur Kraftrekonstruktion von elektro-magnetischen Kräften am TBM wurde mithilfe eines speziellen Versuchsaufbaus mit einem einfachen Versuchsmodell, dem simple pipe mock-up, experimentell validiert. Dabei wurde demonstriert, dass das Versuchsmodell die modalen Charakteristiken des TBM gut repräsentiert.

Die Untersuchung verschiedener Sensorarten und Sensortechnologien hat gezeigt, dass faseroptische Dehnungssensoren für diese Anwendung am geeignetsten sind, da sie immun

gegenüber elektro-magnetischer Beeinflussung sind, hohen Temperaturen widerstehen können und mehrere Messpunkte auf einer Faser eingebracht werden können, um somit die notwendige Anzahl an Signalleitungen zu verringern. Zusätzlich wurde ein genetischer Algorithmus entwickelt, der die Anordnung der Sensor für eine gegebene Anzahl an Sensoren optimieren kann.

Um den Einfluss von Fehlern bei der Modellbildung auf die Kraftrekonstruktionsalgorithmen zu untersuchen, wurde eine Studie anhand von simulierten Dehnungsverläufen am simple pipe mock-up durchgeführt. Zur Beurteilung des Einflusses von Fehlern in den identifizierten Eigenfrequenzen und Eigenvektoren sowie der Anzahl der Sensoren, wurde ein Fehlermaß basierend auf dem mittleren quadratischen Fehler (RMSE) definiert, das für die Eigenschaften der aufgebrachten Kräfte gut geeignet ist. Dabei wurde gezeigt, dass der RSME bei einem Fehler in den Eigenvektoren von 30 % ungefähr 14-mal größer ist, wenn 6 anstatt 16 Sensoren genutzt werden. Im Gegensatz dazu ist der Einfluss der Anzahl der Sensoren bei einem nahezu perfekten Modell vernachlässigbar. Auch der Einfluss des Fehlers in den Eigenfrequenzen ist im Vergleich zum Einfluss des Fehlers in den Eigenvektoren relativ klein.

Der umfassende Vergleich des RMSE von AKF (mit Kompensation der Zeitverzögerung) und MPC hat keinen deutlichen Unterschied gezeigt, was zu der Schlussfolgerung führt, dass der RSME hauptsächlich durch Fehler bei der Modellbildung beeinflusst wird. Aufgrund dieses Ergebnisses und abhängig vom verfügbaren Platz werden insgesamt zwischen 10 und 16 Sensoren benötigt, um Fehler in der Modellbildung und den Ausfall einzelner Sensoren zu kompensieren.

Die Ergebnisse der Experimente mit dem simple pipe mock-up und 16 elektrischen Dehnungssensoren habe gezeigt, dass die Algorithmen für ITER relevante zeitliche Verläufe der anregenden Kräfte eine Genauigkeit der rekonstruierten Kräfte erreichen können, die geeignet ist, theoretische Modelle und Codes zu validieren. Nach einer neuen Definition der Genauigkeit basierend auf dem relativen Linearitätsabweichung können die Kräfte mit einer Genauigkeit von etwa 10 % und die Momente im Bereich von 20 % geschätzt werden.

Contents

List of Symbols

Latin symbols

a	Output of neuron of artificial neural network
b	Bias of neuron of artificial neural network
d_i	Distance of force application point to reference point
$\boldsymbol{e}, e$	Error
e_{MPC}	Slack variable MPC
$\boldsymbol{f}(t)$	Force vector
f_i	i^{th} eigenfrequency
$\boldsymbol{f}(\Omega)$	Force vector (frequency-domain)
f	Transfer function of neuron of artificial neural network
h_{ij}	Elements of frequency response function $\boldsymbol{H}(\Omega)$
$h_{\varepsilon ij}$	Elements of strain frequency response function $\boldsymbol{H}_{\varepsilon}(\Omega)$
i	Index
j	Index
k	Time step
l	l-lead of Inverse Structural Filter
m	Index
m_{MPC}	Control horizon of Model Predictive Controller (MPC)
n	Index
$\boldsymbol{n}(t)$	Modal force vector
o	x,y,z direction in classical bolt pattern analysis
p	Input of neuron of artificial neural network
$\boldsymbol{p}(t)$	Force function vector
p_{MPC}	Prediction horizon of Model Predictive Controller (MPC)
$\boldsymbol{\mathscr{p}}$	Unknown input vector of Augmented Kalman Filter (AKF)
q	Index
$\boldsymbol{r}_i(r_{ji})$	i^{th} eigenvector
$r_{Ijinorm}$	j^{th} element of i^{th} eigenvector of individual I , normalized
$r_j(k)$	Reference value for MPC at time step k
s	Number unknown inputs of Augmented Kalman Filter (AKF)

t	Time
$\boldsymbol{u}(t)$	Continuous-time input vector in state space representation
$\boldsymbol{u}_k$	Discrete-time input vector in state space representation at time step k
$\boldsymbol{u}$	Sequence of inputs $\boldsymbol{u}_k$
$u_{jtarget}(k)$	j^{th} Component of target input of MPC at time step k
$\boldsymbol{v}_k$	Stochastic process noise vector of Kalman filter
$\boldsymbol{w}_k$	Stochastic measurement noise vector of Kalman filter
w	Input weight of neuron of artificial neural network
$w_{k,j}^{y}$	Weight on j^{th} component of MPC measured output error at time step k
$w_{k,j}^{\Delta u}$	Weight on j^{th} component of MPC input increment at time step k
$w_{k,j}^{u}$	Weight on j^{th} component of MPC input vector at time step k
$\mathbf{w}_{SP}$	Weighting vector used for sensor placement
$\boldsymbol{x}(t)$	Continuous-time state vector
$\boldsymbol{x}_k$	Discrete-time state vector
$\hat{\boldsymbol{x}}_k$	Estimate of discrete-time state vector
x_x, x_y, x_z	x,y,z-coordinate of point
$\boldsymbol{y}(t)$	Continuous-time output vector in state space representation
$\boldsymbol{y}_k$	Discrete-time output vector in state space representation
$\boldsymbol{y}$	Sequence of outputs $\boldsymbol{y}_k$
$\boldsymbol{y}(\Omega)$	Output vector (frequency-domain)
$\hat{\boldsymbol{y}}_k$	Predicted discrete-time output vector in state space representation
$y_{jmeasured}(k)$	j^{th} measured output component at time step k
$\boldsymbol{z}(t)$	Continuous-time state vector in modal representation
$\boldsymbol{z}_{a,k}$	Discrete-time state vector in modal representation

$\boldsymbol{\mathcal{A}}$	Discrete-time system matrix
$\hat{\boldsymbol{\mathcal{A}}}$	Inverse discrete-time system matrix
$\boldsymbol{A}_k$	Displacement residue matrix
$\boldsymbol{A}_{\varepsilon k}$	Strain residue matrix
$\boldsymbol{\mathcal{B}}$	Discrete-time input matrix
$\hat{\boldsymbol{\mathcal{B}}}$	Inverse discrete-time input matrix
$\boldsymbol{B}$	Strain-displacement matrix
$\boldsymbol{\mathcal{C}}$	Output matrix

$\widehat{\boldsymbol{\mathcal{C}}}$	Inverse output matrix
$\boldsymbol{\mathcal{D}}$	Direct feed through matrix
$\widehat{\boldsymbol{\mathcal{D}}}$	Inverse direct feed through matrix
$\boldsymbol{D}$	Damping matrix
$\boldsymbol{D}_{\varepsilon}$	Differential operator on strains
$F(I)$	Fitness function
$\boldsymbol{H}(\Omega)$	Frequency response function matrix
$\boldsymbol{H}_{\varepsilon}(\Omega)$	Strain frequency response function matrix
$\boldsymbol{\mathcal{H}}$	Markov parameter matrix
$\boldsymbol{I}$	Identity matrix
I	Individual sensor placement
$\boldsymbol{K}$	Stiffness matrix
$\boldsymbol{\mathcal{K}}$	Gain or blending factor
$\boldsymbol{L}_i$	i^{th} order Tikhonov matrix
$\boldsymbol{M}$	Mass matrix
N	Shape function
$\mathcal{N}$	Normal distribution
$\boldsymbol{\mathcal{P}}_k$	Error covariance matrix
$\boldsymbol{Q}$	Process noise covariance matrix
$\boldsymbol{R}$	Modal matrix
$\boldsymbol{R}_{\boldsymbol{P}out}$	Partial modal output matrix
$\boldsymbol{R}_{\boldsymbol{P}in}$	Partial modal input matrix
$\mathbf{R}_{SP}$	Modal matrix for sensor placement
$\boldsymbol{R}_{SPISortedNormalized}$	Modal matrix for sensor combination I, sorted and normalized
$\boldsymbol{\mathcal{R}}$	Measurement noise covariance matrix
$\boldsymbol{S}_p$	Spatial distribution matrix
$\boldsymbol{S}_{acc}$	Selection matrix for acceleration sensors
$\boldsymbol{S}_v$	Selection matrix for velocity sensors
$\boldsymbol{S}_d$	Selection matrix for displacement sensors
$\boldsymbol{S}_{\varepsilon}$	Differential operator relating displacements to strain measurements
$\boldsymbol{S}_{BP}$	Spatial distribution matrix according to classical bolt pattern analysis
$\boldsymbol{S}$	Covariance matrix of unknown inputs
$\boldsymbol{W}$	Diagonal modal stiffness matrix

Greek symbols

α	Alpha damping coefficient
$\boldsymbol{\alpha}$ (α_{ij})	Diagonal matrix
β	Beta damping coefficient
δ_i	Damping coefficient of i^{th} mode
ε	Strain
$\boldsymbol{\eta}$	Stochastic component vector
λ	Regularization parameter of Tikhonov regularization
ξ_i	Damping ratio of i^{th} mode
ρ_e	Weight on slack variable e_{MPC}
$\boldsymbol{\phi}$	Generalized displacement vector
$\ddot{\boldsymbol{\phi}}_{rb}$	Rigid body modes accelerations vector
$\boldsymbol{\psi}$	Displacement vector
ω_i	i^{th} eigenfrequency
Δ	Diagonal modal damping matrix
Ω	Fourier transform variable

Superscripts and subscripts

$\square^T$	Transpose of □
$\square^+$	Moore-Penrose pseudo-inverse of □
$\square_m$	Related to modal system representation
$\square_c$	Related to continuous-time representation
$\square_a$	Augmented matrix or vector (related to Augmented Kalman Filter)
$\square_\varepsilon$	Related to strain
$\square_{norm}$	Normalized
$\square_{HI}$	Highest element of vector

1 Introduction

As the global energy demand is constantly increasing [1], the energy production by nuclear fusion offers a promising technology to satisfy the energy demand without relying on the increasingly scarce fossil fuels and the related impacts on the environment. On the way towards a future nuclear fusion power plant, the experimental fusion reactor ITER (International Thermonuclear Experimental Reactor) will provide a key contribution answering several physical and technological questions not accessible in current fusion devices. Firstly, components and systems are directly tested in an integral fusion environment (such as, for example, magnets, inner fuel cycle). Furthermore, engineering models and codes necessary to calculate the effects of the conditions present in a fusion environment on the components of a future fusion reactor (e.g. breeding blankets) are validated to allow also for licensing for such a device.

In particular, for the development of the breeding blanket, which is a key component for a nuclear fusion reactor, a specific international program has been implemented [2]. According to this program, six Test Blanket Modules (TBM) will be tested in ITER reproducing different types of blanket concepts for a first validation in a complete fusion environment. In the present work, a methodology suitable to reconstruct electromagnetic forces acting on the experimental component is presented. This allows the validation of computational programs versus experimental results and a direct evaluation of these effects for the operation and safety of the ITER components.

1.1 Nuclear fusion and fusion reactors

Nuclear fusion is a nuclear reaction in which two or more atomic nuclei fuse to a heavier atomic nucleus. In general, if two nuclei with lower masses than iron fuse, energy is released. The idea to use the released energy for electricity production already came up in the mid of the 20^{th} century, but was facing scientific and technological difficulties since the beginning. The most promising fusion reaction is the reaction of the hydrogen isotopes deuterium (D) and tritium (T) due to its large cross-section and high released energy [3]:

$$\mathrm{D} + \mathrm{T} \rightarrow {}^{4}\mathrm{He} + \mathrm{n} + 17.6\ \mathrm{MeV}. \tag{1.1}$$

The fusion reaction necessitates a temperature of about 1.5×10^{8} °C. This requires that the hot matter is efficiently confined to avoid energy losses that will terminate the thermonuclear reaction. As gases become a plasma at these temperatures, a magnetic confinement has been proposed to avoid the contact of the thin hot plasma and the wall of the machine.

Tokamak is the name of the most promising magnetic configuration that is adopted in important plasma machines (e.g. JET, ASDEX) as well as in ITER, which is under construction in Cadarache (France). It consists of a toroidal configuration of closed helix-shaped magnetic lines generated by means of external magnets and of a strong toroidal current induced in the conducting plasma. The plasma is kept in high vacuum conditions to avoid impurities inside a vessel (vacuum vessel). A view of the ITER configuration is shown in Figure 1.1, where the vacuum vessel and the external magnet system are highlighted. A more detailed description of the machine can be found in [4].

Regarding equation (1.1), a first issue is the availability of the thermonuclear fuel deuterium (D) and tritium (T). While deuterium is largely available in seawater, the radioactive hydrogen isotope tritium is scarce on earth. As a result, tritium must be bred in-situ in the nuclear fusion reactor in order to be economically used for energy production. For this purpose, lithium (Li) is used, which offers two important breeding reactions with neutrons for the tritium production in the reactor:

$$^{6}\mathrm{Li} + \mathrm{n} = \mathrm{T} + {}^{4}\mathrm{He} + 4.8\ \mathrm{MeV}, \tag{1.2}$$

$$^{7}\mathrm{Li} + \mathrm{n} = \mathrm{T} + {}^{4}\mathrm{He} - 2.466\ \mathrm{MeV}. \tag{1.3}$$

The second aspect is the utilization of the large amount of energy produced in the nuclear reaction in form of kinetic energy of the particles. This kinetic energy is transformed through the interaction with the matter of the surrounding components in heat that has to be extracted and used for electrical energy production.

Hence, the generation of tritium and the high-grade heat extraction with a coolant for electrical energy production are the main functions that the components surrounding the plasma have to fulfill in order to allow for the continuous fuelling of the machine and to exploit it economically.

The components that accomplish these functions are the so-called breeding blankets, which are large and complex in-vessel components that constitutes about 85% of the inner wall of the vacuum vessel. Several breeding blanket concepts have been proposed and already intensively studied from the 80s based on combinations of different structural materials (e.g. ferritic-martensitic steels, vanadium alloy), coolants (e.g. water, He) and breeding materials (e.g. Li alone in liquid form, as liquid metal alloys or in form of solid compounds) [5]. In the EU, two concepts, namely the Helium Cooled Pebble Bed (HCPB) and the Helium Cooled Lithium Lead (HCLL) blankets, are presently under investigation and have been selected for tests in the ITER program [6]. One of the goals of ITER is to contribute to the construction of a Demonstration fusion reactor (DEMO) already in the mid of this century [7], which will be the last step before the realization of a commercial fusion power plant.

In the meantime, the construction of ITER will be completed. The purpose of ITER is to achieve the most important milestones on the path to a fusion power plant, especially robust burning plasma regimes, the test of the conventional physics solution for power exhaust and the validation of the breeding blanket concepts [7].

Although ITER will not have a functional breeding blanket system, as tritium autonomous generation and electricity production are not in the scope of this machine, it will provide a test bed for several breeding blanket mock-ups called Test Blanket Modules (TBM) [2].

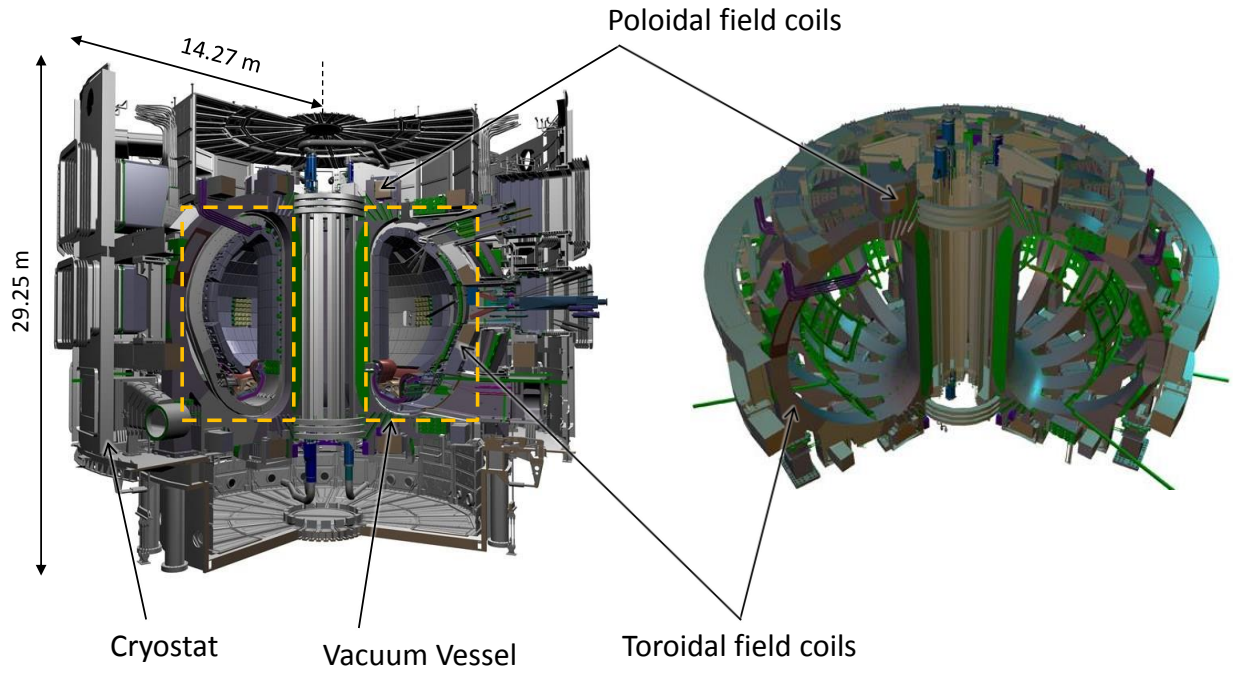

Figure 1.1: Model of ITER with highlighted vacuum vessel (left) and magnets in ITER (right) [8]

1.2 Motivation of this work

The blanket systems in a fusion reactor are subjected to high mechanical and thermal loads. During the entire operating scenario, a main contribution to the high mechanical loads is related to static and transient electromagnetic effects. Mainly two categories of electromagnetic forces are expected to act on the blanket in a nuclear fusion reactor:

(1) Maxwell forces due to the interaction among the magnetized material and the external magnetic field generated by the plasma and poloidal and toroidal coils;

(2) Lorentz's forces caused by the interaction of the magnetic field with eddy currents induced in the electrically conductive structure during electromagnetic transients (e.g. plasma disruptions or vertical displacement events (VDE)).

While Maxwell forces are static forces, whose main effect is to pull the blanket towards the center of the tokamak, high Lorentz forces are generated during fast magnetic field changes generally associated to plasma instabilities with plasma current quench (disruptions) time constants in the order of few tens of ms [9].

During the experimental campaign in ITER, the Test Blanket Module (TBM) will experience similar electromagnetic loads. The TBMs are made of low activation ferritic-martensitic steels, which are magnetic materials. These steels are also considered to be used in DEMO. Moreover, plasma transients following large disruptions are expected relatively frequently during operation. Hence, a part of the validation of the TBM in ITER will deal with these electromagnetic phenomena and with the validation of computational tools.

Especially with regard to the development of future blanket systems for DEMO, it is of importance to develop the engineering models and codes to a high degree of confidence and to check the accuracy of theoretically calculated effects of the environmental conditions on the blanket systems. For this reason, a force reconstruction method that is able to estimate the forces on the TBM in ITER is an essential part of the development of these models and codes.

A pure numerical or theoretical approach has the essential limitation that it is entirely based on theoretical models, which include a significant amount of assumptions and simplifications. For example, in order to reduce the dimension of the FE model mesh and, consequently, the computational time, sub-components that present complex internal structures are usually represented in the FE model using a uniform solid with equivalent physical properties. On the other hand, limitations of the existing simulation codes do not allow the implementation of full self-consistent physical models when particular phenomena are taken into account. One case is the generation of Halo currents that occurs when the plasma collides with the surrounding structure of the vacuum vessel. The effect of these currents (order of magnitude of about 1 MA) flowing out of the plasma through the structure and back in to the plasma [10] is usually calculated separately with an ad-hoc simulation code and only afterwards combined with the results obtained from the FE analysis.

The force reconstruction method has to be part of a system that is directly integrated in ITER in order to reconstruct the forces acting on the TBM during operation. In addition, it is essential that the implemented force reconstruction method is independent from theoretical models a priori fed in. A system in combination with a force reconstruction method that can be used for this purpose has to fulfill the following requirements:

- It has to be able to estimate 3-dimensional forces, that are distributed over the structure,
- it has to have a low sensitivity to modelling errors and
- the type and technology of the sensors have to be usable in a fusion environment allowing for force reconstruction.

However, up to now, no system and force reconstruction method is available meeting all of the mentioned requirements.

For that reason, the aim of this work is to develop a system and method that are applicable in ITER based on an arrangement of sensors that is able to cope with the environmental conditions in a fusion reactor. This is supported by the development of an experimental setup and corresponding mock-ups in order to demonstrate the applicability of the force reconstruction method to the TBM in ITER. A detailed description of the approach is outlined in the next section.

The described aim of this work constitutes the first of three stages towards the final implementation of the system in ITER. The second stage will be dedicated to the validation of electro-magnetic codes based on a simple structure and the third stage comprises the installation of the system in ITER.

1.3 Overview

In Chapter 2, the TBM is introduced and the boundary conditions are defined. The boundary conditions consist of high forces due to electromagnetic effects and the weight of the TBM as well as high maximum temperatures of about 550 °C and a high thermal gradient across the TBM. This poses strong requirements on the fixation of the TBM in ITER, which is addressed by the development of a new concept of an attachment system as part of this work. The concept able to fulfill the requirements is presented and put in relation to former concepts and approaches elaborated in the past.

In Chapter 3, the force reconstruction methods suitable for the application to the TBM are deduced. After a short introduction into force reconstruction, the state of the art is discussed introducing also the related terminology and concepts. In Section 3.3, the already existing force reconstruction methods are evaluated with regard to the application to the TBM. The Augmented Kalman Filter, a combined deterministic-stochastic approach, is selected from the already existing methods and extended to meet the requirements for the intended application.

In addition, a new method for force reconstruction that combines the advantages of a combined deterministic-stochastic method and an optimization algorithm is developed. The algorithm based on a model predictive controller is proposed for the first time to be used as force reconstruction method. Furthermore, a new genetic algorithm specially adapted for the general sensor placement related to force reconstruction is presented.

In Chapter 3.4, possible sensor types and technologies that can be used for the proposed force reconstruction methods are discussed. At first, the harsh environmental conditions consisting of high temperatures, high electromagnetic fields and high radiation, which pose strong requirements to the sensors, are presented. After that, a possible sensor configuration consisting of a dedicated arrangement of strain sensors is described based on a brief review of related sensor technologies representing the reference configuration for the subsequent part of the work.

In Chapter 4, the experimental validation and the test mock-ups are described. A testing device able to generate the necessary excitation forces is developed. In addition, two related mock-ups are designed based on FEM analyses and their relevance for the experimental validation with regard to the real TBM is demonstrated. Finally, a new performance criterion for the evaluation of reconstructed forces is formulated and the possibility to validate the force reconstruction methods for distributed forces with the experimental setup is shown.

In Chapter 5, the two force reconstruction methods are studied and compared based on numerically generated sensor data, which also allows investigating the influence of modelling errors on the reconstructed forces. For this purpose, a set of test cases is defined to represent a complete set of possible excitations.

Chapter 6 is dedicated to the experimental setup and the experimental results. At first, the detailed design and fabrication of the experimental setup and mock-ups is presented. Then, the model identification is described and the results for the test cases are given. Based on the results, a new way to define the accuracy of a force reconstruction system in analogy to a force transducer is developed.

Finally, the main results are summarized in Chapter 7 and based on them an outlook of future developments to be conducted is provided.

2 Test Blanket Module and attachment system

The Test Blanket Module can be considered as a mock-up of a breeding blanket concept developed for the DEMO reactor that will be tested for the first time under a relevant and integral fusion environment in ITER. It constitutes one of the most important parts of the technological testing exploitation of the ITER machine with a large founded program active in the EU since the 90s. It has to provide information on the performance of the tested blanket concepts related to tritium breeding, the conversion of the energy coming from the plasma into thermal energy and the transmission of this thermal energy to the cooling circuit.

In total six different TBM concepts are going to be installed in ITER, which implement different concepts of tritium breeding or cooling media. In addition, four versions of each TBM concept will be tested with specific objectives in the following order: the Electro Magnetic module (EM-TBM), the Thermal/Neutronic module (TN-TBM), the Neutronic/Tritium & Thermo-Mechanic module (NT/TM-TBM) and the Integral TBM (INT-TBM). During the testing phase of the EM-TBM, only pure hydrogen plasmas or hydrogen and helium plasmas will be generated. For this reason, the EM-TBM will not be exposed to neutron or gamma radiation.

Two of these blanket concepts are developed in the frame of the European Breeding Blanket Program. One of these concepts, the Helium Cooled Pebble Bed (HCPB) blanket design, has been developed at KIT. Characteristics of this design are the use of a ceramic breeding material and the beryllium multiplier in form of pebble beds and helium at high pressure as coolant. The pebble beds are divided into several compartments, the so-called Breeder Units (BU), each of them containing a ceramic breeder and a beryllium neutron multiplier material in form of pebble beds. In total, the HCPB TBM consists of 16 BUs in two rows. A purge gas flow of helium at low pressure is used to extract the generated tritium from the ceramic breeder pebble bed. Figure 2.1 shows the HCPB TBM and indicates the orientation of the TBM in relation to the vacuum vessel by the directions poloidal, toroidal and radial [11]. The definition of these directions is based on the torus-like shape of the vacuum vessel and illustrated in Figure 2.2. The location of the HCPB TBM in ITER next to another TBM concept in Equatorial Port Plug 16 can be seen as well in Figure 2.2.

Inside the port plug frame, the TBM is connected to a water-cooled shield [12], which has the task to shield the components behind the TBM from neutron irradiation. The connection interface between TBM back plate and shield is highlighted in Figure 2.3. The connecting parts in-between these two components are not shown in Figure 2.3.

The connection is established by a so-called attachment system. The design of this system is especially interesting, as it has to be stiff to withstand the external mechanical loads, e.g. electromagnetic forces, but flexible enough with respect to thermal expansions in order to avoid the formation of large stresses. These contradicting requirements are described in detail in Section 2.1. In KIT, this issue has been studied since many years with the proposal of several solutions. An overview of these concepts including the actual status is given in Section 2.2. As part of this work, different concepts have been investigated and further improved as well as a new concept for the attachment system has been developed. The new design is also presented in Section 2.2.

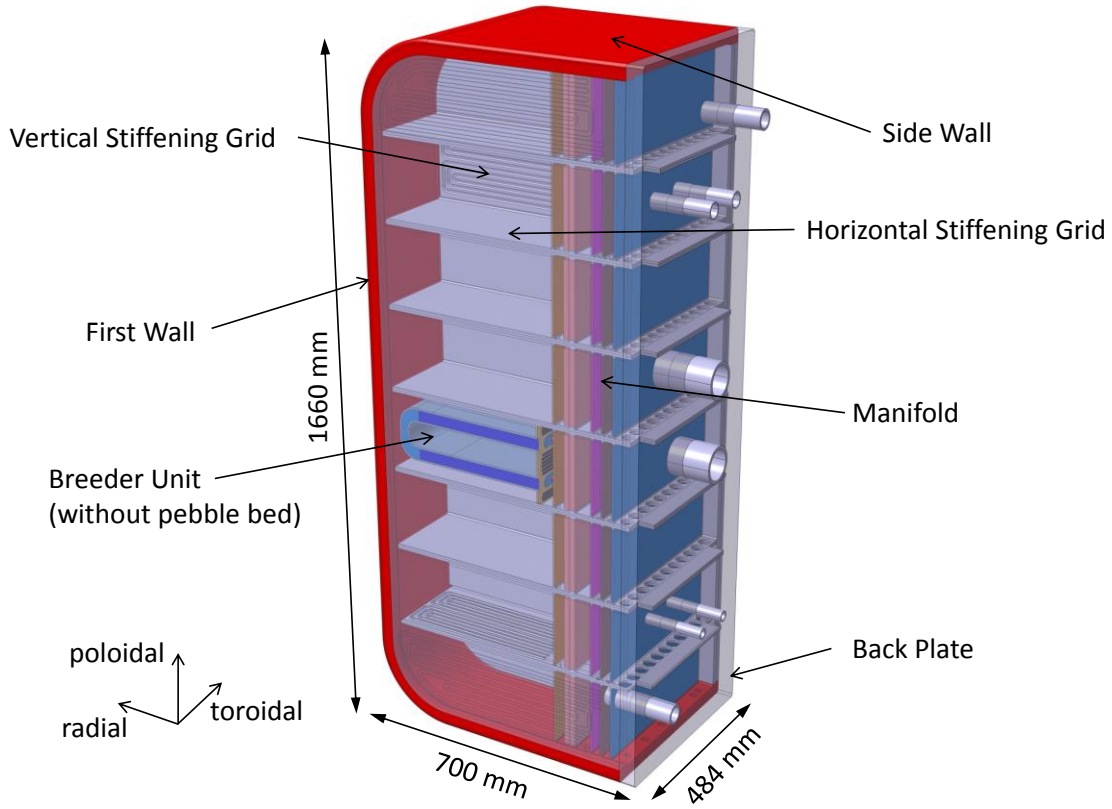

Figure 2.1: Semi-transparent view and components of the Test Blanket Module (TBM) [11]

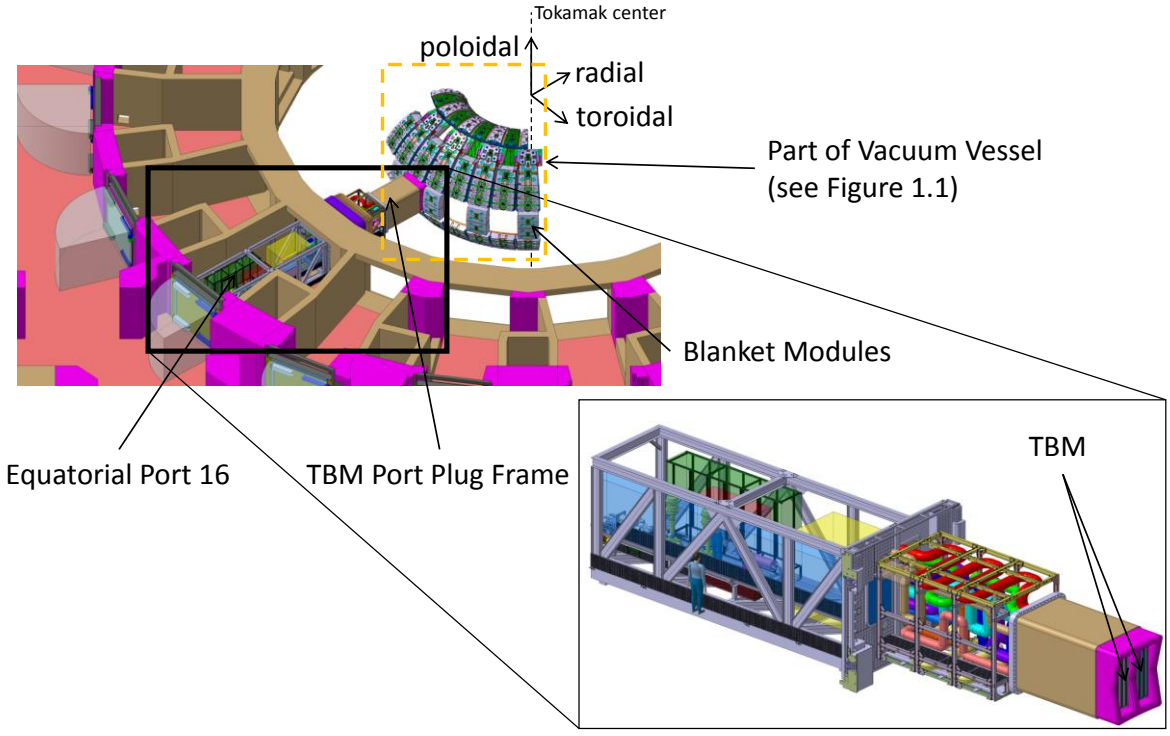

Figure 2.2: Location of the TBMs in Equatorial Port 16 of the ITER configuration [12]

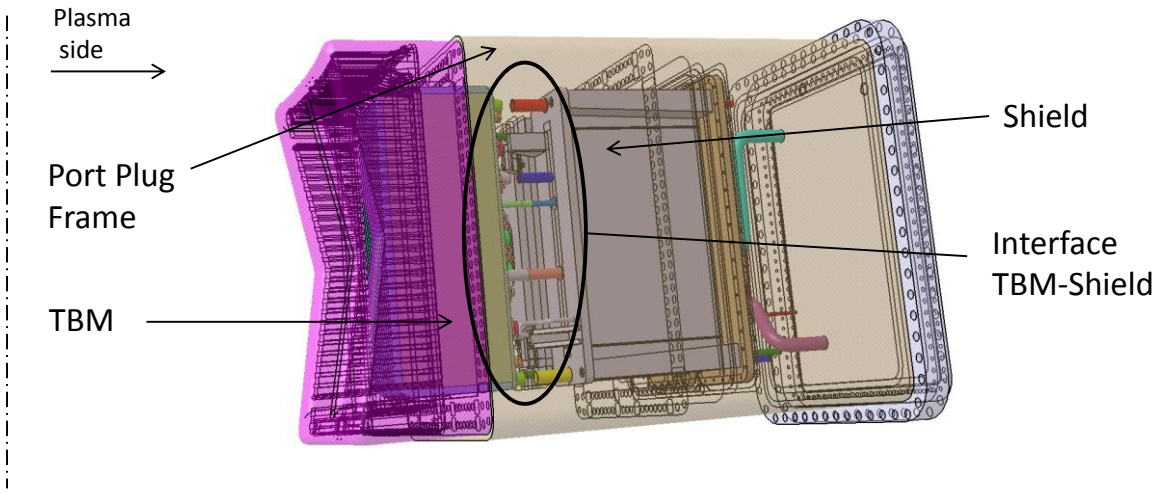

Figure 2.3: Interface TBM-Shield inside the Port Plug Frame adapted from [12]

2.1 Boundary conditions

The boundary conditions of the TBM that have to be considered for the design of the attachment system can be divided into thermal and mechanical boundary conditions. The thermal boundary conditions, which lead to a differential thermal expansion between back plate and shield, demand for a flexible attachment system able to accommodate this relative motion. On the other hand, in order to withstand the high mechanical loads on the TBM, an attachment that reacts rigidly to the mechanical loads is preferable.

2.1.1 Thermal boundary conditions

The thermal boundary conditions have to be distinguished according to different operating states. During the D-T high duty phase, the TBM has a temperature of about 550 °C at the First Wall and 300 °C at the back plate [13]. Figure 2.4 shows the corresponding temperature distribution of a quarter model, which can be considered as steady-state condition during the 400 s-plateau phase of a typical plasma pulse. The higher thermal expansion of the First Wall in contrast to the back plate leads to a warping of the back plate.

Another operating state that has to be considered is tritium outgassing. In order to accelerate the removal of tritium from the BUs, the temperature of the whole TBM is kept at 500 °C [14]. The temperature of the shield is assumed to be at 120 °C at any operating state based on [15].

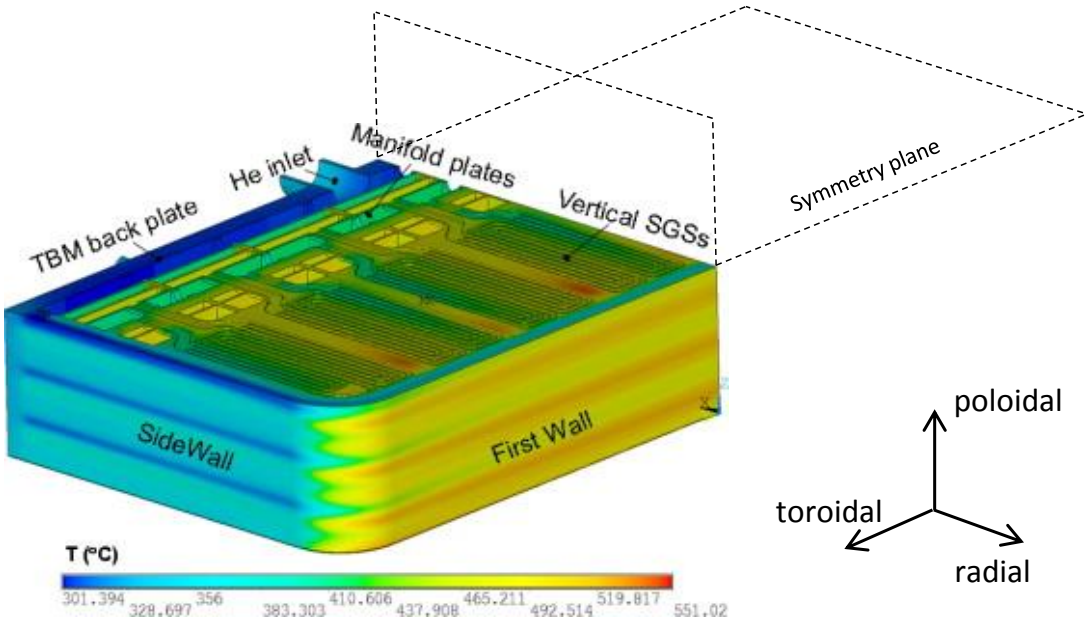

Figure 2.4: Temperature distribution on a quarter model of the TBM in Figure 2.1 during the D-T high duty phase [13].

2.1.2 Mechanical boundary conditions

The mechanical boundary conditions consist of forces due to electro-magnetic effects and the weight of the TBM, which is of about 2 tons. Two important electro-magnetic effects that have to be considered for the design of the attachment system are plasma disruptions and vertical displacement events (VDE). During a plasma disruption, the plasma thermal energy and current are rapidly reduced to zero as a consequence of a loss of confinement. The VDE describes an undesired vertical plasma movement due to a failure of the feedback control system. The different electro-magnetic effects are categorized according to their frequency of occurrence. The electro-magnetic effects that have to be considered for the design of the attachment system are summarized in operating condition category II. The most severe electro-magnetic loading condition belonging to this category is a type II vertical displacement event (VDE) with a duration to zero plasma current equal to a type II plasma disruption. This plasma event generates high Lorentz's forces as high eddy currents are induced in the structure of the TBM box due to the plasma disruption. In addition, Maxwell forces, which apply on magnetized bodies, are acting on the TBM box. The type of the events refers to the duration to zero plasma current. The maximum force values to be expected for the different event types are taken from Cismondi [16] and listed in Table 2.1. They are used for the static analyses.

	Maxwell	Disruption II	VDE II	Weight	Total
Radial force	370 kN	-88 kN	-	-	282 kN
Toroidal force	-	27 kN	-	-	27 kN
Poloidal force	-	-50 kN	90 / -90 kN	-20 kN	20 / -160 kN
Toroidal torsion	-	42 kNm	-	-	42 kNm
Poloidal torsion	-	142 kNm	-	-	142 kNm
Radial torsion	-	360 kNm	-	-	360 kNm

Table 2.1: Maximum electro-magnetic and inertial loads during a vertical displacement event (VDE) II used for static analyses.

For the transient analyses, the time evolution of the forces of Roccella et al. [9] for the TBM in horizontal arrangement are combined with the maximum values equal to the static analyses. The graphs in Figure 2.5 show the time history of forces and moments for a VDE II applied in the transient analyses. The first 8 ms are an artificial ramp-up procedure to normal operation conditions only used in the simulation without considering transient effects.

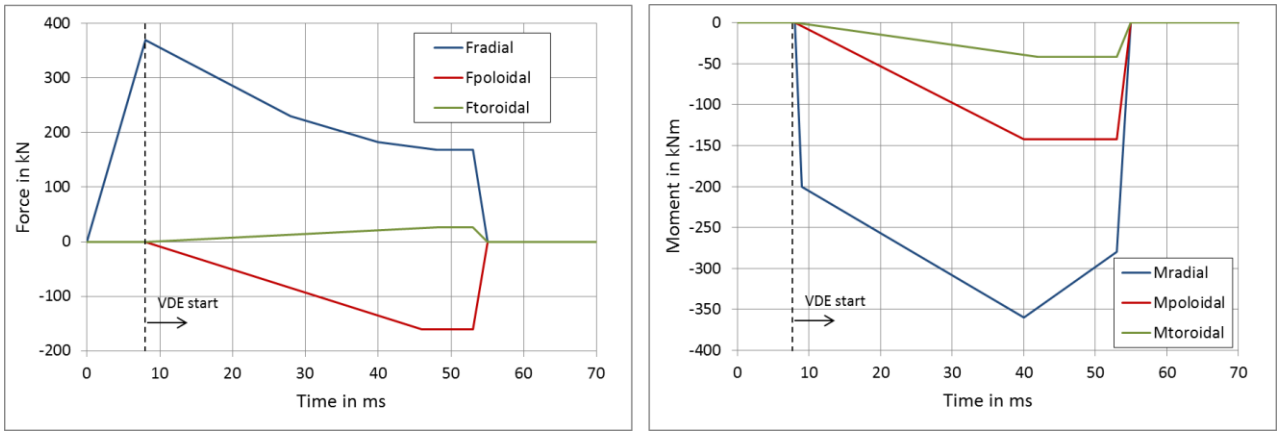

Figure 2.5: Time evolution of the mechanical loads during a VDE II (start at t=8 ms): Forces (left) and moments (right) in relation to the center of the back plate and directions as indicated in Figure 2.1 (based on [9] and [16]).

2.2 Overview of the development of attachment system concepts

The thermal and mechanical boundary conditions pose challenging design requirements to the attachment system. For that reason, over the last years many different designs have been developed by different research groups. Two main aspects have to be considered during the design phase of a concept of the attachment system. Firstly, the TBM has to cope with a temperature span from 550 °C at the first wall to about 300 °C at the back plate during operation. The water-cooled shield, to which the TBM is connected, is kept at a temperature of about 120 °C only. As the TBM is mounted to the shield at room temperature, this leads to different thermal expansions of the TBM and shield throughout the entire operational regime. As the attachment system is the connecting element between TBM and shield, it has to be considered that the attachment system is able to accommodate the relative movement between TBM and shield in order to avoid the formation of high stresses. The second aspect to be considered is the high external loads caused by the electro-magnetic forces. In order to be able to transfer these high forces from the TBM to the shield, the attachment system has to be sufficiently stiff. These two aspects are taken into account in different ways by the attachment system concepts. These contradicting requirements are illustrated in Figure 2.6.

Based on the design of the attachment system for the blanket modules in ITER [17], a concept for an attachment system for the TBM has been developed that addresses the two aspects with two dedicated elements. Four flexible cartridges are used to allow for the different levels of thermal expansion and keys and slots are used to accommodate the high external forces, especially the radial torque, by positive form locking. The concept can be seen in Figure 2.7 [18].

In order to protect the keys against dynamic forces, the keys and the corresponding slots have to remain in permanent contact or at least with very small gaps. This state is difficult to maintain as keys and slots are mounted at room temperature, but under operating conditions, the temperatures differ strongly. This can lead to a loss of contact between key and slot due to the differing thermal expansion and the resulting "banana-shaped" deformation of the TBM box.

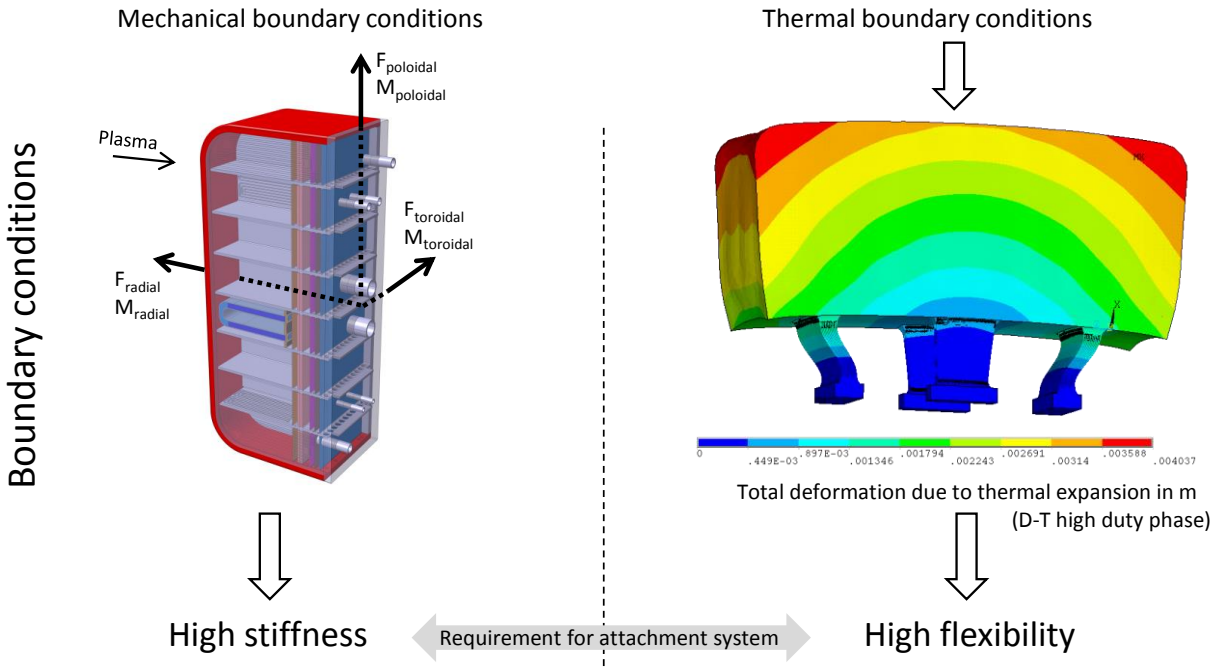

Figure 2.6: Requirements for a blanket attachment system concept. The mechanical (left) and thermal boundary conditions (right) lead to contradicting requirements of high stiffness at simultaneously high flexibility.

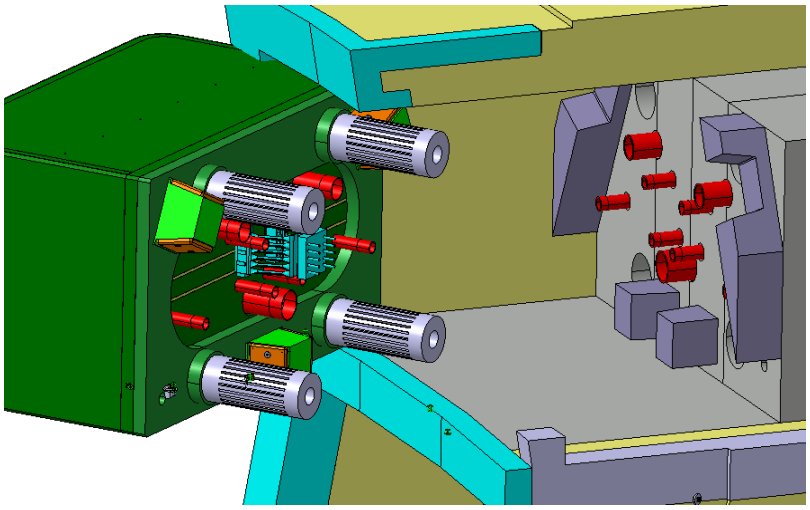

Figure 2.7: Attachment system concept with 4 flexible cartridges and shear keys [18]

A similar concept, developed by CEA, shown in Figure 2.8 consists of a central flexible element to accommodate the thermal expansion and an upper and lower key to resist the high torque [19]. In contrast to the concept with cartridges, only one face of the keys is in contact with the shield. In case the TBM is mounted to the shield in an appropriate way, the contact between key and shield could be maintained under operating conditions. However, there are no details reported about the manufacturing of the 16 central blocks consisting of lamellas as well as its fixation on the back plate.

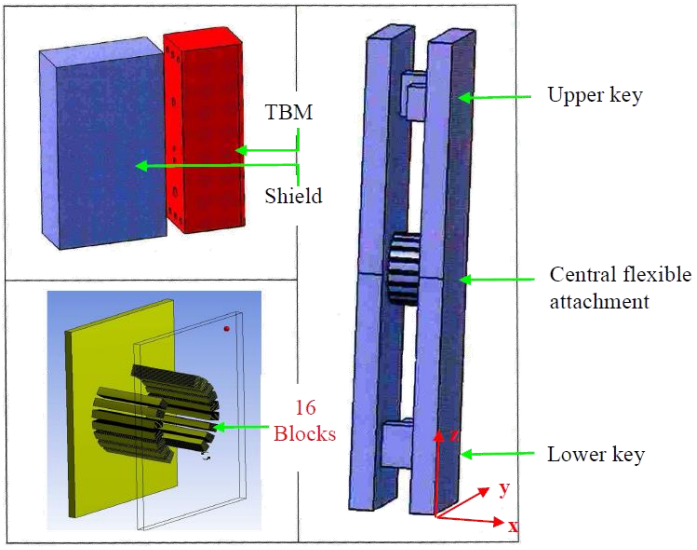

Figure 2.8: Attachment system concept with central flexible element and keys [19]

In order to avoid the problem of gap control between keys and slots, different designs with a joint-like behavior have been proposed. The advantage of these concepts is that all parts are in permanent contact. Two concepts with keys and bolts are depicted in Figure 2.9. The draft design only allows for a rotatory motion [20], whereas the advanced concept can additionally perform a translational motion. Investigations of the advanced concept by Dolensky [21] have shown that the stress level is too high and the pins experience a strong deformation. In addition, the degree of freedom of the joints have to match well the unconstraint displacements of the TBM due to the thermal expansion in order to avoid high stresses.

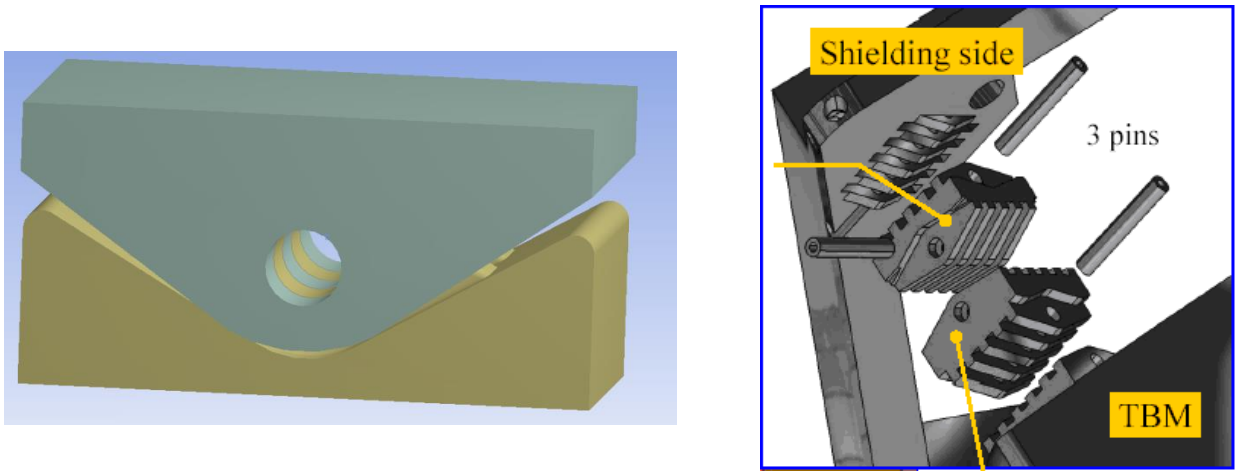

Figure 2.9: Joint-like attachment systems: Draft design (left) [20] and advanced design (right) [21]

As a possible solution to avoid the formation of gaps and to pose less severe constraints on the deformation on the TBM, a concept that only relies on flexible elements was proposed in the frame of the development of the HCPB-TBM at KIT. The design in Figure 2.10 consists of four flexible blocks in radial arrangement around the center of the back plate [22]. Due to the rectangular shape of each block, the block has a higher stiffness in the direction of the long side and a lower stiffness in the direction of the short side. This effect is additionally enlarged as the blocks consist of lamellas. Finally, the blocks are arranged in such a way that the thermal expansion takes place in the direction of the lower stiffness and the high external forces are mainly acting in the direction of the higher stiffness. The high radial torque can be especially well accommodated with this arrangement.

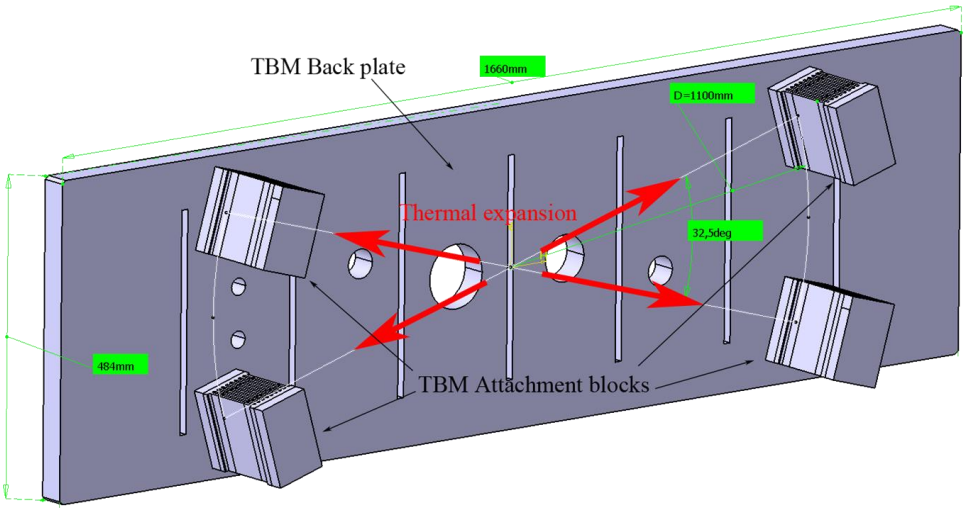

Figure 2.10: Attachment system with 4 flexible blocks with lamellas as proposed in [22]

In preparation for the development of a force reconstruction method on the TBM structure presented in this work, different concepts with flexible attachment blocks have been extensively

investigated. This study includes the influence of the number, arrangement and individual geometry of the blocks with regard to their dimensions, the number of lamellas, the thickness of the lamellas and other design parameters. In addition, several designs for the connection to the back plate and shield have been proposed. The results are discussed in detail in [23, 24, 25].

In order to give an impression on the different possible layouts of the blocks, two of them are presented in Figure 2.11. In Figure 2.12, the latest design of an attachment system with flexible blocks can be seen. As the design of the attachment system has to comply with the design codes that are relevant for ITER, namely RCC-MR [26] and SDC-IC [27], the different concepts have been analyzed in the view of these rules. The evaluation of the stresses of the different designs has shown that the stress levels are very close to the limits given by the corresponding rules or even exceeding them at certain locations. As no significant further improvement of the stress level by local design optimization was expected, the search for a completely different approach seemed to be reasonable. From the investigation of the concepts with flexible attachment blocks, it has been concluded that a design only consisting of flexible blocks is not optimal if the external forces occur from different directions, as the stiffness of the blocks depends on the direction.

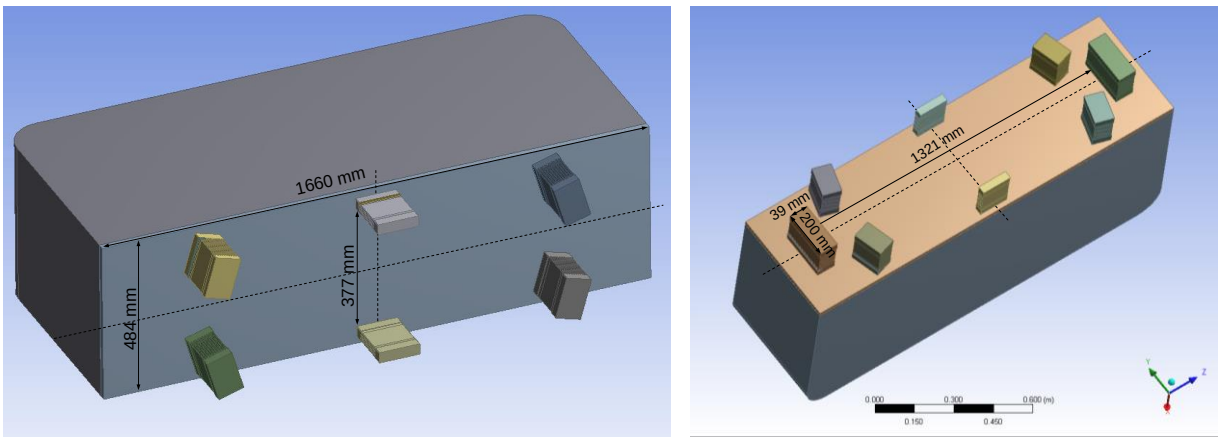

Figure 2.11: Attachment system with 6 (left) and 8 (right) flexible blocks

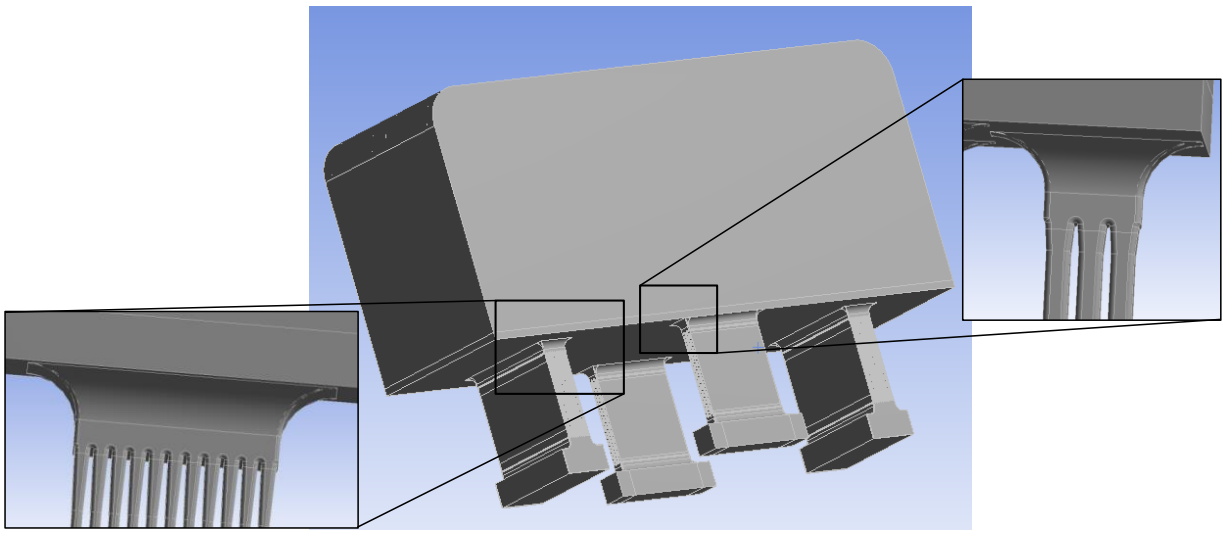

Figure 2.12: Attachment system with 4 flexible blocks representing the latest design of an attachment system with flexible blocks

In order to avoid the use of flexible or joint-like elements, the new approach is based on the idea to place the attachment system at a location where the relative displacements due to the thermal expansion between TBM and shield are small. Consequently, the center of the back plate has been selected for the placement of the attachment system as the TBM expands radially from this point. In order to accommodate the high external forces, especially the high radial torque, an attachment system in the form of a cylinder has been selected, as this shape has the principal capability to resist the forces in all directions and is especially well suited to transfer high torques.

The final design of the attachment system in Figure 2.13 is based on a connecting element in form of a hollow cylinder, in order to be able to route pipes through it. This has only a minor effect on the stiffness of the cylinder. The hollow cylinder has an outer diameter of 420 mm, a wall thickness of 40 mm and a length of 390 mm. As the TBM and the cylinder are made of Eurofer, a reduced activation ferritic martensitic steel, they can be joined by welding. The connection to the shield has to be established by a bolted connection in combination with a splined shaft as the shield consists of stainless steel 316L(N)-IG.

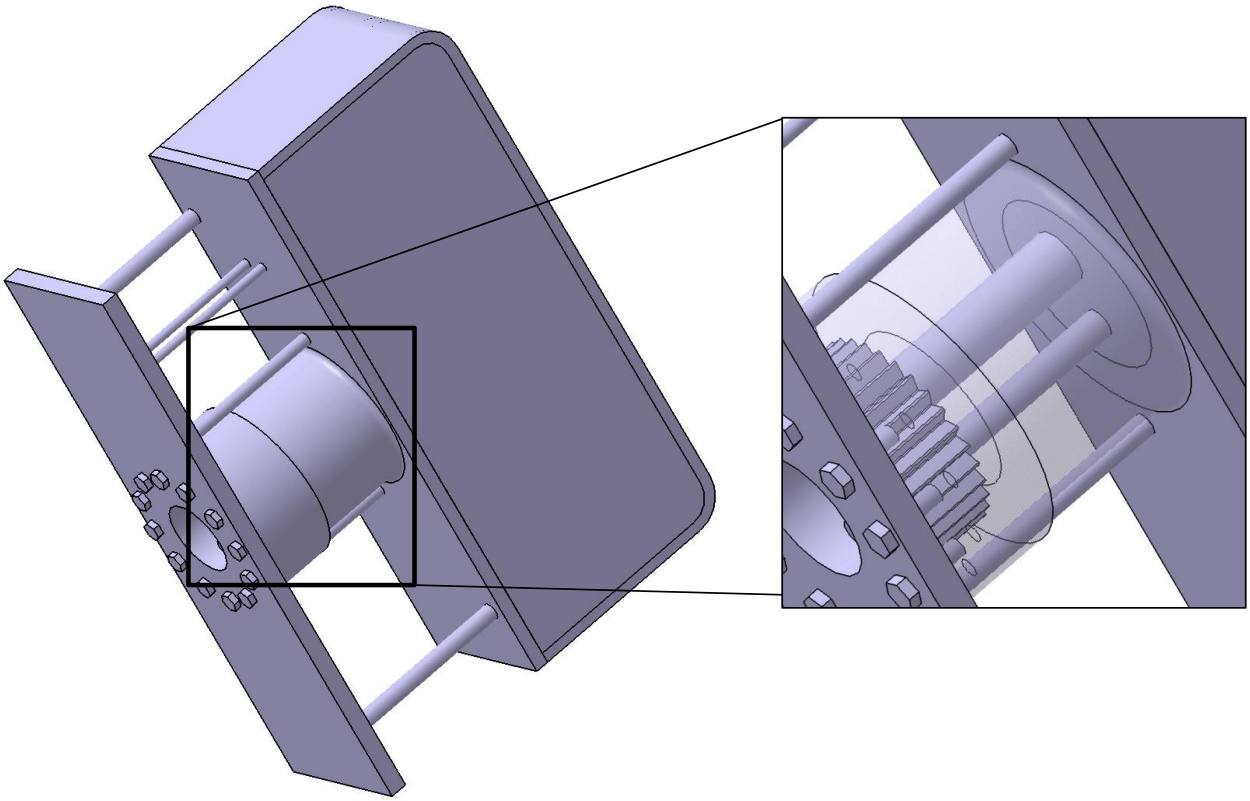

Figure 2.13: Attachment system with hollow cylinder attached to the shield (schematic representation of the shield)

The design of the cylindrical attachment system has to comply as well with the design codes RCC-MR and SDC-IC. Therefore, transient analyses of a VDE II have been carried out to identify the point in time at which the maximum stresses occur. These stresses have to be classified into primary and secondary to be evaluated according to the design rules. As an example, the distribution of secondary stresses and the combination of primary and secondary stresses are shown in Figure 2.14. Due to the symmetric temperature distribution of the TBM

box, the stress distribution of the secondary stresses is also symmetric with maximum stresses along the transition to the back plate. In contrast, the mechanical non-symmetric loads cause local stress concentrations. The evaluation of the design has shown that the concept complies with the design rules as reported in [28, 29].

The attachment system concept based on a hollow cylinder has been developed in the frame of this thesis. This solution represents a possible candidate for the attachment system of the TBM and is suited to be applied in the frame of a force reconstruction method as the load path is well defined and, therefore, it has been selected as reference design for the analyses conducted in this work.

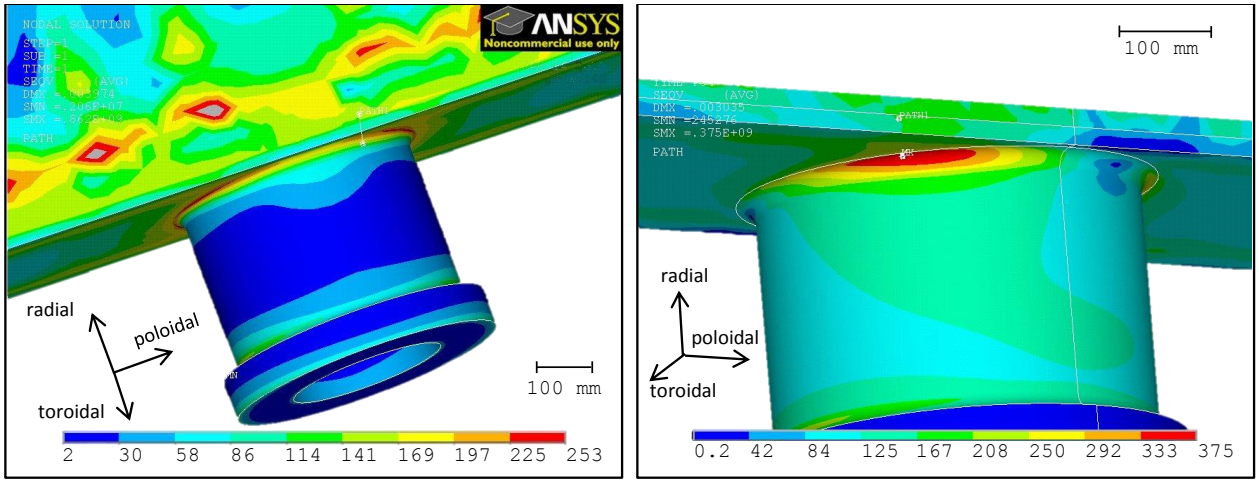

Figure 2.14: Attachment system with hollow cylinder: Secondary von Mises stresses due to thermal boundary conditions in MPa (left) and the combination of primary and secondary von Mises stresses due to thermal and mechanical boundary conditions in MPa (right) at instant of time with highest stresses during a VDE II. The detailed results can be found in [28, 29].

3 Force Reconstruction

The knowledge about the external forces acting on a structure during operation plays a decisive role in the design phase. Here, not only the maximum loads are of interest, but also the load history has to be considered to assess the fatigue behavior. In order to obtain information on the load, either a load transducer has to be placed into the load path or a sensor system has to be mounted or integrated in the structure. A sensor system not being in direct contact with the structure is another option. The selection of an appropriate sensor system depends on numerous factors, as e.g. the properties of the structure and the boundary conditions. Potential sensor types are discussed in detail in chapter 3.4.

Depending on the sensor type, a variety of physical quantities of the system can be acquired. This includes accelerations, displacements or strains. The purpose of force reconstruction is to reconstruct the external forces acting on the structure by relating them to the measured quantities. Depending on the required accuracy, this can be a less complex task, if for example a scale is used to measure a static load. However, it can be more complex if transient external loads acting on a structure have to be determined by sensors not located in the load path.

3.1 Introduction

The measurement types can be grouped in direct and indirect methods [30].

Direct measurement methods relate the measured quantity directly to the desired quantity. In case of a force measurement, this can be realized, for instance, by a load cell located in the load path to detect the external force.

Indirect measurements are lacking of a direct, immediate relation of the measured quantity to the desired one. An indirect force measurement is, for example, the measurement of the closing force of a press by a strain measurement on the frame of the press. Therefore, indirect force measurement methods use the structure itself as force transducer. As a consequence, a precise knowledge of the system properties and its responses to external excitations is essential.

Although a direct force measurement method is preferable due to the simplicity of application, it is often not feasible to place a force transducer into the load path. Major reasons are that a force transducer may

- modify the system properties or
- alter the load path.
- Also the uncertain nature of the forces makes a placement of a sensor difficult.
- In addition, the limitations of a certain sensor type can prevent the use of the sensor at certain locations [31].

Lightweight structures are especially sensitive to an integration of a mass by the installation of a sensor. Also in case of heavy structures, it can be undesirable to introduce additional flexibility in the structure by placing a sensor into the load path. If the forces are not transferred by a mechanical contact or the locations where forces are acting on are not clearly identifiable,

only indirect methods serve an option to assess the load pattern. Furthermore, the boundary conditions in a blanket as e.g. high temperatures, neutron irradiation or hot media may prevent a sensor placement in domains of interest.

An indirect force measurement generally poses a so-called inverse problem [31, 32, 33]. By mathematical means, a pair of a direct (or forward) problem and an inverse problem can be formulated. The inverse problem to be formulated uses a system model, which computes the load pattern based on system responses acquired by the measurement (or model input).

A fundamental difference between the direct and inverse problem is that the inverse problem is most often ill-posed or improperly-posed in the sense of Hadamard [34]. Hadamard states that a mathematical model for a physical problem is well-posed if it has the following three properties:

1. There exists a solution of the problem (existence).
2. There is at most one solution to the problem (uniqueness).
3. The solution depends uniformly continuously on the data (stability). [35]

Hence, if one of these properties is not satisfied, the problem is referred to be ill-posed. The most important property is stability. If the data or measurements are super-imposed by broadband noise the solution does not continuously depend on the data. As a consequence, the true solution cannot be calculated. Another example violating the third condition is the placement of a sensor at a location, where it hardly yields response.

The solution of an inverse problem is given by a transformation of the ill-posed problem into a well-posed problem. Therefore, additional information is added to the solution by means of different regularization methods. Possible regularization methods can be based on, e.g. generalized cross-validation, singular value decomposition, iterative methods, data filtering or Tikhonov regularization [33]:

3.2 State of the art

Indirect force measurement or force reconstruction has been extensively studied during the past years and many different methods have been developed. The methods may be classified into three major categories [33]:

- Deterministic methods,
- Stochastic methods and
- Methods based on artificial intelligence.

In case of the deterministic methods, a model of the system is constructed in such a manner that it relates the outputs of the system directly to the inputs. The system model can be either derived analytically or obtained by a model identification process. For the latter experiments or simulations of the systems are required to identify the model parameters. The obtained model is then formulated either in the frequency domain and/or the time domain.

Stochastic methods are based on statistical relations between output and input. In order to build a regression model of the system, experiments or measurements of the system inputs and outputs during operation have to be performed.

Different approaches based on artificial intelligence can be used for force reconstruction. Prominent examples here are artificial neural networks or evolutionary algorithms. This type of methods, however, necessitates data of the system inputs and the corresponding outputs to conduct the self-learning processes. The database of the inputs and outputs may be obtained by experiments or by simulations.

3.2.1 Deterministic methods

Most of the deterministic methods are based on causal, linear and time-invariant mechanical systems in discrete spatial representation. Before the different force reconstruction methods based on these representations are discussed, the possible representations of these systems are introduced.

These systems can be described by the following system of equations:

$$\begin{aligned} \boldsymbol{M}\,\frac{d\boldsymbol{\psi}^2(\mathrm{t})}{dt^2} + \boldsymbol{D}\frac{d\boldsymbol{\psi}(\mathrm{t})}{dt} + \boldsymbol{K}\boldsymbol{\psi}(t) = \boldsymbol{f}(t) \quad or \\ \boldsymbol{M}\,\ddot{\boldsymbol{\psi}}(\mathrm{t}) + \boldsymbol{D}\dot{\boldsymbol{\psi}}(\mathrm{t}) + \boldsymbol{K}\boldsymbol{\psi}(t) = \boldsymbol{f}(t), \end{aligned} \tag{3.1}$$

with $\boldsymbol{M}$, $\boldsymbol{D}$ and $\boldsymbol{K} \in \mathbb{R}^{n_{dof} \times n_{dof}}$ as the symmetric mass, damping and stiffness matrices with n_{dof} degrees of freedom (dof), the displacement degree of freedom $\boldsymbol{\psi} \in \mathbb{R}^{n_{dof}}$ and the forcing function vector $\boldsymbol{f}(t) \in \mathbb{R}^{n_{dof}}$. This system of equations can be also expressed in continuous state space representation with the state vector $\boldsymbol{x}(t) = \left[\boldsymbol{\psi}(t)\ \dot{\boldsymbol{\psi}}(t)\right]^T \in \mathbb{R}^{2n_{dof}}$ and the n_i-components input vector $\boldsymbol{u}(t) = \boldsymbol{f}(t) \in \mathbb{R}^{n_i}$:

$$\dot{\boldsymbol{x}}(\mathrm{t}) = \boldsymbol{\mathcal{A}}_c\,\boldsymbol{x}(t) + \boldsymbol{\mathcal{B}}_c\,\boldsymbol{u}(t) = \begin{bmatrix} \boldsymbol{0} & \boldsymbol{I} \\ -\boldsymbol{M}^{-1}\boldsymbol{K} & -\boldsymbol{M}^{-1}\boldsymbol{D} \end{bmatrix} \boldsymbol{x}(t) + \begin{bmatrix} \boldsymbol{0} \\ -\boldsymbol{M}^{-1} \end{bmatrix} \boldsymbol{u}(t), \tag{3.2}$$

with the continuous-time system matrix $\boldsymbol{\mathcal{A}}_c \in \mathbb{R}^{2n_{dof} \times 2n_{dof}}$ and the continuous-time input matrix $\boldsymbol{\mathcal{B}}_c \in \mathbb{R}^{2n_{dof} \times n_i}$.

The measured outputs $\boldsymbol{y}(t) \in \mathbb{R}^{n_o}$ are then related to the state vector $\boldsymbol{x}(t)$ and the input vector $\boldsymbol{u}(t)$ by:

$$\boldsymbol{y}(\mathrm{t}) = \boldsymbol{\mathcal{C}}\,\boldsymbol{x}(t) + \boldsymbol{\mathcal{D}}\boldsymbol{u}(t), \tag{3.3}$$

with the output matrix $\boldsymbol{\mathcal{C}} \in \mathbb{R}^{n_o \times 2n_{dof}}$ and the direct feed trough matrix $\boldsymbol{\mathcal{D}} \in \mathbb{R}^{n_o \times n_i}$.

The continuous-time representation of the state-space matrices $\boldsymbol{\mathcal{A}}_c$ and $\boldsymbol{\mathcal{B}}_c$ can be transferred to a discrete-time representation as for example described by Simon [36]. The discrete-time state space formulation of equations (3.2) and (3.3) with the time step k are then given by:

$$\boldsymbol{x}_{k+1} = \boldsymbol{\mathcal{A}}\,\boldsymbol{x}_k + \boldsymbol{\mathcal{B}}\boldsymbol{u}_k, \tag{3.4}$$

$$\boldsymbol{y}_k = \boldsymbol{\mathcal{C}}\,\boldsymbol{x}_k + \boldsymbol{\mathcal{D}}\boldsymbol{u}_k. \tag{3.5}$$

By this the direct problem can be solved by calculating the sequence of output vectors $\boldsymbol{y} = [\boldsymbol{y}_N \quad \boldsymbol{y}_{N-1} \quad \cdots \quad \boldsymbol{y}_0]$ for a given sequence of input vectors $\boldsymbol{u} = [\boldsymbol{u}_N \quad \boldsymbol{u}_{N-1} \quad \cdots \quad \boldsymbol{u}_0]$ and the initial state $\boldsymbol{x}_0$ for times $k = 0 \ldots N$ taking into account that $\sum_{i=0}^{-1} \ldots \stackrel{\text{def}}{=} 0$:

$$\boldsymbol{x}_{k+1} = \boldsymbol{\mathcal{A}}^{k+1}\,\boldsymbol{x}_0 + \sum_{i=0}^{k} \boldsymbol{\mathcal{A}}^i \boldsymbol{\mathcal{B}}\boldsymbol{u}_{k-i}, \tag{3.6}$$

$$\boldsymbol{y}_k = \boldsymbol{\mathcal{C}}\boldsymbol{\mathcal{A}}^k\,\boldsymbol{x}_0 + \boldsymbol{\mathcal{D}}\boldsymbol{u}_k + \sum_{i=0}^{k-1} \boldsymbol{\mathcal{C}}\boldsymbol{\mathcal{A}}^i \boldsymbol{\mathcal{B}}\boldsymbol{u}_{k-1-i}. \tag{3.7}$$

Expression (3.7) can be simplified to:

$$\boldsymbol{y}_k = \boldsymbol{\mathcal{H}}_k^0\,\boldsymbol{x}_0 + \sum_{i=0}^{k} \boldsymbol{\mathcal{H}}_i \boldsymbol{u}_{k-i}, \tag{3.8}$$

where

$$\boldsymbol{\mathcal{H}}_i = \begin{cases} \boldsymbol{\mathcal{D}} & i = 0 \\ \boldsymbol{\mathcal{C}}\boldsymbol{\mathcal{A}}^{i-1}\boldsymbol{\mathcal{B}} & i = 1 \ldots N \end{cases}, \tag{3.9}$$

$$\boldsymbol{\mathcal{H}}_i^0 = \boldsymbol{\mathcal{C}}\boldsymbol{\mathcal{A}}^i \quad i = 0 \ldots N. \tag{3.10}$$

The matrices $\boldsymbol{\mathcal{H}}_i \in \mathbb{R}^{n_o \times n_i}$ are the Markov or discrete impulse response parameters and $\boldsymbol{\mathcal{H}}_i^0 \in \mathbb{R}^{n_o \times n_i}$ represents the influence of the initial conditions $\boldsymbol{x}_0$ on the actual output $\boldsymbol{y}_k$. Equation (3.8) can also be used to obtain the output vector $\boldsymbol{y}_k^0$ for zero initial conditions[1] at time step k:

$$\boldsymbol{y}_k^0 = \boldsymbol{y}_k - \boldsymbol{\mathcal{H}}_k^0\,\boldsymbol{x}_0 = \sum_{i=0}^{k} \boldsymbol{\mathcal{H}}_i \boldsymbol{u}_{k-i}. \tag{3.11}$$

If equation (3.11) is expressed in matrix form, the following equation is obtained:

[1] Zero initial conditions means in this context that accelerations, velocities and displacements are zero for all degrees of freedom.

$$\underbrace{\begin{bmatrix} \boldsymbol{\mathcal{H}}_0 & \boldsymbol{\mathcal{H}}_1 & \cdots & \boldsymbol{\mathcal{H}}_N \\ \mathbf{0} & \boldsymbol{\mathcal{H}}_0 & \cdots & \boldsymbol{\mathcal{H}}_{N-1} \\ \vdots & \vdots & \ddots & \vdots \\ \mathbf{0} & \mathbf{0} & \cdots & \boldsymbol{\mathcal{H}}_0 \end{bmatrix}}_{\boldsymbol{\mathcal{H}}} \underbrace{\begin{bmatrix} \boldsymbol{u}_N \\ \boldsymbol{u}_{N-1} \\ \vdots \\ \boldsymbol{u}_0 \end{bmatrix}}_{\boldsymbol{u}} = \underbrace{\begin{bmatrix} \boldsymbol{y}_N^0 \\ \boldsymbol{y}_{N-1}^0 \\ \vdots \\ \boldsymbol{y}_0^0 \end{bmatrix}}_{\boldsymbol{y}}. \tag{3.12}$$

The mechanical system expressed by the system of equations (3.1) can also be described in modal representation. Therefore, the eigenvalue problem related to (3.1) leads to n_{dof} eigenvectors $\boldsymbol{r}_i$ and eigenfrequencies ω_i. The eigenvectors can be combined in the modal matrix $\boldsymbol{R} = [\boldsymbol{r}_1 \cdots \boldsymbol{r}_N]$. If proportional damping (Rayleigh damping) is assumed, the damping matrix $\boldsymbol{D}$ can be expressed as a linear combination of mass and stiffness matrices $\boldsymbol{M}$ and $\boldsymbol{K}$:

$$\boldsymbol{D} = \alpha \boldsymbol{M} + \beta \boldsymbol{K}. \tag{3.13}$$

In this case, the modal matrix $\boldsymbol{R} \in \mathbb{R}^{n_{dof} \times n_{dof}}$ can be used to diagonalize the system matrices and decouple the equations in the system of equations (3.1). The vector of displacement degrees of freedom $\boldsymbol{\psi}(t)$ can be written as a linear combination of the eigen modes

$$\boldsymbol{\psi}(t) = \boldsymbol{R}\boldsymbol{\phi}(t), \tag{3.14}$$

with the generalized displacements $\boldsymbol{\phi}(t) \in \mathbb{R}^{n_{dof}}$ **.** Subsequently (3.1) is multiplied by $\boldsymbol{R}^T$:

$$\boldsymbol{R}^T \boldsymbol{M} \boldsymbol{R} \ddot{\boldsymbol{\phi}}(t) + \boldsymbol{R}^T \boldsymbol{D} \boldsymbol{R} \dot{\boldsymbol{\phi}}(t) + \boldsymbol{R}^T \boldsymbol{K} \boldsymbol{R} \boldsymbol{\phi}(t) = \boldsymbol{R}^T \boldsymbol{f}(t). \tag{3.15}$$

If the eigenvectors are scaled to a unity modal mass, the following representations hold: $\boldsymbol{R}^T \boldsymbol{M} \boldsymbol{R} = \boldsymbol{I} \in \mathbb{R}^{n_{dof} \times n_{dof}}$, $\boldsymbol{R}^T \boldsymbol{K} \boldsymbol{R} = diag(\omega_i^2) = \boldsymbol{W} \in \mathbb{R}^{n_{dof} \times n_{dof}}$ and therefore $\boldsymbol{R}^T \boldsymbol{D} \boldsymbol{R} = \alpha \boldsymbol{I} + \beta \boldsymbol{W} = \Delta \in \mathbb{R}^{n_{dof} \times n_{dof}}$. Inserting these relations into (3.15) leads to n_{dof} uncoupled linear differential equations:

$$\boldsymbol{I} \ddot{\boldsymbol{\phi}}(t) + \Delta \dot{\boldsymbol{\phi}}(t) + \boldsymbol{W} \boldsymbol{\phi}(t) = \boldsymbol{R}^T \boldsymbol{f}(t) = \boldsymbol{n}(t), \tag{3.16}$$

with the modal force vector $\boldsymbol{n}(t)$.

The representations of causal, linear and time-invariant mechanical systems in discrete spatial representation by a deterministic model and the corresponding parameters and variables are summarized in Figure 3.1.

In the following, the most important force reconstruction methods based on deterministic models are shortly presented always in relation to the previously discussed representations of the system, namely the Inverse Structural Filter, optimization problems, the Partial Modal Matrix method, the frequency domain method and the unknown input observer.

Figure 3.1: Overview of the representations of a causal, linear and time-invariant mechanical systems in discrete spatial representation by a deterministic model. The figure compares the discrete-time and continuous-time representation in form of differential equations and in state-space notation as well as in spatial and modal coordinates. The corresponding notation of the symbols is given in the table below.

Inverse Structural Filter

The Inverse Structural Filter (ISF) is directly related to the discrete convolution in equation (3.11) and was first developed by Steltzner and Kammer [37]. In order to solve the inverse problem for this system, which corresponds to a deconvolution problem, the state space equations (3.4) and (3.5) are modified to interchange input and output.

$$\boldsymbol{x}_{k+1} = \widehat{\boldsymbol{\mathcal{A}}}\,\boldsymbol{x}_k + \widehat{\boldsymbol{\mathcal{B}}}\boldsymbol{y}_k, \tag{3.17}$$

$$\boldsymbol{u}_k = \widehat{\boldsymbol{\mathcal{C}}}\,\boldsymbol{x}_k + \widehat{\boldsymbol{\mathcal{D}}}\boldsymbol{y}_k, \tag{3.18}$$

with

$$\begin{aligned} \widehat{\boldsymbol{\mathcal{A}}} &= [\boldsymbol{\mathcal{A}} - \boldsymbol{\mathcal{B}}\boldsymbol{\mathcal{D}}^{+}\boldsymbol{\mathcal{C}}], \quad \widehat{\boldsymbol{\mathcal{B}}} = \boldsymbol{\mathcal{B}}\boldsymbol{\mathcal{D}}^{+}, \\ \widehat{\boldsymbol{\mathcal{C}}} &= -\boldsymbol{\mathcal{D}}^{+}\boldsymbol{\mathcal{C}}, \qquad \widehat{\boldsymbol{\mathcal{D}}} = \boldsymbol{\mathcal{D}}^{+}, \end{aligned} \tag{3.19}$$

where $\boldsymbol{\mathcal{D}}^{+}$ denotes the Moore-Penrose pseudo-inverse of $\boldsymbol{\mathcal{D}}$. Similar to the direct problem in equation (3.11), the input sequence $\boldsymbol{u}$ can be expressed by a deconvolution for a given sequence of outputs $\boldsymbol{y}$ and initial zero conditions[2]:

$$\boldsymbol{u}_k = \sum_{i=0}^{k} \widehat{\boldsymbol{\mathcal{H}}}_i \boldsymbol{y}_{k-i}^{0}. \tag{3.20}$$

The inverse Markov parameters are now defined by:

$$\widehat{\boldsymbol{\mathcal{H}}}_i = \begin{cases} \widehat{\boldsymbol{\mathcal{D}}} & i = 0 \\ \widehat{\boldsymbol{\mathcal{C}}}\widehat{\boldsymbol{\mathcal{A}}}^{i-1}\widehat{\boldsymbol{\mathcal{B}}} & i = 1 \dots N \end{cases}. \tag{3.21}$$

Steltzner and Kammer discuss several aspects that may occur if the ISF is used by means of the equations (3.20) and (3.21). At first, the pseudo-inverse of the direct feedthrough matrix $\boldsymbol{\mathcal{D}}^{+}$ can only be calculated if it has a full column rank, which is not given by non-minimum phase structural systems. Secondly, the direct feedthrough matrix $\boldsymbol{\mathcal{D}}$ is zero for so-called non-collocated structures where inputs and sensor are not at the same location. In order to overcome these problems, the authors propose to use a non-causal, general „l -lead“ inverse model which is stepping forward in time. This approach yields to:

$$\boldsymbol{u}_k = \sum_{i=0}^{k} \widehat{\boldsymbol{\mathcal{H}}}_i \boldsymbol{y}_{k+l-i}^{0}, \tag{3.22}$$

with the “l -lead” l and the inverse Markov parameters $\widehat{\boldsymbol{\mathcal{H}}}_i$ as defined in (3.21). However, the state space matrices that are used to build the inverse Markov parameters now have to be modified to represent the stepped-forward system:

[2] Initial zero conditions in this context means that accelerations, velocities and displacements are zero for all degrees of freedom.

$$\widehat{\boldsymbol{\mathcal{A}}} = [\boldsymbol{\mathcal{A}} - \boldsymbol{\mathcal{B}}(\boldsymbol{\mathcal{C}}\boldsymbol{\mathcal{A}}^{l-1}\boldsymbol{\mathcal{B}})^{+}(\boldsymbol{\mathcal{C}}\boldsymbol{\mathcal{A}}^{l})], \quad \widehat{\boldsymbol{\mathcal{B}}} = \boldsymbol{\mathcal{B}}(\boldsymbol{\mathcal{C}}\boldsymbol{\mathcal{A}}^{l-1}\boldsymbol{\mathcal{B}})^{+},$$
$$\widehat{\boldsymbol{\mathcal{C}}} = -(\boldsymbol{\mathcal{C}}\boldsymbol{\mathcal{A}}^{l-1}\boldsymbol{\mathcal{B}})^{+}(\boldsymbol{\mathcal{C}}\boldsymbol{\mathcal{A}}^{l}), \qquad \widehat{\boldsymbol{\mathcal{D}}} = (\boldsymbol{\mathcal{C}}\boldsymbol{\mathcal{A}}^{l-1}\boldsymbol{\mathcal{B}})^{+}. \tag{3.23}$$

Steltzner and Kammer also found that a finite length ISF can be used to treat difficult non-minimum phase, non-collocated, structural systems. There are different ways to obtain the Markov parameters. Steltzner and Kammer identified the Markov parameters directly from experiments in a least squares sense. Allen and Carne used a modal approach to derive the Markov parameters and developed a delayed, multi-step inverse structural filter (DMISF) which leads to a more stable ISF in most cases [38]. The ISF algorithm of Steltzner and Kammer is presented graphically in Figure 3.2.

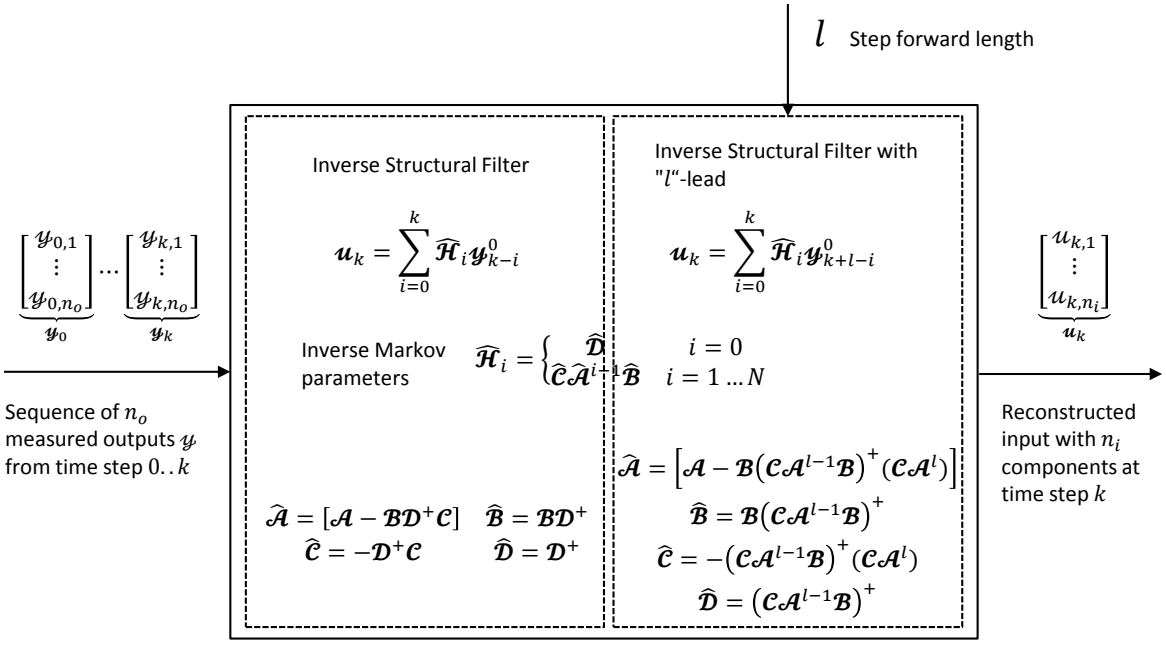

Figure 3.2: Inverse Structural Filter (ISF). The inputs $\boldsymbol{u}_k$ are estimated based on a sequence of measured outputs $\boldsymbol{y}$ by means of a deconvolution. The inverse Markov parameters $\widehat{\boldsymbol{\mathcal{H}}}_i$ are calculated from the system matrices. A stepped forward ISF with "l"-lead is proposed to overcome the problems of non-minimum phase and non-collocated structures.

Optimization problems

A straightforward solution to the problem stated in equation (3.12) would be to solve this equation for the input sequence $\boldsymbol{u}$ by using the pseudo-inverse of the non-square Markov parameter matrix:

$$\boldsymbol{u} = \boldsymbol{\mathcal{H}}^{+}\boldsymbol{y}. \tag{3.24}$$

This approach corresponds to the least squares solution of the problem. However, this produces meaningless results due to the ill-posedness of the problem. To avoid this, a regularization method has to be introduced. One of most commonly used methods is the Tikhonov

regularization or damped least squares, as applied by Nordberg and Gustafsson [39] and Uhl [33]. The minimization problem in equation (3.24) is therefore extended by a regularization term to impose certain restrictions on the solution $\boldsymbol{u}$:

$$\min_{\boldsymbol{u}}\{\|\boldsymbol{\mathcal{H}}\boldsymbol{u}-\boldsymbol{y}\|_2^2+\lambda\|\boldsymbol{L}_i\boldsymbol{u}\|_2^2\}. \tag{3.25}$$

The weighting between the minimization of the residual norm and the minimization of the regularization term is controlled by the regularization parameter λ. $\boldsymbol{L}_i$ is the i-th order Tikhonov matrix. The zeroth-order Tikhonov matrix corresponds to the identity matrix giving preference to solutions with a smaller norm. Figure 3.3 gives an overview of the general parameters and variables involved in an optimization algorithm.

A method often used in the numerical solution of the minimization problem in equation (3.25) is the dynamic programming method. It is based on Bellman's Principle of Optimality and leads to a recurrence formula for the solution of the minimization problem, see e.g. [33, 39, 40, 41]. The regularization parameter λ can be determined by the L-curve method [42] or general cross-validation [43, 32]. Apart from the approach presented here, a vast variety of other optimization algorithms exists to solve this minimization problem.

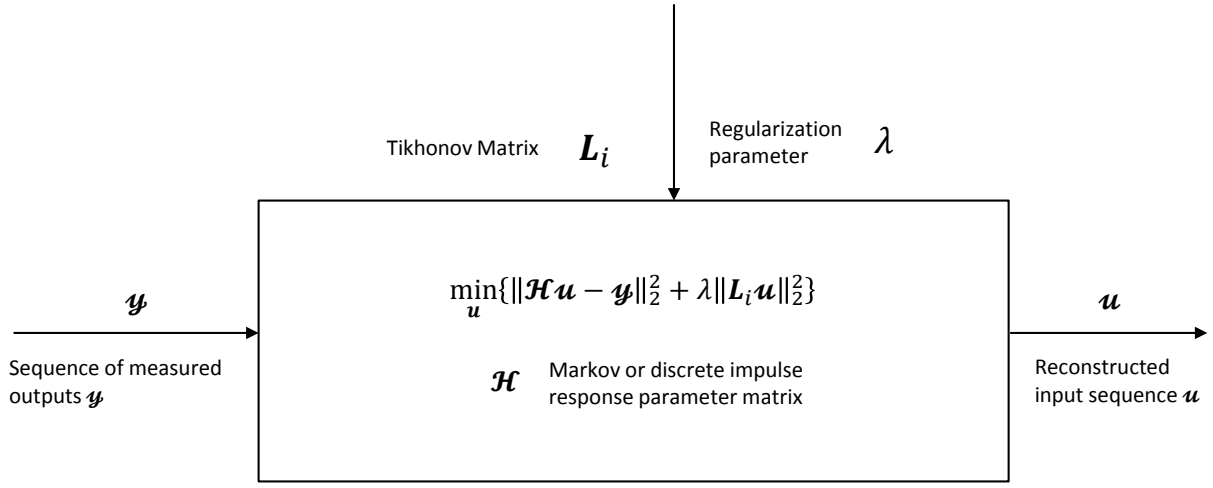

Figure 3.3: Optimization algorithm. Based on a sequence of measured outputs $\boldsymbol{y}$, a minimization problem is formulated, which includes a regularization term. The weighting between the minimization of the residual norm and the regularization term is controlled by the regularization parameter $\boldsymbol{\lambda}$.

Partial Modal Matrix method

In order to be able to apply the Partial Modal Matrix (PMM) method, the mechanical system has to be formulated in modal representation as given in (3.16).

The straightforward solution to obtain the forcing function vector $\boldsymbol{f}(t)$ is to multiply equation (3.16) by the inverse of $\boldsymbol{R}^T$:

$$(\boldsymbol{R}^T)^{-1}\left(\boldsymbol{I}\ddot{\boldsymbol{\phi}}(t) + \Delta\dot{\boldsymbol{\phi}}(t) + \boldsymbol{W}\boldsymbol{\phi}\right)(t) = \boldsymbol{f}(t). \tag{3.26}$$

However, the transposed modal matrix $\boldsymbol{R}^T$ can be inverted only if the modal matrix $\boldsymbol{R}$ is a square matrix. This requires that all eigenvectors for all degrees of freedom of the system have to be identified. A second requirement to allow for a solution of equation (3.26) is the availability of measurements from all degrees of freedom. These two requirements are not matched by most of the considered systems.

In order to overcome these problems, the PMM method uses only partial modal matrices. The PMM $\boldsymbol{R}_{\boldsymbol{P}out}$ links the measured outputs to the generalized displacement $\boldsymbol{\phi}(t)$, velocity $\dot{\boldsymbol{\phi}}(t)$ and acceleration $\ddot{\boldsymbol{\phi}}(t)$. The measured quantity $\boldsymbol{\psi}(t)$, $\dot{\boldsymbol{\psi}}(t)$ or $\ddot{\boldsymbol{\psi}}(t)$ depends on the sensor type and the other quantities have to be derived thereof.

$$\underbrace{\boldsymbol{\phi}(t)}_{n_m\times 1} = \underbrace{(\boldsymbol{R}_{\boldsymbol{P}out})^+}_{n_m\times n_o}\underbrace{\boldsymbol{\psi}}_{n_o\times 1}(t), \qquad \underbrace{\dot{\boldsymbol{\phi}}(t)}_{n_m\times 1} = \underbrace{(\boldsymbol{R}_{\boldsymbol{P}out})^+}_{n_m\times n_o}\underbrace{\dot{\boldsymbol{\psi}}(t)}_{n_o\times 1}, \qquad \underbrace{\ddot{\boldsymbol{\phi}}(t)}_{n_m\times 1} = \underbrace{(\boldsymbol{R}_{\boldsymbol{P}out})^+}_{n_m\times n_o}\underbrace{\ddot{\boldsymbol{\psi}}(t)}_{n_o\times 1}, \tag{3.27}$$

where n_m is the number of considered modes, n_o the number of measured outputs and $n_m \leq n_o$ in order to determine a unique pseudo-inverse of the PMM $\boldsymbol{R}_{\boldsymbol{P}out}$.

The PPM $\boldsymbol{R}_{\boldsymbol{P}in}$ relates the input force vector $\boldsymbol{f}(t)$ to the modal force vector $\boldsymbol{n}(t)$. Hence, equation (3.26) can be solved for a subset of degree of freedom of the system by the use of $\boldsymbol{R}_{\boldsymbol{P}in}$ and the relations in (3.27):

$$\underbrace{\boldsymbol{f}(t)}_{n_i\times 1} = \underbrace{(\boldsymbol{R}_{\boldsymbol{P}in}^T)^+}_{n_i\times n_m}\left(\underbrace{\boldsymbol{I}}_{n_m\times n_m}\ddot{\boldsymbol{\phi}}(t) + \underbrace{\Delta}_{n_m\times n_m}\dot{\boldsymbol{\phi}}(t) + \underbrace{\boldsymbol{W}}_{n_m\times n_m}\boldsymbol{\phi}(t)\right). \tag{3.28}$$

The matrices $\boldsymbol{I}$, Δ and $\boldsymbol{W}$ in equation (3.28) contain only modal parameters of the considered modes and $n_i \leq n_m$ for a unique pseudo-inverse of $\boldsymbol{R}_{\boldsymbol{P}in}^T$.

The PMM method is suitable for non-collocated systems, where, the PMM $\boldsymbol{R}_{\boldsymbol{P}out}$ and $\boldsymbol{R}_{\boldsymbol{P}in}$ are not identical. In contrast, for collocated systems with the same number of inputs and outputs the two matrices are identical. This method was applied by Genaro and Alves [44] and used by Xia et al. [45] for a railway wagon model. The general algorithm with related parameters and variables is shown in Figure 3.4.

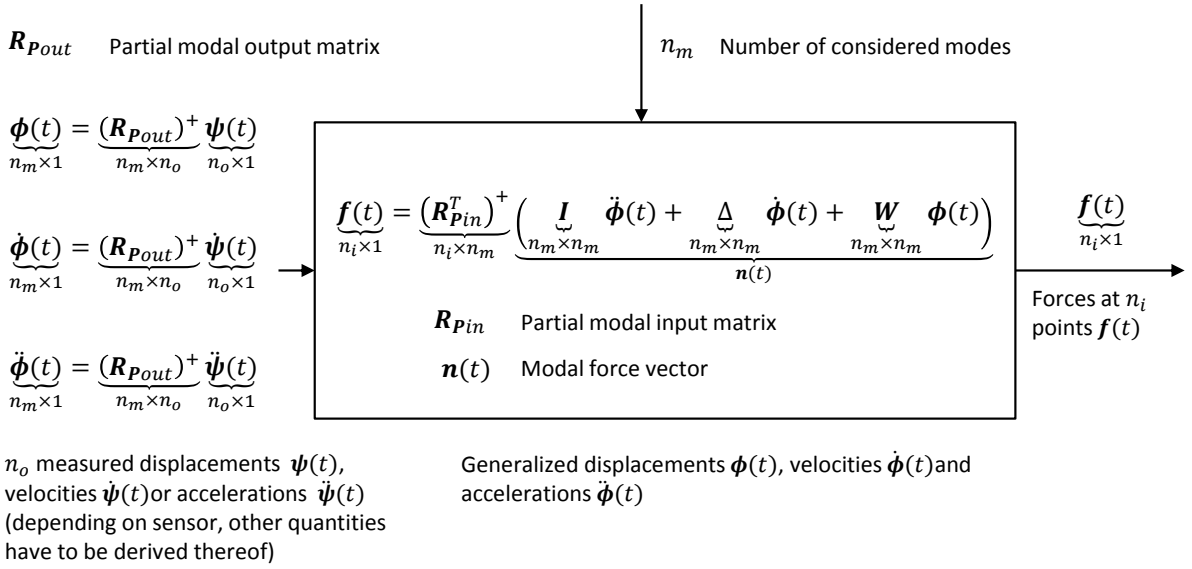

Figure 3.4: Partial Modal Matrix (PMM) algorithm. The model of the mechanical system is formulated in modal representation with a reduced number of modes n_m. The measurements ($\boldsymbol{\psi}(t)$, $\dot{\boldsymbol{\psi}}(t)$ or $\ddot{\boldsymbol{\psi}}(t)$) are linked to the generalized kinematic quantities ($\boldsymbol{\phi}(t)$, $\dot{\boldsymbol{\phi}}(t)$ or $\ddot{\boldsymbol{\phi}}(t)$) by the partial modal output matrix $\boldsymbol{R_{Pout}}$. The modal force vector $\boldsymbol{n}(t)$ is multiplied by the transposed pseudo-inverse of the partial modal input matrix $\boldsymbol{R_{Pin}}$ to obtain the forces $\boldsymbol{f}(t)$ at the input locations.

Another method to be mentioned in this context is the Sum of Weighted Accelerations Technique (SWAT), which is closely related to the PMM method. The SWAT method developed by Gregory, Priddy and Smallwood [46] estimates the sum of forces acting on the center of gravity. The basic assumption is a sufficient "Knowledge of the rigid-body modal coordinates to determine the sum of all externally applied forces" [47]. Therefore, only the generalized accelerations of the rigid body modes $\ddot{\boldsymbol{\phi}}_{rb}(t)$ are extracted from the generalized accelerations $\ddot{\boldsymbol{\phi}}(t)$ in equation (3.27):

$$\underset{6\times 1}{\ddot{\boldsymbol{\phi}}_{rb}(t)} = \underset{6\times n_m}{[\boldsymbol{I}\quad \boldsymbol{0}]}\ \underset{n_m\times n_o}{(\boldsymbol{R_{Pout}})^+}\ \underset{n_o\times 1}{\ddot{\boldsymbol{\psi}}(t)}. \tag{3.29}$$

Finally, the sum of the forces applied to the body is obtained by multiplying the rigid body accelerations $\ddot{\boldsymbol{\phi}}_{rb}(t)$ by the rigid body mass properties. Further insight into this method and related advancements can be found in [48, 49].

Frequency Domain Method

All force reconstruction methods presented so far describe the relation between system inputs and outputs in the time domain. Another approach is to describe this relationship in the frequency domain. Therefore, the input forces $\boldsymbol{f}(\Omega)$ and measured outputs $\boldsymbol{y}(\Omega)$ are related by:

$$\underset{n_o\times 1}{\boldsymbol{y}(\Omega)} = \underset{n_o\times n_i}{\boldsymbol{H}(\Omega)}\ \underset{n_i\times 1}{\boldsymbol{f}(\Omega)}, \tag{3.30}$$

where $\boldsymbol{H}(\Omega)$ is the frequency response function (FRF) matrix. The elements of this matrix represent the FRF for each input-output combination. If the number of outputs n_o exceeds the number of input forces n_i, the pseudo-inverse of $\boldsymbol{H}(\Omega)$ can be used to calculate the input forces:

$$\underbrace{\boldsymbol{f}(\Omega)}_{n_i \times 1} = \underbrace{\left(\boldsymbol{H}(\Omega)\right)^{+}}_{n_i \times n_o} \underbrace{\boldsymbol{y}(\Omega)}_{n_o \times 1}. \tag{3.31}$$

In order to apply this method, the time domain measurement data has to be transferred to the frequency domain by a discrete Fourier transform. This algorithm is illustrated in Figure 3.5. The FRF matrix $\boldsymbol{H}(\Omega)$ can be either determined from measurement data or from the derivation from a modal model. Examples for the frequency domain method can be found in [49, 50].

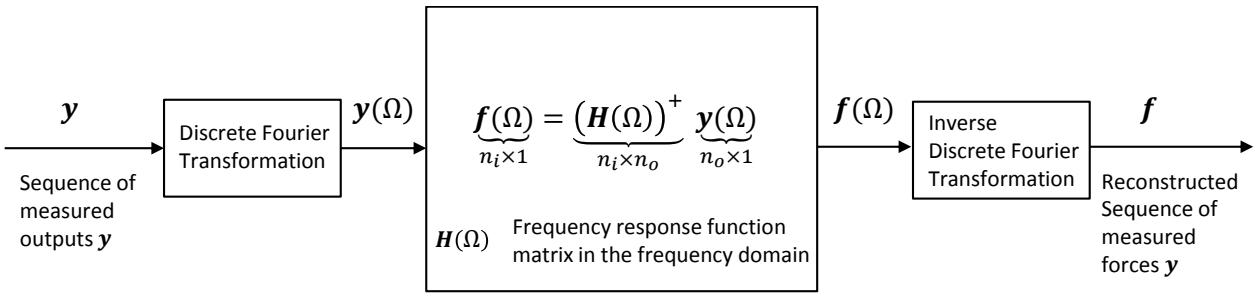

Figure 3.5: Frequency Domain Method. The measured output sequence $\boldsymbol{y}$ is transferred to the frequency domain by a discrete Fourier transformation and subsequently multiplied by the pseudo-inverse of the frequency response function matrix $\left(\boldsymbol{H}(\Omega)\right)^{+}$. The reconstructed forces $\boldsymbol{f}$ are obtained by an inverse discrete Fourier transformation.

Unknown Input Observer

In control theory, the state observer is a well-known concept and frequently used for control tasks. The state observer is based on the state space representation of a system as defined by equations (3.2) to (3.5). Figure 3.6 shows the principle of a state observer: A model of the system is connected in parallel to the real system with equal inputs. The measured outputs and the reconstructed outputs from the model are compared and the difference is fed back into the state observer as observer error.

The model of the system is now controlled in such a way that the observer error is reduced to zero as time evolves and, therefore, the reconstructed states converge to the real states.

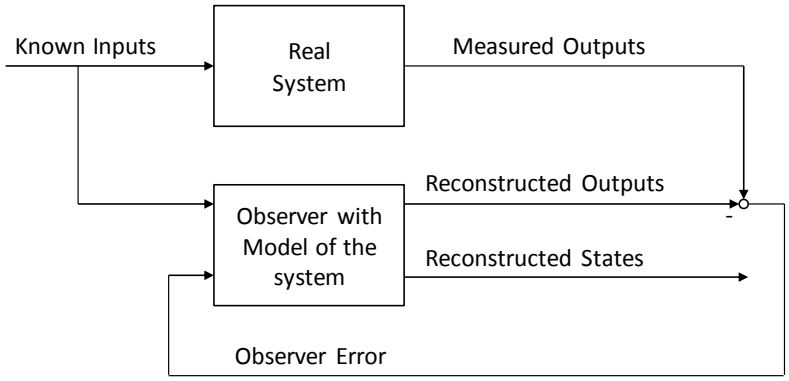

Figure 3.6: Schematic of the logic of a state observer. The observer error, i.e. the difference between the reconstructed outputs and the measured outputs, is fed back to the observer to adapt the estimates of the states.

If the inputs to the system are not known, an observer can also be designed to estimate these unknown inputs. The most common approach to construct an Unknown Input Observer (UIO) is to extend the states by the unknown inputs for a simultaneous estimate of states and inputs. This is depicted in Figure 3.7. One important requirement for the design of an UIO for force reconstruction is a sufficiently fast convergence of the reconstructed states and inputs. A variety of designs for UIOs has been developed and one possible solution, an Augmented Kalman filter, will be discussed in more detail in Section 3.3.1.

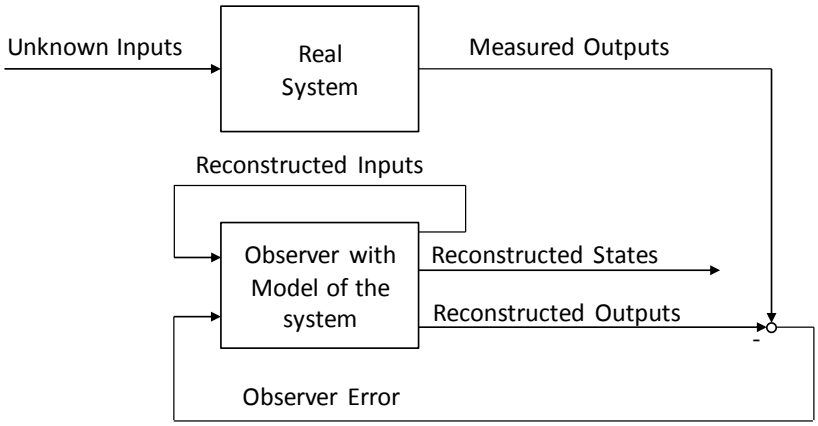

Figure 3.7: Schematic of the logic of an Unknown Input Observer (UIO). If the inputs of the system are unknown, the observer simultaneously estimates the states and the unknown inputs based on the observer error.

3.2.2 Stochastic methods

Stochastic methods are based on elaboration of statistical relations between input and output. Hence, they can also be regarded as a way to solve force identification problems. Although, there are many applications of stochastic methods for this purpose, they are mainly not focused on reconstructing a force history. In contrast to the force reconstruction methods discussed so far, the stochastic methods try to estimate the actual force based on measured parameters. The regression models used in most cases are derived from experimental data or data acquired during

operation. For instance, Haas and Imber use a regression model to identify loads on helicopter components [51].

3.2.3 Methods based on artificial intelligence

Methods based on artificial intelligence summarize all problem-solution methods exhibiting a similar behavior to what is considered as human intelligence. Some of the main characteristics of human intelligence are understanding language, learning, reasoning and solving problems. Since the mid-1950s, different methods have been developed that incorporate these aspects of human intelligence [52]. Examples of these algorithms are [33]:

- Fuzzy Logic,
- Artificial Neural Networks,
- Evolutionary Algorithms.

Fuzzy logic

Fuzzy logic is widely applied in control tasks where classical control technology is difficult to implement. The control rules are specified in linguistic terms and can therefore incorporate the knowledge of experts when a mathematical model of the system is difficult to determine. The values of parameters are first translated according to so-called membership functions into linguistic terms like for example “the temperature is very low, low, medium, high or very high”. This process is called “Fuzzification”. The relations of the input and output variables are then described by linguistic rules, e.g. “If the temperature is high, then set heater to low”. The level of activation is now checked for every rule. The next step is the “Defuzzification”. According to different Defuzzification methods, the levels of activation for each rule are evaluated to generate sharp values as control inputs [53].

Artificial neural networks

Artificial neural networks (ANN) are inspired by their biological counterpart, like for example the human brain, and consist of interconnected neurons.

A single-input neuron, which represents the smallest element of an ANN, is depicted in Figure 3.8. The output a of the neuron is calculated as given in Figure 3.8 with the input p, the weight w and the bias b. A variety of functions can be used as transfer function f. The selection of an appropriate transfer function mainly depends on the problem to be solved.

The transfer functions that are most often used are the hard limit transfer function, the linear and the log-sigmoid transfer function. The hard limit transfer function sets the output to 1 if the argument is larger than 0 or, otherwise, the output remains at 0. For the linear transfer function the output equals to the argument and for the log-sigmoid transfer function, the output is located between 0 and 1 for any argument.

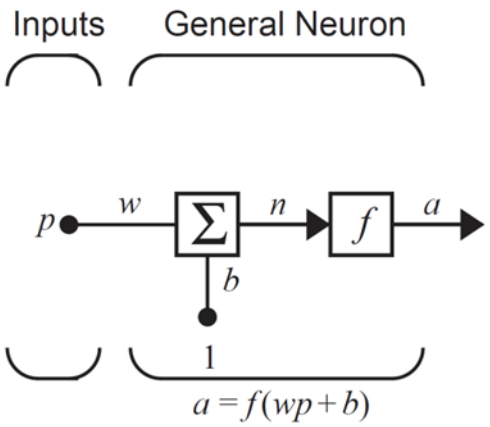

Figure 3.8: Schematic logics of an Artificial Neural Network (ANN). General Neuron from [54]. The output a of the neuron is calculated by the transfer function f with input p, weight w and bias b.

In most cases, one single neuron is not sufficient to describe a system of independent input variables. Therefore, a higher number of neurons may be connected to form layers of neurons. The number of layers and the number of neurons in each layer then defines the architecture of the ANN. Figure 3.9 sketches schematically three layers of an ANN with single neurons receiving multiple inputs. The first layer represents the input layer and the last layer is named output layer. The layers in between are the so-called hidden layers. While the number of neurons in the input and output layer is easy to determine and depend on the numbers of inputs and outputs, the number of hidden layers and neurons in each of these layers can only be predicted for a few problems.

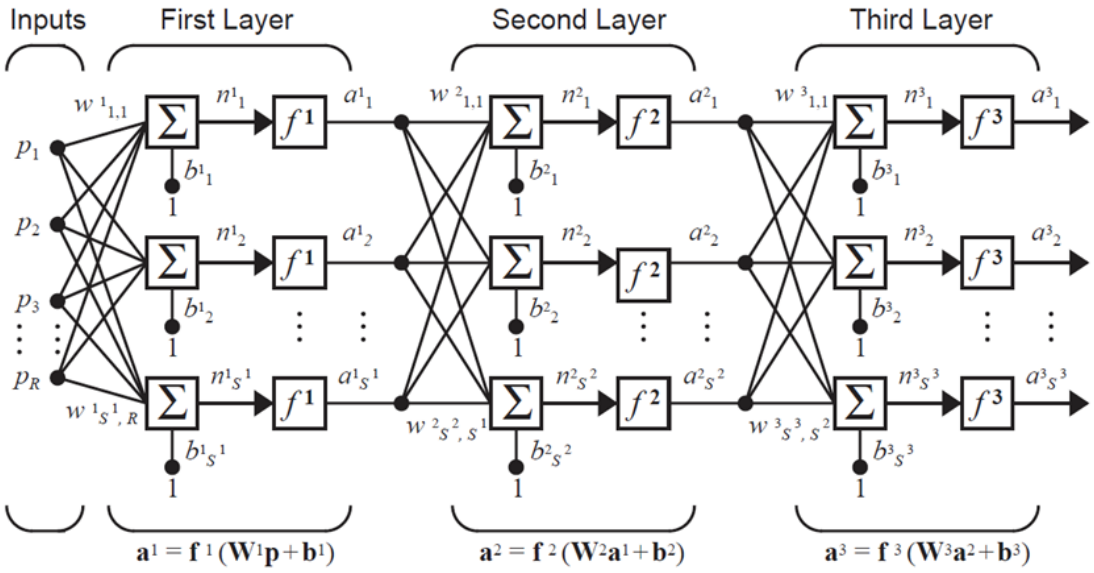

Figure 3.9: Schematic example of the process logics of Artificial Neural Networks based on layers of neurons from [54]

Another important concept for ANN is the use of recurrent layers, which is illustrated in Figure 3.10. Here, the neurons in recurrent layers merge into a delay block D and the output of the neurons is fed back to the input.

The major capability of an ANN is the ability to learn and adapt to a given problem. The learning process means the capability of ANNs to modify the weights and biases of the network. Therefore, different learning algorithms can be applied, which can be classified into three main groups:

- supervised learning,
- reinforcement (or graded) learning and
- unsupervised learning.

During the supervised learning, a set of training samples is given to the network and the output is compared to the desired output. Then the weights and biases are adjusted by a learning rule to move the network outputs closer to the desired values.

In case of reinforcement learning, a sequence of input samples is provided to the network and the performance of the network is rated by a grade, which is used to adjust the network.

The unsupervised learning does not require any output values. Here, the responses of the network are directly compared to the inputs. This learning method is often used for clustering operations [54]. A force reconstruction by means of ANN has been demonstrated by Trivailo and Carn [55], where they used an Elman back-propagation network to assess the aerodynamic loadings on a military airplane by measured strain data.

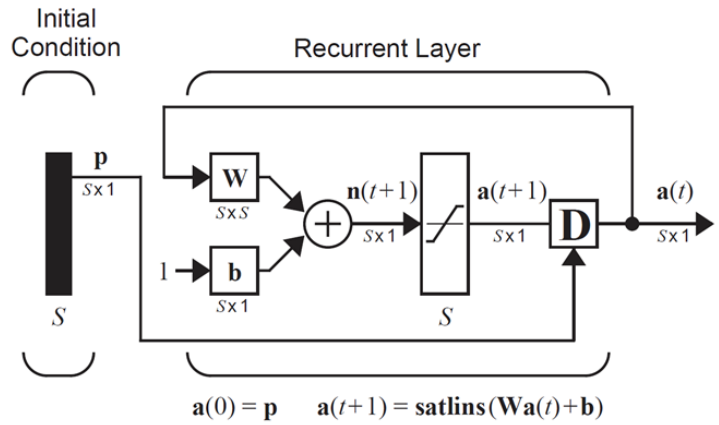

Figure 3.10: Schematic logics of Artificial Neural Networks relying on recurrent layers from [54]

Evolutionary algorithms

Evolutionary algorithms mimic the biological evolution by using similar processes as found in nature. They belong to the class of metaheuristic methods, which finds approximate solutions for numerical and combinatorial optimization problems by means of an iterative progression process. The biological processes utilized in evolutionary algorithm are:

1. Generation of an initial population of individuals,
2. Evaluation of the fitness of each individual by a fitness function,
3. Selection of the fittest individuals for reproduction and
4. Creation of a new generation of individuals involving crossover and mutation.

During the problem solution flow, the processes 2 to 4 are repeated until a predefined termination criterion is matched, which may be given by either the number of iterations or the specified average fitness. The initial population is generated in most cases by a random process. Each of the generated individuals represents a potential possible solution of the problem, which may not necessarily be physical. The definition of the fitness function is the key element in the design of an evolutionary algorithm. The fitness function can either simply correspond to the optimization problem or may contain additional constraints on the possible solutions.

Other important processes are crossover, which exchanges parts of the parameters of parent individuals, and mutation, which randomly changes individual parameters.These two processes are responsible for the creation of new individuals and therefore represent new solutions [56].

The implementation of a generic algorithm belonging to evolutionary algorithms is described in detail in Section 3.4.4 since it is used for the optimization of the sensor placement. This type of algorithm has been successfully employed by Hashemi and Kargarnovin for force reconstruction to identify forces on a simply supported beam [57].

3.3 Force reconstruction on the TBM structure during operation

A method that can be applied for force measurement on the TBM during operation has to be able to reconstruct transient forces with the focus on forces that are generated by electromagnetic effects. These forces are distributed over the structure and have an expected duration of tens of milliseconds. Due to the transient nature of the forces on the TBM, not only the maximum forces are of interest, but also their precise time history. Furthermore, the force reconstruction method has to be based on a number of sensors attached to the structure of the TBM in order to obtain sensor measurements during operation. The number of sensors is limited by the available space for the sensor placement and the signal cables.

The force reconstruction methods have been grouped into three groups: deterministic methods, stochastic methods and methods based on artificial intelligence.

The stochastic methods use a regression model to estimate forces based on measured parameters. However, the focus of these methods is not on the reconstruction of transient forces, but rather on forces at distinct points in time. They are often applied if several different effects have an influence on the system. In addition, the regression model is based on the minimization on data obtained during operation or experiments. Therefore, it has to be assured that the sample data well represents all possible excitations. If an inappropriate high number of parameters is included in the regression model, overfitting [58] may occur and the model loses its ability to predict excitations, which are not included in the sample data.

The methods based on artificial intelligence work with a self-learning process. This learning process requires, similar to the stochastic methods, a set of training data to adapt the parameter of

the model of the system. Here again, the ability to predict excitations that are not contained in the sample date has to be evaluated. This is expressed by the generalization performance [59]. For instance, a stopping criterion for the learning process of the back-propagation algorithm (usually applied for training of multi-layer neural networks) has to be defined, as the learning process cannot be shown to converge [60].

Although several methods have been developed to control overfitting or the generalization performance, it is unreasonable to apply a force reconstruction method in ITER based on sample or training data obtained by experiments, when no reliable estimations can be made, how well the data represents the real excitations in ITER.

In contrast, deterministic methods use a model of the system that directly relates the inputs to the outputs. This means that the model of the system is directly deduced from parameters, which represent the properties of the system and have been identified by a modal analysis or experiments. For that reason, the model is independent of sample data.

The inverse structural filter (ISF) works with a deterministic model. However, a stepped-forward ISF has to be used in order to reconstruct forces on a non-collocated structure, where input and sensors are not at the same location. A method to find the necessary step forward length, the "l-lead", is not specified in the related publications and has been determined by the comparison of the results with different values of the parameter [37]. Another kind of regularization is not included in the algorithm.

The Partial Modal Matrix (PMM) method is based on a deterministic model as well. Due to the modal representation of the system model, the method is well suitable for the estimation of distributed forces. However, additional information in form of a regularization parameter cannot be considered. The frequency domain methods are well suited for the estimation of periodic input signals, which is not the case for the excitation forces on the TBM. If the non-periodic excitations occur with only short time delays, it will probably be difficult to define a sufficiently large time window in order to achieve a high resolution of the discrete Fourier transform.

Up to now, optimization problems have been treated as a general concept. They are based on a deterministic model, which can be represented in spatial as well as in modal coordinates. The possibility to introduce additional information on the solution is given by a regularization term. Force reconstruction methods based on an Unknown Input Observer (UIO) incorporate a deterministic model in spatial or modal representation as well. The regularization can be included in the design of the observer.

From the comparison of the different force reconstruction methods, it can be concluded that a method based on a deterministic model will have a higher reliability than a method based on sample data. In order to reconstruct distributed forces, a modal representation of the system is required to reduce the number of inputs. In addition, the method should include a kind of regularization to provide a higher flexibility on the control of the solution. These requirements are met by optimization methods and the Unknown Input Observer (UIO).

There exist several possibilities for the design of an UIO. A very interesting design was proposed by Laurens et al. [61] as it additionally offers the capability to consider modelling errors. This is achieved by simultaneously estimating the inputs as well as the states of the system. The UIO

was dubbed Augmented Kalman Filter (AKF), because it incorporates the rules of the Kalman filter theory. Although the algorithm is based on a deterministic model, the authors describe it as a stochastic-deterministic approach, due to the stochastic nature of the Kalman filter. In the same work, Lourens et al. have also compared the performance of the AKF and a dynamic programming algorithm, which belongs to the group of optimization problems. They conclude that the AKF outperforms the optimization algorithm due to its capability to incorporate modelling errors. These errors become more important, if the forces are estimated for a long time span, as the deviation between real system and model becomes higher.

The authors also note that the accuracy of the solution of pure deterministic methods is bound by the accuracy of the model. On the other hand, they notice problems in the force estimate using a non-collocated sensor configuration, where input location and sensor location are not at the same point.

Based on this conclusion, a new method that combines the advantages of the AKF algorithm and an optimization algorithm is proposed for force reconstruction in this work. The Model Predictive Controller (MPC), which is widely applied to control industrial processes, has the capability to incorporate modelling errors and, unlike the AKF, to consider future values for every solution step.

So far, the discussion of the different force reconstruction methods has been related to the algorithm itself only, which represents the core of a force reconstruction system and therefore defines the distinct features of each method. Apart from that, both algorithms, AKF and MPC, use the same reduced-order modal model that has to be identified in advance by an experimental modal analysis. Furthermore, the distributed forces have to be represented by a spatial distribution for both algorithms in the same way. Finally, they can be based on the measurements of any kinematic quantity, which are linked to the states by the output matrix.

The Augmented Kalman Filter and the Model Predictive Controller algorithm, which have been selected for the force reconstruction on the TBM, are derived with regard to force reconstruction in the next two sections. The description of the modal model and the representation of the force distribution, which is common to both algorithms, will be given in section 5.3.1.

3.3.1 Augmented Kalman Filter

At the beginning of this section, the classical Kalman filter equations are presented. Subsequently, the Augmented Kalman Filter (AKF) technique is derived as a general Unknown Input Observer. The adaption of the AKF to a prescribed mechanical system in order to conduct a force reconstruction is done in a subsequent step. The derivation of the AKF is presented following Lourens et al. [61, 62].

The classical Kalman filter

The so-called Kalman filter consists of a set of equations that recursively compute the estimates of the process state by minimizing the mean of the squared errors. The process is therefore

expressed as a discrete-time linear stochastic difference equation with the stochastic process and measurement noise vectors $\boldsymbol{w}_k \in \mathbb{R}^n$ and $\boldsymbol{v}_k \in \mathbb{R}^m$ at the time step k:

$$\boldsymbol{x}_k = \boldsymbol{\mathcal{A}}\boldsymbol{x}_{k-1} + \boldsymbol{\mathcal{B}}\boldsymbol{u}_{k-1} + \boldsymbol{w}_{k-1}, \tag{3.32}$$

and the measurements are related to the states by:

$$\boldsymbol{y}_k = \boldsymbol{\mathcal{C}}\boldsymbol{x}_k + \boldsymbol{v}_k, \tag{3.33}$$

with the state vector $\boldsymbol{x}_k \in \mathbb{R}^n$, the system matrix $\boldsymbol{\mathcal{A}} \in \mathbb{R}^{n\times n}$, the input matrix $\boldsymbol{\mathcal{B}} \in \mathbb{R}^{n\times v}$, the input vector $\boldsymbol{u}_k \in \mathbb{R}^v$, the measurement vector $\boldsymbol{y}_k \in \mathbb{R}^m$ and the output matrix $\boldsymbol{\mathcal{C}} \in \mathbb{R}^{m\times n}$.

The process noise and measurement noise are assumed to be independent, white[3] and exhibiting normal distributions:

$$\boldsymbol{w} \sim \mathcal{N}(0, \boldsymbol{Q}), \tag{3.34}$$

$$\boldsymbol{v} \sim \mathcal{N}(0, \boldsymbol{\mathcal{R}}), \tag{3.35}$$

with the process noise covariance matrix $\boldsymbol{Q} \in \mathbb{R}^{n\times n}$ and the measurement noise covariance matrix $\boldsymbol{\mathcal{R}} \in \mathbb{R}^{m\times m}$.

By definition, $\hat{\boldsymbol{x}}_k^-$ is the a priori state estimate at time step k with knowledge of the process prior to time step k. Then, $\hat{\boldsymbol{x}}_k$ is the a posteriori state estimate at time step k taking into account the measurements $\boldsymbol{y}_k$. With these two definitions, an a priori and an a posteriori estimate error, $\boldsymbol{e}_k$and $\boldsymbol{e}_k^-$, can be formulated:

$$\boldsymbol{e}_k^- \equiv \boldsymbol{x}_k - \hat{\boldsymbol{x}}_k^-, \tag{3.36}$$

$$\boldsymbol{e}_k \equiv \boldsymbol{x}_k - \hat{\boldsymbol{x}}_k. \tag{3.37}$$

The a priori and the a posteriori estimate error covariance matrix, $\boldsymbol{\mathcal{P}}_k^-$ and $\boldsymbol{\mathcal{P}}_k$, are then expressed by:

$$\boldsymbol{\mathcal{P}}_k^- = E[\boldsymbol{e}_k^- \, \boldsymbol{e}_k^{-T}], \tag{3.38}$$

$$\boldsymbol{\mathcal{P}}_k = E[\boldsymbol{e}_k \, \boldsymbol{e}_k{}^T]. \tag{3.39}$$

The Kalman filter is a predictor-corrector algorithm finding an a posteriori state estimate $\hat{\boldsymbol{x}}_k$ as a linear combination of an a priori estimate $\hat{\boldsymbol{x}}_k^-$ and a weighted difference between the actual measurement $\boldsymbol{y}_k$ and the predicted measurement $\boldsymbol{\mathcal{C}}\hat{\boldsymbol{x}}_k^-$. This leads to:

$$\hat{\boldsymbol{x}}_k = \hat{\boldsymbol{x}}_k^- + \boldsymbol{\mathcal{K}}(\boldsymbol{y}_k - \boldsymbol{\mathcal{C}}\hat{\boldsymbol{x}}_k^-), \tag{3.40}$$

[3] White noise means in this context Gaussian white noise with zero mean and constant variance

with the gain or blending factor matrix $\boldsymbol{\mathcal{K}}$ minimizing the a posteriori estimate covariance (3.39). One form of the resulting matrix $\boldsymbol{\mathcal{K}}$ is then:

$$\boldsymbol{\mathcal{K}}_k = \boldsymbol{\mathcal{P}}_k^- \boldsymbol{\mathcal{C}}^T (\boldsymbol{\mathcal{C}} \boldsymbol{\mathcal{P}}_k^- \boldsymbol{\mathcal{C}}^T + \boldsymbol{\mathcal{R}})^{-1}. \tag{3.41}$$

The algorithm can be separated into two steps: a time update or prediction step and a measurement or correction step. Thus, the discrete Kalman filter time update equations read as:

$$\hat{\boldsymbol{x}}_k^- = \boldsymbol{\mathcal{A}} \hat{\boldsymbol{x}}_{k-1} + \boldsymbol{\mathcal{B}} \boldsymbol{u}_{k-1}, \tag{3.42}$$

$$\boldsymbol{\mathcal{P}}_k^- = \boldsymbol{\mathcal{A}} \boldsymbol{\mathcal{P}}_{k-1} \boldsymbol{\mathcal{A}}^T + \boldsymbol{\mathcal{Q}}, \tag{3.43}$$

and the discrete Kalman filter measurement update equations are:

$$\boldsymbol{\mathcal{K}}_k = \boldsymbol{\mathcal{P}}_k^- \boldsymbol{\mathcal{C}}^T (\boldsymbol{\mathcal{C}} \boldsymbol{\mathcal{P}}_k^- \boldsymbol{\mathcal{C}}^T + \boldsymbol{\mathcal{R}})^{-1}, \tag{3.44}$$

$$\hat{\boldsymbol{x}}_k = \hat{\boldsymbol{x}}_k^- + \boldsymbol{\mathcal{K}}_k (\boldsymbol{y}_k - \boldsymbol{\mathcal{C}} \hat{\boldsymbol{x}}_k^-), \tag{3.45}$$

$$\boldsymbol{\mathcal{P}}_k = (\boldsymbol{I} - \boldsymbol{\mathcal{K}}_k \boldsymbol{\mathcal{C}}) \boldsymbol{\mathcal{P}}_k^-. \tag{3.46}$$

The equations (3.42) to (3.46) are repeated at every time step with an initial guess for the state estimate $\hat{\boldsymbol{x}}_{k-1}$ and the a posteriori estimate error covariance $\boldsymbol{\mathcal{P}}_{k-1}$ for the first step.

The state-space equations defined in (3.32) and (3.33) for the Kalman filter assume that the input vector $\boldsymbol{u}_{k-1}$ is known and does not include a direct feedthrough matrix $\boldsymbol{\mathcal{D}}$ in contrast to the general state-space equations in (3.4) and (3.5).

The Augmented Kalman Filter

Therefore, the Kalman filter has to be modified to be applicable to the given problem and act as an Unknown Input Observer. The modified Kalman filter is named Augmented Kalman Filter (AKF) as the states $\boldsymbol{x}_k$ are augmented by the s unknown inputs $\boldsymbol{p}_k \in \mathbb{R}^s$. Thereby, the unknown inputs $\boldsymbol{p}_{k+1}$ at time k+1 are related to the unknown inputs $\boldsymbol{p}_k$at time k by:

$$\boldsymbol{p}_k = \boldsymbol{p}_{k-1} + \boldsymbol{\eta}_{k-1}, \tag{3.47}$$

in which $\boldsymbol{\eta}_k \in \mathbb{R}^s$ denotes the stochastic component. By this approach, the AKF method changes the unknown input value. The process $\boldsymbol{\eta}_k$ is also assumed to be independent, white and with normal distribution:

$$\boldsymbol{\eta} \sim \mathcal{N}(0, \boldsymbol{\mathcal{S}}), \tag{3.48}$$

with the covariance matrix $\boldsymbol{\mathcal{S}} \in \mathbb{R}^{s \times s}$.

If the augmented state vector $\boldsymbol{x}_{a,k} \in \mathbb{R}^{(n+s)}$,

$$\boldsymbol{x}_{a,k} = \begin{bmatrix} \boldsymbol{x}_k \\ \boldsymbol{p}_k \end{bmatrix}, \tag{3.49}$$

is inserted in the state-space equation (3.32) and considering equation (3.47) the AKF state equation yields:

$$\boldsymbol{x}_{a,k} = \boldsymbol{\mathcal{A}}_a \boldsymbol{x}_{a,k-1} + \boldsymbol{w}_{a,k-1} = \begin{bmatrix} \boldsymbol{\mathcal{A}} & \boldsymbol{\mathcal{B}} \\ \boldsymbol{0} & \boldsymbol{I} \end{bmatrix} \begin{bmatrix} \boldsymbol{x}_{k-1} \\ \boldsymbol{p}_{k-1} \end{bmatrix} + \begin{bmatrix} \boldsymbol{w}_{k-1} \\ \boldsymbol{\eta}_{k-1} \end{bmatrix}, \tag{3.50}$$

where $\boldsymbol{A}_a \in \mathbb{R}^{(n+s)\times(n+s)}$ denotes the augmented system matrix and $\boldsymbol{w}_{a,k} \in \mathbb{R}^{(n+s)}$ the augmented process noise vector. Due to the newly obtained augmented noise vector $\boldsymbol{w}_a$, the noise covariance matrix $\boldsymbol{Q}$ has also to be modified to a augmented noise covariance matrix $\boldsymbol{Q}_a \in \mathbb{R}^{(n+s)\times(n+s)}$:

$$\boldsymbol{Q}_a = \begin{bmatrix} \boldsymbol{Q} & \boldsymbol{0} \\ \boldsymbol{0} & \boldsymbol{S} \end{bmatrix}. \tag{3.51}$$

The covariance matrix $\boldsymbol{S}$ can be conceived as a regularization parameter, which controls the smoothness of the estimated inputs.

The measurements can now be related to the new state vector of the AKF $\boldsymbol{x}_{a,k}$ via:

$$\boldsymbol{y}_k = \boldsymbol{C}_a \boldsymbol{x}_{a,k} + \boldsymbol{v}_k = [\boldsymbol{C} \quad \boldsymbol{\mathcal{D}}] \boldsymbol{x}_{a,k} + \boldsymbol{v}_k, \tag{3.52}$$

with the augmented output matrix $\boldsymbol{C}_a \in \mathbb{R}^{m\times(n+s)}$.

AKF adaption for force reconstruction

The next step is to modify the representation of causal, linear and time-invariant mechanical systems in discrete spatial representation as expressed by equation (3.1) in such a way that it can be implemented into the AKF. Therefore, equations (3.1) are modified to consider a spatial force distribution matrix $\boldsymbol{S}_p(t) \in \mathbb{R}^{n_{dof}\times n_i}$, which reads to:

$$\boldsymbol{M}\, \ddot{\boldsymbol{\psi}}(\mathrm{t}) + \boldsymbol{D}\dot{\boldsymbol{\psi}}(\mathrm{t}) + \boldsymbol{K}\boldsymbol{\psi}(t) = \boldsymbol{f}(t) = \boldsymbol{S}_p(t)\boldsymbol{p}(t). \tag{3.53}$$

Herein, $\boldsymbol{p}(t) \in \mathbb{R}^{n_i}$ is the force function vector.

Then the AKF system formulation in state-space representation reads to:

$$\dot{\boldsymbol{x}}(\mathrm{t}) = \boldsymbol{\mathcal{A}}_c\, \boldsymbol{x}(t) + \boldsymbol{\mathcal{B}}_c\, \boldsymbol{u}(t) = \begin{bmatrix} \boldsymbol{0} & \boldsymbol{I} \\ -\boldsymbol{M}^{-1}\boldsymbol{K} & -\boldsymbol{M}^{-1}\boldsymbol{D} \end{bmatrix} \boldsymbol{x}(t) + \begin{bmatrix} \boldsymbol{0} \\ \boldsymbol{M}^{-1}\boldsymbol{S}_p \end{bmatrix} \boldsymbol{u}(t), \tag{3.54}$$

with the state vector $\boldsymbol{x}(t) = [\boldsymbol{\psi}(t) \quad \dot{\boldsymbol{\psi}}(t)]^T \in \mathbb{R}^{2n_{dof}}$ and the input vector $\boldsymbol{u}(t) = \boldsymbol{p}(t)$.

The measured outputs are related to measurements of different sensor types suitable for mechanical systems by:

$$\boldsymbol{y}(\mathrm{t}) = \boldsymbol{S}_{acc}\,\ddot{\boldsymbol{\psi}}(\mathrm{t}) + \boldsymbol{S}_v\dot{\boldsymbol{\psi}}(\mathrm{t}) + \boldsymbol{S}_d\boldsymbol{\psi}(t) + \boldsymbol{S}_\varepsilon\boldsymbol{\psi}(t), \tag{3.55}$$

where $\boldsymbol{S}_{acc},\ \boldsymbol{S}_v,\ \boldsymbol{S}_d \in \mathbb{R}^{n_o \times n_{dof}}$ are selection matrices for accelerations, velocities and displacements. They relate the measurement location to the sensor type. The matrix $\boldsymbol{S}_\varepsilon \in \mathbb{R}^{n_o \times n_{dof}}$ is a differential operator representing the relation of displacements to strain measurements. Equation (3.55) can be transformed to an output equation in state-space representation:

$$\begin{aligned} \boldsymbol{y}(\mathrm{t}) &= \boldsymbol{\mathcal{C}}\,\boldsymbol{x}(t) + \boldsymbol{\mathcal{D}}\boldsymbol{u}(t) \\ &= [\boldsymbol{S}_d + \boldsymbol{S}_\varepsilon - \boldsymbol{S}_a\boldsymbol{M}^{-1}\boldsymbol{K} \quad \boldsymbol{S}_v - \boldsymbol{S}_{acc}\boldsymbol{M}^{-1}\boldsymbol{D}]\boldsymbol{x}(t) \\ &+ \left[\boldsymbol{S}_{acc}\boldsymbol{M}^{-1}\boldsymbol{S}_p\right]\boldsymbol{u}(t). \end{aligned} \tag{3.56}$$

In order to be able to use a reduced-order system representation, the system of equations (3.53) is transferred to the modal representation as described in Section 3.2.1:

$$\boldsymbol{I}\ddot{\boldsymbol{\phi}}(\mathrm{t}) + \Delta\dot{\boldsymbol{\phi}}(\mathrm{t}) + \boldsymbol{W}\boldsymbol{\phi}(\mathrm{t}) = \boldsymbol{R}^T\boldsymbol{S}_p\boldsymbol{p}(\mathrm{t}). \tag{3.57}$$

The system state equation in modal form is given by:

$$\dot{\boldsymbol{z}}(\mathrm{t}) = \boldsymbol{\mathcal{A}}_{c,m}\,\boldsymbol{z}(t) + \boldsymbol{\mathcal{B}}_{c,m}\,\boldsymbol{u}(t) = \begin{bmatrix} \boldsymbol{0} & \boldsymbol{I} \\ -\boldsymbol{W} & -\Delta \end{bmatrix}\boldsymbol{z}(t) + \begin{bmatrix} \boldsymbol{0} \\ \boldsymbol{R}^T\boldsymbol{S}_p \end{bmatrix}\boldsymbol{u}(t), \tag{3.58}$$

with the state vector $\boldsymbol{z}(t) = [\boldsymbol{\phi}(t) \quad \dot{\boldsymbol{\phi}}(t)]^T \in \mathbb{R}^{2n_{dof}}$ and the input vector $\boldsymbol{u}(t) = \boldsymbol{p}(t)$.

The measured outputs (equation (3.56)) are connected to the state vector $\boldsymbol{z}(t)$ by:

$$\begin{aligned} \boldsymbol{y}(\mathrm{t}) &= \boldsymbol{\mathcal{C}}_m\,\boldsymbol{z}(t) + \boldsymbol{\mathcal{D}}_m\boldsymbol{u}(t) \\ &= [\boldsymbol{S}_d\boldsymbol{R} + \boldsymbol{S}_\varepsilon\boldsymbol{R} - \boldsymbol{S}_{acc}\boldsymbol{R}\boldsymbol{W} \quad \boldsymbol{S}_v\boldsymbol{R} - \boldsymbol{S}_a\boldsymbol{R}\Delta]\boldsymbol{z}(t) + \left[\boldsymbol{S}_a\boldsymbol{R}\boldsymbol{R}^T\boldsymbol{S}_p\right]\boldsymbol{u}(t). \end{aligned} \tag{3.59}$$

As the AKF is a discrete-time algorithm, the continuous-time state-space matrices $\boldsymbol{\mathcal{A}}_{c,m}$ and $\boldsymbol{\mathcal{B}}_{c,m}$ have to be transferred to their discrete-time representation, $\boldsymbol{\mathcal{A}}_m$ and $\boldsymbol{\mathcal{B}}_m$, by means of a discretization scheme, which reads to:

$$\boldsymbol{\mathcal{A}}_m = e^{\boldsymbol{\mathcal{A}}_{c,m}\Delta t} \quad \boldsymbol{\mathcal{B}}_m = [\boldsymbol{\mathcal{A}}_m - \boldsymbol{I}]\boldsymbol{\mathcal{A}}_{c,m}^{-1}\boldsymbol{\mathcal{B}}_{c,m}, \tag{3.60}$$

where Δt denotes the time step interval.

Inserting the matrices $\boldsymbol{\mathcal{A}}_m$, $\boldsymbol{\mathcal{B}}_m$ of eq. (3.60) and $\boldsymbol{\mathcal{C}}_m$, $\boldsymbol{\mathcal{D}}_m$ of eq. (3.59) into the state equation and measurement equation of the AKF, namely eq. (3.50) and (3.52), yields the AKF functions:

$$\boldsymbol{z}_{a,k} = \boldsymbol{\mathcal{A}}_{a,m}\boldsymbol{z}_{a,k-1} + \boldsymbol{w}_{a,k-1} = \begin{bmatrix} \boldsymbol{\mathcal{A}}_m & \boldsymbol{\mathcal{B}}_m \\ \boldsymbol{0} & \boldsymbol{I} \end{bmatrix}\begin{bmatrix} \boldsymbol{z}_{k-1} \\ \boldsymbol{p}_{k-1} \end{bmatrix} + \begin{bmatrix} \boldsymbol{w}_{k-1} \\ \boldsymbol{\eta}_{k-1} \end{bmatrix}, \tag{3.61}$$

$$\boldsymbol{y}_k = \boldsymbol{\mathcal{C}}_{a,m}\boldsymbol{z}_{a,k} + \boldsymbol{v}_k = [\boldsymbol{\mathcal{C}}_m \quad \boldsymbol{\mathcal{D}}_m]\boldsymbol{z}_{a,k} + \boldsymbol{v}_k. \tag{3.62}$$

As mentioned, the AKF can also be deduced by a reduced-order modal model. In such a case, the corresponding matrices in equations (3.57) to (3.62) have to be replaced by their reduced-order

counterpart as shown for the PPM method in Section 3.2.1. The AKF for a reduced-order model is discussed in detail in Section 5.3.1, where it is applied to real data.

3.3.2 Model Predictive Controller

The model predictive controller (MPC) is a control method widely applied in industry to control industrial processes. It is closely related to optimal control and therefore belongs to the category of optimization algorithms. In order to find the optimal sequence of input variables, an objective function is minimized. Due to the capability of the MPC to predict future realizations of the variables, the objective function includes present as well as future parameters. The future parameters are predicted with an explicit model of the process [63].

The objective function can be defined in different ways. In the following discussion, as the MPC algorithm is implemented as provided by the MATLAB MPC Toolbox, a quadratic error criterion is used. Therefore, the optimization problem that has to be solved is given by:

$$\begin{aligned}\min_{\Delta u(k|k),\dots,\Delta u(m_{MPC}-1+k|k),e_{MPC}} \Bigg\{ \sum_{i=0}^{p_{MPC}-1} \Bigg(\sum_{j=1}^{n_y} \Big| w_{i+1,j}^{y} \Big(y_j(k+i+1|k) \\ - r_j(k+i+1) \Big) \Big|^2 + \sum_{j=1}^{n_u} \Big| w_{i+1,j}^{\Delta u} \, \Delta u_j(k+i|k) \Big|^2 \\ + \sum_{j=1}^{n_u} \Big| w_{i+1,j}^{u} \Big(u_j(k+i|k) - u_{jtarget}(k+i) \Big) \Big|^2 \Bigg) + \rho_e \, e_{MPC}^2 \Bigg\},\end{aligned} \tag{3.63}$$

where $\Delta u_j(k|k)$ corresponds to the input increment at time step k based on information available at time step k and m_{MPC} is the control horizon, up to which the next input variables are calculated. The slack variable e_{MPC} is used to relax constraints on the variables y_j, Δu_j and u_j. The prediction horizon p_{MPC} specifies the number of time steps, for which the optimization problem is solved. The index j denotes the j^{th} component of a vector. The number of input and output variables is given by n_u and n_y. $w_{i+1,j}^{y}$, $w_{i+1,j}^{\Delta u}$, $w_{i+1,j}^{u}$ are weights on the related terms. The reference values for the output variables are defined by r_j. Desired values for the input variables can be set by $u_{jtarget}$ and finally ρ_e corresponds to the weight on the slack variable e_{MPC}.

The MPC works in a stepwise manner, which means that only the first input increment $\Delta \boldsymbol{u}(k|k)$ for time step k is kept to calculate the input $\boldsymbol{u}(k)$ at time step k. All other input increments are discarded and the optimization problem is solved again for the next time step $k+1$ now incorporating the information available at time step $k+1$. Therefore, a state observer is used to estimate the updated states of the system based on the now available measurements. The observer gain is designed using Kalman filtering techniques. A comprehensive description of the implemented state estimator can be found in [64].

The stepwise implementation of the MPC algorithm is an important advantage over other optimization algorithms as it enables the MPC to take into account errors in the explicit prediction model due to the continuous update of the states.

Application of MPC algorithm to force reconstruction

The MPC algorithm, as implemented in MATLAB, is already applicable to force reconstruction as it is. The model implemented for the prediction of future values and the state estimator is the same reduced-order system that is used in the AKF and defined in equations (3.58) and (3.59). Nevertheless, some elements of the optimization problem, as stated in equation (3.63), are not suitable for force reconstruction and consequently can be omitted. This concerns the constraints defining upper or lower bounds on the variables and the related slack variable e_{MPC} as well as target values for the inputs $u_{jtarget}$, for the reason that no assumptions about this properties can be made. Hence, the optimization problem suitable for force reconstruction reduces to:

$$\min_{\Delta u(k|k),\dots,\Delta u(p_{MPC}-1+k|k)} \left\{ \sum_{i=0}^{p_{MPC}-1} \left(\sum_{j=1}^{n_y} \left| w_{i+1,j}^{y} \left(y_j(k+i+1|k) - y_{jmeasured}(k+i+1) \right) \right|^2 + \sum_{j=1}^{n_u} \left| w_{i+1,j}^{\Delta u} \, \Delta u_j(k+i|k) \right|^2 \right) \right\}. \tag{3.64}$$

In order to estimate the excitation forces corresponding to the input variables $u_j(k)$, the reference values $r_j(k)$ for each time step k are replaced by the measured outputs $y_{jmeasured}(k)$. However, the MPC algorithm cannot be used for online force reconstruction because at least $k + p_{MPC}$ measurements have to be available.

Another difference between the application of the MPC to force reconstruction and an industrial process concerns the selection of the prediction horizon p_{MPC}, the control horizon m_{MPC} and the weights $w_{i+1,j}^{y}$ and $w_{i+1,j}^{\Delta u}$. If the control horizon m_{MPC} is chosen to be smaller than the prediction horizon p_{MPC}, the last calculated inputs $u_j(m_{MPC})$ are kept for time steps $m_{MPC} \dots p_{MPC}$. As the force estimates are likely to change over the entire prediction horizon, the control horizon has to be equal to the prediction horizon. Moreover, the ratio of the weights $w_{i+1,j}^{y}$ and $w_{i+1,j}^{\Delta u}$ can be seen as a regularization parameter to control the smoothness of the solution.

3.4 Sensors suitable for force reconstruction

The force reconstruction methods selected in Section 3.3 require as input data the measurement of kinematic quantities, i.e. acceleration, velocity, displacement as well as strain. Even if a wide range of sensors can be used to obtain these measurements, the sensors to be installed in ITER have to be carefully selected. The instrumentation for the TBM has to cope with environmental conditions simultaneously never encountered before in diagnostic design: high

levels of neutron and gamma fluxes, neutron heating, vacuum, high and transient magnetic fields in pulsed operation.

A summary of the environmental conditions relevant for the selection of suitable sensors is reported in Section 3.4.1. Then, based on the actual state of art, two main sensor technologies have been identified matching the requirements: sensors with an electrical sensing element and sensors with an optical sensing element. They are described in Section 3.4.2. Subsequently, the different types of sensors that can be realized with these sensing elements are discussed and suitable sensors for the application in ITER are proposed in Section 3.4.3. As only a limited number of sensors can be applied to the TBM, a method to optimize the sensor placement is presented in Section 3.4.4.

3.4.1 Environmental conditions of the TBM in ITER

Four versions of each TBM concept will be tested during different plasma operation phases in ITER. While the first version of the TBM, the Electro Magnetic TBM (EM-TBM), is installed in ITER, only pure hydrogen or hydrogen-helium plasmas will be generated. Consequently, the EM-TBM will not be subjected to neutron or gamma irradiation. However, the other versions of the TBM will be tested during plasma operation phases with pure deuterium or deuterium-tritium plasmas, which generate different levels of neutron radiation. Among them, the Integral TBM (INT-TBM) will experience the highest neutron and gamma fluxes during the deuterium-tritium high duty phase. For this reason, Table 3.1 lists the most demanding boundary conditions for the EM-TBM, which is not subjected to neutron irradiation, and the INT-TBM during the deuterium-tritium high duty phase.

	Electro Magnetic module (EM-TBM)	Integral TBM (INT-TBM)
Plasma operation phase	Hydrogen-helium	Deuterium-tritium high duty
Maximum helium cooling system outlet temperature	500 °C [4]	500 °C
Maximum helium cooling system inlet temperature	300 °C	300 °C
Maximum magnetic field	5 T	5 T
Surface heat load	270 kW	270 kW
Volumetric heat load	-	667 kW
Neutron flux	-	$10^{12} – 10^{14}$ $cm^{-2}s^{-1}$
Gamma flux	-	data not available

Table 3.1: Boundary conditions of the EM-TBM during the hydrogen-helium operation phase and the INT-TBM during the deuterium-tritium high duty phase [65].

The maximum temperature of both TBM versions will be at about 550 °C at the first wall and 300 °C at the back plate. The maximum magnetic field strength around the TBM is expected to be about 5 T. Volumetric heating and neutron and gamma fluxes only occur for the INT-TBM. At

[4] This temperature level is reached, if additional heaters are present in the EM-TBM.

present, the available information is not sufficient to define the requirements on the sensors with regard to neutron and gamma radiation. The radiation hardness of sensors is generally expressed in the sensor specifications by an integrated neutron flux and integrated gamma flux. The available calculations of the neutron flux give an order of magnitude of 10^{14} $cm^{-2}s^{-1}$ at the first wall and 10^{12} $cm^{-2}s^{-1}$ at the back plate [66]. The corresponding calculations of the gamma flux are not yet concluded. However, as the durations of the different operating phases in ITER are not yet precisely defined, the estimation of the integrated quantities needed for the comparison with the sensor specifications is not possible.

3.4.2 Sensors with electrical or optical sensing element

At the end of the measurement chain, the measured quantity has to be converted to an electrical signal in order to be processed by standard data acquisition systems. Nevertheless, the sensing element itself can respond to the measured quantity with an electrical or optical signal. Hence, different physical effects can be used to measure kinematic quantities depending on the sensing element type. The physical effects that are relevant for the measurement of kinematic quantities with an electrical sensing element are e.g. a potentiometer, the effects of induction or capacity, ultrasound or the piezoelectric effect. The operating principles of an optical sensing element are based on optical effects such as quantum-optical effects, interference or intensity changes. An extensive description can be found in [67]. This section is focused on general differences between the two types of sensing elements. However, it is important to note in this context that all relevant kinematic quantities can be measured with electrical and optical sensing elements.

The important difference between the two types of sensing elements is the point where the measured quantity is converted to an electrical signal. Generally, this conversion takes places close to the measuring point in sensors with an electrical sensing element. In contrast, the optical signal of an optical sensing element can be routed far away from the measuring point in order to be finally converted to an electrical signal. Optical fibers are used for this purpose in most cases. Due to the different points of signal conversion, sensors with electrical and optical sensing elements differ in their reaction to disturbances from the environment.

Sensors with electrical sensing element

As the use of sensors in the temperature range experienced by the TBM is not unusual for technical applications, like for example monitoring of gas turbines, a variety of sensors with electrical sensing element exist that can withstand these temperatures. For example, the ZC-series strain gauges from Vishay PG, Inc., which consist of Kanthal, are bonded to the surface by a ceramic adhesive. They are able to resist temperatures up to 1150 °C [68]. In addition, mineral insulated cables can be used for wiring at high temperatures.

Several physical effects appear if the sensing element or the electrical circuits are exposed to high or alternating magnetic fields. The magnetostrictive effect can lead to a deformation of the test object or the sensing element. The magnetoresistive effect, which changes the resistivity of electrically conducting materials, causes measurement errors, if, for example, the change of resistance is the measured quantity. In addition, electrical voltages are induced in the sensing element and the lead wires by changing magnetic fields [69].

These effects can be reduced by a number of countermeasures, but can never be eliminated. Materials with a low magnetoresistance can be used to reduce the magnetoresistive effect, as for example Constantan in strain gauges [69]. Induced voltages can be reduced by a special design of the sensing element in order to create an additional current flow in opposite direction or by covering the sensing element with a Mu-metal. When applying this method, the grounding of the Mu-metal is essential. In order to counteract induced voltages in the lead wires, twisted and shielded cables can be used. Detailed descriptions of these measures can be found in [70]. For example, the HPB displacement sensors from Capacitec, Inc. have been successfully applied in the particle accelerator CERN at a location with a magnetic field of 2 T [71] and the H-Series strain gauges of Vishay PG, Inc. have been successfully used in fusion research applications with flux densities of up to 5 T [72].

In ITER, both neutron and gamma radiation are present, which lead to heating of the sensor and damage in terms of change of the material properties. Apart from the characteristics of the radiation, the influence of radiation strongly depends on the materials used for the sensor and for the bonding of the sensor to the structure. The relevant properties of the material are molecular structure, geometry, molecular size, molecular weight, dimensions, volume, thickness and density [69]. Therefore, are general statement of the radiation hardness of sensors with electrical sensing element cannot be made. It rather depends on the individual design and materials used for the sensor. Nevertheless, a variety of sensors has been developed and successfully applied in a nuclear environment. For instance, the PY Extreme Environment Non-Contact Displacement Transducer from RDP Electrosense can withstand a radiation dose of 10^9 Gy [73].

Sensors with optical sensing element

When sensors with optical sensing element are used, the optical signal is guided to the detector by an optical fiber. However, it is also possible to integrate the sensing element directly inside the fiber, like in a Fiber Bragg grating (FBG) sensor [74] or a Fiber Fabry-Perot Interferometric (FFPI) sensor [75]. In any case, the optical fiber is the critical part that has to resist the environmental conditions.

For high temperature applications, the most suitable optical fibers are made of silica or sapphire. The type II FBG fabricated with a femtosecond laser can withstand temperatures up to 1200 °C in a silica fiber and 1745 °C in a sapphire fiber [76]. If a protection of the fiber is necessary, the coating of the fiber is the limiting factor. Nevertheless, it is still possible to reach an operating temperature of about 700 °C with a gold coating [77].

Optical fibers are affected by gamma and neutron radiation in three ways. Firstly, the radiation-induced absorption increases the absorption of light by defects in the fiber. Secondly, the radiation-induced luminescence generates light inside the fiber. The third effect is a change of the refractive index, which results in a shift of the reflected wavelength in FBG sensors where it, for example, represents the measured quantity to determine strain or temperature [78]. The radiation sensitivity of the fiber strongly depends on the chemical composition of the fiber. Possible procedures to increase the radiation hardness of the fibers are hydrogen-loading or doping with bismuth, germanium or fluorine. An extensive review of the radiation effects on silica-based optical fibers, also related to an application in ITER, is given by Girard et al [79]. In [80], hydrogen-loaded and aluminum coated pure silica core fibers were assessed at a fast neutron flux

(>0.1 MeV) up to 2×10^{12} $cm^{-2}s^{-1}$ and an ionizing dose-rate up to 317 Gy/s with a total neutron fluence of 5×10^{16} cm^{-2} and ionizing dose of 10 MGy. At these conditions, the radiation-induced absorption is less than 1 dB at a wavelength of 630 nm.

Two additional properties, which make the application of optical fibers very attractive, are their immunity to electromagnetic interference and their capability for distributed sensing by introducing several FBG in a single fiber [81].

3.4.3 Sensors suitable for the application to the TBM

The comparison of sensors with electrical and optical sensing element shows that both types of sensing elements can withstand temperatures up to 500 °C. Regarding the sensibility to electromagnetic interference, an important difference between the two types of sensing elements exists nevertheless. The sensors with optical sensing element are intrinsically immune to electromagnetic inference in contrast to sensors with electrical sensing element. Even though a number of countermeasures to reduce the sensibility of electrical sensors to electromagnetic fields is available, a certain influence of the electromagnetic fields on the sensor cannot be excluded. The performance of sensors with electrical sensing element under high electromagnetic fields has to be at least tested in a dedicated experiment.

The comparison between the neutron and gamma radiation conditions and the sensor specifications is difficult due to the missing information related to the gamma flux and the duration of the D-T high duty phase in ITER. Additionally, it has to be checked if the irradiation conditions, on which the sensor specifications are based, are comparable to the conditions in ITER with regard to the neutron and gamma spectra. Finally, a distinct difference in terms of radiation hardness between sensors with optical and electrical sensing element is not obvious. It is important to note though that the radiation hardness is not relevant in the case of the EM-TBM, where no radiation is present.

From the comparison of the properties of the different types of sensing elements with regard to the environmental conditions in ITER, it can be concluded that both sensing elements can be applied at ITER relevant temperatures and show a comparable behavior under neutron and gamma radiation. However, the optical sensing element is immune to electromagnetic interference and therefore preferable for the application in ITER. Another advantage of an optical sensing element is the possibility of distributed sensing, which significantly reduces the amount of signal lines.

As discussed in the previous section, all relevant kinematic quantities can be measured with an electrical sensing element as well as with an optical sensing element. The type of sensor itself, nevertheless, has certain advantages and disadvantages with respect to the placement or the installation and the measured quantity, independent of the type of the sensing element. An acceleration sensor has to be placed at locations with an expected high acceleration signal, which applies to points along the edges of the TBM box. Due to the limited space between the TBM box and the port plug frame, the acceleration sensors can only be installed on the back plate. Furthermore, acceleration sensors are not suitable for the measurement of quasi-static forces.

The same restrictions for the placement of the sensors apply for velocity and displacement sensors. In addition, these types of sensor require an external reference to determine the corresponding quantity. For this reason, it has to be assured that the structure surrounding the TBM can be regarded as a fixed reference in order not to measure the movement of the surrounding structure. Strain sensors have to be placed at locations of high strains that are related to the movement of the box. These points are mainly located on the attachment system, which transfers the forces acting on the TBM to the shield.

Acceleration, velocity and displacement sensors can all be placed at the back plate. Velocity and displacement sensors need an external reference that can be regarded as fixed. This reference points are difficult to define in the surrounding of the TBM, as motion of the reference itself cannot be excluded. On the other hand, acceleration sensors are not suitable for the reconstructing of slowly changing or quasi-static forces. As strain sensors have none of these drawbacks, this type of sensor can be regarded as most suitable for the application for force reconstruction on the TBM.

Optical strain gauges can be replaced by electrical strain gauges of similar size considering the sensing area in an experimental setup, where no high magnetic fields are present, as they are comparable in strain sensitivity.

3.4.4 Sensor placement

In order to obtain the sensor measurements necessary for the application of the force reconstruction methods, the structure has to be equipped with a set of sensors. Several aspects have to be considered for the selection of suitable sensor positions, especially if only a limited number of sensors can be used. In the following discussion, the position of a sensor always refers to a sensor location and orientation. Firstly, a good signal-to-noise ratio is required. The points, where high measurement signals are expected, depend on the physical quantity that is measured by the sensor as well as on the characteristics of the force, which is supposed to be reconstructed. On the other hand, at some locations a sensor placement is impossible due to, for example, limited space or unsuitable environmental conditions. Additionally, the size of the sensor itself has to be considered when placing sensors close to each other.

The points of high measurement output signals can either be determined analytically for simple geometries or with the support of FEM software for geometries being more complex. The modes relevant to represent the dynamic behavior of the system can be identified by conducting a modal analysis of the system. If the excitation of certain modes can be excluded due to the known excitation pattern, these modes do not have to be further considered for the placement of the sensors.

The eigenvectors corresponding to the n_m considered modes can be used to identify the locations with the highest signals in the related mode. If each eigenvector $\boldsymbol{r}_i$ is normalized to the element with the highest absolute value of the eigenvector r_{iHI}, the relative signal level for each mode can be assigned to the possible sensor locations. This can be summarized in the modal matrix for placement of the sensors $\mathbf{R}_{SP} \in \mathbb{R}^{n_{sl} \times n_m}$.

$$\mathbf{R}_{SP} = \begin{bmatrix} \left|\frac{r_{11}}{r_{1HI}}\right| & \cdots & \left|\frac{r_{1n_m}}{r_{n_mHI}}\right| \\ \vdots & & \vdots \\ \left|\frac{r_{n_{sl}1}}{r_{1HI}}\right| & \cdots & \left|\frac{r_{n_{sl}n_m}}{r_{n_mHI}}\right| \end{bmatrix} = \begin{bmatrix} r_{11norm} & \cdots & r_{1n_mnorm} \\ \vdots & & \vdots \\ r_{n_{sl}1norm} & \cdots & r_{n_{sl}n_mnorm} \end{bmatrix}, \tag{3.65}$$

where n_{sl} corresponds to the number of possible sensor locations. This matrix can now be used to find a set of sensors that is able to detect the considered modes with a maximum signal level while respecting the constraints due to limited space. This corresponds to a multi-objective optimization problem, which is well suited for a genetic algorithm and commonly applied for sensor placement, see, for example, Yi et al. [82]. The program flow chart of the evolutionary algorithm adapted for the optimization of the sensor placement for force reconstruction is shown in Figure 3.11. The algorithm is implemented in the software MATLAB.

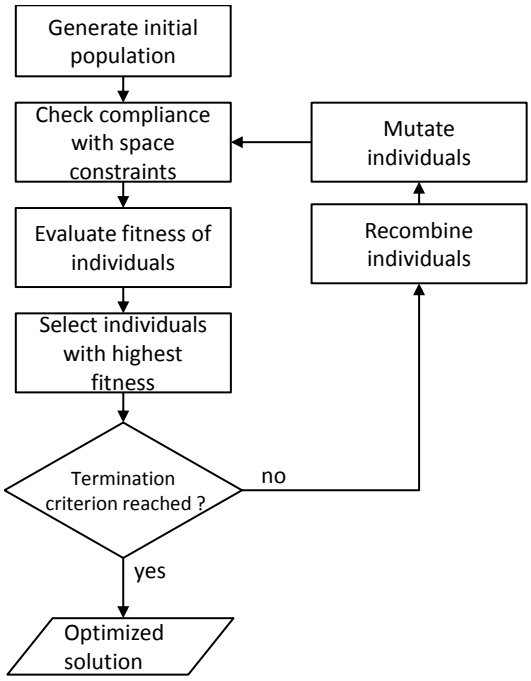

Figure 3.11: Program sequence of the evolutionary algorithm developed for sensor placement.

Depending on the number of sensors n_o that is going to be applied to the structure, an initial population of 10^5 individuals is created by randomly selecting combinations of n_o sensor positions. Each individual is checked for compliance with the space constraints and subsequently kept or discarded. The remaining individuals are evaluated according to the fitness function and then sorted by the fitness value. The fitness function F(I) for each individual I is defined as follows:

$$\mathrm{F}(I) = \left\| \boldsymbol{R}_{SPISortedNormalized}^{T} \, \mathbf{w}_{SP} \right\|_1 = \left\| \begin{bmatrix} r_{I11norm} & \cdots & r_{In_o1norm} \\ \vdots & & \vdots \\ r_{I1n_mnorm} & \cdots & r_{In_on_mnorm} \end{bmatrix} \begin{bmatrix} 1 \\ 0.8 \\ 0.6 \\ 0.4 \\ 0.2 \\ 0 \\ \vdots \\ 0 \end{bmatrix} \right\|_1, \quad (3.66)$$

with the modal matrix for each individual I containing the normalized absolute values of the elements of the eigenvector corresponding to the selected sensors sorted in decreasing order $\boldsymbol{R}_{SPISortedNormalized} \in \mathbb{R}^{n_o \times n_m}$ and the weighting vector on the sorted eigenvectors $\mathbf{w}_{SP} \in \mathbb{R}^{n_o \times 1}$. The weighting vector $\mathbf{w}_{SP}$ avoids that the detection of a single mode is overrated.

The $2{\times}10^4$ individuals with the highest fitness values are kept and the average fitness is calculated. The optimization is terminated, if the average fitness shows no further improvement compared to the previous iteration. If not, 10^4 new individuals are created by randomly selecting two old individuals and combining them by randomly selecting sensor positions of the two old combinations. In the mutation step, each sensor position of the new individuals is either increased or decreased, each with a probability of 5%. Finally, the next iteration is started with the population consisting of $2{\times}10^4$ old and 10^4 new individuals.

4 Experimental validation and test mock-ups

In order to investigate the application of the force reconstruction methods to a real system, an experimental setup has been designed and built with the aim to validate the theoretically developed force reconstruction methods. As the conditions in ITER can only be represented to a certain degree by a testing device, the validation is based on a set of test cases that allows for the transfer to ITER-relevant excitation patterns. This means, as the system is represented by a modal model in the force reconstruction algorithms, the test cases cover the excitations of different combinations of all modes contained in the modal model with ITER-like durations. Therefore, even if an excitation pattern in ITER does not exactly correspond to one single test case, the excitation pattern still corresponds to the excitation of the combination of the same modes, which are contained in the test cases. In addition, the experimental setup and corresponding mock-ups are designed in such a way that the applied forces generate the same reaction of the mock-ups as distributed forces, which are characteristic for the electromagnetic forces in ITER. The concept of the experimental setup is outlined in Section 4.1.

For the experimental validation, two test mock-ups have been designed with two different focuses. In order to test the force reconstruction methods with an experimental setup, a testing device has to be built that can reproduce different loading scenarios. As the TBM has a big and massive structure to resist the high EM loads, a suitable testing device for a full-size TBM mock-up should have the capability to generate forces in the same order of magnitude as they occur in ITER. This approach would lead to an unnecessary big and expensive testing device. Therefore, a reduced-sized TBM mock-up with attachment system has been designed with modal characteristics and strain levels at lower excitation forces comparable with a full-size TBM. The box structure with an internal stiffening grid allows the validation of electro-magnetic simulations if a testing device is used that can generate electro-magnetically induced currents. Therefore, it is well suited for experimental program in the second stage. Another mock-up, the simple pipe mock-up, was developed for the experimental program in the first stage. It consists of simple pipe with a rigid plate that is attached to the top of the pipe. With this mock-up, higher strain levels and thus higher measurement signals can be achieved under the same loading conditions as the reduced-sized TBM mock-up. However, due to the simple structure, the mode shapes of this mock-up differ more from the mode shapes of the TBM. Due to the similarity of the TBM and the mock-ups, it can be demonstrated that the model reduction as well as the number and arrangement of sensors used for the experimental setup are also relevant for the force reconstruction on the TBM. The relevance of the two designs is discussed in detail in section 4.2. A method to evaluate the performance of force reconstruction methods is introduced in section 4.3. Finally, the type of force application in the experiment is discussed in section 4.4.

During the construction of ITER, a testing device will be required in the pre-installation phase of the TBM to test and calibrate the measurement system. This includes the model identification as well as the determination of the accuracy of the system as demonstrated with the experimental setup in chapter 6. The knowledge obtained by the experiment will then support the design of such a device. Another important point is the possibility to perform all steps necessary for the implementation of the method on a real system and to understand possible difficulties that may occur during the implementation. For example, the experimental modal analysis, which is necessary to identify a system model, can only be carried out on a real system, where it has to deal with a certain amount of non-linearity and non-proportional damping. In addition, the

experiment is required to compare the experimentally determined modal model and the theoretical modal model. Finally, the experiment demonstrates the overall feasibility of the implementation of the force reconstruction methods on a real system.

4.1 Design of the experimental setup

The experimental validation of the force reconstruction methods necessitates a test stand able to excite simplified mock-ups in such a manner that their reactions to the excitation are representative for a TBM.

The straightforward solution is a system able to generate transient magnetic fields of different plasma events as expected in ITER. This approach in turn faces two major difficulties:

- A testing device with an arrangement of coils able to generate high magnetic fields associated with a similar load pattern.
- The applied forces are not accessible for a direct measurement to compare them to the reconstructed forces in order to validate the force reconstruction methods if the real load source is applied.

Abandoning forcing based on electro-magnetic effects simplifies the setup without loss of generality.

If in turn forces are applied at discrete points instead of applying a continuous force distribution on the surface, these difficulties can be overcome. This is depicted in Figure 4.1. By applying forces at discrete points, they can be measured by a force sensor. Hence, the design of an experimental setup with a testing device to apply punctual forces as the most promising concept is further investigated assuming that the same reactions of the system can be generated like with a distributed force. This aspect is discussed in section 4.4. The detailed selection and design of the experimental setup is described in section 6.1.

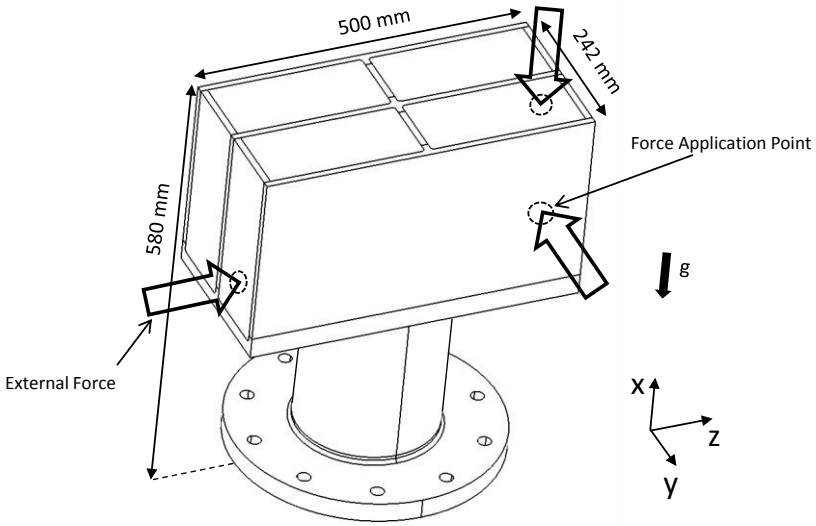

Figure 4.1: Schematic representation of the experimental setup: The external forces are applied at discrete points.

4.2 Design and relevance of the test mock-ups with regard to force reconstruction on the TBM

In order to allow for an immediate transfer of test setup to blanket scenarios three major requirements have to be met:

- The geometry of the mock-up has to correspond to the structural part of the TBM.
- The modal characteristics of the mock-up and the TBM have to be similar.
- The attainable strain levels of both should be comparable.

On this basis two mock-ups are developed iteratively, which are depicted in Figure 4.2. The detailed design and fabrication of the mock-ups are described in Section 6.2.

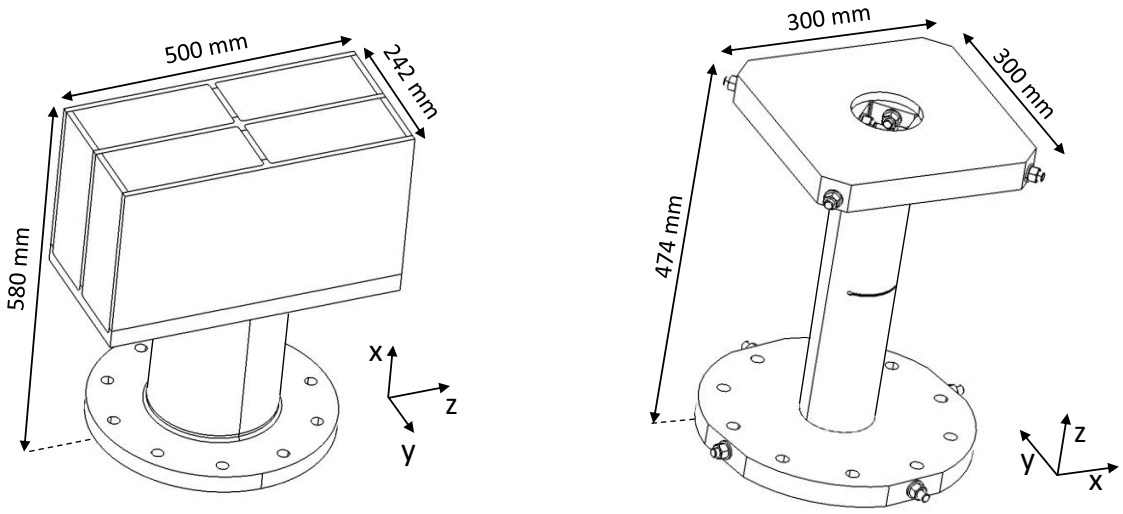

Figure 4.2: Two mock-ups designed to represent the TBM in the experiments: Reduced-sized mock-up (left) and simple pipe mock-up (right)

The strains serving the inputs for the force reconstruction methods are measured on the cylindrical attachment system. In order to fulfill the first requirement, both designs incorporate a cylindrical element that connects the more rigid part of the mock-up to the support. The similarity of the connecting part of the mock-ups and the attachment system of the TBM guarantees that the forces are transferred to the support in a similar way by deforming a cylindrical element.

The modal characteristics refer to the reduced order models of the systems. As the force reconstruction algorithms are based on models in modal representation, the model reduction corresponds to a reduced number of modes that are considered to describe the behavior of the system.

For the model reduction, the effective masses [83] have been calculated based on numerical modal analyses of the different system with the simulation software ANSYS. The accumulated fraction of the effective mass of the total mass for the ten first modes of each system is listed in appendix A. The relevant modes for each system have been selected by summing up the effective mass of each mode starting at the mode with the lowest eigenfrequency until more than 90 % of

the total mass (or moment of inertia) for each excitation direction is reached. According to this criterion, each system can be represented by the first six modes. Hence, the comparison of the modal characteristics, defined by the eigenfrequencies and modes shapes, between the two mock-ups and the TBM is based on these first six modes. A good accordance of these criteria for the different mock-ups assures that the number of sensors, the sensor placement and the strain measurement system are relevant with regard to the application to the TBM. The comparison of the computed modal characteristics of mock-ups and TBM is listed in Table 4.1.

	TBM		Reduced-sized mock-up		Simple pipe mock-up	
Mode No.	Mode shape	Eigenfrequency	Mode shape	Eigenfrequency	Mode shape	Eigenfrequency
1	1st bending	65 Hz	1st bending	100 Hz	1st bending	42 Hz
2	2nd bending	91 Hz	2nd bending	106 Hz	2nd bending	52 Hz
3	1st torsion	112 Hz	1st torsion	176 Hz	1st torsion	80 Hz
4	3rd bending	260 Hz	3rd bending	367 Hz	3rd bending	279 Hz
5	1st axial	286 Hz	1st axial	480 Hz	4th bending	298 Hz
6	4th bending	417 Hz	4th bending	514 Hz	1st axial	360 Hz

Table 4.1: Comparison of modal characteristics of the TBM and the test mock-ups

The comparison of the modal characteristics shows that both mock-ups and the TBM exhibit similar eigenfrequencies. The TBM and the mock-ups can be described by a modal model considering six modes in a frequency range from 42 Hz to 514 Hz. In addition, the mode shapes corresponding to the motion pattern of the structure are identical for the different systems. As an example, the mode shapes of the 1st bending modes and 1st torsion mode are shown in Figure 4.3 and Figure 4.4.

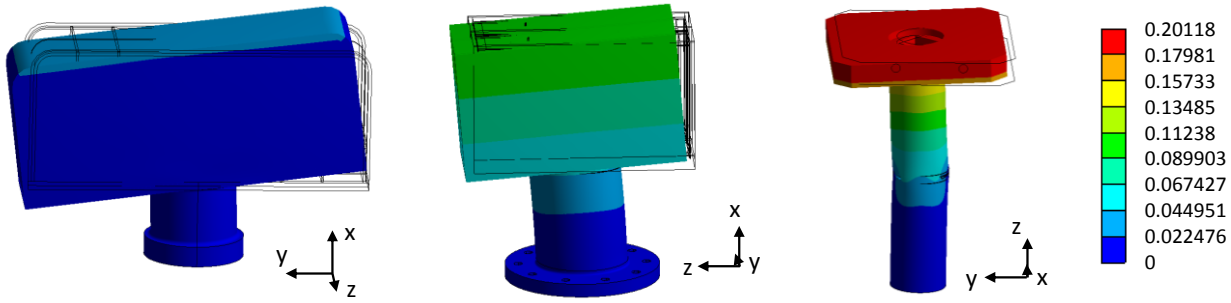

Figure 4.3: Comparison of 1st bending mode by means of the y-component of the mass-normalized eigenvector of the TBM (left), the z--component of the mass-normalized eigenvector of the reduced-sized mock-up (center) and the y-component of the mass-normalized eigenvector of the simple pipe mock-up (right).

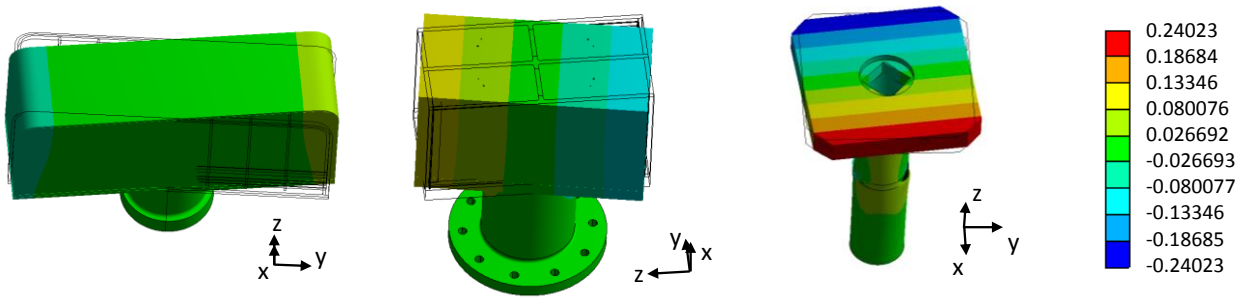

Figure 4.4: Comparison of 1st torsion mode by means of z-component of the mass-normalized eigenvector of the TBM (left), y-component of the mass-normalized eigenvector of the reduced-sized mock-up (center) and x--component of the mass-normalized eigenvector the of simple pipe mock-up (right).

The strain level refers to the maximum strain that can be expected at the measurement points on the TBM due to electro-magnetic forces in ITER or on the mock-ups due to the excitation by the testing device. However, a single value for the strain level cannot be specified, as a "worst case scenario" does not exist.

Although the maximum strain on the structure always varies depending on the location of the sensor in combination with the characteristics of the exciting forces, an order of magnitude of the reachable strains can be defined. For this purpose, different scenarios with the characteristics of the electro-magnetic forces in ITER in terms of the order of magnitudes and transient behavior have been simulated with a TBM model. From these results, an average of the maximum strains in the order of 10^{-4} m/m at possible strain sensor positions has been obtained. The same approach based on the test cases defined for the experiment has been used to determine the strain level on the simple pipe mock-up and the reduced-sized mock-up. The average maximum strains at possible sensor locations of the two mock-ups are as well in the order of 10^{-4} m/m. Nevertheless, as the part of the attachment of the reduced-sized mock-up has a higher stiffness, the strains on the simple pipe mock-up are higher by a factor of about 2.

4.3 Evaluating the performance of force reconstruction methods

In order to compare the performance of the force reconstruction methods under different conditions and to investigate the impact of different parameters, a performance criterion has to be introduced. In the literature related to force reconstruction, no consistent method to evaluate the performance of a force reconstruction algorithm is described. In turn, relative as well as absolute error definitions are formulated to describe the performance of an algorithm.

A relative L2 error norm is applied by Nordström and Nordberg [84], Jacquelin et al. [32] and Steltzner and Kammer [37]. Although Steltzner and Kammer apply this error definition to transient forces, they note that this definition is not appropriate for transient forces as a discrepancy between estimated force and actual force after the decay of the actual force increases the error.

Allen and Carne [38] define a relative error of the peak force between the estimated and reconstructed force of a hammer impact. However, this error definition is only appropriate for a hammer impact as only a single time point can be considered.

An absolute L2 error norm is used by Lourens et al. [61] for a sine-sweep excitation force. Although this error definition is suitable for the relative comparison of different algorithms or conditions for the same excitation force, it neither can be compared to other excitation forces nor provides an intuitive value of the amount of error in the reconstructed force. An error measure for the hammer impact experiments is not specified in the related publication.

The force reconstruction of electro-magnetic forces in ITER only deals with transient forces that are significantly longer than a hammer impact. In addition, an error measure that gives an intuitive value comparable to other excitation forces would be desirable. Hence, none of the above stated error measures is suitable for the evaluation of the performance of force reconstruction methods related to ITER relevant excitation forces.

Therefore, the root-mean-square error (RMSE) is proposed as an error measure for long-term excitation forces. Although a relative error is commonly defined in this context, this error definition cannot be applied in this study as the considered excitation forces contain zero components for the total duration of the excitation leading to an infinite relative error. For that reason, a mean error in the units of the components of the input vector $\boldsymbol{u}(t)$ is given by the proposed RMSE. As the input vector $\boldsymbol{u}(t)$ consists of force components (F_x, F_y, F_z) and moment components (M_x, M_y, M_z), a separate error measure can be specified for forces and moments in the following way:

$$RMSE_F = \sqrt{\frac{\sum_{k=1}^{n}\left(\left(\hat{F}_{x,k} - F_{x,k}\right)^2 + \left(\hat{F}_{y,k} - F_{y,k}\right)^2 + \left(\hat{F}_{z,k} - F_{z,k}\right)^2\right)}{n}}, \tag{4.1}$$

$$RMSE_M = \sqrt{\frac{\sum_{k=1}^{n}\left(\left(\hat{M}_{x,k} - M_{x,k}\right)^2 + \left(\hat{M}_{y,k} - M_{y,k}\right)^2 + \left(\hat{M}_{z,k} - M_{z,k}\right)^2\right)}{n}}. \tag{4.2}$$

Herein k denotes the time step, n the length of the considered period, $\hat{F}_{x,k}$, $\hat{F}_{y,k}$, $\hat{F}_{z,k}$ the reconstructed force components, $F_{x,k}$, $F_{y,k}$, $F_{z,k}$ the reference force components, $\hat{M}_{x,k}$, $\hat{M}_{y,k}$, $\hat{M}_{z,k}$ the reconstructed moment components and $M_{x,k}$, $M_{y,k}$, $M_{z,k}$ the reference moment components.

Although this error measure scales with the excitation forces, it is a useful and intuitive quantity to compare the influence of errors in the model on the reconstructed forces for the same test case. It represents the mean deviation of the reconstructed force component at each point in time and therefore respects the error due to a time delay as well as an error in the magnitude of the force.

4.4 Different distributions of forces

In the real blanket application, the forces are acting close to the outer surface of the box, but only a rough estimate of the real force distribution can be currently predicted. This originates from the uncertainties of the simplified electro-magnetic models to predict the forces. In order to validate these simplified models, a quantity has to be defined to compare the results of the electro-magnetic analyses and the results of the force reconstruction. Dependent on the model of

the system used in the implemented force reconstruction method only a limited number of independent input parameters can be estimated. These parameters can be linked to a force distribution on the TBM box by a spatial force distribution matrix $\boldsymbol{S}_p$ as introduced in equation (3.53). Hence, two equivalent expressions for the modal force vector $\boldsymbol{n}(t)$ exist in the modal representation of the system:

$$\boldsymbol{I}\ddot{\boldsymbol{\phi}}(\mathrm{t}) + \Delta\dot{\boldsymbol{\phi}}(\mathrm{t}) + \boldsymbol{W}\boldsymbol{\phi}(\mathrm{t}) = \boldsymbol{R}^T\boldsymbol{f}(t) = \boldsymbol{R}^T\boldsymbol{S}_p\boldsymbol{p}(\mathrm{t}) = \boldsymbol{n}(t). \tag{4.3}$$

The modal matrix $\boldsymbol{R}$ will be identified by an experimental modal analysis before the installation of the TBM in ITER. The time-dependent force distribution vector $\boldsymbol{f}(t)$ will be calculated by electro-magnetic analyses. As the real spatial force distribution $\boldsymbol{S}_p$ on the TBM can only be roughly predicted, the modal force vector $\boldsymbol{n}(t)$ is a suitable quantity to compare the results of the electro-magnetic analyses and the force reconstruction.

However, under the hypothesis that the TBM box can be regarded as a rigid body, the exact force distribution can be neglected. Hence, a simple force distribution according to the classical bolt pattern analysis (CBPA) [85], as it is commonly used in FE analyses [86], can be applied to the corresponding surfaces and the resulting forces and moments can be described at a central point of the structure. The force distribution matrix according to the classical bolt pattern analysis $\boldsymbol{S}_{BP}$ in combination with the parameter vector $\boldsymbol{p}(t) = \left[F_x(t)\ F_y(t)\ F_z(t)\ M_x(t)\ M_y\ (t) M_z(t)\right]^T$ representing the forces and moments at a reference point is derived in appendix B. Under this hypothesis, two different force distributions according to the CPBA are compared by simulated strain measurements on the attachment. Both force distributions represent the same time histories of resulting forces and moments at the same reference point at the center of the back plate. The time histories of the exemplary load case are given in Figure 4.5. The corresponding strain responses of the different distributions are plotted in Figure 4.6. The difference in the strain measurement at the peak values of strain gauge 1 is about 5 % for this load case. Nevertheless, the validity of the hypothesis of the rigidity of the TBM box will have to be carefully investigated especially with regard to the final design of the attachment system.

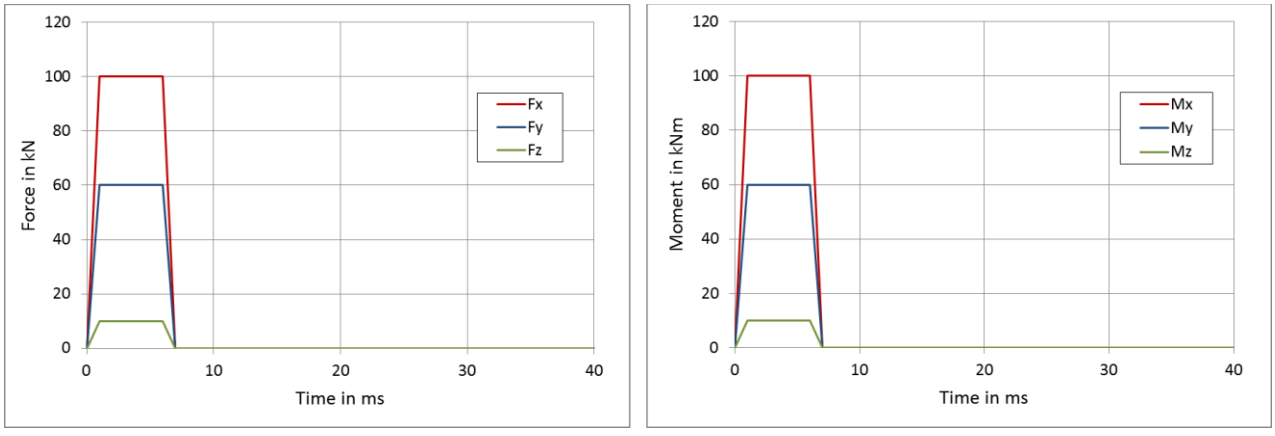

Figure 4.5: Force distribution according to the classical bolt pattern analysis on the TBM: The graph shows the time histories of the resulting forces (left) and moments (right) at the center of the back plate of the TBM.

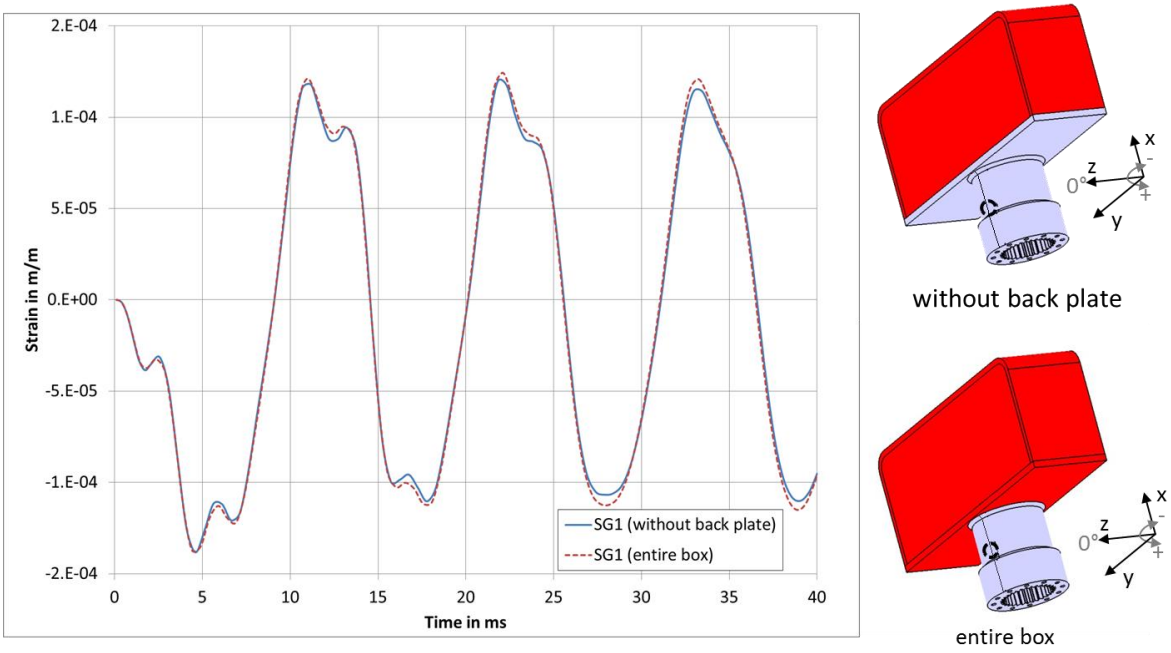

Figure 4.6: Simulated normal strain in x-direction at strain gauge 1 (SG1) for force distributions on different surfaces (indicated in red) according to the CBPA on the TBM box. The strain gauge (marked by the dashed circle) is located on the cylinder at an angle of 0° and a distance of 59 mm from the back plate.

In contrast to the TBM, the design of the reduced-sized mock-up including the part representing the attachment system is finalized. Consequently, the hypothesis of a rigid box can be investigated by a numerical modal analysis on this mock-up. For this purpose, a modal analysis with a model, where the part of the box is represented by a rigid body, and a fully flexible model is conducted. As the force reconstruction methods are based on strain measurements, the difference in the eigenfrequencies and strain eigenvectors are compared. The maximum relative difference in the eigenfrequencies is 3.68 %, as listed in Table 4.2. According to the performance criterion defined in section 4.3, this deviation is negligible with regard to the error in the force reconstruction as shown in section 5.4.2. The maximum deviation of the elements of the strain eigenvector at possible sensor locations on the attachment part are listed as well in Table 4.2. This difference approximately doubles the absolute error in the force reconstruction compared to a perfectly matching reduced-order model, as discussed in section 5.4.2. This is regarded as acceptable.

Mode No.	Eigenfrequencies		Relative difference of eigenfrequencies	Maximum relative difference between strain eigenvectors
	Rigid box	Flexible box		
1	100.2 Hz	99.5 Hz	0.73 %	2.43 %
2	106.9 Hz	105.8 Hz	0.98 %	2.34 %
3	177.5 Hz	175.8 Hz	0.94 %	2.44 %
4	375.1 Hz	367.1 Hz	2.14 %	6.60 %
5	490.6 Hz	479.8 Hz	2.20 %	7.15 %
6	533.5 Hz	513.8 Hz	3.68 %	10.19 %

Table 4.2: Comparison of eigenfrequencies and strain eigenvectors of the reduced-sized mock-up with rigid box and flexible box for the first six considered modes based on a numerical modal analysis. The maximum relative difference between the strain eigenvector refers to an element-wise comparison relative to the maximum absolute element of the corresponding eigenvector.

Under the hypothesis of a rigid structure of the box, the force distribution according to the CBPA can also be applied to the reduced sized mock-up to represent the force distribution as a resulting force and moment combination at a reference point as described before. The forces are applied as punctual forces normal to the surface similar to the experimental setup and distributed over the box according to the CBPA. To illustrate the impact on the strain measurements, the time histories of an exemplary load case of the punctual forces and the forces distribution have been defined in such a way that the time histories of the resulting forces and moments at the center of the box in Figure 4.7 are equal. The simulated resulting strain at strain gauge 1 on the cylinder is plotted for both cases in Figure 4.8. The strain measurement at strain gauge 1 shows a deviation of about 3 % at the peak values for this load case.

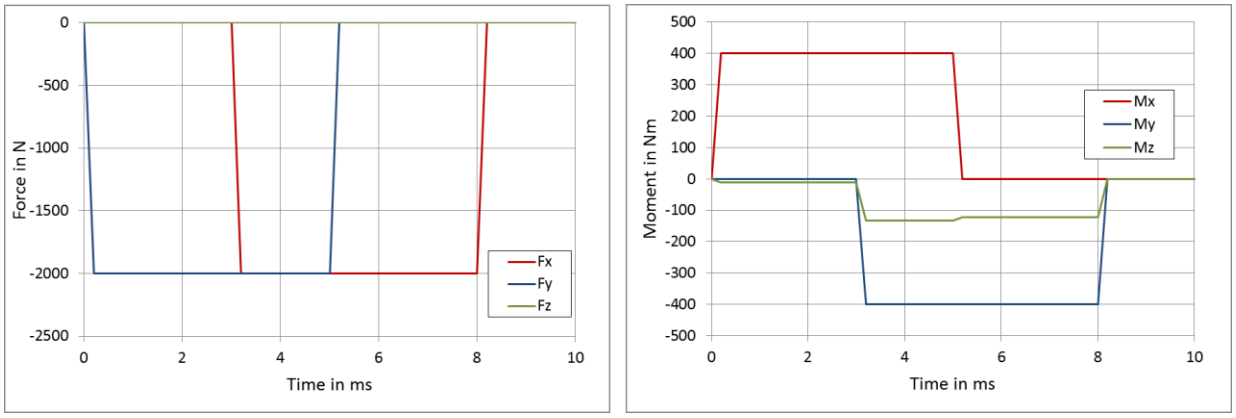

Figure 4.7: Force distribution according to the classical bolt pattern analysis on the reduced-sized mock-up: The graph shows the time histories of the resulting forces (left) and moments (right) at the center of the box of the reduced-sized mock-up.

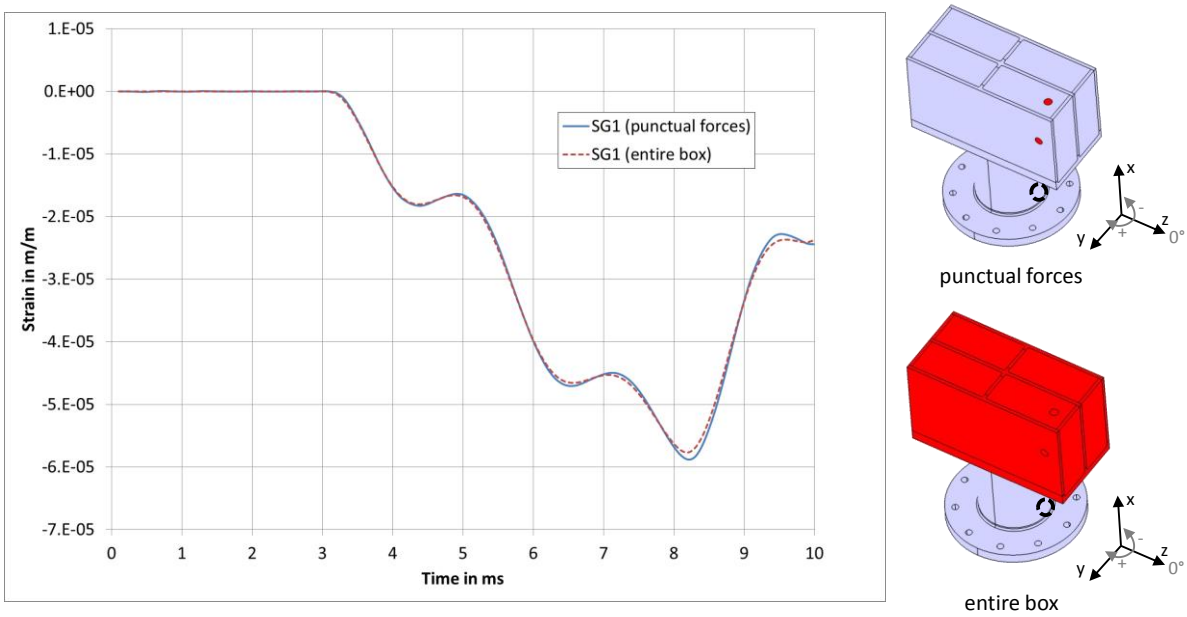

Figure 4.8: Comparison of the simulated normal strain in x-direction at strain gauge 1 (SG1) between punctual and distributed forces on the reduced sized mock-up. The force application points or surfaces are indicated in red. The punctual forces are applied normal to the surface. The distributed forces are distributed according to the CBPA. The location of the strain gauge is marked by a circle at an angle of 0° and 80 mm below the back plate.

The hypothesis of a rigid top plate of the simple pipe mock-up is investigated by a numerical modal analysis as well. A modal analysis has been performed with a model with a rigid top plate and with a model with a flexible top plate. The eigenfrequencies and strain eigenvectors of the considered modes have a maximum relative difference of 4.55 % and 8.44 %, as listed in Table 4.3. Hence, analogous to the reduced-sized mock-up, this is regarded as acceptable.

Mode No.	Eigenfrequencies		Relative difference of eigenfrequencies	Maximum relative difference between strain eigenvectors
	Rigid top plate	Flexible top plate		
1	41.9 Hz	41.9 Hz	0.03 %	0.65 %
2	51.6 Hz	51.6 Hz	0.03 %	0.29 %
3	80.5 Hz	80.3 Hz	0.19 %	2.97 %
4	290.5 Hz	279.0 Hz	4.14 %	7.56 %
5	312.0 Hz	298.4 Hz	4.55 %	8.44 %
6	374.5 Hz	359.8 Hz	4.07 %	7.72 %

Table 4.3: Comparison of eigenfrequencies and strain eigenvectors of the simple pipe mock-up with rigid top plate and flexible top plate for the first six considered modes based on a numerical modal analysis. The maximum relative difference between the strain eigenvector refers to an element-wise comparison relative to the maximum absolute element of the corresponding eigenvector.

To illustrate the influence of the hypothesis of a rigid top plate on the strain measurements of the simple pipe mock-up, a test case has been simulated applying two different force distributions. For this purpose, the forces are applied at discrete points in the same way as in the experiments on the top plate and a force distribution is specified resulting in the same forces and moments at the center of the top plate. The time histories can be seen in Figure 4.9. The simulated strain at a strain gauge on the pipe due to these excitations is presented in Figure 4.10. The deviation in the measured strain at strain gauge 1 for the presented load case is below 1 % at the peak values.

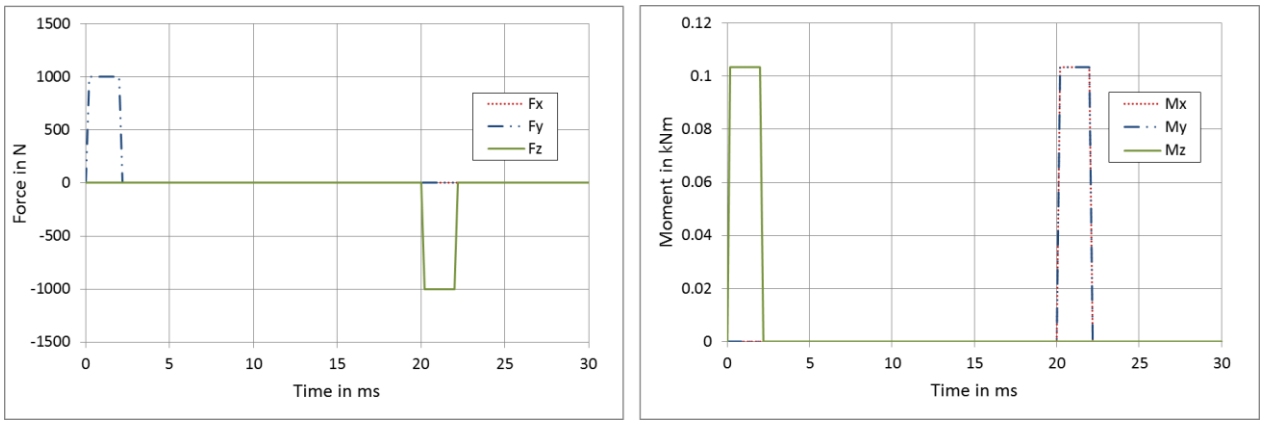

Figure 4.9: Force distribution according to the classical bolt pattern analysis on the simple pipe mock-up: The graph shows the time histories of the resulting forces and moments at the center of the top plate of the simple pipe mock-up.

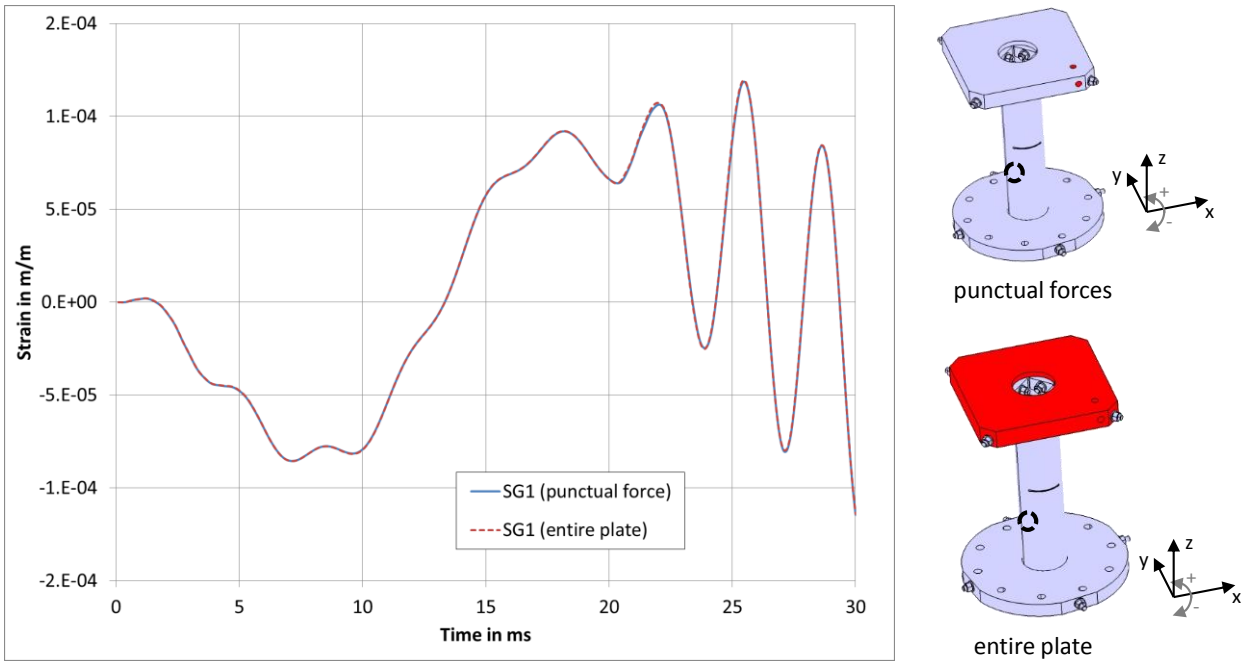

Figure 4.10: Comparison of normal strain in z-direction at strain gauge 1 (SG1) between punctual and distributed forces on the simple pipe mock-up. The force application points or surfaces are indicated in red. The punctual forces are applied normal to the surface. The distributed forces are distributed according to the CBPA. The location of the strain gauge 1 in the setup with six sensors is marked by a circle and given in appendix C.

Finally, it can be concluded that the modal force vector $\boldsymbol{n}(t)$ is a suitable comparative quantity for the results of the electro-magnetic analyses and the force reconstruction as no assumption has to be made about the force distribution on the TBM. The stiffness properties of the TBM are respected in the model at any time.

Regarding the reduced-sized mock-up and the simple pipe mock-up, it has been shown that the part representing the TBM box is sufficiently stiff to apply a force distribution according to the classical bolt pattern analysis. Therefore, the forces applied in the experiment can be represented as resulting forces and moments at a reference point. With respect to the TBM, the hypothesis of a rigid box still needs confirmation, since this strongly depends on the ultimate design.

5 Setup of simulation and results with simulated data

In this chapter, the setup and results of simulations of different test cases are presented. The simulations have been carried out in order to investigate the force reconstruction methods at defined conditions. Simulation in this context means that the strain data are obtained by simulating different test cases with the FEA software ANSYS. However, the force reconstruction algorithms themselves are implemented in the same way for both simulated and experimental data.

Nevertheless, one important difference exists in the model of the system that is used in the implementation of the algorithms. In both cases, the system is described by a reduced order model. However, the model used for force reconstruction with simulated strain data is directly derived from an analytically solved modal analysis in ANSYS. In contrast, the model used in the force reconstruction with experimental data is determined by an experimental modal analysis.

For that reason, the eigenfrequencies and eigenvectors obtained from the analytical modal analyses in ANSYS correspond to the modal parameters of the model used in the simulations to generate the strain data. On the other hand, the modal parameters estimated in an experimental modal analysis can only be determined with a certain accuracy. Therefore, only the numerically generated strain data can be used to investigate the influence of errors in the identified model on the force reconstruction algorithms as defined errors can be introduced in the perfectly matching model. In order to compare the force reconstruction using simulated strain data with the force reconstruction using experimental data, a set of test cases has been defined. The definition of the test cases is based on the simple pipe mock-up as it is presently used in the experimental setup. The test cases are described in Section 5.1.

5.1 Test cases

The test cases have been defined in such a way that they cover a wide range of possible loading patterns. For this reason, the test cases consist of different short-term and long-term excitations in combination with different excitation directions. The short-term excitations are similar to a hammer impact as used for the experimental modal analyses. The long-term excitations are oriented on the time history of the electro-magnetic forces during a plasma disruption in ITER as described in Section 2.1.2.

The test cases are defined by the schematic time history in Figure 5.1 with the scenarios defined in Table 5.1. The rise and fall times in the scenarios 1 to 3 represent the range of typical rise and fall times expected during a plasma disruption in ITER [87].

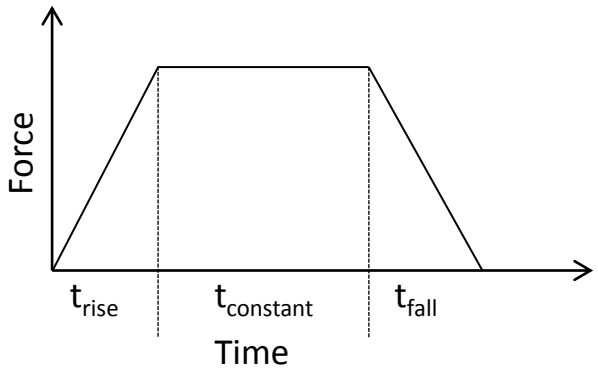

Figure 5.1: Schematic to define the time history of excitation forces.

	Rise time t_{rise}	Time of constant force $t_{constant}$	Fall time t_{fall}
Hammer Impact (HI)	0.2 ms	1.8 ms	0.2 ms
Scenario 1 (SC1)	2 ms	20 ms	2 ms
Scenario 2 (SC2)	20 ms	20 ms	2 ms
Scenario 3 (SC3)	2 ms	20 ms	20 ms

Table 5.1: Different scenarios of the time history of the excitation forces.

The forces are applied to the mock-up as punctual forces, where the application points have been selected in such a way that the mock-up is excited from all possible directions. Additionally, different combinations of normal modes are present in the motion of the mock-up for the different excitation scenarios. The seven defined test cases consist of single and double excitation scenarios. They are depicted in Figure 5.2 and Figure 5.3. The main excited modes for each test case are listed in Table 5.2. With the double excitation cases, it is also possible to introduce a time delay between the two excitation forces in the simulation. For each test case, a hammer impact and a long-term scenario has been simulated resulting in a total number of 14 test cases.

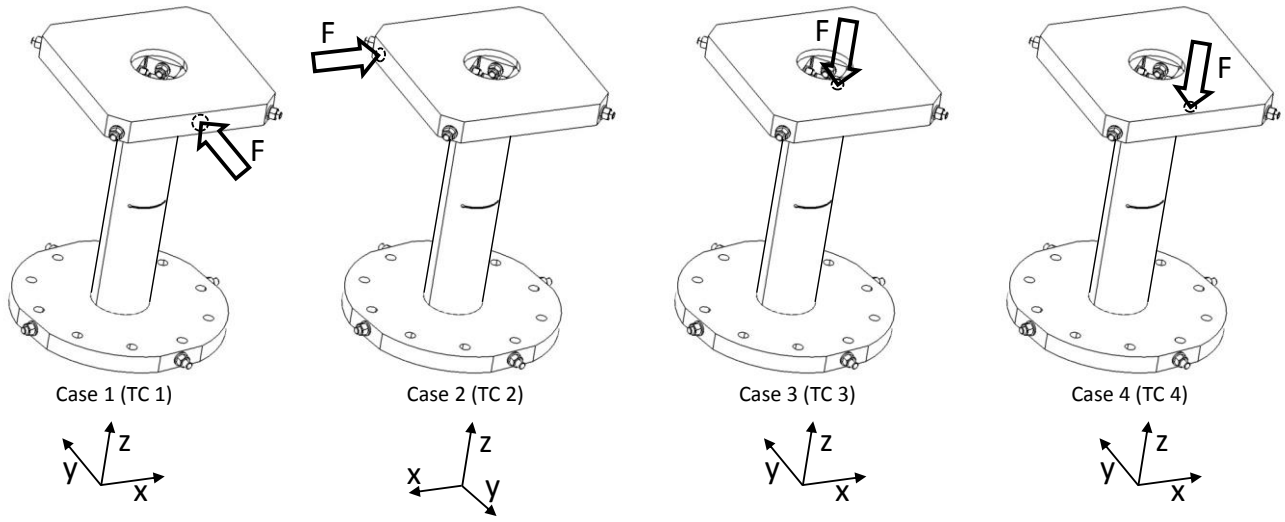

Figure 5.2: Test cases 1-4 with single force excitation locations.

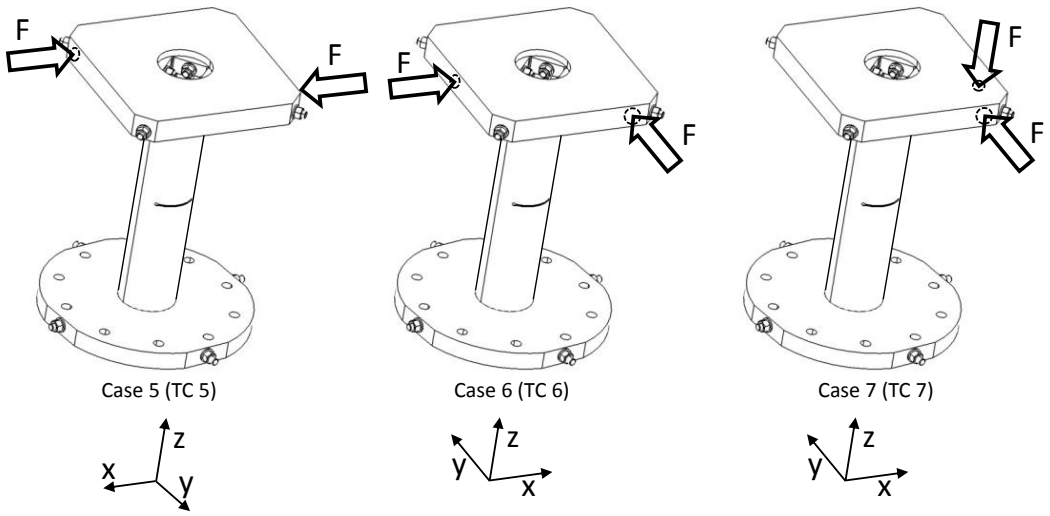

Figure 5.3: Test cases 5-7 with double excitation locations.

Mode No.	Mode shape	TC 1	TC 2	TC 3	TC 4	TC 5	TC 6	TC 7
1	1st bending	●	-	○	●	-	●	●
2	2nd bending	-	●	-	-	-	●	○
3	1st torsion	-	●	-	-	●	-	●
4	3rd bending	-	●	-	-	-	●	●
5	4th bending	●	-	○	●	-	●	●
6	1st axial	-	-	●	●	-	-	●

Table 5.2: Main excited modes for each test case (TC) on simple pipe mock-up (● strongly excited, ○ lightly excited). A light excitation of a mode is defined by the element related to the force application degree of freedom of the corresponding eigenvector. A light excitation corresponds an absolute value less than 50 % compared to other force application degree of freedom on the top plate for the same mode.

The definition of the test cases has been chosen aiming to obtain a set of loading conditions that allows investigating the force reconstruction methods with a complete set of possible types of excitation. For each test case, a different combination of modes can be excited. The short-term and long-term excitations can be used to control the transferred impulse. As the test cases in combination with a long-term excitation are essential to analyze the application of the force reconstruction methods in ITER, the short-term excitations are mainly used to study the limitations of the methods applied.

5.2 Simulation of the simple pipe mock-up

In order to generate the strain recordings needed as input data for the force reconstruction algorithms, each test case is simulated with the FEM software ANSYS. For that purpose, a full method transient analysis with a simplified model of the simple pipe mock-up has been set up. The FEM model with the force application points and the applied FEM mesh are presented in Figure 5.4. For an efficient computation, shell elements have been used to represent the structure of the pipe. The whole model contains about 6.7×10^4 elements and 2.5×10^4 nodes. The bottom of the pipe is modeled as a fixed support and the plate and the pipe are in bonded contact.

In order to consider damping effects in the simulation, a Rayleigh damping has been assumed in the model. The α and β damping constants therein have been chosen in such a way that a constant damping ratio of 0.001 in the range of the frequencies of the relevant modes is present. The selected damping ratio is in the same order of magnitude as the damping ratio of the real structure determined in the experiment. The time step has been chosen based on the guideline for the Newmark time integration scheme recommending a minimum of 20 cycles per highest frequency of interest. Hence, the time step has been set to 0.1 ms (~27 cycles) corresponding also to the sampling rate of the data acquisition system in the experiment.

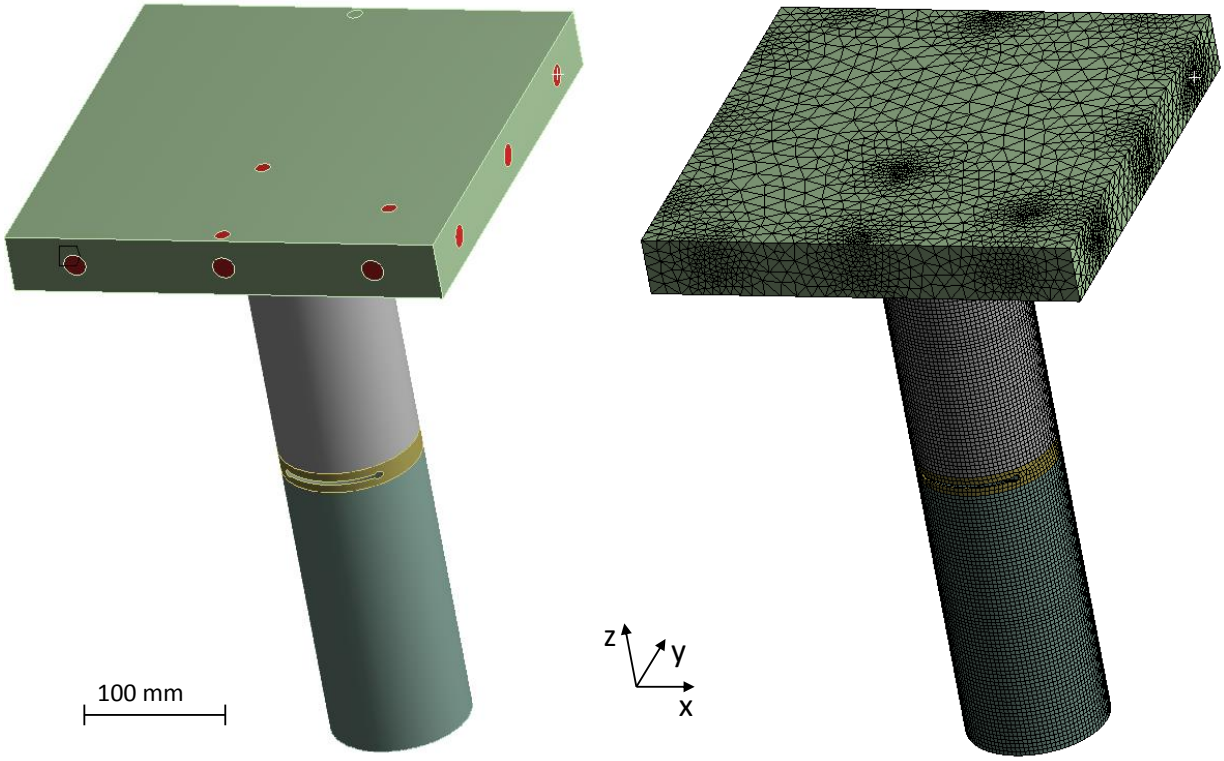

Figure 5.4: Simplified FEM model of the simple pipe mock-up with the force application points (left) and the FEM mesh (right) used in the analysis. The origin of the coordinate system is located on the bottom of the cylinder on the cylinder axis.

5.3 Implementation of the force reconstruction methods

The force reconstruction methods are implemented in MATLAB. Both algorithms, AKF and MPC, work with a reduced-order modal model of the system. The model is taken from an analytical modal analysis in ANSYS and errors are intentionally introduced to investigate their impact on the force reconstruction. This is described in detail in Section 5.3.1. For each algorithm, a regularization parameter has to be specified. The selected method to determine a suitable parameter is described in Section 5.3.2. Due to the predictor corrector nature of the AKF, a time delay in the reconstructed forces can occur if a high amount of regularization is used. A suitable procedure to partly reduce the time delay is discussed in Section 5.3.3.

5.3.1 Models used in the force reconstruction algorithms

The algorithms are implemented with a modal model of the system in state-space representation. Therefore, the system matrix $\boldsymbol{\mathcal{A}}_{c,m}$, the input matrix $\boldsymbol{\mathcal{B}}_{c,m}$, the output matrix $\boldsymbol{\mathcal{C}}_m$ and the direct feed through matrix $\boldsymbol{\mathcal{D}}_m$ have to be specified as input data. The required parameters are taken from the numerical modal analysis with ANSYS.

In accordance with equation (3.58), if the eigenvectors are scaled to unity modal mass, the matrix $\boldsymbol{\mathcal{A}}_{c,m}$ consists of the identity matrix $\boldsymbol{I}$, the diagonal matrix $\boldsymbol{W}$ with the squared eigenfrequencies of the modes, as selected in Section 4.2, and the diagonal damping matrix Δ. The damping values correspond to the parameters used in the simulation.

The input matrix $\boldsymbol{\mathcal{B}}_{c,m}$, as presented in equation (3.58), is given by the transposed modal matrix $\boldsymbol{R}^T$ and, in case of distributed forces, a force distribution matrix $\boldsymbol{S}_p$. Although discrete force application points have been specified in the simulations in order to correspond to the conditions in the experiment, the force reconstruction methods have to be designed to reconstruct distributed forces with regard to the application in ITER. For this reason, the modal force vector $\boldsymbol{n}(t)$ has been defined as comparative quantity in Section 4.4. However, for the simple pipe mock-up, it has been shown that a force distribution according to the classical bolt pattern analysis can be assumed. This leads to a more general formulation of the algorithms, as the implemented model is independent of the force application points on the top plate in this way and the input can be expressed as resulting forces and moments at a reference point. The modal matrix $\boldsymbol{R}$ contains the displacement eigenvectors of the selected modes of the reduced-order model. The elements of the displacement eigenvectors belong to the degree of freedom of the area on which the forces are applied. In case of the simple pipe mock-up, this corresponds to the top plate. If the input vector $\boldsymbol{u}(t)$ in equation (3.58) represents the resulting forces and moments at a reference point of the structure, the force distribution matrix $\boldsymbol{S}_p$ can be derived according to the classical bolt pattern analysis.

The right side of equation (3.58) is now given by:

$$\begin{aligned}\dot{\boldsymbol{z}}(\mathrm{t}) &= \boldsymbol{\mathcal{A}}_{c,m}\,\boldsymbol{z}(t) + \boldsymbol{\mathcal{B}}_{c,m}\,\boldsymbol{u}(t) = \begin{bmatrix} \boldsymbol{0} & \boldsymbol{I} \\ -\boldsymbol{W} & -\Delta \end{bmatrix}\boldsymbol{z}(t) + \begin{bmatrix} \boldsymbol{0} \\ \boldsymbol{R}^T\boldsymbol{S}_p \end{bmatrix}\boldsymbol{u}(t) \\ &= \begin{bmatrix} \boldsymbol{0} & & & \boldsymbol{I} & & \\ -\omega_1^2 & & -(\alpha+\beta\omega_1^2) & & & \\ & \ddots & & & \ddots & \\ & & -\omega_6^2 & & & -(\alpha+\beta\omega_6^2) \end{bmatrix}\boldsymbol{z}(t) \\ &+ \begin{bmatrix} r_{1DOF1} & \cdots & r_{1DOFn} \\ \vdots & & \vdots \\ r_{6DOF1} & \cdots & r_{6DOFn} \end{bmatrix}\begin{bmatrix} \boldsymbol{0} \\ \boldsymbol{S}_{BP} \end{bmatrix}\begin{bmatrix} F_x(t) \\ F_y(t) \\ F_z(t) \\ M_x(t) \\ M_y(t) \\ M_z(t) \end{bmatrix},\end{aligned} \tag{5.1}$$

with the force distribution matrix according to the classical bolt pattern analysis $\boldsymbol{S}_{BP} \in \mathbb{R}^{n_{dof}\times 6}$.

The matrices $\boldsymbol{\mathcal{C}}_m$ and $\boldsymbol{\mathcal{D}}_m$ are defined in equation (3.59). As strain sensors have been identified as suitable for the application of the force reconstruction methods in ITER, the selection matrices for acceleration, velocity and displacement sensors, $\boldsymbol{S}_{acc}$, $\boldsymbol{S}_v$ and $\boldsymbol{S}_d$, are zero. Hence, equation (3.59) reduces to:

$$\begin{aligned} \boldsymbol{y}(\mathrm{t}) &= \boldsymbol{\mathcal{C}}_m\, \boldsymbol{z}(t) + \boldsymbol{\mathcal{D}}_m \boldsymbol{u}(t) \\ &= [\boldsymbol{S}_d \boldsymbol{R} + \boldsymbol{S}_\varepsilon \boldsymbol{R} - \boldsymbol{S}_a \boldsymbol{R} \boldsymbol{W} \quad \boldsymbol{S}_v \boldsymbol{R} - \boldsymbol{S}_{acc} \boldsymbol{R} \Delta] \boldsymbol{z}(t) \\ &+ \left[\boldsymbol{S}_{acc} \boldsymbol{R} \boldsymbol{R}^T \boldsymbol{S}_p\right] \boldsymbol{u}(t) = [\boldsymbol{S}_\varepsilon \boldsymbol{R}] \boldsymbol{z}(t) + [\boldsymbol{0}] \boldsymbol{u}(t). \end{aligned} \tag{5.2}$$

The matrix product $\boldsymbol{S}_\varepsilon \boldsymbol{R}$ is equivalent to the strain modal matrix $\boldsymbol{R}_\varepsilon$ consisting of the strain eigenvectors for the selected modes $\boldsymbol{r}_{\varepsilon 1} \ldots \boldsymbol{r}_{\varepsilon 6}$:

$$\boldsymbol{S}_\varepsilon \boldsymbol{R} = \boldsymbol{R}_\varepsilon = \begin{bmatrix} r_{\varepsilon 1 SG1} & \cdots & r_{\varepsilon 6 SG1} \\ \vdots & & \vdots \\ r_{\varepsilon 1 SGn} & \cdots & r_{\varepsilon 6 SGn} \end{bmatrix}. \tag{5.3}$$

The single elements $r_{\varepsilon i SGj}$ of each strain eigenvector $\boldsymbol{r}_i$ are related to the i^{th} strain eigenvector and the j^{th} strain gauge. The values of the strain eigenvectors are also taken from a modal analysis in ANSYS.

The model described by the matrices $\boldsymbol{\mathcal{A}}_{c,m}$, $\boldsymbol{\mathcal{B}}_{c,m}$ and $\boldsymbol{\mathcal{C}}_m$ exactly matches the model being used in the simulations to generate the strain recordings in terms of a reduced-order model. Therefore, this model is used in the investigation of the force reconstruction methods as reference for a perfectly matching model.

In order to study the influence of errors in the model on the reconstructed forces, errors are intentionally introduced in the model. For these purpose, three parameters have been identified in previous tests strongly affecting the reconstructed forces:

- the eigenfrequencies of the considered modes,
- the strain eigenvectors
- and the number of sensors.

Although the number of sensors is not directly related to the model of the system, it plays an important role in compensating the errors in the model.

Table 5.3 summarizes the parameters varied to investigate their influence on the force reconstruction methods. In order to simulate an error in the eigenfrequencies, they have been increased by 5%. The errors in the strain eigenvectors are assumed to be normally distributed with a mean value equal to the nominal value and a standard deviation corresponding to 1 %, 10 % or 30 % of the nominal value. Six is the minimum number of sensors to detect six modes and 16 is the maximum number of sensors used in the experiment limited by the number of input channels of the data acquisition system.

Error in eigenfrequencies (EEF)	Error in strain eigenvectors (EEV)	Number of sensors (NumS)
0 %	0 %	6
	1 %	10
5 %	10 %	
	30 %	16

Table 5.3: Parameters considered in the model which is used in the simulation to investigate influence on reconstructed forces.

The positions of the sensors have been independently optimized for each number of sensors as described in Section 3.4.4. The positions of the sensors are indicated in Figure 5.5 for each case.

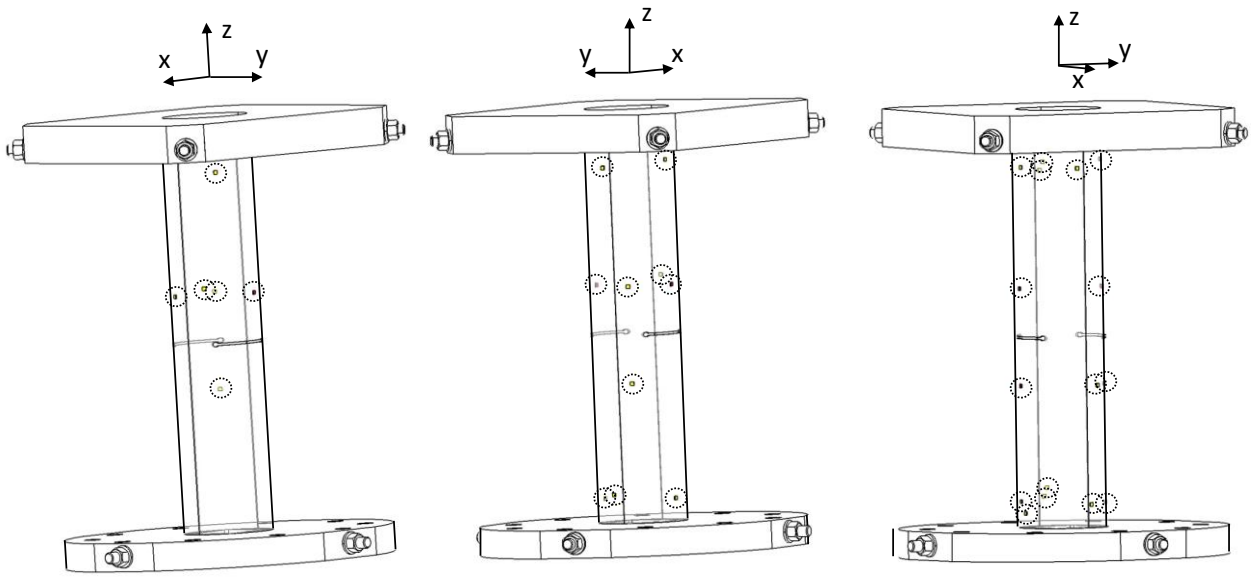

Figure 5.5: Sensor positions on the simple pipe mock-up used in the simulated test cases: 6 sensors (left), 10 sensors (center) and 16 sensors (right). The positions are additionally listed in tabular form in appendix C.

5.3.2 Method to determine suitable regularization parameter

Most force reconstruction methods, including AKF and MPC, work with a kind of regularization. The amount of regularization included in the solution of the problem is defined by a regularization parameter or a set of regularization parameters. As the necessary amount of regularization depends on the specific problem, a method or criterion has to be applied in order to find suitable parameters for the given problem.

The purpose of regularization methods is to transform an ill-posed problem into a well-posed problem by incorporating additional information. The additional information depends on the underlying problem and it is often related to the smoothness of the solution. As high change rates of the reconstructed electro-magnetic forces are not expected, the smoothness of the solution is

controlled by the diagonal covariance matrix $\boldsymbol{S}$ in the AKF and by the weighting factors $w_{i+1,j}^{y}$ and $w_{i,j}^{\Delta u}$ in the MPC algorithm.

For the AKF, the regularization parameter corresponds to the diagonal covariance matrix $\boldsymbol{S}$ contained in the augmented process noise covariance matrix $\boldsymbol{Q}_a$. As no assumptions are made about the different characteristics of the force components to be reconstructed, the diagonal elements of the matrix $\boldsymbol{S}$ are equal. According to the definition of the regularization parameter being the variance of the estimated forces, a high value allows the AKF to change its estimates faster.

The regularization parameter of the MPC algorithm are the weighting factors $w_{i+1,j}^{y}$ with constant weighting factors $w_{i,j}^{\Delta u}$. Similar to the AKF, the weighting factors are equal for the different force components. If the weighting factors on the input increment $w_{i,j}^{\Delta u}$ are kept unchanged, higher weighting factors on the strain error $w_{i+1,j}^{y}$ lead to higher input increments Δu_j and therefore faster changes of the input parameters u_j.

Suitable regularization parameters can be found by applying a standard regularization estimation method, the L-curve method, as described by Hansen [42] and applied to the AKF by Lourens et al. [61]. The L-curve method is a graphical method to display the influence of the regularization on the solution and therefore can be used as a tool to select a suitable regularization parameter. For this purpose, a norm of the regularized solution is plotted over a norm of the residuals or errors for different regularization parameters. For the regularized solution, a smoothing norm is defined as squared 2-norm of the input increments, which also corresponds to the regularization term in the MPC, as:

$$\sum_{k=1}^{N} \|\boldsymbol{\Delta u}_k\|_2^2, \tag{5.4}$$

with the time step k in the considered time interval of N time steps. The norm of the residuals is defined in the same way and reads to:

$$\sum_{k=1}^{N} \|\boldsymbol{y}_k - \boldsymbol{C}\hat{\boldsymbol{x}}_k\|_2^2 = \sum_{k=1}^{N} \|\boldsymbol{y}_k - \hat{\boldsymbol{y}}_k\|_2^2, \tag{5.5}$$

in which $\boldsymbol{y}_k$ is the measurement vector and $\hat{\boldsymbol{y}}_k$ the predicted measurement vector.

If the smoothing norm is plotted over the error norm for different regularization parameters in a double logarithmic plot, the resulting curve resembles the letter L. The L-curve for test case 1 using the MPC algorithm and the specified model is shown in Figure 5.6. It can be seen that with a decreasing regularization parameter, which corresponds to a higher level of regularization, the error norm generally increases and the smoothing norm decreases. However, starting from a certain level of the regularization parameter, the smoothing norm increases significantly faster and the error norm stays nearly constant. This point is considered as the corner of the L-shape

and represents a good compromise between minimizing the error norm and limiting the increase of the smoothing norm.

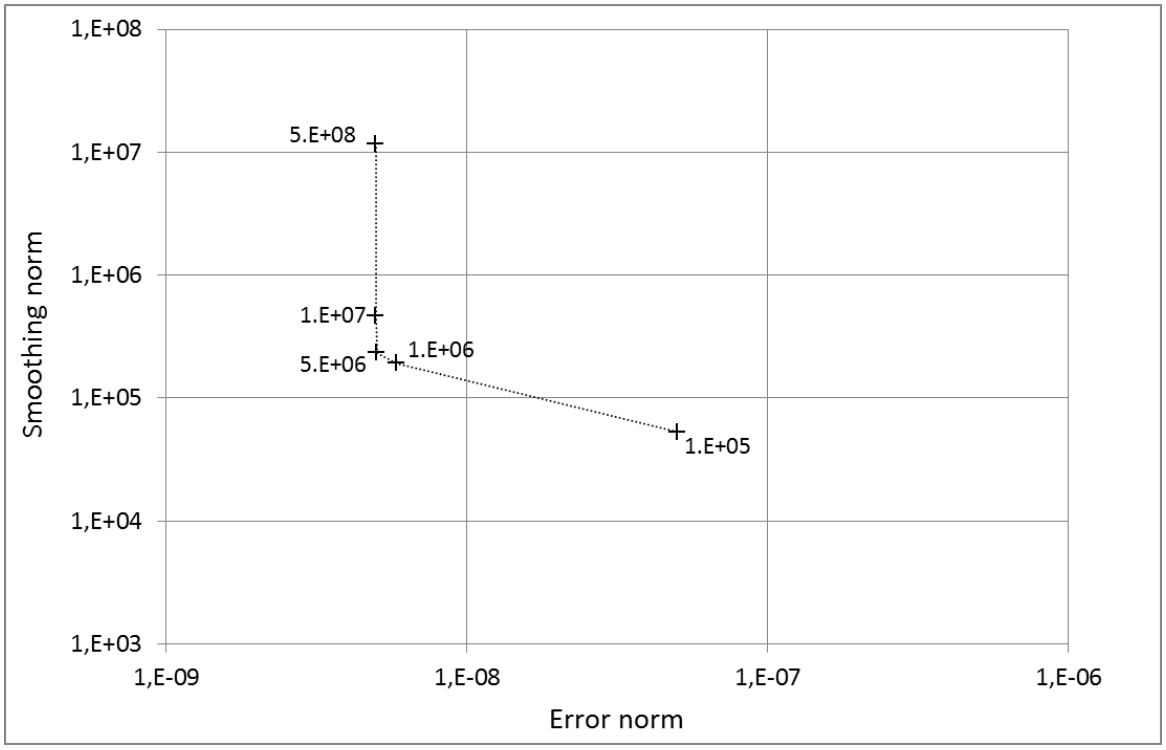

Figure 5.6: Plot of the L-curve for the MPC algorithm for test case 1 (hammer impact) with the model with an error in the eigenfrequencies of 0%, an error in the eigenvectors of 0% and 16 sensors. The values of the regularization parameter are marked by a cross with the corresponding value. The corner of the L-curve can be identified between the values 10^6 and 5×10^6.

Corresponding to the L-curve, the reconstructed force in y-direction for test case 1 is plotted in Figure 5.7 for different levels of regularization. The regularization parameter selected according to the L-curve method corresponds to $w_{i+1,j}^{y} = 5\times10^6$. Here, the reconstructed force closely follows the reference force with a slight overshot of about 20 % and a time delay less than 1 ms. This can be regarded as a sufficient accuracy taking into account the short duration of the input force and the inertia of the system. Higher regularization parameters lead to oscillations with an increasing frequency around the reference value as the algorithm performs stronger adaptions of its estimates expressed by the gain matrix $\boldsymbol{\mathcal{K}}$ for the AKF or a higher weight $w_{i+1,j}^{y}$ on the error term for the MPC.

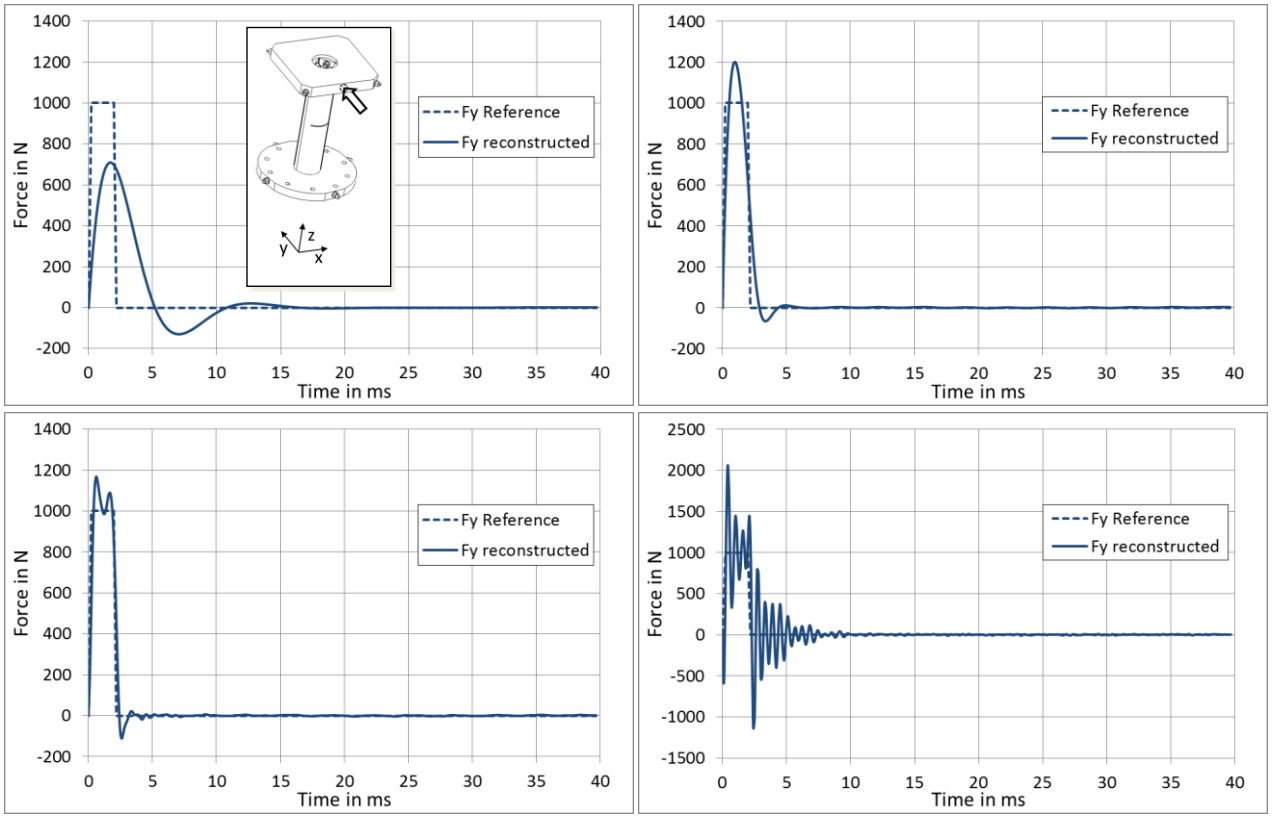

Figure 5.7: Reconstructed and reference force component in y-direction by the MPC algorithm for test case 1 (hammer impact) with the model with an error in the eigenfrequencies of 0 %, an error in the eigenvectors of 0 % and 16 sensors. The regularization parameter $w_{i+1,j}^{y}$ corresponds to 10^5 (top left), 5×10^6 (top right), 10^7 (bottom left) and 5×10^8 (bottom right).

With the L-curve method, a regularization parameter can be found leading to a force estimation with a performance being on average 20 % worse than choosing the parameter directly based on the performance criterion. Of course, the performance criterion can only be calculated for known excitation forces. Furthermore, the general difficulty to define an objective performance criterion has to be considered as discussed in Section 4.3. For example, Jacquelin et al. also conclude, "there exists a range of good values to regularize the problem" [32] after having investigated different methods to determine the optimal regularization parameters.

5.3.3 Compensation of time delay in the AKF algorithm

Due to the predictor-corrector nature of the AKF algorithm, the algorithm adjusts its estimates of the excitation forces based on the measurement innovations or residuals, which represent the difference between predicted output and measured output. If the problem is solved with a high amount of regularization, the AKF only slowly adjusts the estimates of the forces, as a relatively high measurement innovation is necessary for a fast adaption. This leads to a time delay Δt_{AKF} in the reconstructed forces, as shown for one force component in Figure 5.8.

In order to estimate and reduce this time delay, a simple procedure has been implemented in the final algorithm. At first, the reconstructed excitation forces are used to solve the forward problem of the regarded problem and hence to calculate the outputs of the strain sensors

assuming that the reconstructed forces are the true excitation forces. The strain signal obtained from the forward problem can now be compared to the measured strain signal, as depicted in Figure 5.8 for strain gauge 8 (SG 8).

By calculating the cross-correlation between these two strain time histories for each strain sensor for a time window corresponding to twice the duration of a long-term excitation, a time delay estimate for each sensor is determined. The final time delay used to correct the excitation force estimates corresponds to the median of the individual time delays. The program flow chart of this technique is illustrated in Figure 5.9. The time delay depends on the level of regularization for the particular load case and is in the range of a few milliseconds.

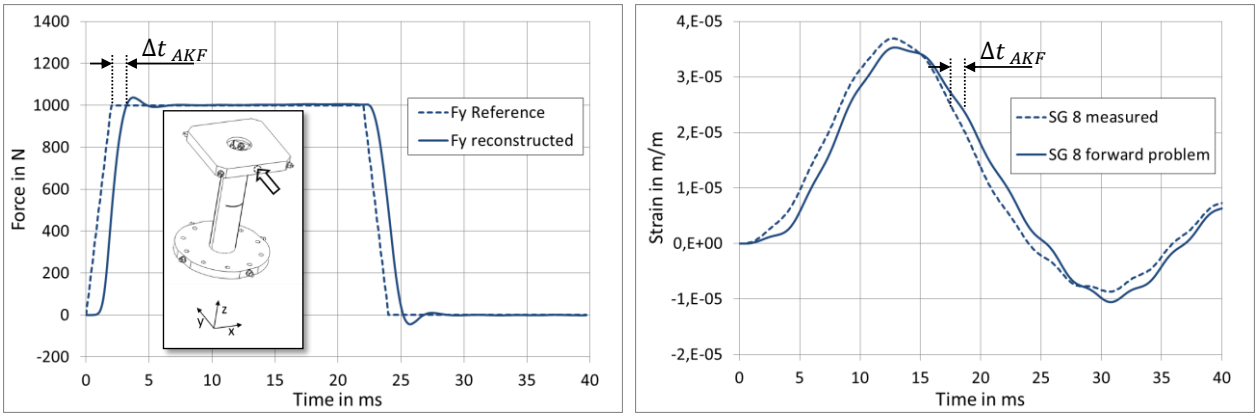

Figure 5.8: Compensation of time delay in the AKF algorithm: Reconstructed and reference force component in y-direction with the AKF algorithm for test case 1 (scenario 1) with an error in the eigenfrequencies of 0%, an error in the eigenvectors of 0% and 16 sensors (left). The strain recording obtained by solving the forward problem based on the reconstructed forces and the experimentally measured strain at strain gauge (SG) 8 are shown in the right graph.

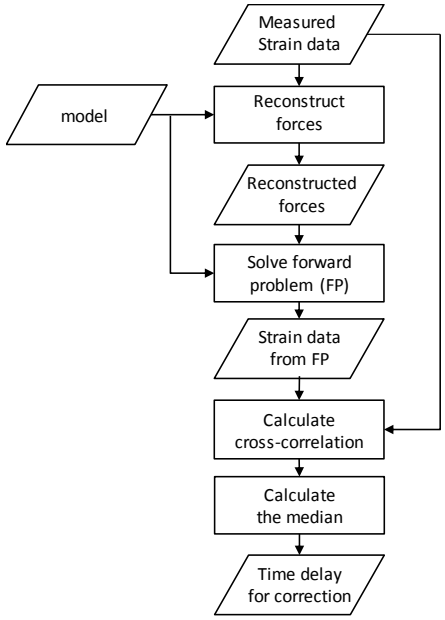

Figure 5.9: Compensation of time delay in the AKF algorithm: Program flow chart. The cross-correlation between the measured strain data and the strain data obtained by solving the forward problem based on the reconstructed forces is used to calculate the time delay.

5.4 Results and comparison of AKF and MPC

In this section, an overview of the force reconstruction results for the different test cases in combination with different models is given. In addition, the impact of modelling errors on the force reconstruction is discussed. Exemplary results are presented in Section 5.4.1. The impact of modelling errors on the force reconstruction and a general comparison of the AKF and MPC algorithm is discussed in Section 5.4.2.

5.4.1 Test case results for different models

The force reconstruction methods have been tested with different models. The regularization parameter is individually chosen for each combination of test case and model according to the L-curve method. The weights on the input increments $w_{i,j}^{\Delta u}$ of the MPC algorithm are kept at a value of 0.1 as the amount of regularization is only depending on the ratio between the weights $w_{i,j}^{\Delta u}$ and $w_{i+1,j}^{y}$. The diagonal values of the covariance matrices $\boldsymbol{Q}$, $\boldsymbol{\mathcal{R}}$ and $\boldsymbol{\mathcal{P}}_{-1}$ of the AKF algorithm are set to 10^{-16}, 10^{-12} and 10, respectively. As diagonal elements of the covariance matrices $\boldsymbol{Q}$ and $\boldsymbol{\mathcal{R}}$, the square root of these values corresponds to a small percentage of the maximum values of the underlying quantities. In general, the force reconstruction has shown a very low sensitivity to these values compared to the regularization parameter $\boldsymbol{\mathcal{S}}$. The time delay in the reconstructed forces with the AKF method has been corrected following the procedure in Section 5.3.3.

In this context, a selection of results is presented, which is representative for the different models with errors in the eigenfrequencies and eigenvectors as defined in Table 5.3. The reconstructed forces are shown for the MPC and AKF algorithm and for different numbers of sensors. The applied forces are plotted for comparison as reference forces in each graph. Therefore, this section illustrates the influence of the considered models on the reconstructed forces as well as it gives an overview of the different test cases. As the results discussed in this section only represent a part of the possible combinations of test case and model, a discussion considering all results will follow in section 5.4.2.

Figure 5.10 shows the results of test case 3 with a hammer impact obtained by a model without artificial errors. The MPC algorithm with six sensors has been used to identify the excitation forces. Despite the short duration of the excitation forces and the related high force gradients, the time history of the forces is well reconstructed with a time delay less than 1 ms.

For test case 6 (scenario 1) and the same model, the reference forces in x and y direction in Figure 5.11 have been identified with a time delay of 2 ms. The AKF algorithm estimates very well the reference forces with a $RMSE_F$ =63 N and a $RMSE_M$ =2.3 Nm.

The results in Figure 5.12 and Figure 5.13 have been calculated with an error in the eigenfrequencies and eigenvectors of the identified model of 0% and 10%, respectively. In Figure 5.12, it can be seen that the use of a higher number of sensors in test case 4 (scenario 3) yields a significantly better force estimate as the error in the eigenvectors can be better compensated. This is also reflected in the error measure in Table 5.4. The comparison between MPC and AKF in Figure 5.13 for test case 5 with a hammer impact illustrates a very accurate force estimation with a minor time delay of about 2 ms in the AKF estimate.

If the error in the eigenvectors of the identified model is increased to 30% and the error in the eigenfrequencies remains at 0%, the model with the higher number of sensors outperforms again the model with a lower number of sensors for test case 5 (scenario 1) as illustrated in Figure 5.14. The corresponding RSME are given in Table 5.5. The high difference in the $RMSE_M$ is clearly visible in the reconstructed moment components. The error in the components of the strain eigenvector of the torsion mode with high absolute values leads to an underestimation of the reconstructed Moment M_z. In addition, this error causes oscillations in the reconstructed force component F_x and moment component M_y in the eigenfrequency of the torsion mode.

In Figure 5.15, the forces reconstructed by the AKF and MPC algorithm for test case 3 (scenario 2) are very similar. This is confirmed by the error measure in Table 5.6.

The results for a model with an error in the eigenfrequencies and eigenvectors of 5% and 0%, respectively, are presented in Figure 5.16 and Figure 5.17. The forces applied in test case 2 by a hammer impact in Figure 5.16 are still well reconstructed. However, the model with a higher number of sensors gives a better estimate. The error in the eigenfrequencies is visible for both numbers of sensors after the absence of the excitation forces as the algorithm is compensating the error in the frequencies of the excited modes. In addition, the higher regularization parameter of the AKF is noticeable as discussed in section 5.3.2.

The same effects are present for test case 7 (scenario 1) and the same model in Figure 5.17. In addition, it can be seen that the MPC algorithm follows better the excitation forces over time, which results in a slightly better error measure in Table 5.7.

A model with an error in the eigenvectors and the eigenfrequencies of 10% and 5%, respectively, is used in Figure 5.18 and Figure 5.19 to reconstruct the excitation forces. Again, a higher number of sensors for test case 1 (scenario 1) in Figure 5.18 results in a better force estimation with the corresponding RSME in Table 5.8. For test case 2 (scenario 2) in Figure 5.19, the two algorithms give very similar results with again a minor time delay of about 2 ms in the AKF. This is also reflected in the error measure in Table 5.9.

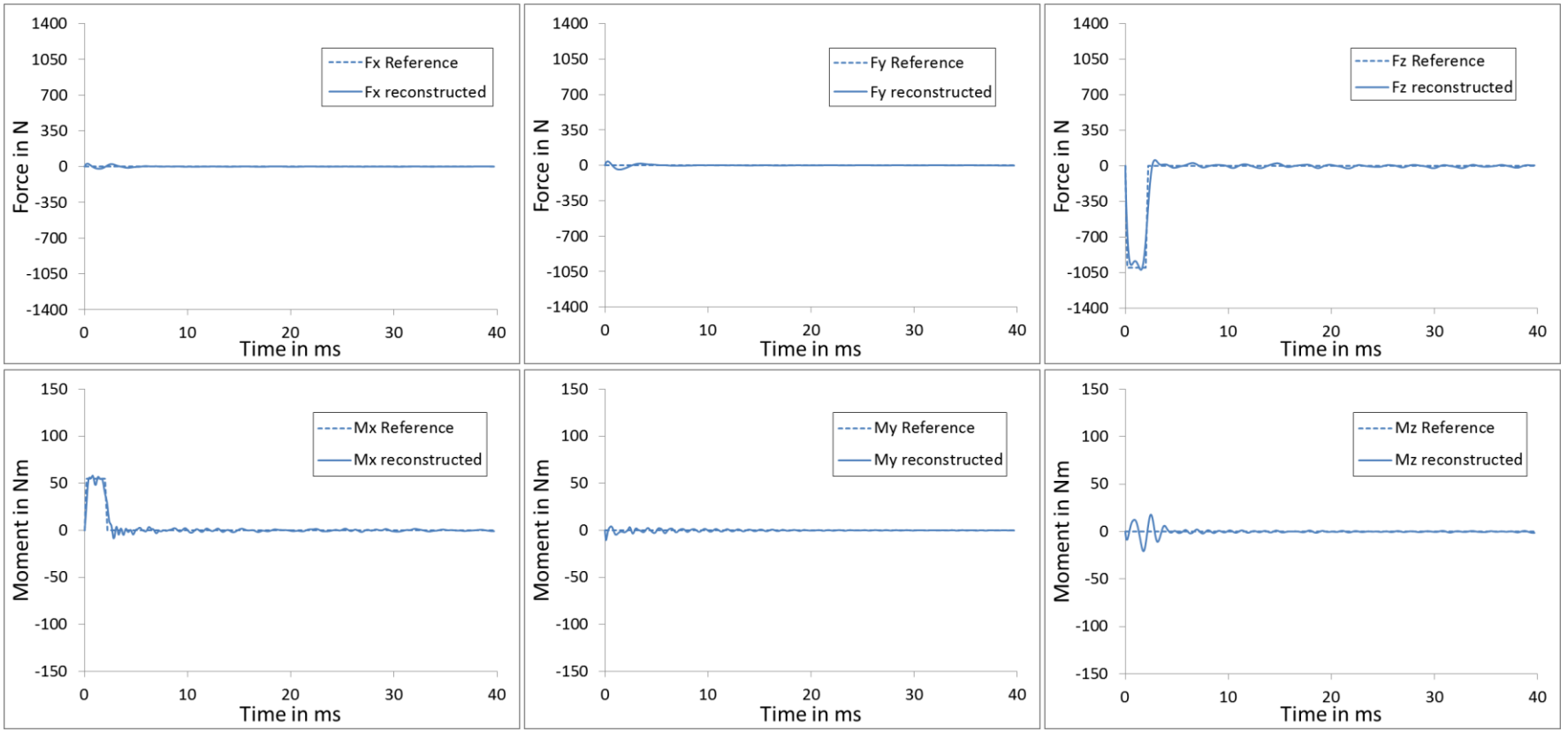

Figure 5.10: Test case 3 (hammer impact): Force reconstruction by the MPC algorithm with the model with an error in the eigenfrequencies and eigenvectors of 0%. The reconstructed forces are shown for the model with 6 sensors.

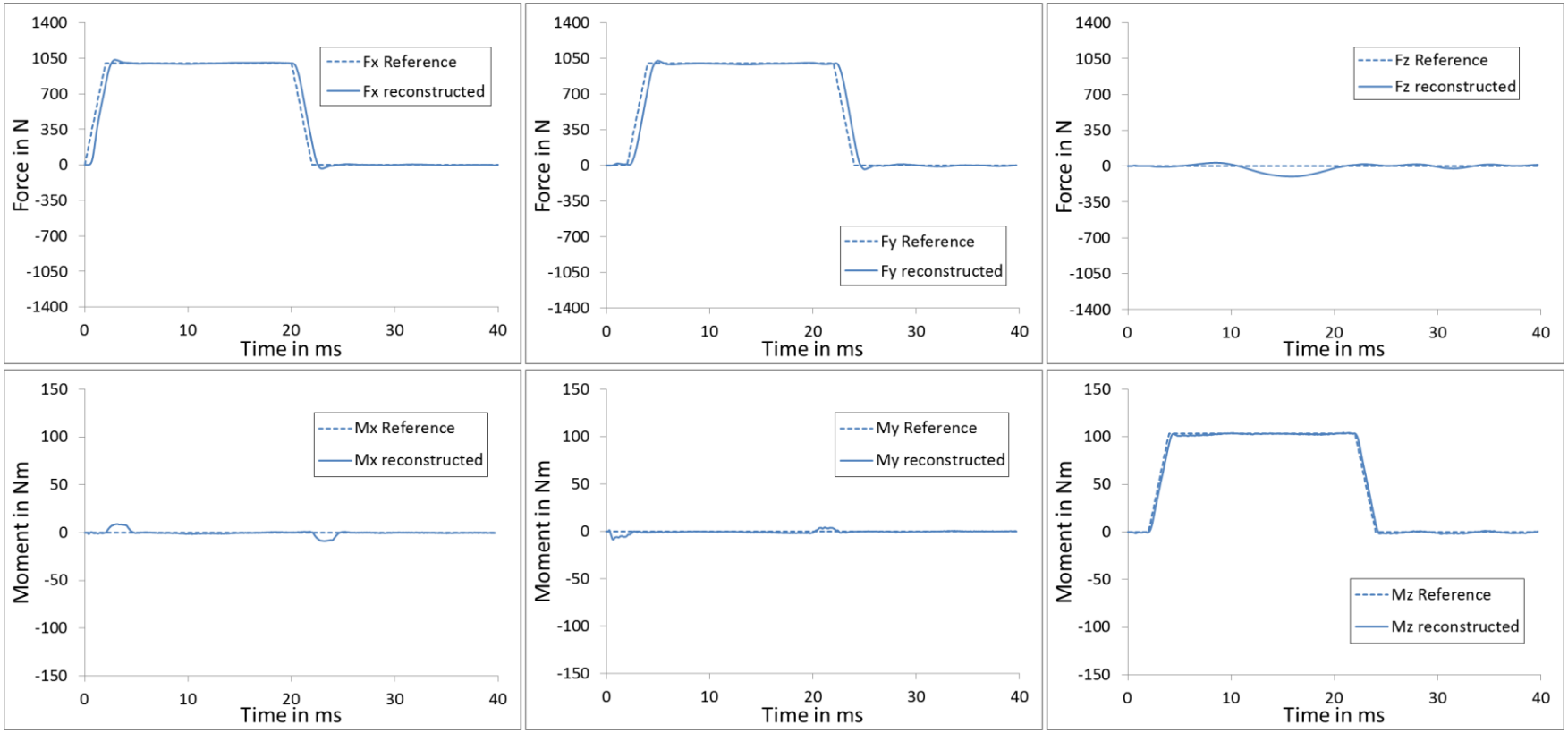

Figure 5.11: Test case 6 (scenario 1): Force reconstruction by the AKF algorithm with the model with an error in the eigenfrequencies and eigenvectors of 0%. The reconstructed forces are shown for the model with16 sensors.

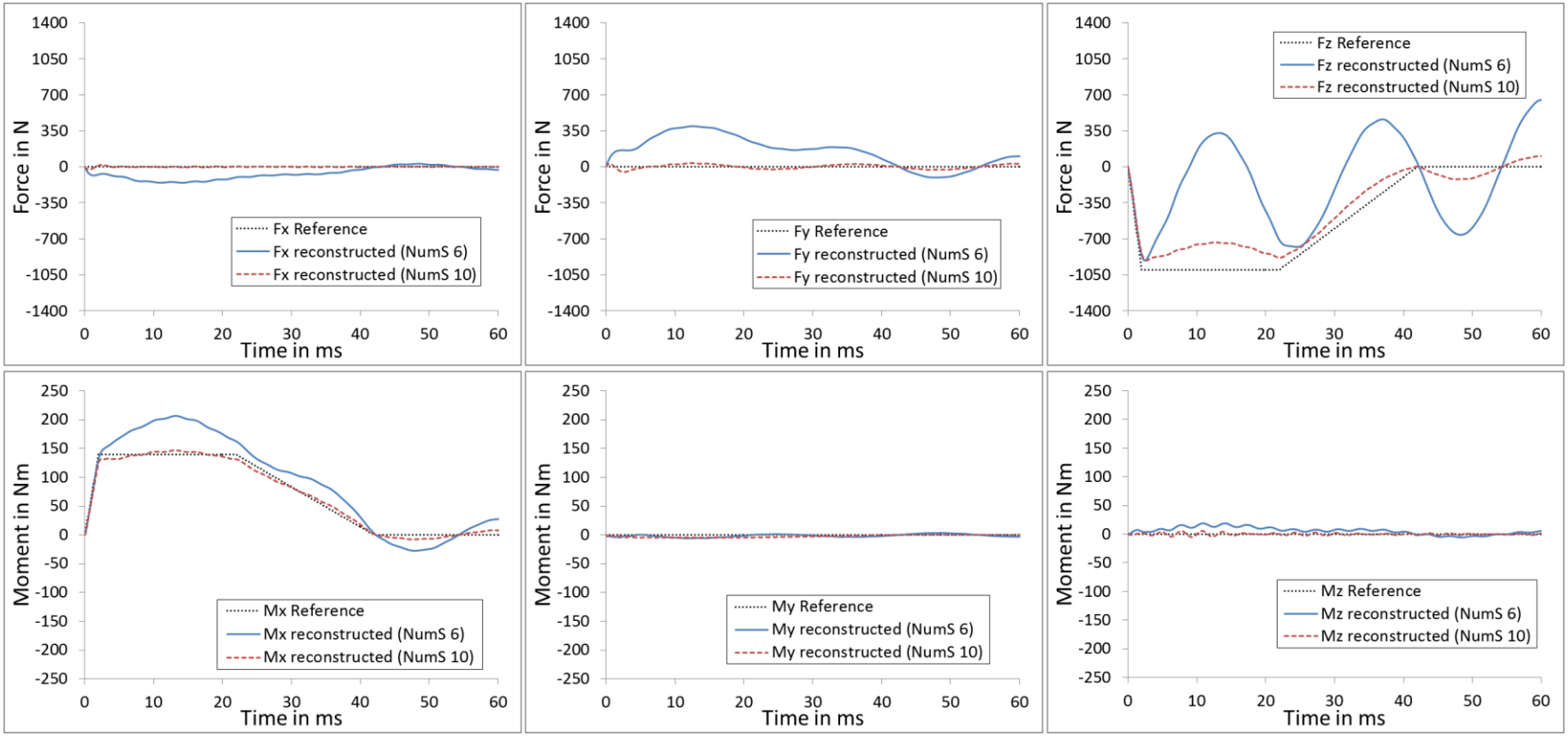

Figure 5.12: Test case 4 (scenario 3): Force reconstruction by the MPC algorithm with the model with an error in the eigenfrequencies and eigenvectors of 0% and 10%. The reconstructed forces for the model with 6 (NumS 6) and 10 sensors (NumS 10) are shown.

	NumS 6	NumS 10
$RMSE_F$	394 N	84 N
$RMSE_M$	20.3 Nm	4.6 Nm

Table 5.4: RSME for test case 4 (scenario 3) for the MPC algorithm with the model with an error in the eigenfrequencies and eigenvectors of 0% and 10%. The RMSE are listed for the model with 6 sensors (NumS 6) and 10 sensors (NumS 10).

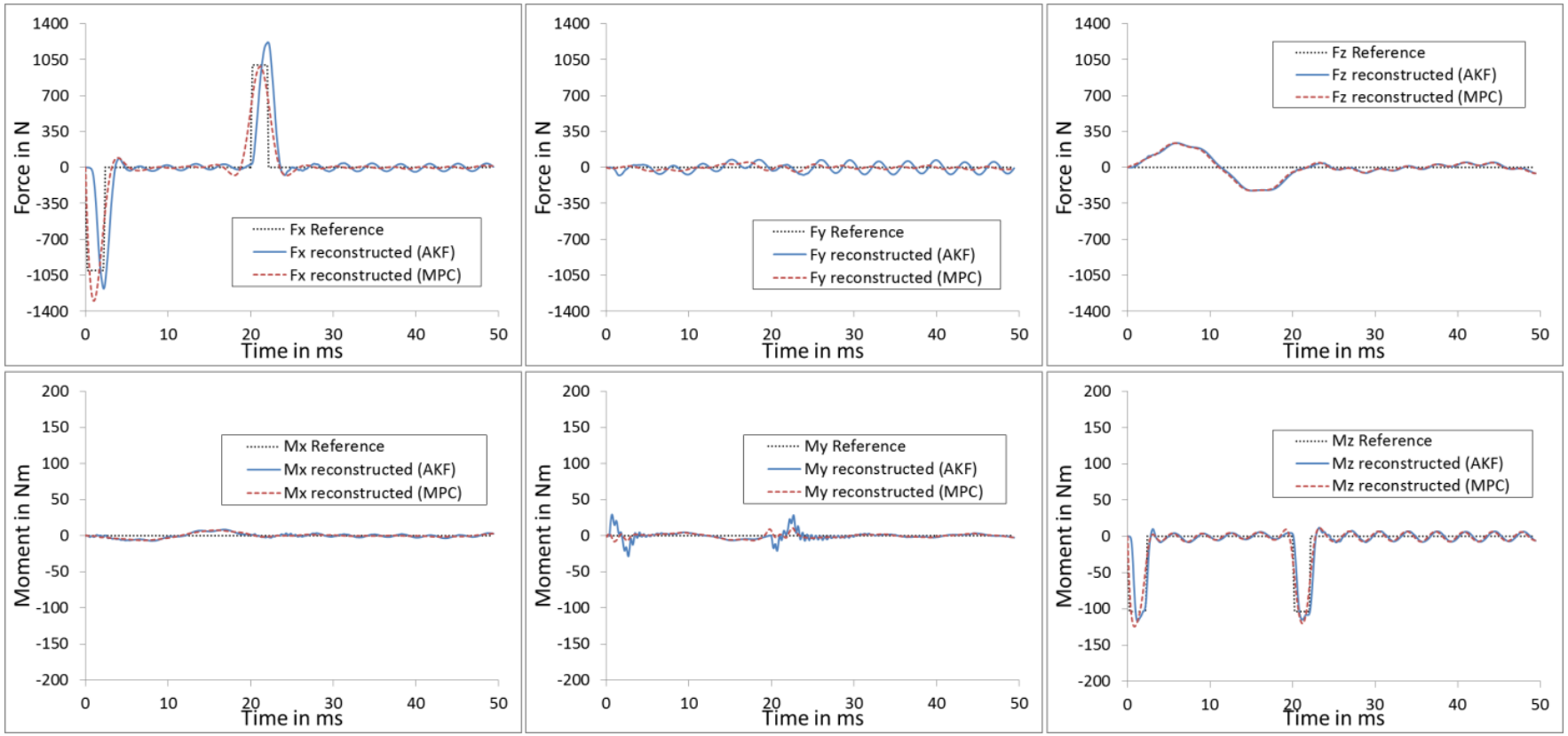

Figure 5.13: Test case 5 (hammer impact): Force reconstruction by the MPC and AKF algorithm with the model with an error in the eigenfrequencies and eigenvectors of 0% and 10%. The reconstructed force for the model with 16 sensors are shown.

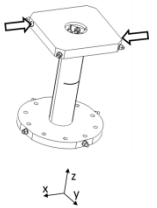

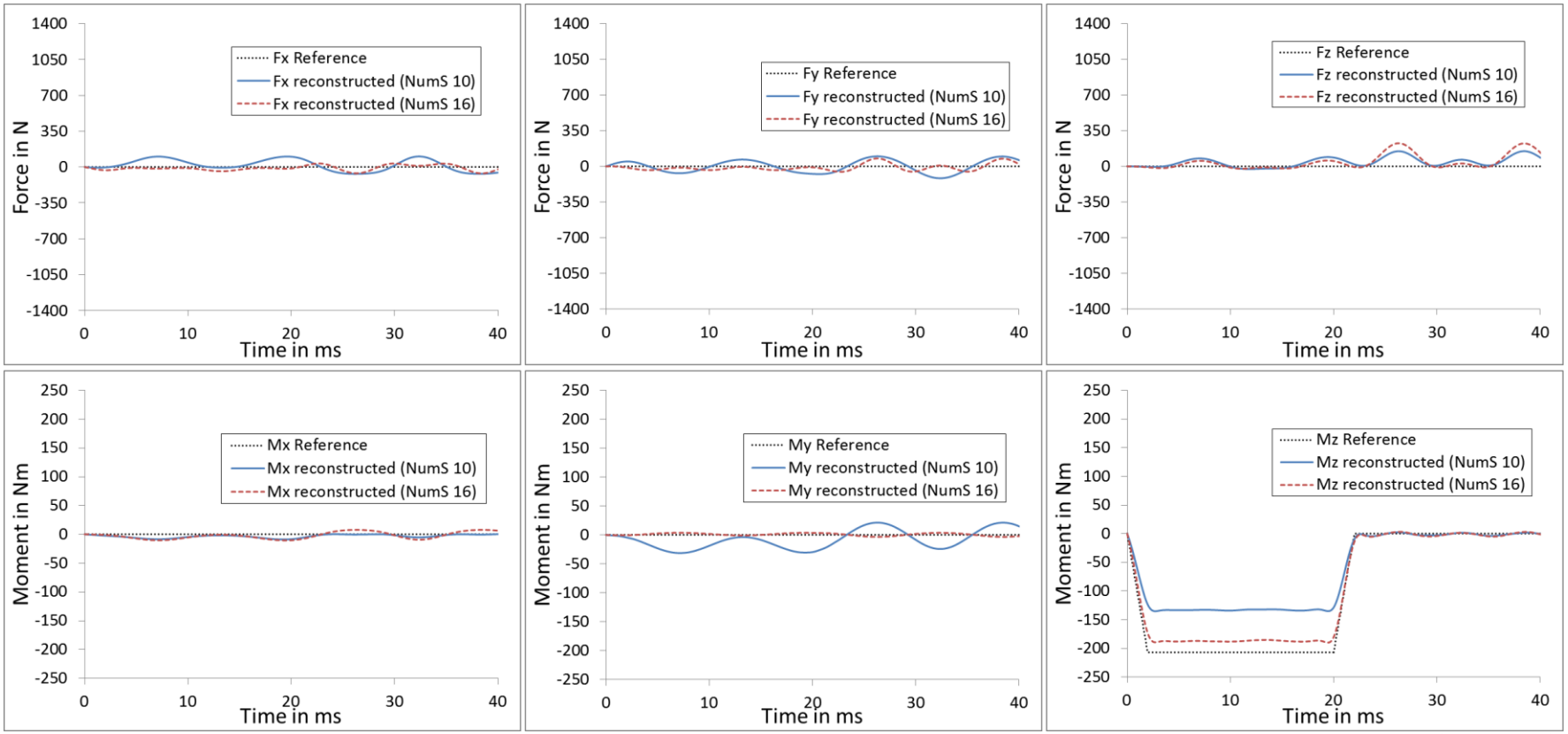

Figure 5.14: Test case 5 (scenario 1): Force reconstruction by the MPC algorithm with the model with an error in the eigenfrequencies and eigenvectors of 0% and 30%. The reconstructed forces for the model with 10 (NumS 10) and 16 sensors (NumS 16) are shown.

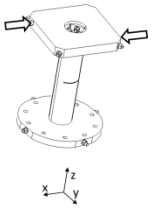

	NumS 10	NumS 16
$RMSE_F$	60 N	54 N
$RMSE_M$	30.7 Nm	8.8 Nm

Table 5.5: RSME for test case 5 (scenario 1) for the MPC with the model with an error in the eigenfrequencies and eigenvectors of 0% and 30%. The RMSE are listed for the model with 10 sensors (NumS 10) and 16 sensors (NumS 16).

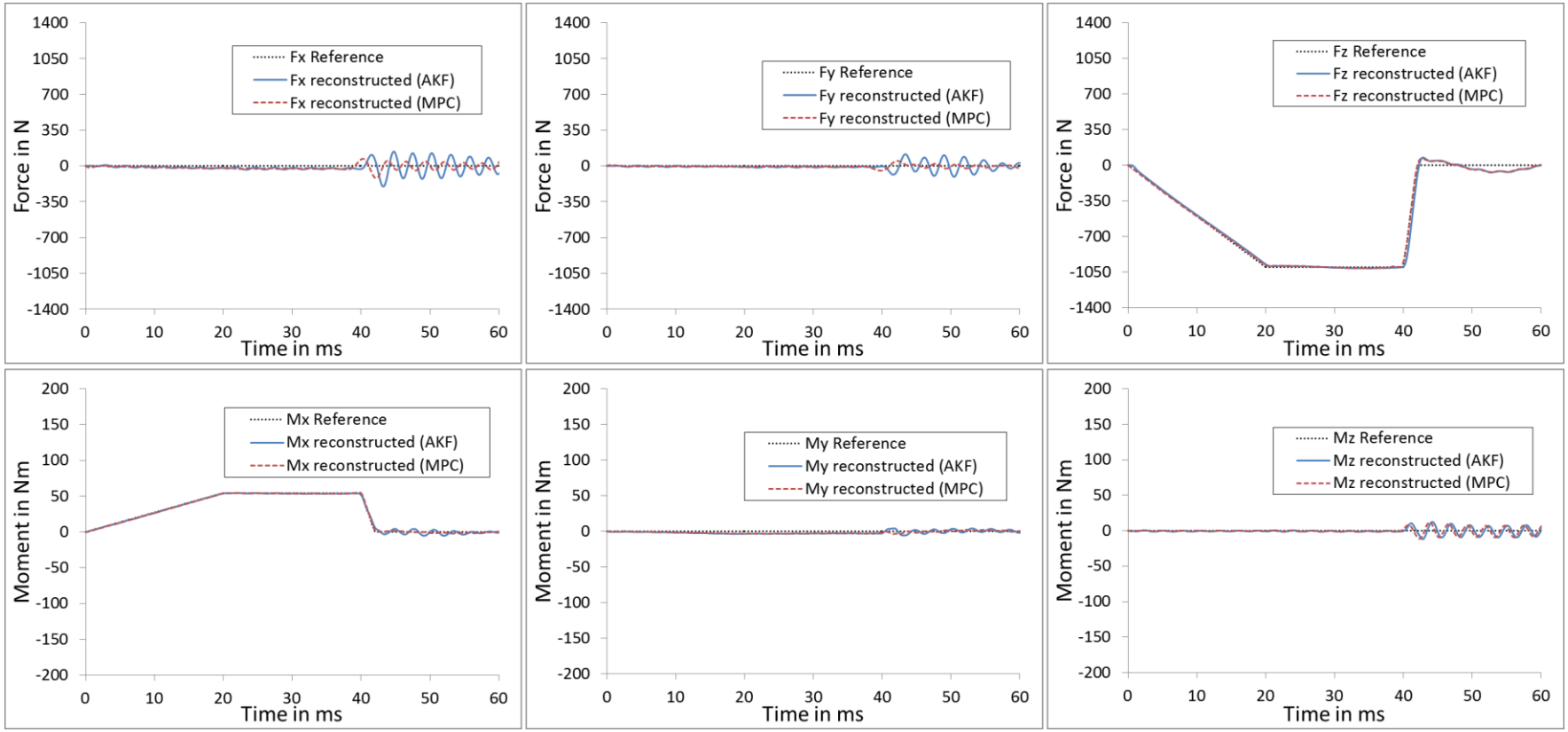

Figure 5.15: Test case 3 (scenario 2): Force reconstruction by the MPC and AKF algorithm with the model with an error in the eigenfrequencies and eigenvectors of 0% and 30%. The reconstructed forces are shown for the model with 16 sensors.

	AKF	MPC
$RMSE_F$	42 N	24 N
$RMSE_M$	2.8 Nm	2.6 Nm

Table 5.6: RSME for test case 3 (scenario 2) for the MPC and AKF algorithm with the model with an error in the eigenfrequencies and eigenvectors of 0% and 30%. The RSME are listed for the model with 16 sensors.

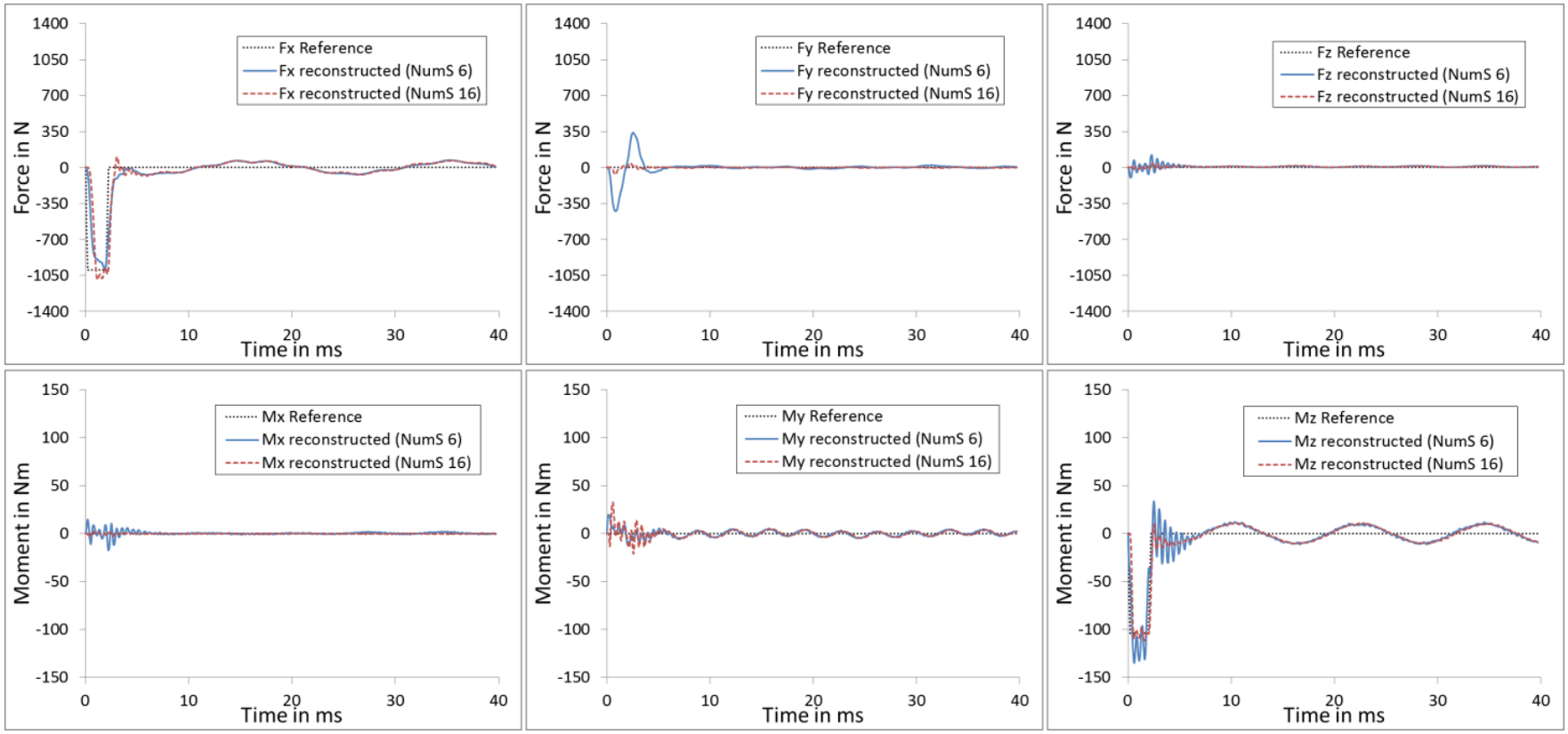

Figure 5.16: Test case 2 (hammer impact): Force reconstruction by the AKF algorithm with the model with an error in the eigenfrequencies and eigenvectors of 5% and 0%. The reconstructed forces for the model with 6 (NumS 6) and 16 sensors (NumS 16) are shown.

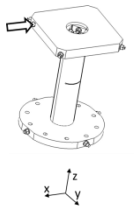

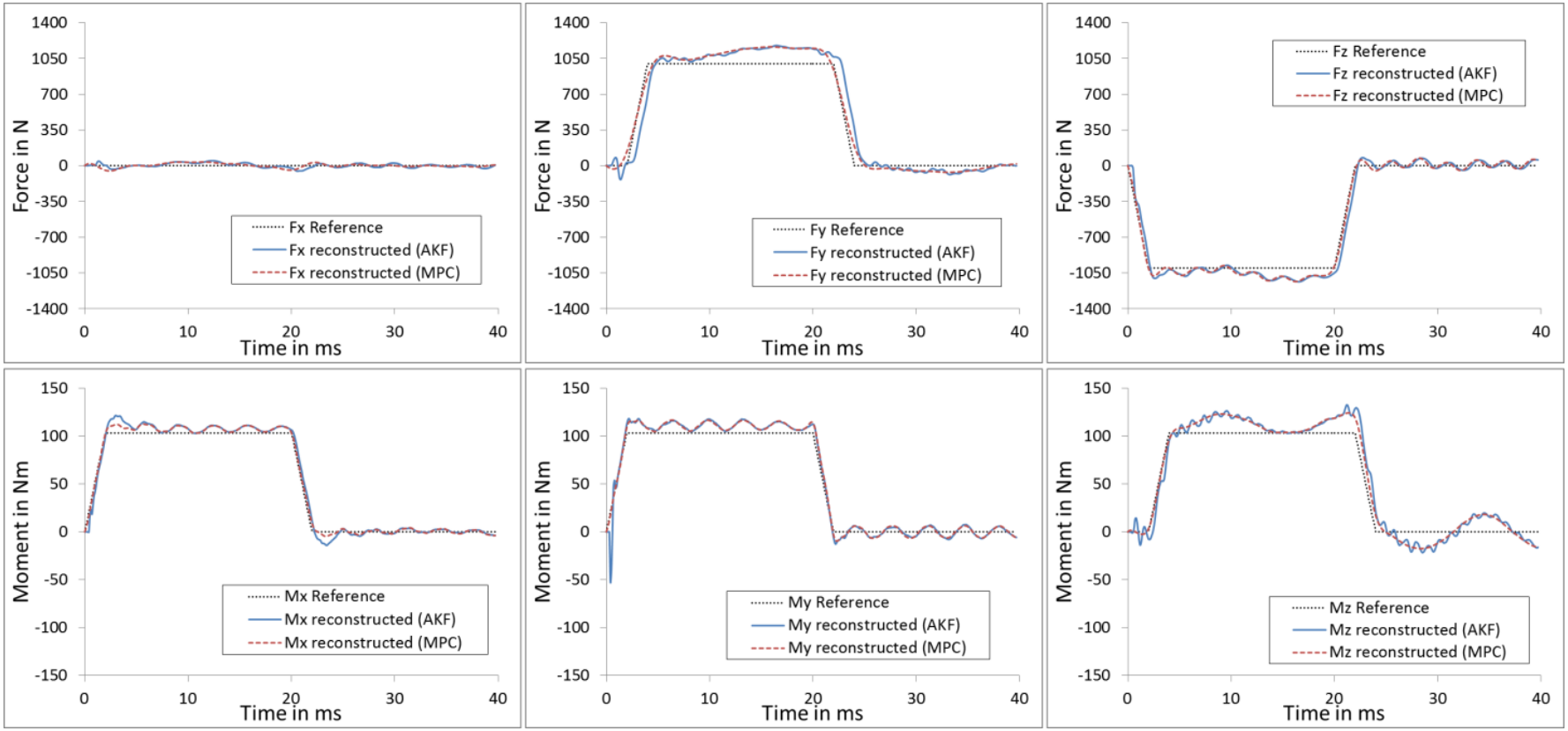

Figure 5.17: Test case 7 (scenario 1): Force reconstruction by the MPC and AKF algorithm with a model with an error in the eigenfrequencies and eigenvectors of 5% and 0%. The reconstructed forces for the model with 10 sensors are shown.

	AKF	MPC
$RMSE_F$	84 N	59 N
$RMSE_M$	10.0 Nm	8.2 Nm

Table 5.7: RSME for test case 7 (scenario 1) for the MPC and AKF algorithm with a model with an error in the eigenfrequencies and eigenvectors of 5% and 0%.. The RMSE are listed for the model with 10 sensors.

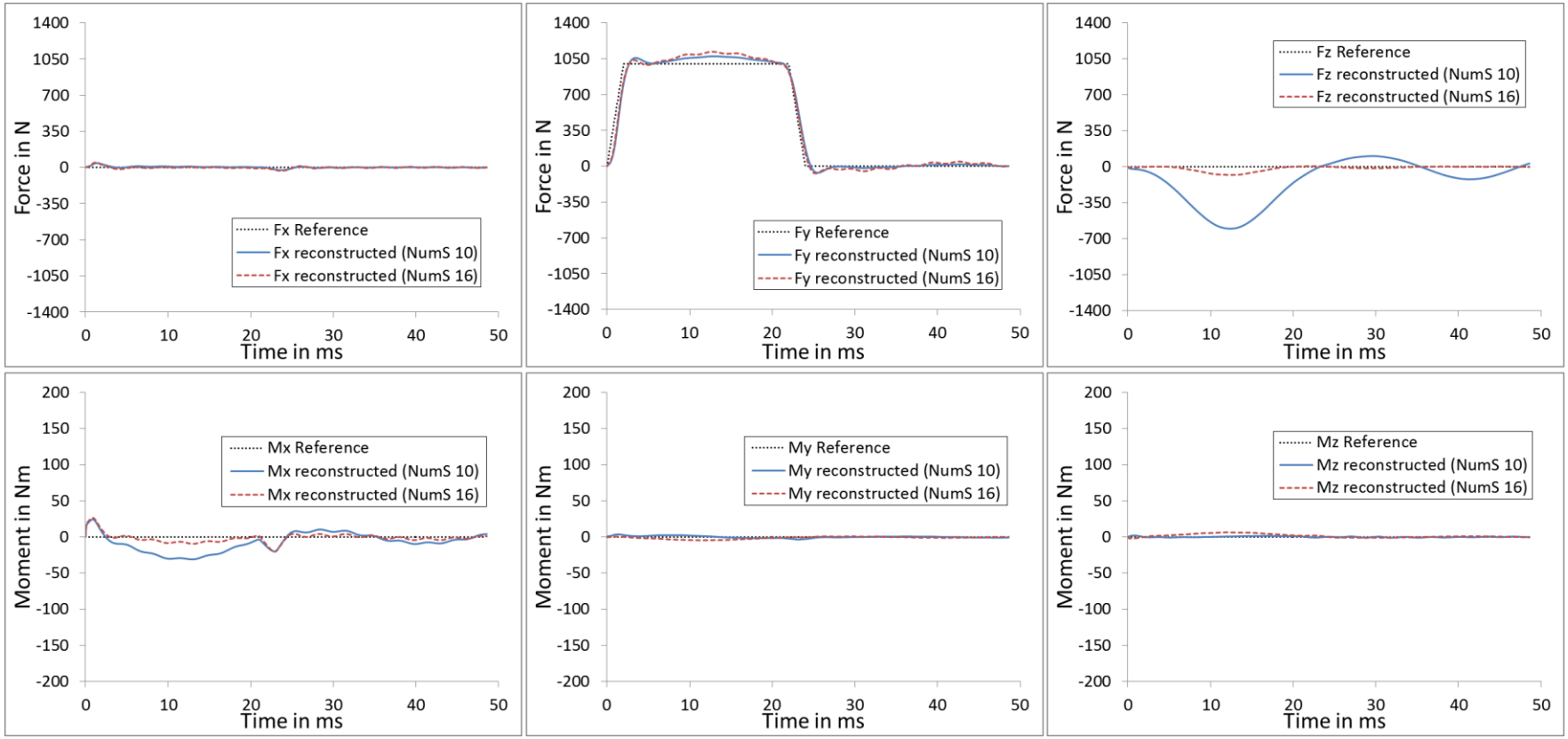

Figure 5.18: Test case 1 (scenario 1): Force reconstruction by the AKF algorithm with the model with an error in the eigenfrequencies and eigenvectors of 5% and 10%. The reconstructed forces for the model with 10 (NumS 10) and 16 sensors (NumS 16) are shown.

	NumS 10	NumS 16
$RMSE_F$	151 N	41 N
$RMSE_M$	8.5 Nm	4.2 Nm

Table 5.8: RSME for test case 1 (scenario 1) for the AKF algorithm with the model with an error in the eigenfrequencies and eigenvectors of 5% and 10%. The RMSE are listed for the model with 10 (NumS 10) and 16 (NumS 16) sensors.

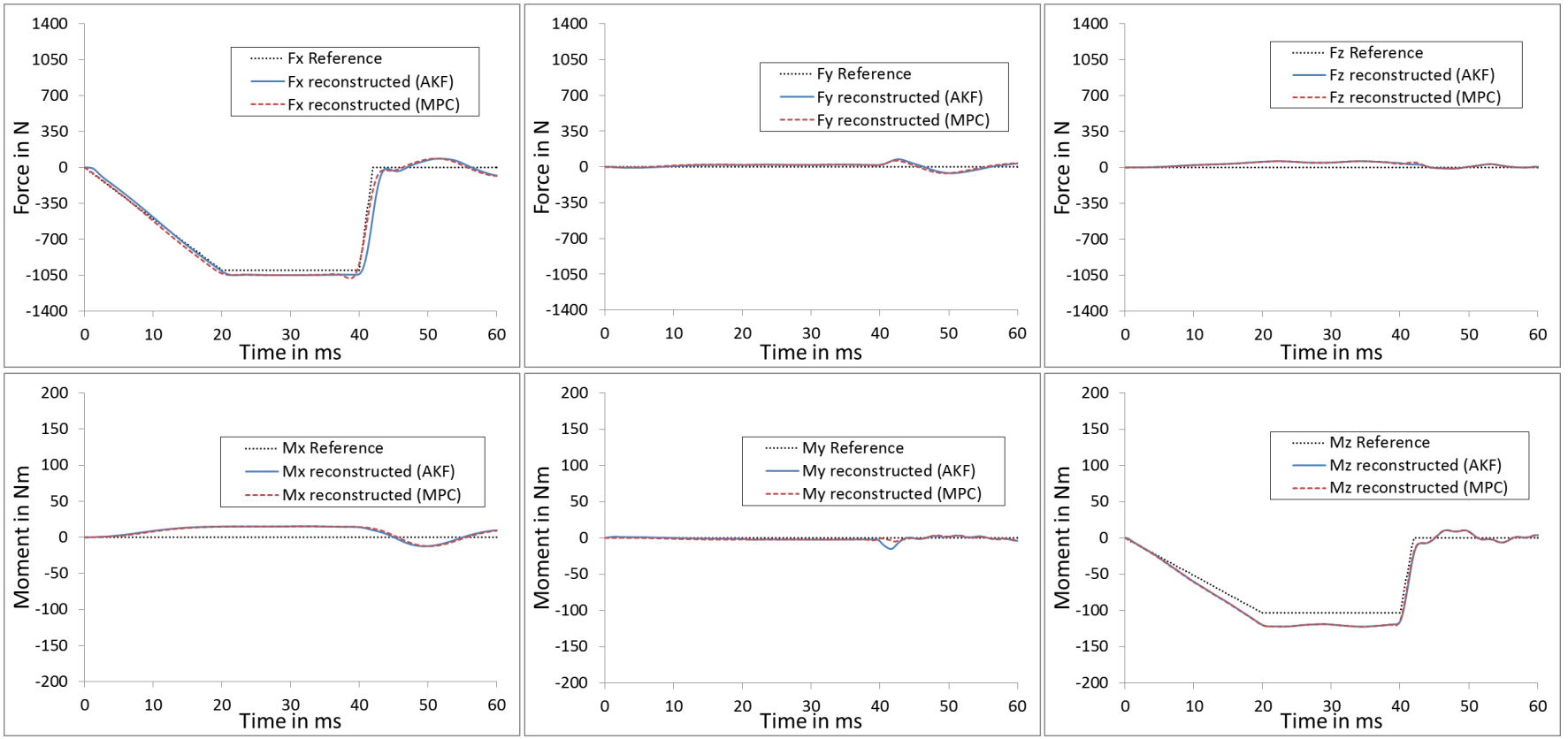

Figure 5.19: Test case 2 (scenario 2): Force reconstruction by the MPC and AKF algorithm with the model with an error in the eigenfrequencies and eigenvectors of 5% and 10%. The reconstructed forces for the model with 10 sensors are shown.

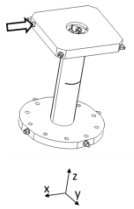

	AKF	MPC
$RMSE_F$	56 N	40 N
$RMSE_M$	9.8 Nm	9.6 Nm

Table 5.9: RSME for test case 2 (scenario 2) for the MPC and AKF algorithm with the model with an error in the eigenfrequencies and eigenvectors of 5% and 10%. The RMSE are listed for the model with 10 sensors.

5.4.2 Impact of modelling errors on force reconstruction and comparison of MPC and AKF

In the preceding section, the results for individual test cases with different models and the MPC and AKF algorithm have been compared in order to see the influence on the reconstructed force history. The test cases have been defined in such a way that they cover a wide range of loading conditions. For that reason, the individual comparison of each test case is not sufficient to get an overall picture of the impact of different models on the force reconstruction and the test cases have to be considered as an entire set. Therefore, an average of the RSME of the test cases with long-term excitation, $RSME_{Fa}$ and $RMSE_{Ma}$, is defined which expresses an overall tendency. The average RSME for the models with an error in the eigenfrequencies of 0% and an error in the eigenvectors of 5% are given in Figure 5.20.

As the RSME scales with the excitation forces, the relative change of the average RSME for the test cases is used to evaluate the impact of modelling errors on the force reconstruction. When comparing the average RSME of the different models, it always has to be considered that even the model defined by an error in the eigenfrequencies and eigenvectors of 0 % does not represent a perfectly matching model as it consists of a reduced number of modes.

From the $RMSE_{Fa}$ for the model with an error in the eigenfrequencies of 0% presented in the upper left graph in Figure 5.20, the following observations can be made. For an error in the eigenvectors of 0%, the $RSME_{Fa}$ is at a low level of about 25 to 75 N for both algorithms and all sensor configurations in relation to the $RSME_{Fa}$ at higher error levels of up to 2400 N. In contrast, a significant increase of the $RSME_{Fa}$ to about 500 N for the model with an error in the eigenvectors of 10 % and 6 sensors can already be observed. This $RSME_{Fa}$ corresponds to more than 6 times the $RSME_{Fa}$ of the model with an error in the eigenvectors of 0 % and as well 6 sensors. The $RSME_{Fa}$ of the models with 10 and 16 sensors only doubles for the same conditions. Regarding the model with an error in the eigenvectors of 10 %, the $RSME_{Fa}$ of the model with 6 sensors is about 400 % higher than the $RSME_{Fa}$ of the models with 10 and 16 sensors. For the models with an error in the eigenvectors of 30 %, also the difference in the $RSME_{Fa}$ between the models with 10 and 16 sensors becomes more obvious with an increase of about 250 %. The difference in the $RSME_{Fa}$ for this condition between the model with 6 and 16 sensors is at about 1400 %. The $RSME_{Fa}$ of the models with an error in the eigenfrequencies of 5 % in the upper right graph in Figure 5.20 is for all conditions about 20 % higher compared to the models with an error in the eigenfrequencies of 0 %.

The impact of modelling errors on the $RSME_{Ma}$ is similar to the impact on the $RSME_{Fa}$. The $RSME_{Ma}$ of the model with an error in the eigenfrequencies and eigenvectors of 0 % and 10 % is 400 % higher for the model with 6 sensors than for the models with 10 and 16 sensors. The $RSME_{Ma}$ for the model with an error in the eigenvectors of 30 % increases from the model with 16 sensors to the model with 10 sensors by 300 %. A high difference is also obvious between the model with 6 sensors and 16 sensors under these conditions with an increase of 3400 %.

The influence of the error in the eigenfrequencies of 5 % on the $RSME_{Ma}$ decreases from the model with an error in the eigenvectors of 0 % with approximately 100 % to 5 % for an error in the eigenvectors of 30 %.

The difference of the $RSME_{Fa}$ and $RSME_{Ma}$ between the MPC and AKF algorithm for the same conditions is small compared to the influence of the errors in the model. The $RSME_{Fa}$ and $RSME_{Ma}$ of the AKF are in general 20 % higher than the MPC. This shows that the major influence on the errors in the force reconstruction are due to the errors in the model as both algorithms use the same model. Nevertheless, the MPC shows a slightly smaller error as the AKF algorithms always shows a minor shift in the reconstructed forces.

Regarding the number of sensors, it can be concluded that 6 sensors are already sufficient to allow for small errors in the reconstructed forces, if the errors in the identified model are close to 0 %. As this requirement is unlikely to be met by an experimental modal analysis, the range up to an error in the eigenfrequencies and eigenvectors of 5 % and 10 % is more realistic. In this range, 10 and 16 sensors show similar errors in the force reconstruction. Nevertheless, it is more reasonable to apply 16 sensors as the errors for a model with 10 sensors strongly increase from an error in the eigenvectors of 10 %. In addition, the failure of single sensors can be more easily compensated by 16 sensors.

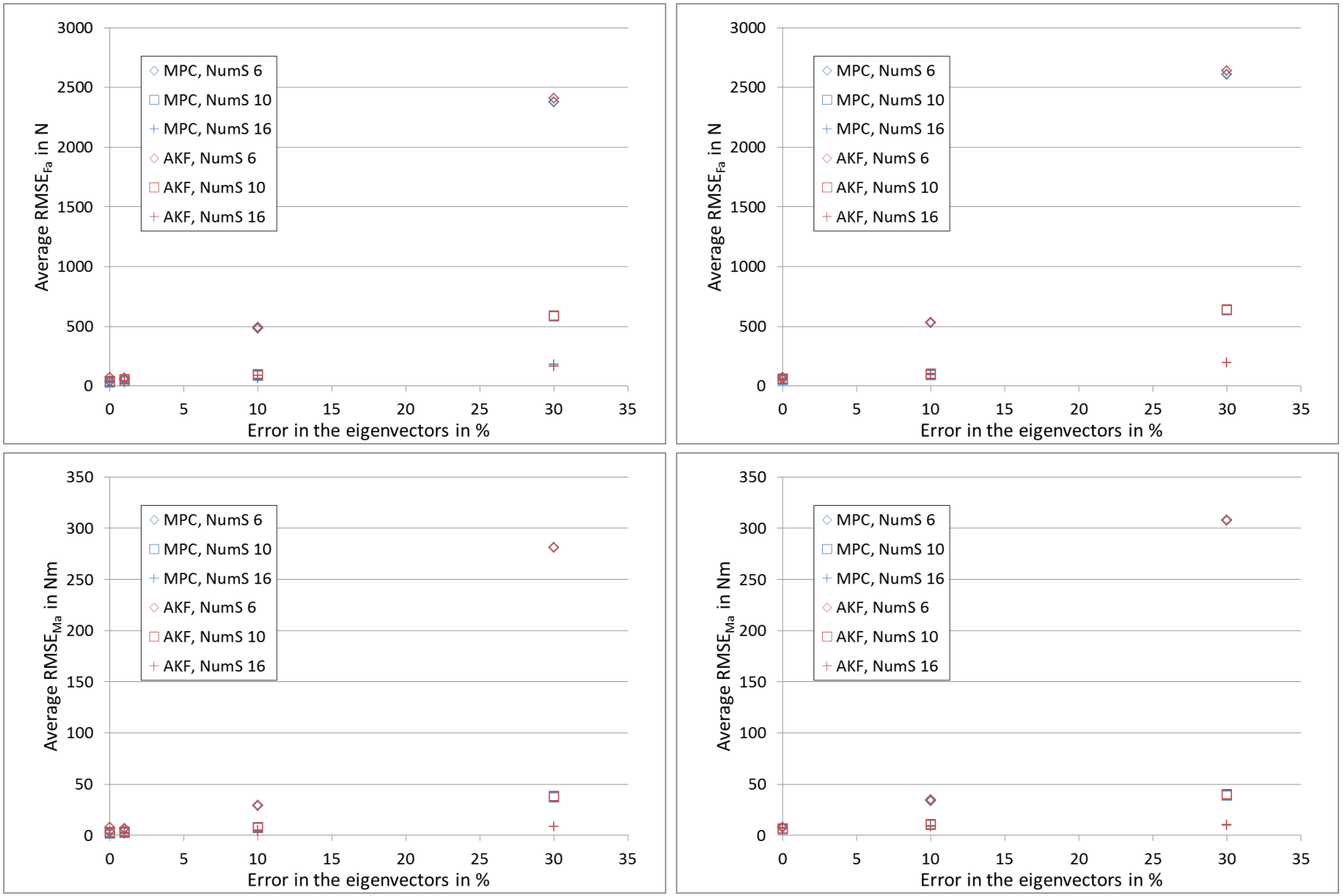

Figure 5.20 Average RMSE for the force reconstruction of the long-term excitation test cases for the models with an error in the eigenfrequencies of 0% (left) and 5% (right). The average RMSE for the forces ($RMSE_{Fa}$) and moments ($RMSE_{Ma}$) is shown for the force reconstruction by the MPC and AKF algorithm for the models with 6 (NumS 6), 10 (NumS 10) and 16 (NumS 16) sensors.

6 Experimental setup and evaluation of experimental results

For the experimental validation of the force reconstruction methods, an experimental setup and two corresponding mock-ups have been built. Based on the discussion in chapter 4, a design of the experimental setup has been selected able to apply punctual forces on the mock-ups. The realization of the experimental setup and the related components are explained in section 6.1. The detailed design and fabrication of the reduced-sized mock-up and the simple pipe mock-up are described in section 6.2.

In contrast to the force reconstruction with simulated strain data in chapter 0, the model used with the force reconstruction methods and experimentally obtained strain data is determined by an experimental modal analysis. The procedure and results of modal analysis for the simple pipe mock-up are given in section 6.3.

Finally, the evaluation of the force reconstruction with the AKF and MPC method based on the defined test cases is presented in section 6.4. A way to detect excitation events based on recorded strain data is shown in section 6.4.1 and the results of the test cases are discussed in section 6.4.2. The chapter is concluded with a new definition of an accuracy of force reconstruction systems in section 6.4.3.

6.1 Design and components of the experimental setup

For the experimental setup, a suitable actuator has to be selected able to apply punctual forces on the mock-up. Therefore, it has to be easy to control, powerful, lightweight and cost-effective. The actuator in combination with the controller has to be able to reproduce the different scenarios defined in section 5.1 with minimum rise and fall times of 2 ms and maximum forces in the order of several hundred Newton. The moving part of the actuator has to be lightweight as it is in contact with the mock-up and therefore represents an additional mass to the system.

Linear solenoids are able to fulfill these requirements, especially with regard to cost-effectiveness, and therefore have been selected as actuator type. In order to apply the defined test cases, two solenoids, each equipped with a force sensor, are needed. The two solenoids are connected in parallel to a digital servo power amplifier. The power amplifier is controlled by a modular data acquisition system, which is also used to record the measurements of the sensors.

Electrical strain gauges are used as replacement for optical strain gauges to measure the strain on the structure, as the mock-up is not tested in an ITER-like environment and electrical strain gauges have a comparable accuracy. In addition, an acceleration sensor is attached to the mock-up for the modal analysis. A representation of the experimental setup is illustrated in Figure 6.1. The mock-up and the frame, which represents the supporting structure for the solenoids, are mounted on a steel plate with notches. The frame is made of profiles from the Bosch aluminum profile system. A CAD model and a picture of the complete setup can be seen in Figure 6.2 and Figure 6.3. In the following, each component is described separately.

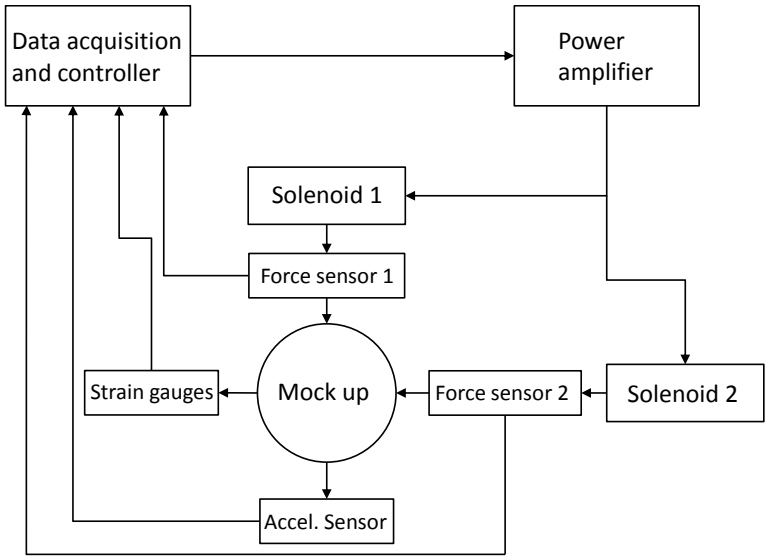

Figure 6.1: Experimental setup and components (schematic).

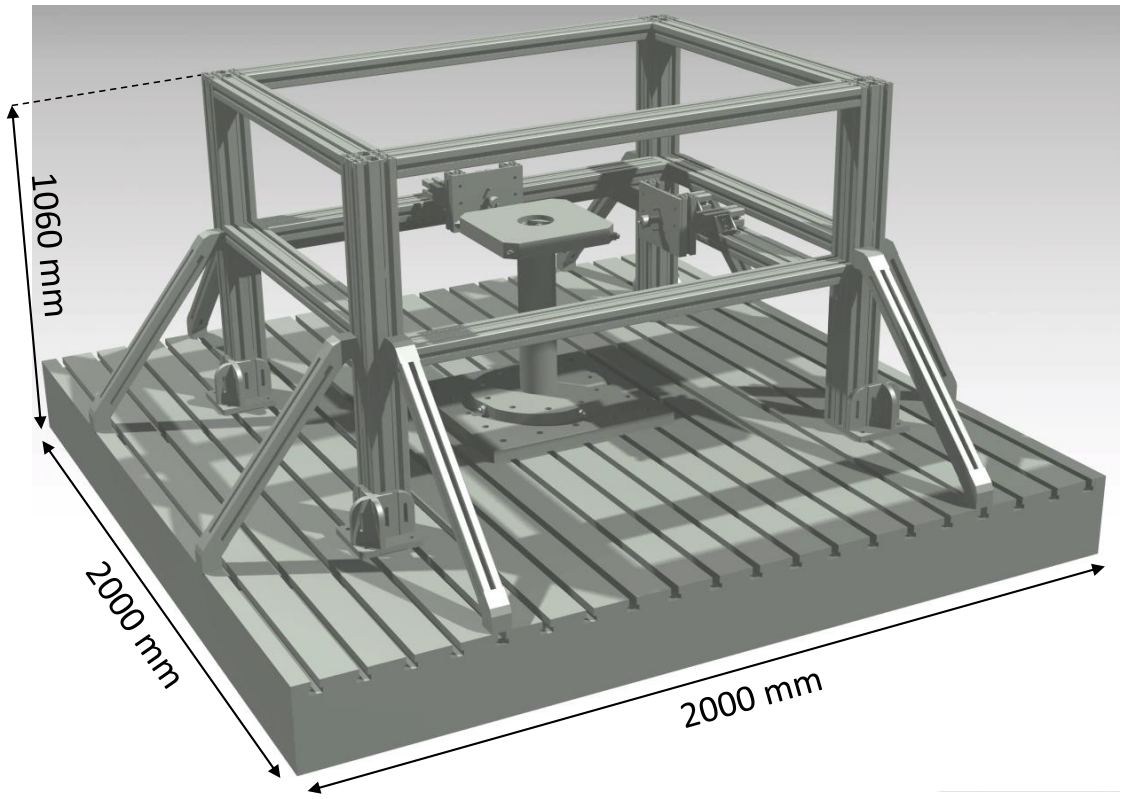

Figure 6.2: Experimental setup (CAD model) mounted on a frame.

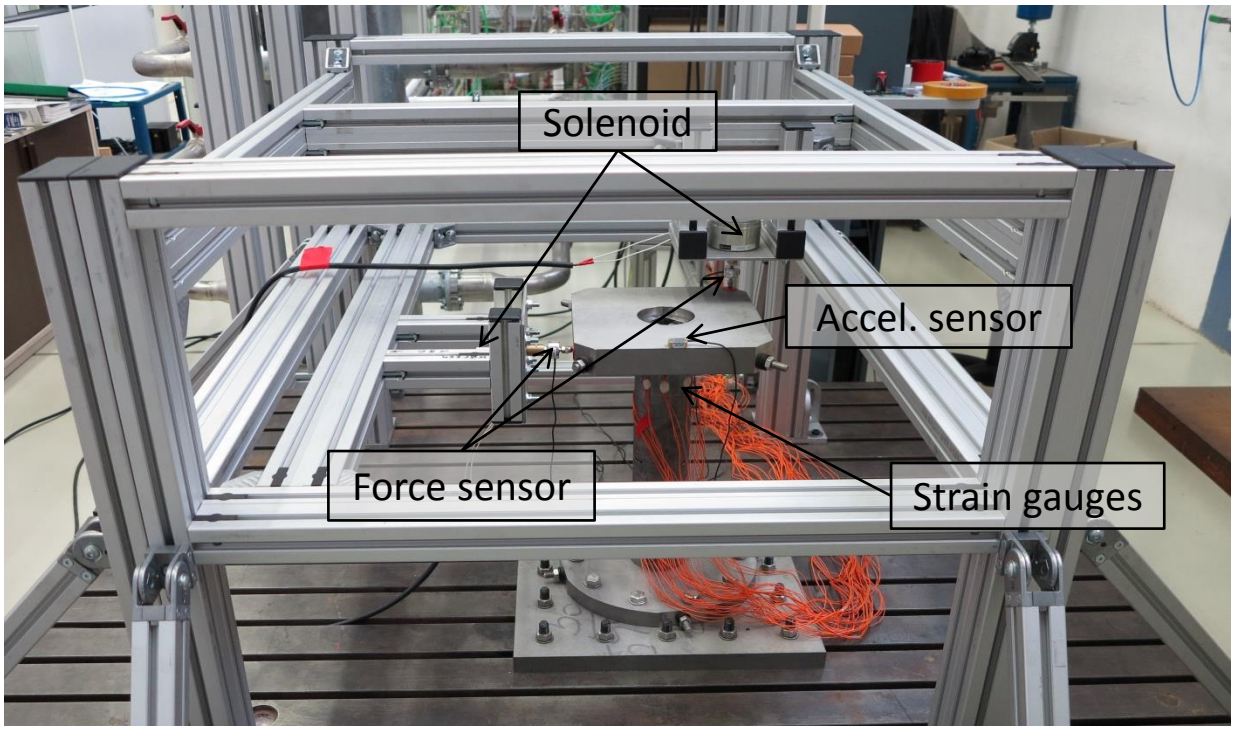

Figure 6.3: Full experimental setup with two solenoids.

Linear solenoid

Two Push Pull Solenoids 870F from Geeplus Europe Ltd. are used for the force application. They are able to achieve a maximum force of 2 kN and a maximum stroke of 10 mm. The maximum power consumption is 410 W. One solenoid with force sensor is shown in Figure 6.4.

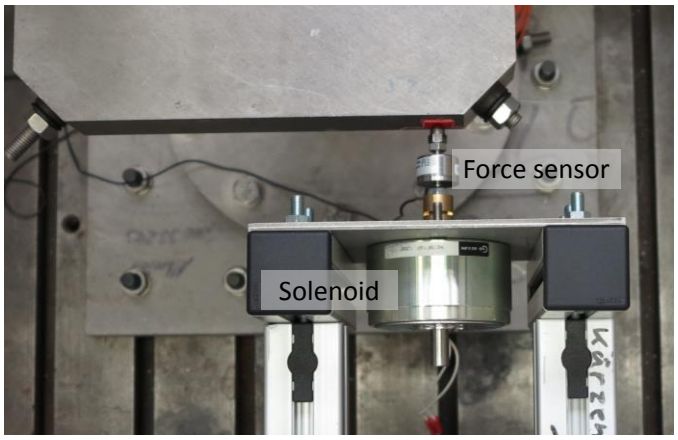

Figure 6.4: Linear solenoid and force sensor in the used experimental configuration.

Force sensor

One force sensor KM26z from ME-Meßsysteme GmbH is attached to each solenoid by an adapter. The tip is formed by a cap nut. The force sensor is designed for a nominal force of 2 kN with accuracy class 1. The eigenfrequency is higher than 5 kHz.

Digital servo power amplifier

The digital servo power amplifier DPC 460 from UNITEK Industrie Elektronik GmbH, shown in Figure 6.5, is used to power the solenoids. Depending on the test case, either one solenoid is connected to the power amplifier or both solenoids are connected in parallel. The power amplifier has a maximum output power of 35 kW, a maximum output voltage of 400 V and a maximum output current of 120 A. The set point of the current controller of the power amplifier is controlled by an analog 0-10 V input connected to the data acquisition system. The high possible output power of the power amplifier in comparison with the power of the solenoids is necessary, as the power amplifier has to counteract the high inductance of the solenoids.

Figure 6.5: Digital servo power amplifier DPC 460 used in the setup.

Acceleration sensor

The acceleration sensor AS28 from ME-Meßsysteme GmbH is used for the experimental modal analysis. It is attached to the structure by a double-sided adhesive tape. The measurement range of the sensor is ±20 g with accuracy class 0.5. The eigenfrequency is higher than 1500 Hz.

Strain gauges

The mock-up is equipped with 16 electrical strain gauges from the series Y from Hottinger Baldwin Messtechnik GmbH (HBM). The size of the measuring grid carrier is 9.2 mm×5.9 mm and the measuring grid itself has the dimensions 1.5 mm×2.3 mm. The exact arrangement of the sensors is given in the appendix D. The Z70 superglue, a cyanoacrylate adhesive, from HBM is

used to attach the strain gauges to the structure. A strain relief point consisting of the two components superglue X60 from HBM is placed on the wires of each strain gauge.

Modular data acquisition system

The modular data acquisition system CompactDAQ from National Instruments Corporation Ltd. is used to record the measurements coming from the strain gauges, the force sensors and the acceleration sensor. In addition, the system generates the set values for the power amplifier. The different inputs and outputs are provided by a number of modules that are inserted in the chassis. Two 8-channel 24-bit quarter-bridge analog input modules NI 9236 provide in total 16 channels for electrical strain gauges in quarter bridge configuration. The force sensors and the acceleration sensor are connected to a 4-channel 24-bit half/full-bridge analog input module NI 9237. A 4-channel 16-bit analog ±10 V voltage output module NI 9263 is used to control the power amplifier. The maximum common sample rate of the modules is 10 kHz. Figure 6.6 shows the chassis with modules.

Figure 6.6: Modular data acquisition system CompactDAQ

A program for the CompactDAQ system has been developed in the visual programming language LabVIEW that generates the set values for the power amplifier and simultaneously records the measurements from the sensors. The force history can be specified in terms of values of electrical current with an arbitrary number of support points within the total number of samples. The program determines the intermediate values by linear interpolation.

6.2 Design and fabrication of the mock-ups

The experimental setup has been designed with the aim to test two different mock-ups, the reduced-sized mock-up and the simple pipe mock-up. As discussed in chapter 4, the reduced-sized mock-up represents the TBM with a box structure and an internal stiffening grid. Therefore, it also allows the validation of electro-magnetic codes in a suitable experimental setup. With the simple pipe mock-up, higher strains levels at the same loading conditions can be achieved. The detailed design and fabrication of the two mock-ups is described in section 6.2.1 and 6.2.2.

6.2.1 Reduced-sized mock-up

Figure 6.7 shows a CAD model with dimensions and an exploded view of the reduced-sized mock-up. The goal of the design is to represent the dimensions of the real TBM with a reduction factor of 2. However, two dimensions deviate from this rule. The length of the box had to be further reduced to be weldable with the available electron beam welding machine. In addition, the thickness of the cylinder had to be reduced to generate a higher strain level, as illustrated in Figure 6.8. In contrast to the real TBM, the mock-up is empty. For that reason, the missing mass is compensated by significantly increasing the thickness of the plates forming the box. The parts, which are all made of stainless steel 1.4301 by milling, are shown before the assembly by electron beam welding in Figure 6.9.

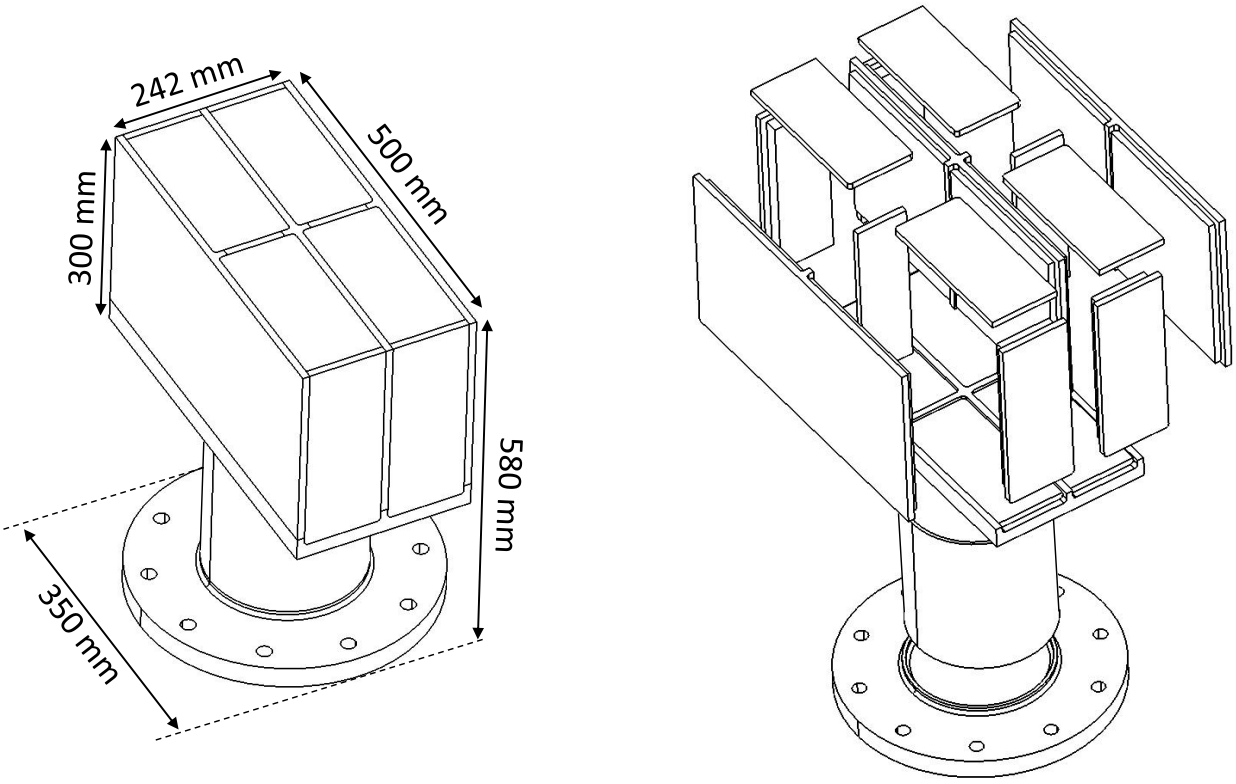

Figure 6.7: Reduced-sized mock-up: Dimensions (left) and exploded view (right).

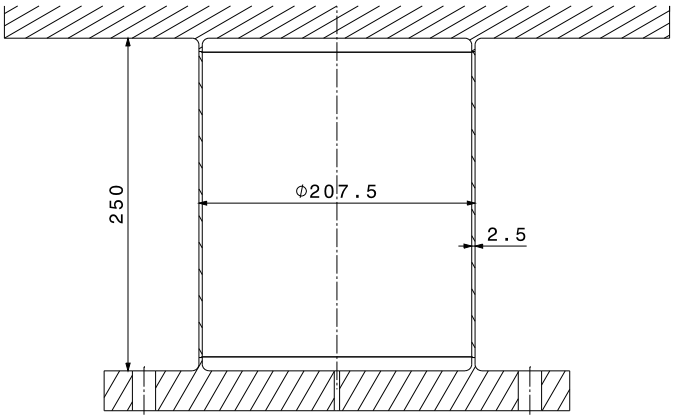

Figure 6.8: Reduced-sized mock-up: Dimensions of cylinder in mm.

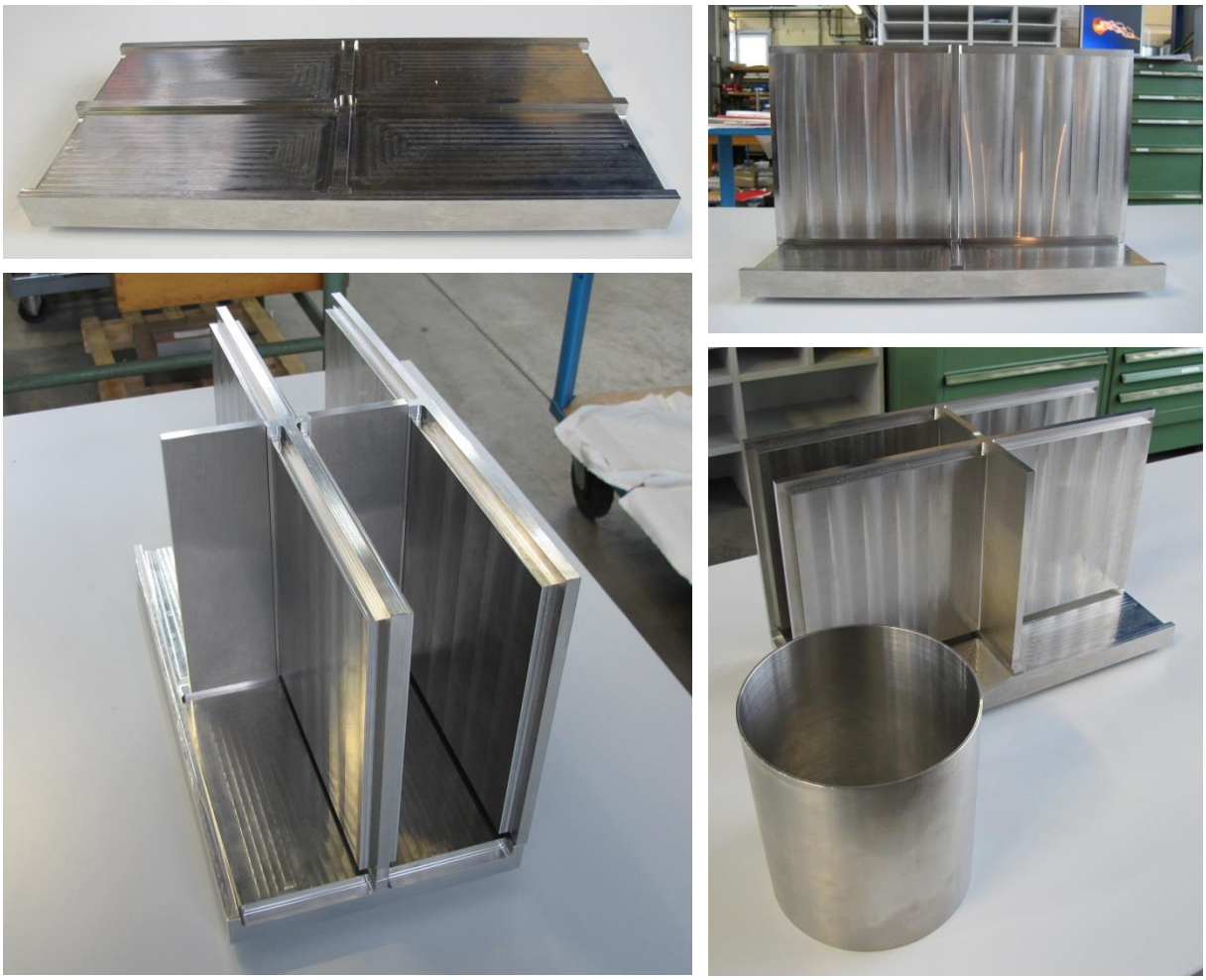

Figure 6.9: Reduced-sized mock-up: Manufactured parts before assembly by electron beam welding.

6.2.2 Simple pipe mock-up

Figure 6.10 shows the CAD model with dimensions and a sectional view of the simple pipe mock-up. The height of the mock-up corresponds approximately to the height of the center of the reduced-sized mock-up. The diameter and the thickness of the pipe are significantly reduced to achieve a higher strain level. Due to two 90°-slots at mid-length of the pipe, the stiffness characteristic of the pipe is changed in order to avoid repeated eigenvalues and therefore better represent the modal characteristics of the TBM. The pipe is clamped to the top plate and base plate by four blocks each. The entire mock-up is fixed to the adapter plate by ten screws. A picture of the adapter plate and base plate can be seen in Figure 6.11 and a side view and top view of the mock-up is shown in Figure 6.12. The pipe is a seamless cold drawn pipe for precision applications according to EN 10305-1 and made of steel E235+C. Stainless steel 1.4301 has been used for all other parts.

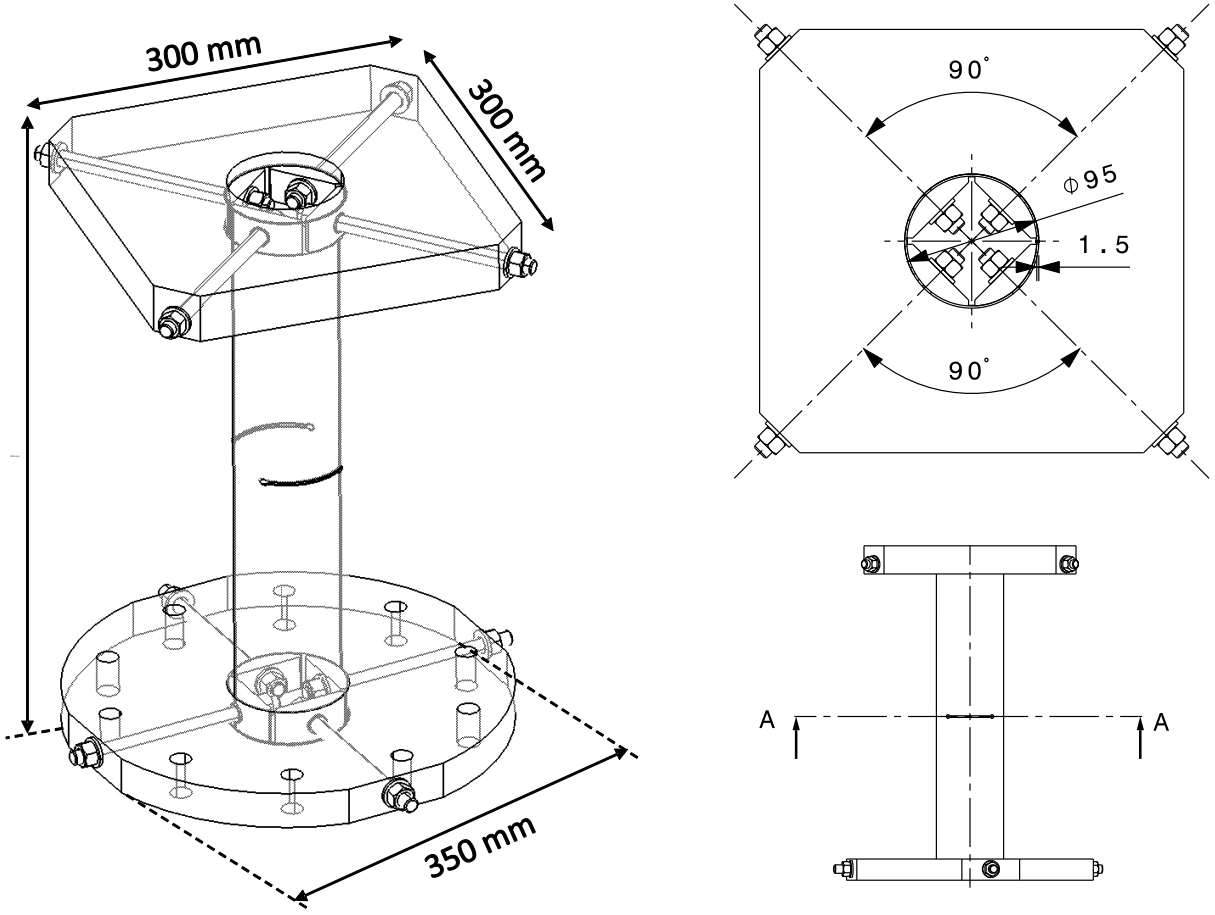

Figure 6.10: Simple pipe mock-up: Dimensions (left) and sectional view (right).

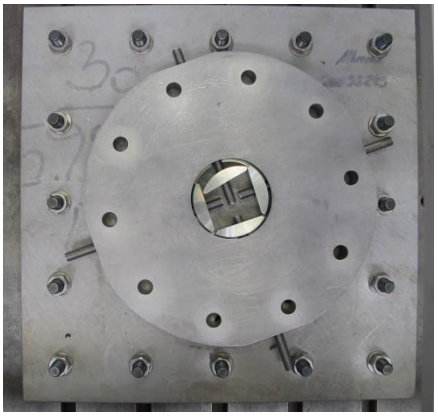

Figure 6.11: Simple pipe mock-up: Adapter plate and base plate

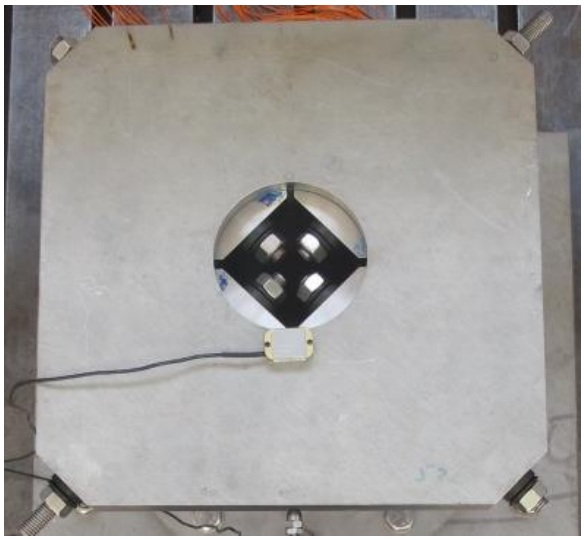

Figure 6.12: Simple pipe mock-up: Side view (left) and top view (right).

6.3 Modal analysis

The model of the simple pipe mock-up implemented in the force reconstruction algorithms for the application with experimentally obtained strain data is determined by an experimental modal analysis. In order to excite the mock-up, an impact excitation with a duration of about 2 ms is used. The response of the structure is measured by an acceleration sensor and the strain

gauges. The excitation points and acceleration measurement points on the top plate are indicated by black filled circles in Figure 6.13. The excitation and measurement direction is always normal to the surface. The positions of the strain gauges are marked by small squares on the pipe in Figure 6.13 as well. The exact positions and orientations of the excitation and measurement points and the strain gauges are given in appendix D.

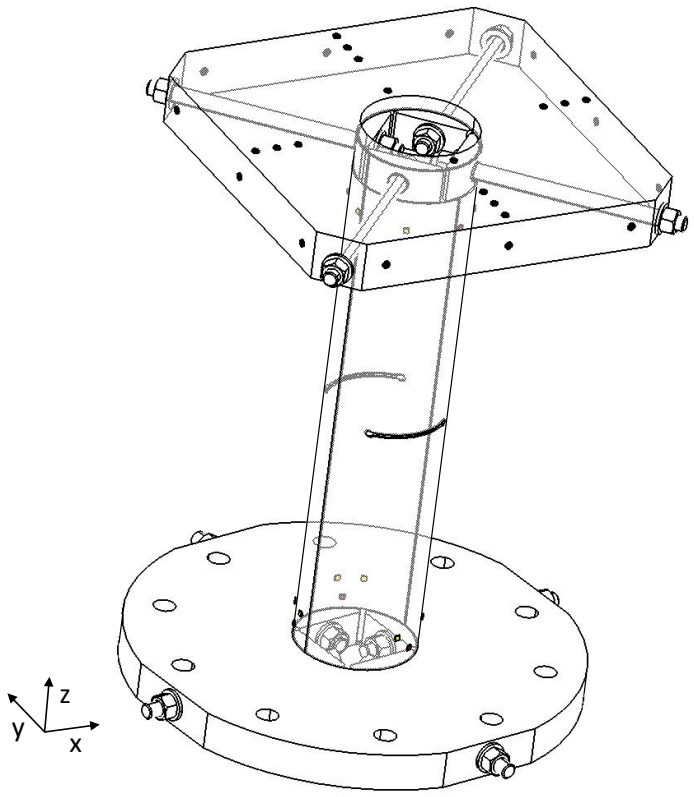

Figure 6.13: Experimental modal analysis: Excitation and measurement positions on top plate and sensor positions on pipe. The positions are listed in appendix D.

The algorithms for the calculation of the frequency response functions (FRF) and the modal parameter estimation are implemented in LabVIEW using the available function blocks for modal analysis. The FRFs are each estimated from five repeated input/output measurements. Two algorithms are used for the modal parameter estimation. A Least Square Complex Exponential fit (LSCE) is applied for the lightly damped modes and a Frequency Domain Polynomial fit (FDPI) for the more heavily damped modes.

The eigenfrequencies and damping ratios estimated by the experimental modal analysis and the eigenfrequencies of the FE model are given for comparison in Table 6.1. The mode shapes of the FE model are illustrated in Figure 6.15. The mode shapes of the real mock-up, which are represented by the degrees of freedom on the top plate as specified in Figure 6.13, are compared to the mode shapes of the FE model according to the Modal Assurance Criterion (MAC), which provides a measure of consistency (degree of linearity) between estimates of different eigenvectors [88]. The results in Figure 6.14 show a high consistency between the modal eigenvectors of the FE model and the estimated modal eigenvectors of the real mock-up with MAC values higher than 0.9 for the considered modes, where unity represents a consistent

correspondence. The values of the deformation eigenvectors as well as the determination and the values of the strain eigenvectors can be found in appendix D.

Finally, as the damping ratios obtained by the experimental modal analyses are affected by window function applied to the measured data before the Fast Fourier Transformation (FFT), the identified model has been used to compare calculated strains and measured strains based on the same excitations to tune the damping ratios. Based on this comparison, the damping ratios of the 4th and 5th mode have been changed to 0.3 %.

Mode No.		FE model	EMA	
		f_i	f_i	ξ_i
1	1st bending	42 Hz	40 Hz	0.2 %
2	2nd bending	52 Hz	48 Hz	0.2 %
3	1st torsion	80 Hz	82 Hz	0.5 %
4	3rd bending	279 Hz	262 Hz	0.6 %
5	4th bending	298 Hz	267 Hz	0.6 %
6	1st axial	360 Hz	336 Hz	2 %

Table 6.1: Comparison of eigenfrequencies f_i of the FE model and eigenfrequencies f_i and damping ratios ξ_i from the Experimental Modal Analysis (EMA).

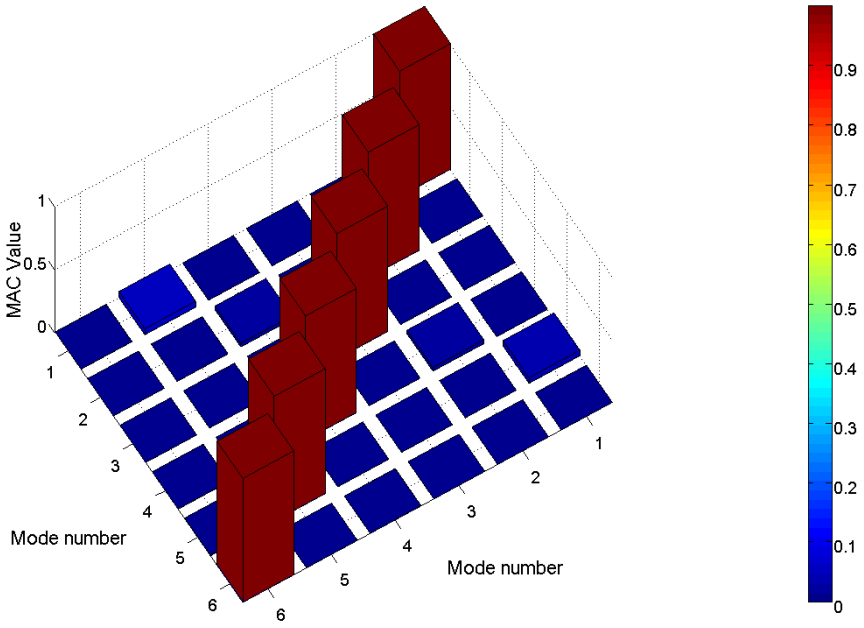

Figure 6.14: Modal analysis: Results of Modal Assurance Criterion (MAC) for the displacement eigenvectors of the FE model and the real structure.

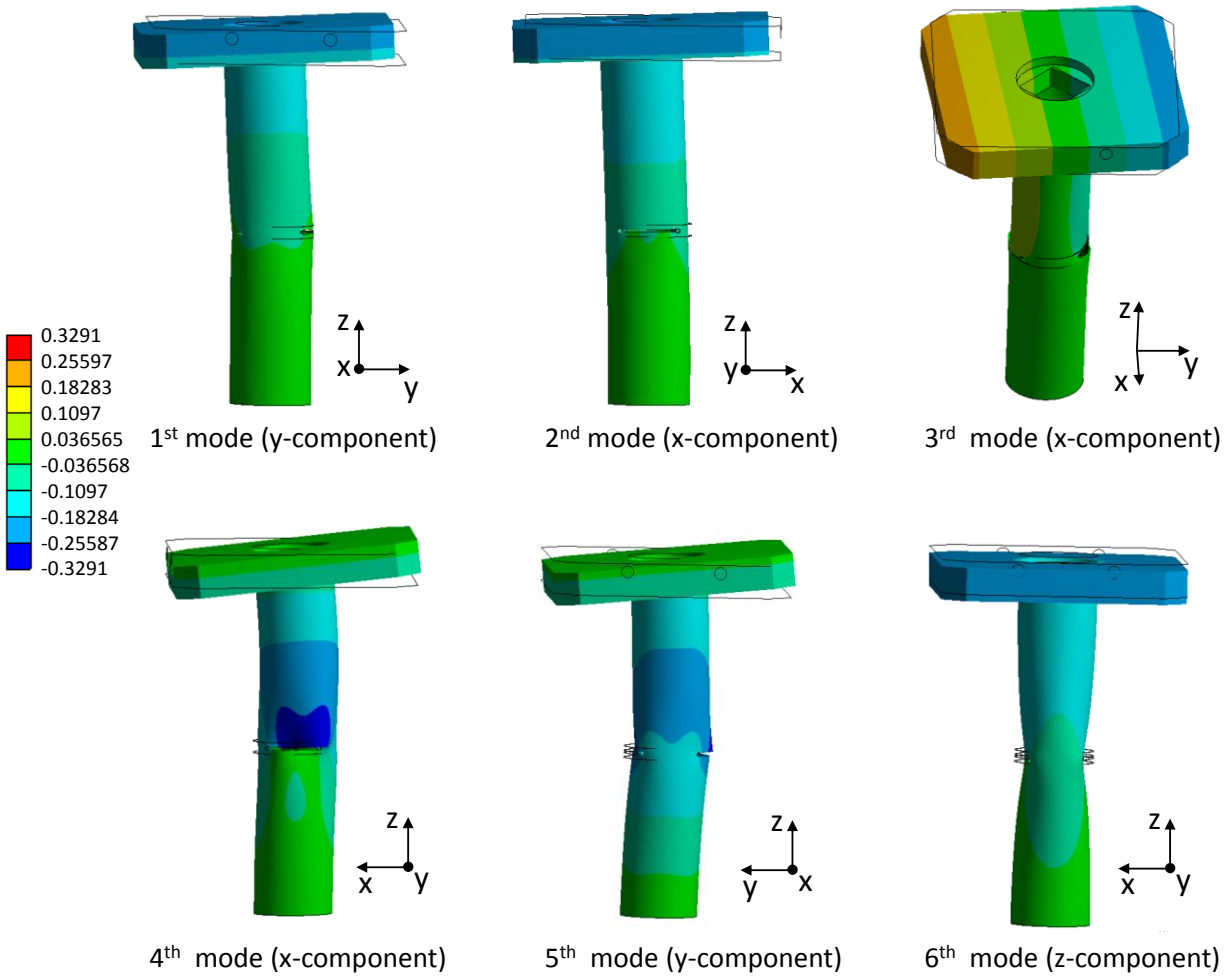

Figure 6.15: Results of modal analysis in ANSYS: mode shapes and deformation components of the mass-normalized eigenvector.

6.4 Evaluation of the force reconstruction algorithms

The experimental setup is used to apply the test cases defined in Section 5.1 to the simple pipe mock-up. In a real application, the exact starting point of an excitation is unknown. Therefore, a method that facilitates the detection of an excitation force is presented in Section 6.4.1. The results of the reconstruction of the different test cases for both algorithms are given in Section 6.4.2. In addition to the evaluation of the performance of the force reconstruction methods based on the RSME, an accuracy definition in analogy to a standard force transducer is developed in Section 6.4.3.

6.4.1 Method to detect excitation events

If force reconstruction is applied to a real system, the sensor signals are continuously recorded during operation. However, the occurrence of each excitation event needs to be

separately detected as the regularization parameters have to be individually adapted for each excitation event and the L-curve method used for this purpose is related to a certain time span.

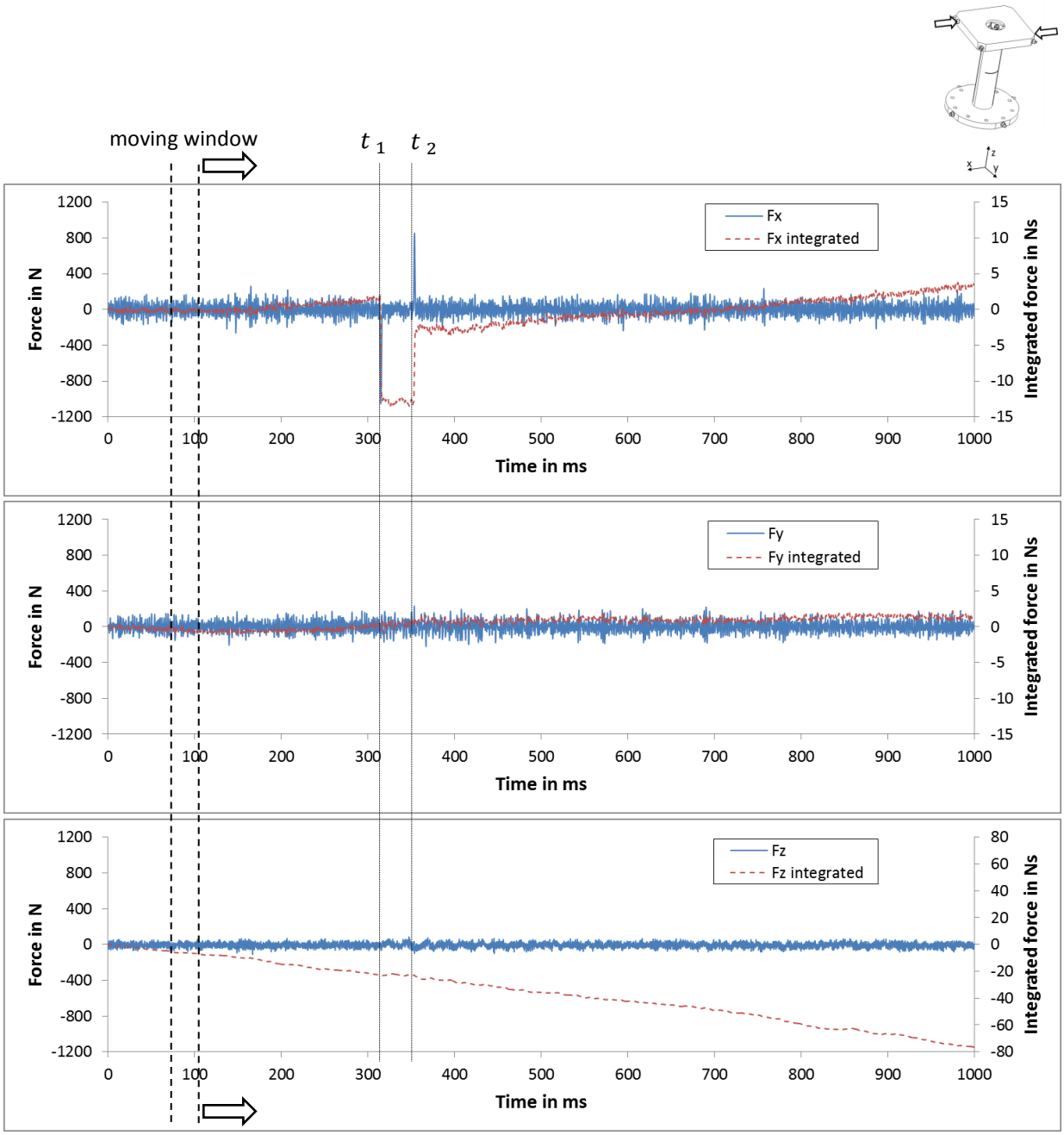

Figure 6.16: Method to detect start of excitation: The reconstructed force components for test case 5 (hammer impact) are plotted in blue for a time span of 1 second. The integrated force components for each time step corresponds to the red line. The difference of the integrated force is determined within a moving window for every time step.

Nevertheless, it strongly depends on the characteristics of the excitation events, if a method is suitable to detect them. The method presented here is therefore only suitable for high force pulses with short durations in relation to the overall recording time, as it applies to the electromagnetic events in ITER. The main idea of this method is to detect a short-time impulse

transfer to the system. For this purpose, the forces components are estimated for the entire recording time with a small amount of regularization. The reconstructed forces are then integrated from the start to each time point as shown for the force components and moment components in Figure 6.16 and Figure 6.17.

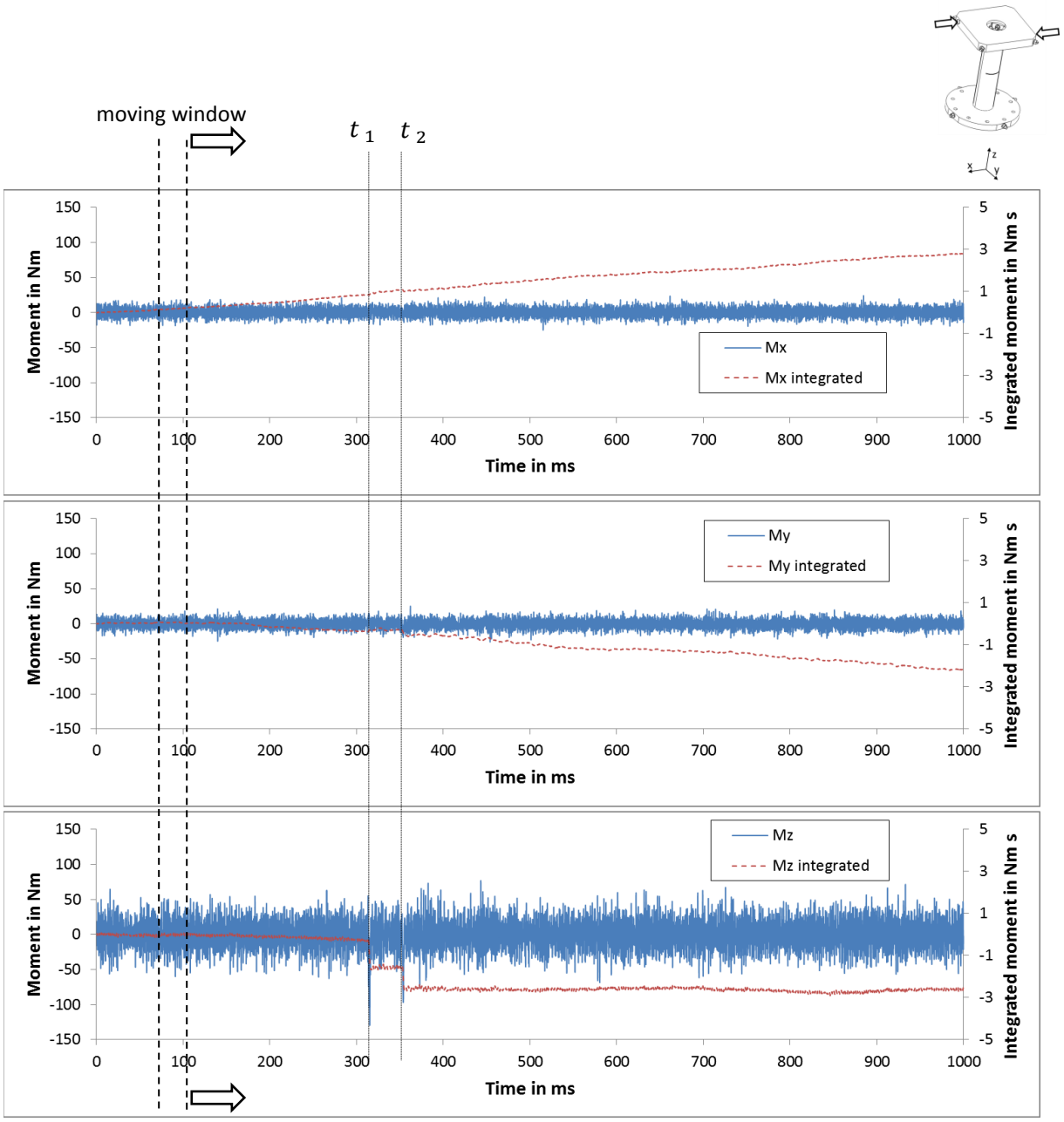

Figure 6.17: Method to detect start of excitation: The reconstructed moment components for test case 5 (hammer impact) are plotted in blue for a time span of 1 second. The integrated force components for each time step corresponds to the red line. The difference of the integrated moment is determined within a moving window for every time step.

From these graphs, the excitation events at t_1 and t_2 for the force component in x-direction and the moment component around the z-axis are already noticeable due to the high change in the integrated force or moment component. Furthermore, a slow drift of some of the integrated force

components is visible due to a small offset in the reconstructed forces. In order to clarify the fast change, a moving window over the integrated forces or moments can be defined, in which the difference between the end point and start point is calculated with the meaning of a change rate. The result of this procedure with absolute values of the integrated force or moment components can be seen in Figure 6.18.

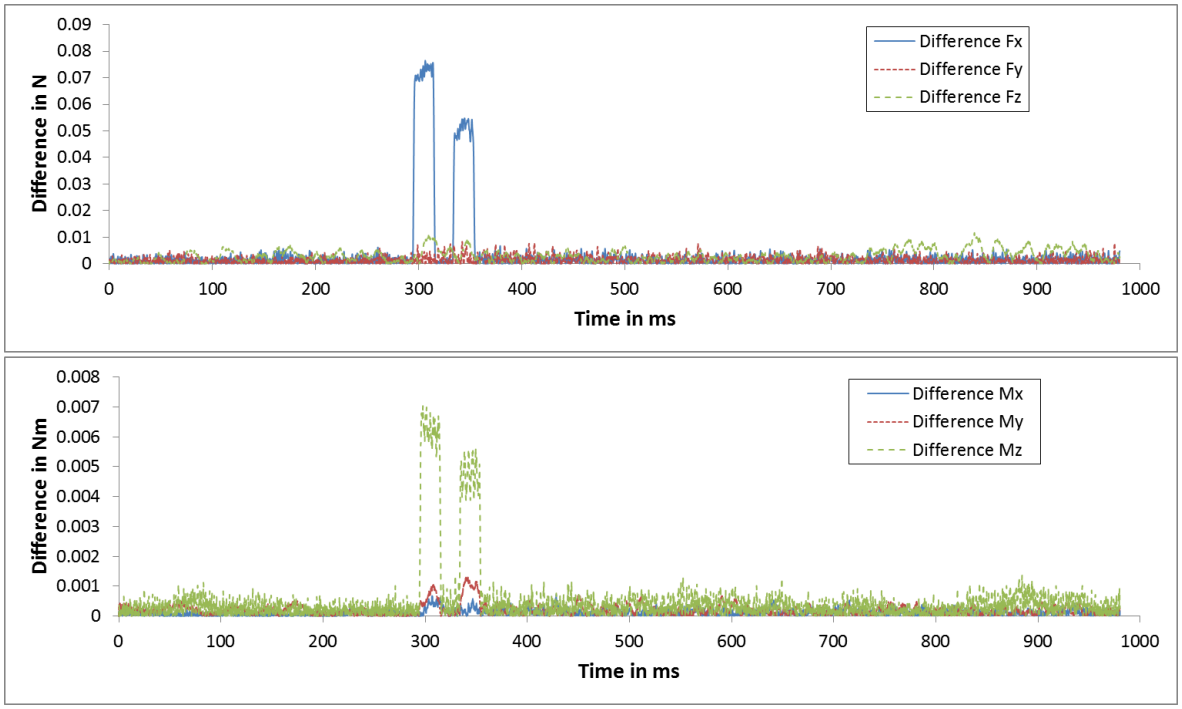

Figure 6.18: Method to detect start of excitation: The difference in the 20 ms moving time window of the integrated force or moments component is represented for each component at every time step. The differences are calculated based on the absolute values.

6.4.2 Results of the force reconstruction for the test cases

The regularization parameters of the force reconstruction algorithms have been determined in the same way as for the test cases with simulated strain data. The constant parameters are specified as given in Section 5.4.1. The individual regularization parameters for each test case have been selected with the L-curve method. All 16 strain sensors are used to estimate the excitation forces. The strain data has been recorded with a sampling frequency of 10 kHz. In order to remove noise at frequencies higher than the considered eigenfrequencies, the strain data has been filtered with a Savitzky-Golay filter with a polynomial order of 2 and 12 side points acting as a lowpass filter with a cutoff frequency of about 400 Hz.

The results are shown for all test cases with focus on the long-term excitations. The reconstructed forces are graphically presented for the MPC and AKF algorithm and the RSME is given for the long-term excitations to compare the two algorithms.

Figure 6.19 shows the results of test case 1 for scenario 1. Both algorithms estimate well the excitation forces with an $RSME_F$ of 22 N for a maximum input force of 250 N. This is also

reflected in a very similar RMSE in Table 6.2. However, the start of the force in y-direction is reconstructed slightly before its actual occurrence due the necessary compensation of the time delay in the AKF.

In test case 2, the excitation force additionally causes a moment around the z-axis. The results are presented for both algorithms in Figure 6.20. The force and the related moment are well reconstructed with a $RSME_F$ of 16 N and 18 N for a maximum force of 260 N and a $RSME_M$ of 1.3 Nm and 2.1 N at a maximum moment of 26 Nm, also listed in Table 6.3. The higher error of the estimated moments by the AKF algorithm is related to the time delay in the reconstruction of the time history of the moment M_z.

The results of the force reconstruction for test case 3 are shown in Figure 6.21. Apart from a good estimation of the excitation force and the related moment with a $RSME_F$ of 21 N and 28 N at a maximum force of 680 N and a $RSME_M$ of 2.3 Nm and 5.5 Nm at a maximum moment of 39 Nm, a higher erroneous estimate of the moment M_z by the AKF is noticeable. This behavior is related to the selection of the regularization parameter. On one hand, the smaller amount of regularization in the AKF algorithm for this test case leads to a more accurate reconstruction of the forces over time. This can be recognized in the estimated force F_z. On the other hand, this results in higher oscillations in the reconstructed forces. This results in a significantly higher RMSE for the AKF for the moment estimates in Table 6.4.

The excitation force in z-direction in test case 4 is applied at the edge of the top plate. The influence of the selection of the regularization parameter is again visible as described for test case 3. A higher deviation in the reconstruction of Moment M_x in Figure 6.22 is noticeable as well. This deviation is related to the dependency of the force reconstruction on the input location expressed by the matrix product $\boldsymbol{R}^T\boldsymbol{S}_p$ in equation (5.1). The modal matrix $\boldsymbol{R}$ again is dependent on the accuracy of the identified displacement eigenvectors $\boldsymbol{r}_i$. Table 6.5 summarizes the RMSE.

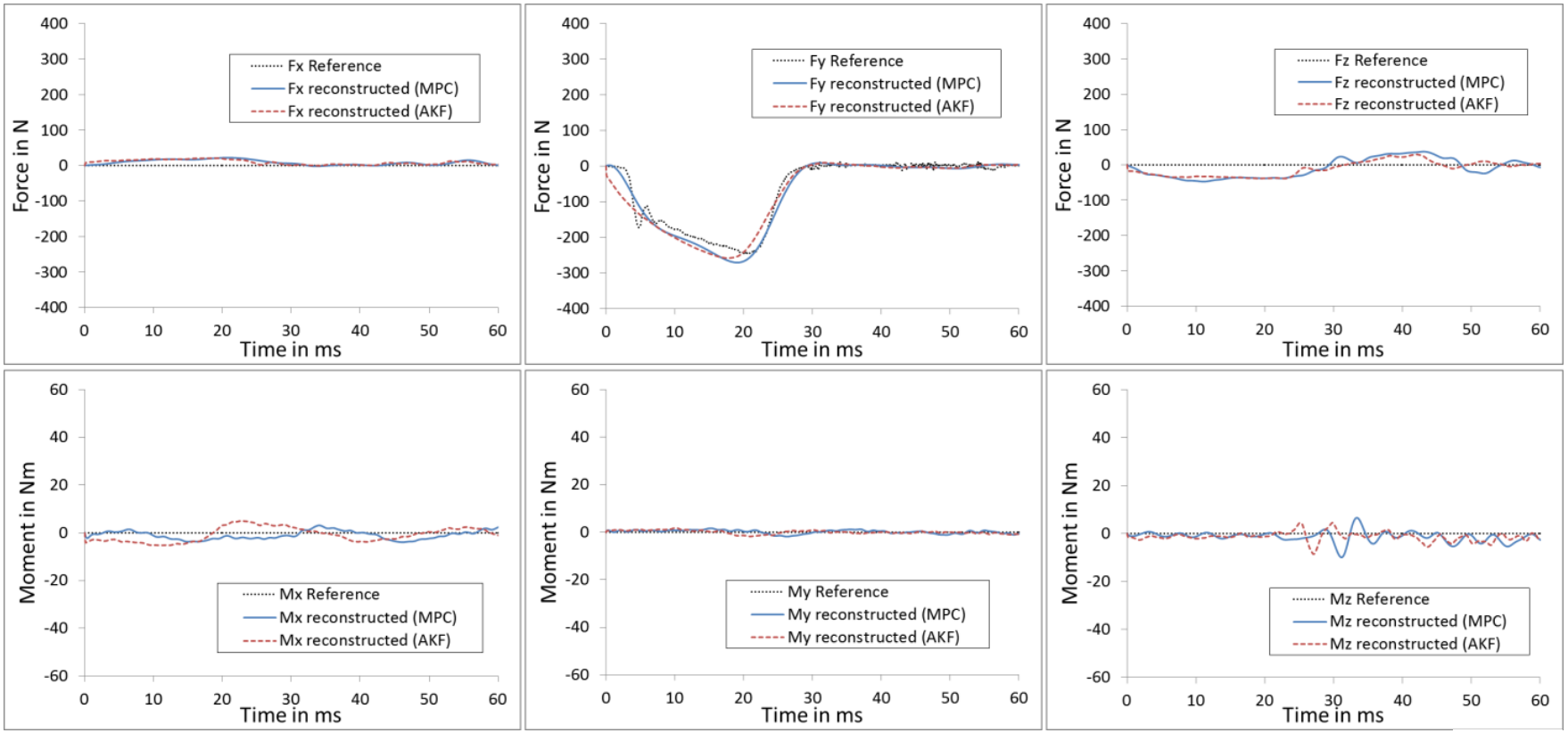

Figure 6.19: Test case 1 (scenario 1): Force reconstruction by the MPC (blue) and AKF (red) algorithm. The measured reference force is plotted with a dotted line.

	MPC	AKF
$RMSE_F$	22 N	22 N
$RMSE_M$	1.9 Nm	2.3 Nm

Table 6.2: RSME for test case 1 (scenario 1) for the MPC and AKF algorithm

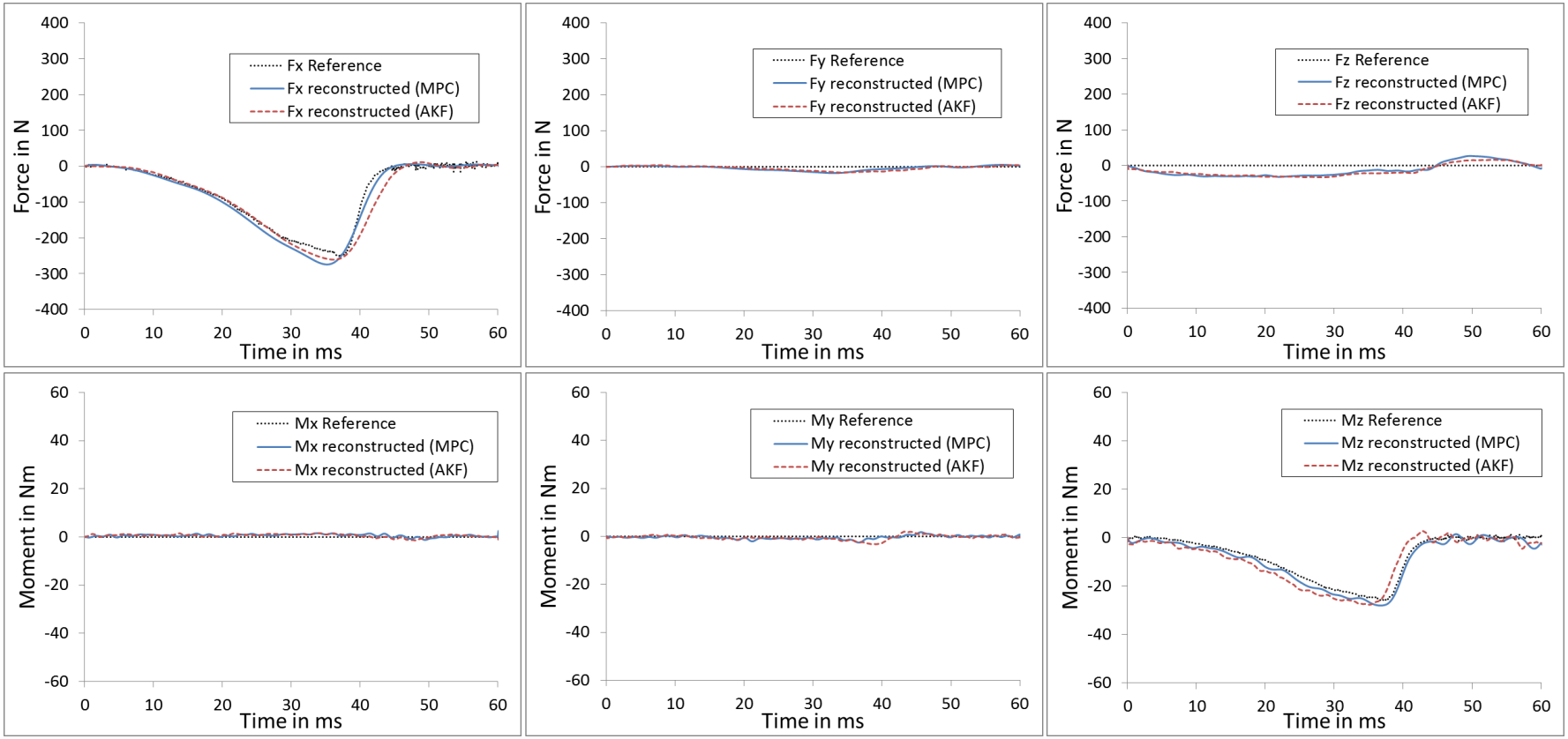

Figure 6.20: Test case 2 (scenario 2): Force reconstruction by the MPC (blue) and AKF (red) algorithm. The measured reference force is plotted with a dotted line.

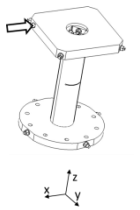

	MPC	AKF
$RMSE_F$	16 N	18 N
$RMSE_M$	1.3 Nm	2.1 Nm

Table 6.3: RSME for test case 2 (scenario 2) for the MPC and AKF algorithm

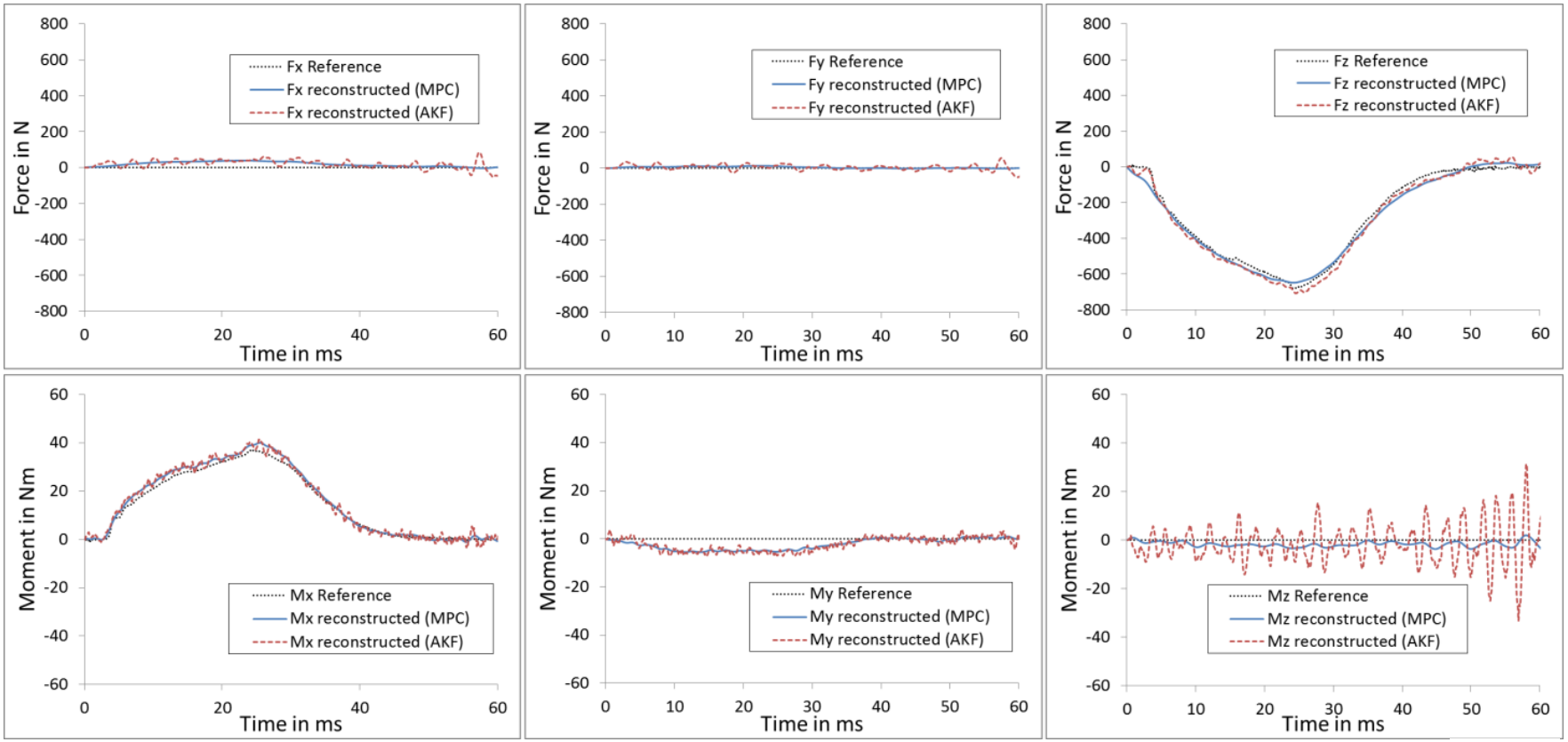

Figure 6.21: Test case 3 (scenario 3): Force reconstruction by the MPC (blue) and AKF (red) algorithm. The measured reference force is plotted with a dotted line.

	MPC	AKF
$RMSE_F$	21 N	28 N
$RMSE_M$	2.3 Nm	5.5 Nm

Table 6.4: RSME for test case 3 (scenario 3) for the MPC and AKF algorithm

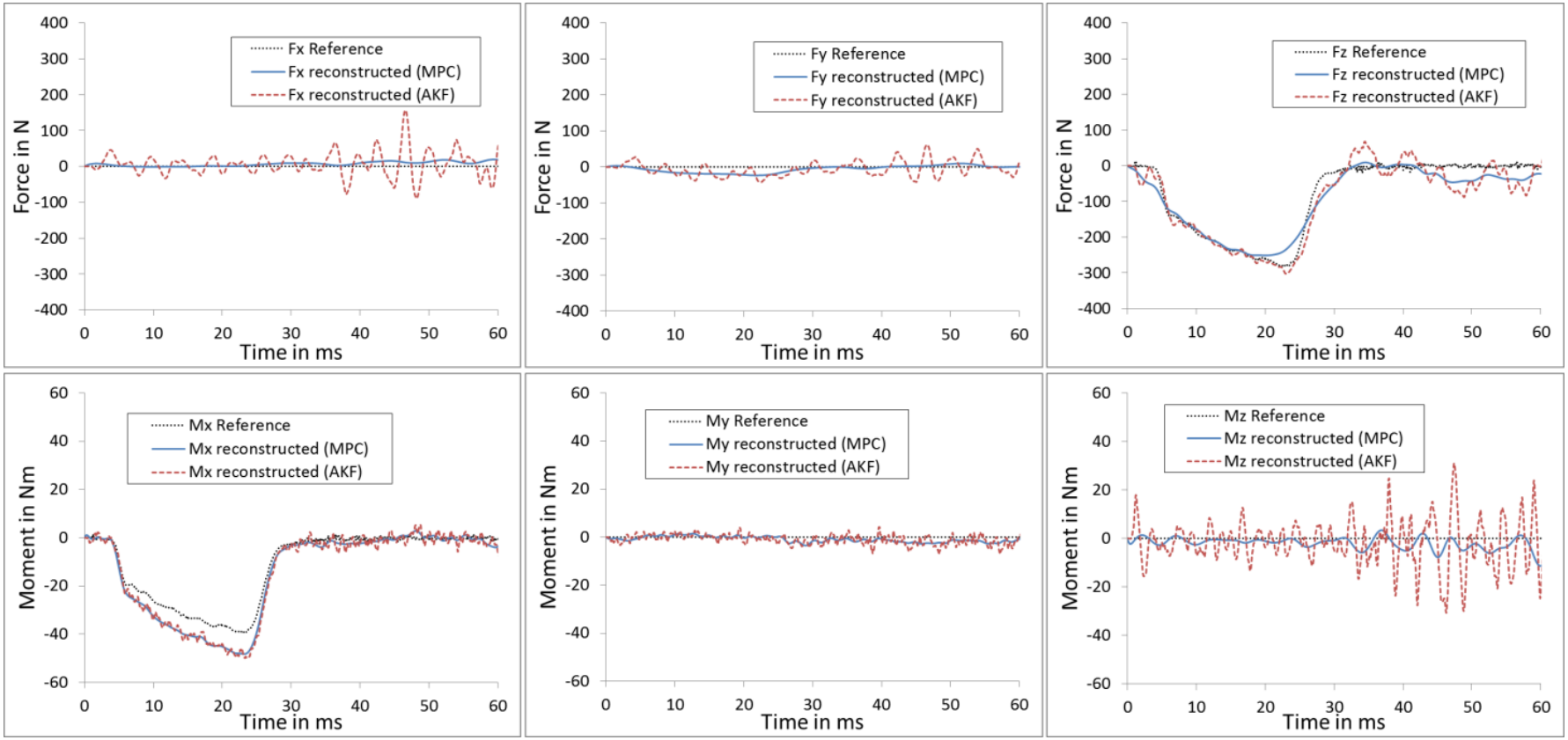

Figure 6.22: Test case 4 (scenario 1): Force reconstruction by the MPC (blue) and AKF (red) algorithm. The measured reference force is plotted with a dotted line.

	MPC	AKF
$RMSE_F$	18 N	30 N
$RMSE_M$	3.3 Nm	6.2 Nm

Table 6.5: RSME for test case 4 (scenario 1) for the MPC and AKF algorithm

In test case 5, the mock-up has been excited at two different points on the structure. The results are shown for an excitation with two hammers in Figure 6.23 and with two solenoids in Figure 6.24. The hammer impacts are applied with a time delay of about 40 ms, while the forces by the two solenoids are applied simultaneously.

The two hammer impacts are detected very accurately with a slightly higher accuracy in the reconstruction of the forces over time by the MPC. Due to the necessary lower regularization in order to allow the algorithms to follow the fast changing forces, the error in the estimates is higher.

The simultaneous excitation with the two solenoids only causes a moment around the z-axis, which is estimated with a high accuracy with a $RSME_M$ of 2.4 Nm and 2.2 Nm at a maximum moment of 44 Nm. The deviation in the estimate of the force F_z is due to the manual correction of an offset present in the strain data of all strain gauges during the time span of the excitation. This deviation can also be seen in the $RMSE_F$ in Table 6.6, where only the estimates are considered up to the end of the excitation as the exact point for the removal of the manual correction of the offset is difficult to determine. This fact also leads to higher deviations of the estimates after the end of the excitation.

In test case 6, the mock-up is excited from two directions causing two force components and one moment component. The hammer impacts and the small time delay are well identified as presented in Figure 6.25. The excitations of the two solenoids are also reconstructed with an acceptable accuracy and a $RSME_F$ of 49 N and 48 N at a maximum force of 260 N and a $RSME_M$ of 2.1 Nm and 2.2 Nm at a maximum moment of 25 Nm. Here again, the offset in the strain data due to excitation with the two solenoids has to be considered as described for test case 5. The results are shown in Figure 6.26. The RSME is calculated from the estimates up to the end of the excitation and given in Table 6.7.

The excitation pattern in test case 7 excites all considered modes of the structure. The hammer impacts in Figure 6.27 are well identified. Due to the necessary low regularization, erroneous estimates of the moment M_z are noticeable. Here, the influence of the errors in the identified eigenvectors again becomes more dominant.

In contrast to the short-term excitation, the error in the reconstructed moment M_z can be significantly reduced with a higher regularization for the long-term excitation, which represents the ITER relevant excitation. The force estimates are shown in Figure 6.28. Here again, as discussed for test case 5, the impact of the manual correction of the strain data necessary due to the excitation by the two solenoids is noticeable. The RSME is given in Table 6.8.

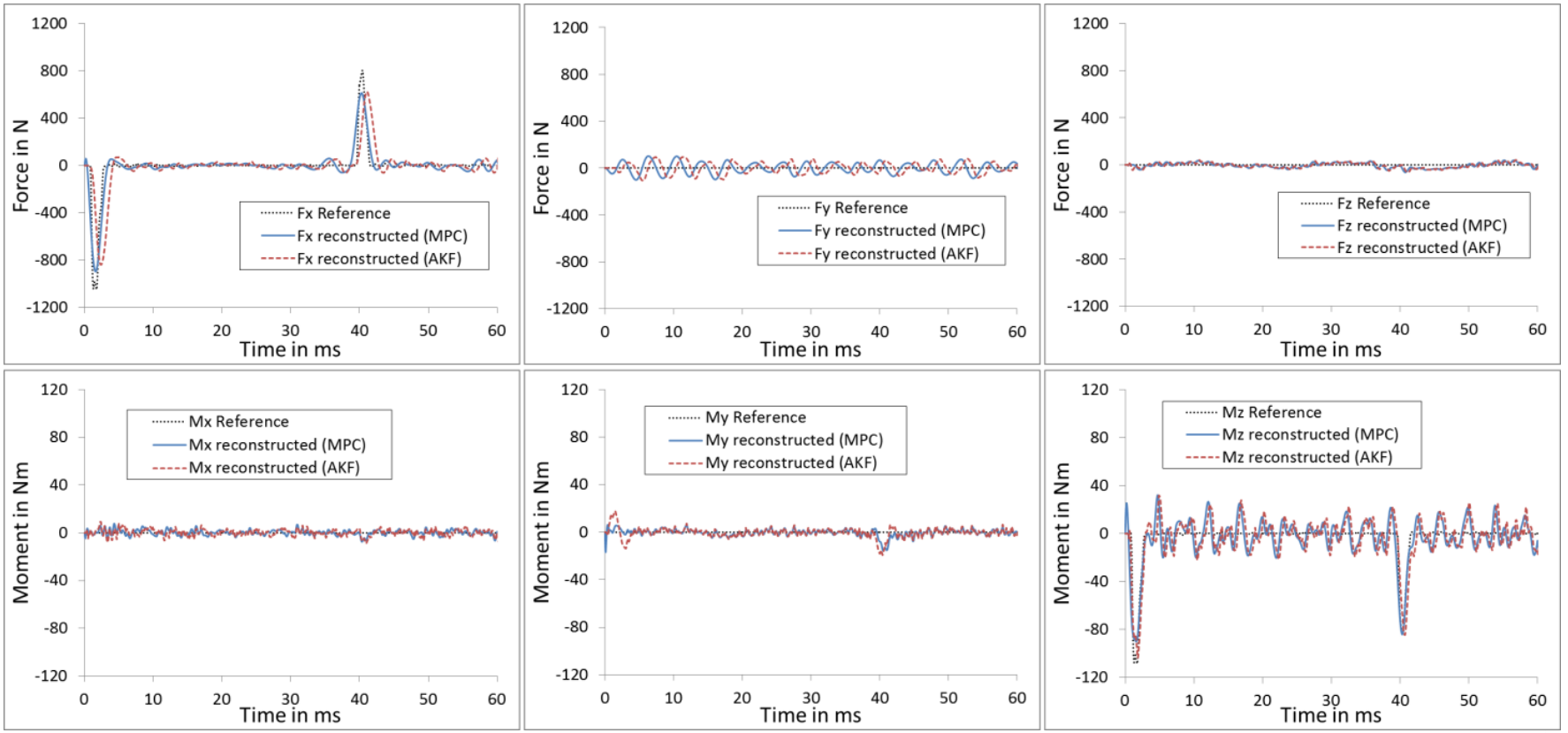

Figure 6.23: Test case 5 (hammer impact): Force reconstruction by the MPC (blue) and AKF (red) algorithm. The measured reference force is plotted with a dotted line.

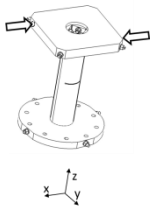

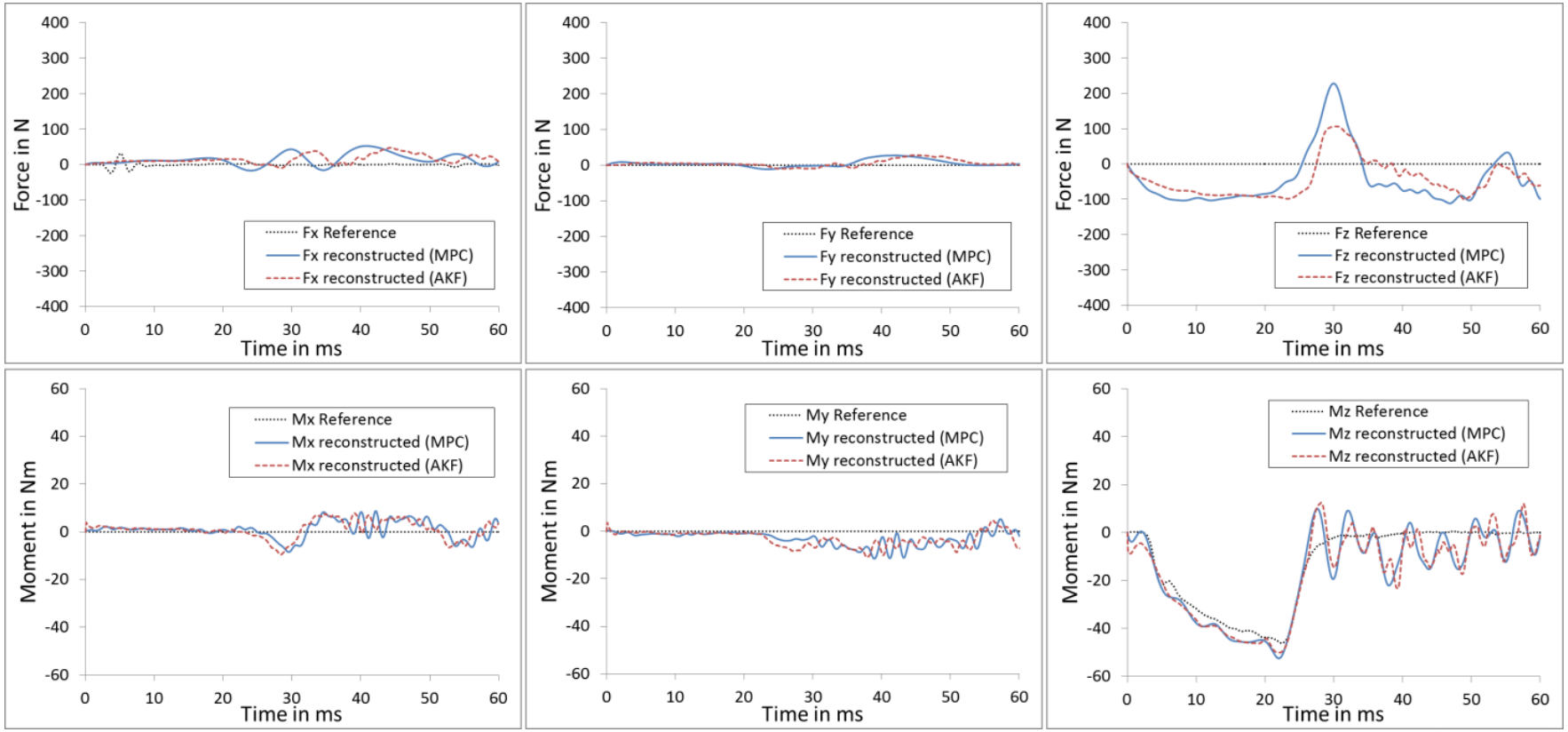

Figure 6.24: Test case 5 (scenario 1): Force reconstruction by the MPC (blue) and AKF (red) algorithm. The measured reference force is plotted with a dotted line.

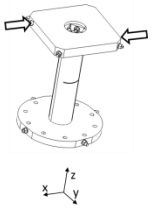

	MPC	AKF
$RMSE_F$	49 N	47 N
$RMSE_M$	2.4 Nm	2.2 Nm

Table 6.6: RSME for test case 5 (scenario 1) for the MPC and AKF algorithm

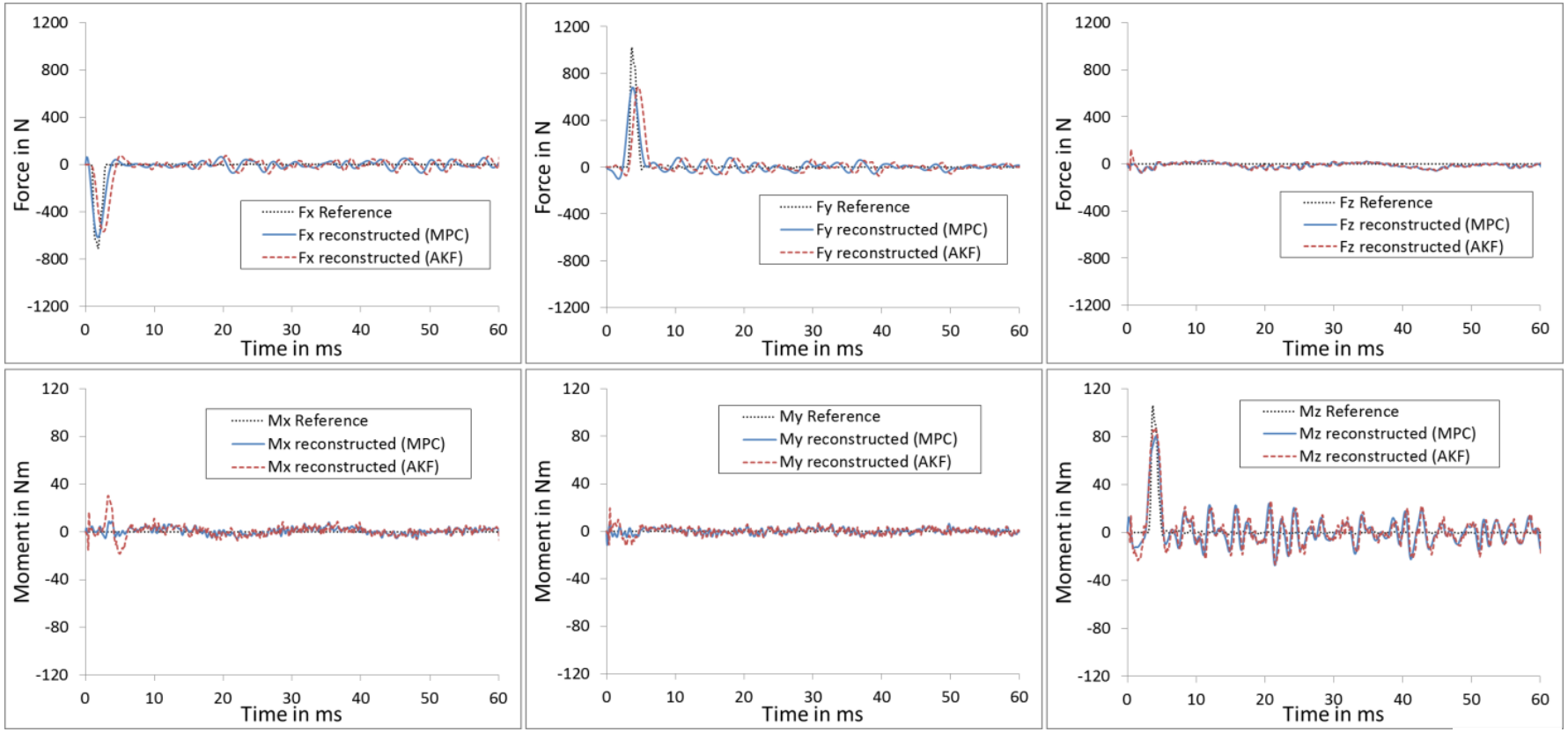

Figure 6.25: Test case 6 (hammer impact): Force reconstruction by the MPC (blue) and AKF (red) algorithm. The measured reference force is plotted with a dotted line.

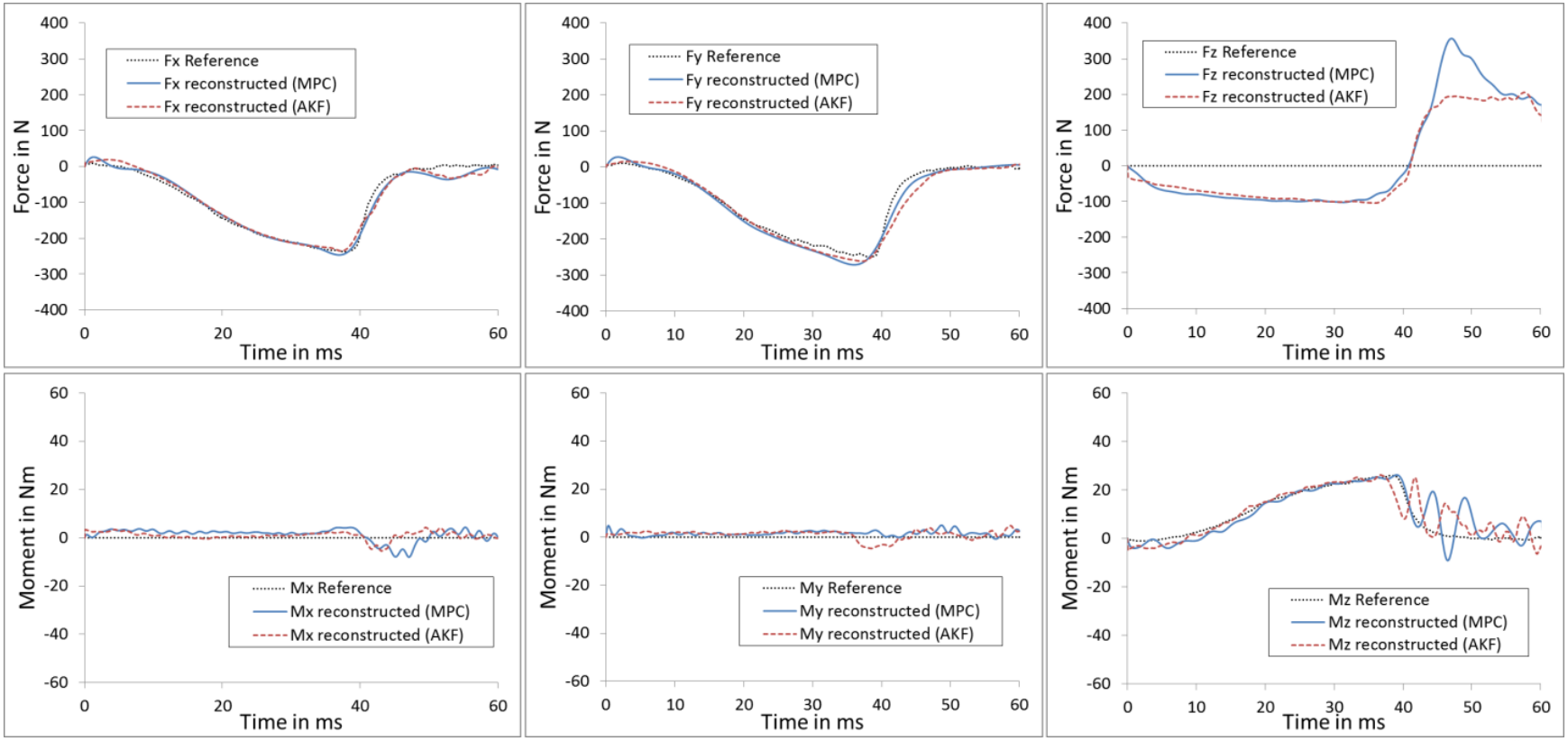

Figure 6.26: Test case 6 (scenario 2): Force reconstruction by the MPC (blue) and AKF (red) algorithm. The measured reference force is plotted with a dotted line.

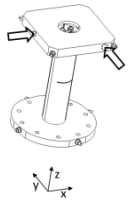

	MPC	AKF
$RMSE_F$	49 N	48 N
$RMSE_M$	2.1 Nm	2.2 Nm

Table 6.7: RSME for test case 6 (scenario 2) for the MPC and AKF algorithm

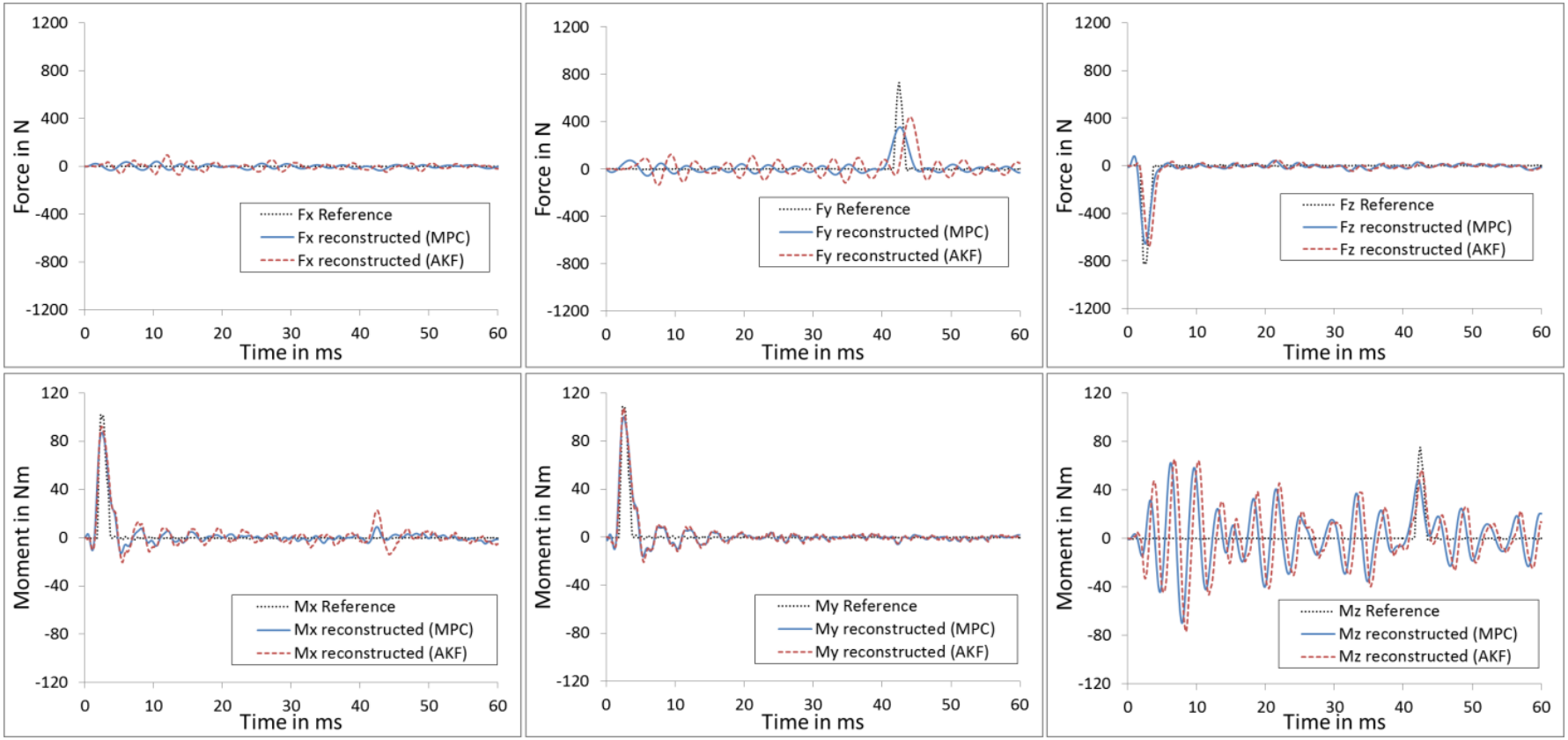

Figure 6.27: Test case 7 (hammer impact): Force reconstruction by the MPC (blue) and AKF (red) algorithm. The measured reference force is plotted with a dotted line.

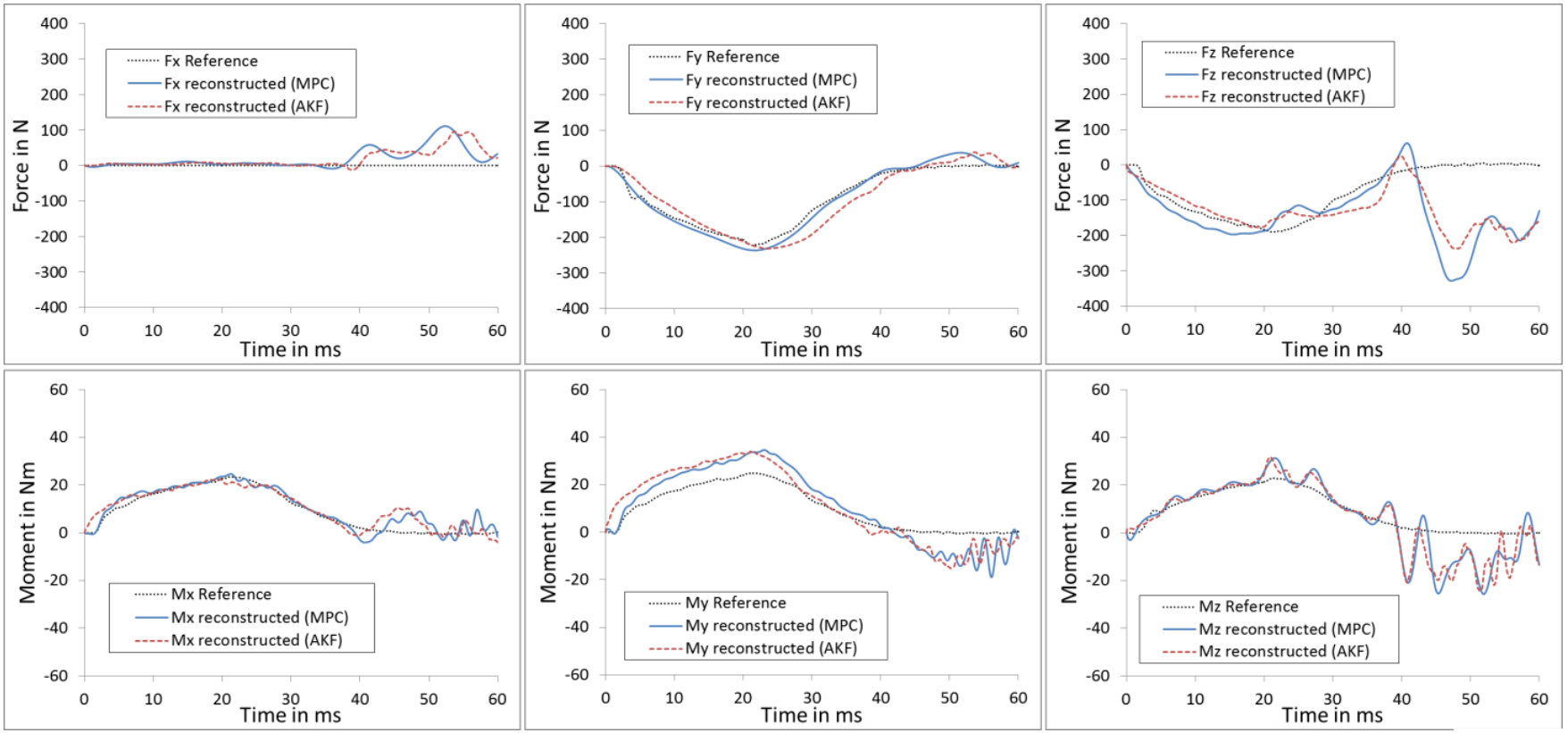

Figure 6.28: Test case 7 (scenario 3): Force reconstruction by the MPC (blue) and AKF (red) algorithm. The measured reference force is plotted with a dotted line.

	MPC	AKF
$RMSE_F$	21 N	27 N
$RMSE_M$	4.5 Nm	4.9 Nm

Table 6.8: RMSE: RSME for test case 7 (scenario 3) for the MPC and AKF algorithm

6.4.3 Definition of an accuracy of force measurement systems based on force reconstruction algorithms

A force reconstruction algorithm in combination with a structure that is equipped with a suitable set of sensors has the task of a force transducer. Nevertheless, the comparison with a classical force transducer or load cell is difficult as a force reconstruction method is an indirect measurement method and the application of a load cell corresponds to a direct method. However, as an accuracy or performance criterion for a force reconstruction algorithm is difficult to define, as discussed in Section 4.3, the attempt is made to transfer a part of the well-defined characteristics of force transducers in the VDI guideline 2638 [89] to force reconstruction methods.

The measurement of transient forces with a force transducer is only considered in the guideline by specifying a fundamental resonant frequency of the sensor. The fundamental resonant frequency limits the use of the sensor to dynamic forces below this frequency, where the influence of the dynamic behavior of the sensor itself can be neglected. In this case, a further consideration of the measurement of dynamic forces is obsolete.

In contrast to a standard force transducer, the resonant frequencies of a structure that is used in conjunction with a force reconstruction method are likely to lie within the frequency range of the applied forces. For this reason, a fundamental resonant frequency cannot be defined and the RSME criterion has been introduced to consider the accuracy of the reconstruction of the time history as well.

Apart from the temporal accuracy, the accuracy of the measured signal itself can be defined. For a standard force transducer, a comparison of measured and true force for every time point is possible. On the other hand, the same procedure applied to reconstructed forces would be influenced by a possible time delay between true input forces and reconstructed forces. However, this problem can be overcome by defining the deviation of the estimated forces from the true forces in a small time window with a quasi-constant force of a suitable transient forces.

An error criterion that is commonly used to specify the accuracy of a force transducer with regard to the single value of the measured force is the relative linearity error. This error is defined as the maximum deviation of a characteristic curve from the reference straight line in relation to the upper limit of the measurement range. In other words, it is defined as the maximum deviation of the measured force value from the true force value in relation to the upper limit of the measurement range within the measurement range.

In order to apply this error definition to the force reconstruction methods, the force components have to be regarded separately and an upper limit of the measurement range has to be specified. In order to define this error in a conservative way, the maximum force of each test case can be taken as upper limit. Tests with different levels of excitation forces have confirmed the applicability of this approach as the relative linearity error is equal or decreasing with an increasing force level. In addition, the error has been defined for the excitation location with the highest error. The resulting relative linearity errors for the simple pipe mock-up are summarized in Table 6.9.

	F_x	F_y	F_z	M_x	M_y	M_z
Relative linearity error	12 %	10 %	10%	25 %	28 %	9 %

Table 6.9: Relative linearity error for simple pipe mock-up.

The relative linearity errors are not given separately for the AKF and MPC algorithm as the error only depends on the accuracy of the identified model. Based on the resulting errors, it can be seen that a good accuracy with an error of about 10 %, except for the reconstructed moments M_x and M_y, can already be achieved with a basic setup for the model identification. By comparing test case 3 and 4, it is obvious that the higher error in the moments M_x and M_y is related to the excitation location.

Finally, it can be concluded that the accuracy of a force reconstruction method is not only related to the method that is applied, but rather the entire system consisting of the structure itself, the sensors and especially the identified model of the structure has to be considered to evaluate the accuracy of the force reconstruction system. Hence, the proposed and developed force reconstruction algorithms in combination with a more sophisticated modal analysis system are well suitable to achieve an accuracy better than 10 % in terms of the relative linearity error. Nevertheless, the individual accuracy of a force reconstruction system can only be determined in a pre-installation test.

7 Conclusion and outlook

The development of a method to reconstruct forces on the TBM during operation up to the final installation of this system in ITER has been divided in three stages. In the first stage, which is covered by this work, the problem to measure the forces acting on the TBM during normal and off-normal operation in ITER has been analyzed in detail based on present literature. Furthermore, different solutions have been developed and implemented and the applicability to the TBM in ITER has been experimentally validated taking into account the state of art of methods, instrumentation and TBM design.

A review of possible methods for force measurement has shown that only indirect force measurement methods are suitable for this application. In fact, due to the complex force distribution acting on the TBM during off normal events, discrete force application points necessary for the application of direct force measurement methods cannot be identified. The investigation of different force reconstruction methods has shown that methods suitable for the application to the TBM have to be based on a modal model of the system in order to reconstruct the distributed forces. Furthermore, they have to incorporate a stochastic element that continuously adapts the states of the model in order to be more robust against modelling errors.

An already existing force reconstruction method that fulfills these criteria is the Augmented Kalman Filter (AKF), a deterministic-stochastic approach. Hence, this algorithm was selected as possible candidate and extended to be able to reconstruct the distributed three-dimensional forces. Nevertheless, the AKF is a predictor-corrector algorithm and therefore not able to consider future measurement signals for the reconstruction.

In order to overcome this drawback, an algorithm able to include future measurement signals has been proposed as second candidate. The algorithm combines an optimization algorithm, which takes into account future values for the optimization, and a state observer based on Kalman filter techniques for the adaption of the states of the model. This algorithm used in a similar implementation as model predictive controller (MPC) has been proposed for force reconstruction for the first time.

The two algorithms, AKF and MPC, have been implemented and their application to the reconstruction of electromagnetic forces on the TBM has been experimentally validated by a dedicated experimental setup with a basic mock-up, namely the simple pipe mock-up. It has been demonstrated that the mock-up represents well the modal characteristics of the TBM.

From the consideration of different sensor technologies with regard to the environmental conditions in ITER, it can be concluded that strain sensors are the most suitable sensor type in order to obtain measurements of the motions of the TBM. They are of small size and can be placed on the attachment system behind the TBM, where the temperatures and radiation are lower. Furthermore, strain sensors based on optical fibers are proposed as they are immune to electromagnetic interference, able to withstand high temperatures and several sensing points can be introduced in one fiber reducing the necessary number of signal wires. For the first stage of the experimental validation, electrical strain sensors have been considered fully satisfactory for the scope of the experiment.

Due to restrictions imposed by the geometry and the instrumentation layout, only a limited number of sensors can be applied to the TBM and the mock-up. For this reason, a genetic algorithm has been developed that is able to optimize the sensor placement for a given number of sensors. The algorithm based on an analytical modal analysis of the system finds an arrangement for the specified number of sensors that detects all relevant modes with the highest possible measurement signals.

In order to investigate the influence of modelling errors on the force reconstruction algorithms, a study based on simulated strain data with the simple pipe mock-up has been conducted. In particular, the study was focused on the effect of errors in the eigenfrequencies and eigenvectors of the modal model and the number of sensors. For the evaluation of the impact of the modelling errors, an error measure based on the root mean squared error (RSME) has been defined, which is well suited for the characteristics of the applied forces. It was shown that the RSME with an error in the eigenvectors of 30% is about 14 times higher if 6 sensors are used instead of 16 sensors. In contrast, the influence of the number of sensors for a perfectly matching model turned out to be negligible. The impact of the error in the eigenfrequencies also proved to be relatively small compared to the error in the eigenvectors.

The overall comparison of the RSME of the AKF (with compensation of the time delay) and the MPC has shown no significant difference leading to the conclusion that the RSME is mainly influenced by modelling errors. Based on these results and depending on the available space, a total number of sensors between 10 and 16 sensors is required to compensate modelling errors and to also consider the failure of single sensors. Nevertheless, it is important to note that the AKF always needs a correction of the time delay and consequently can never reach the same accuracy of the reconstruction of the time history as the MPC. On the other hand, the AFK algorithm is more efficient in terms of computation time.

The results of the experiments with the simple pipe mock-up and 16 electrical strain sensors have shown that for ITER relevant durations of the excitation forces the algorithms are able to achieve an accuracy in the reconstruction of forces suitable for the validation of engineering models and codes. In order to get an estimation of the accuracy of the force reconstruction system in analogy to a classical force transducer, a new accuracy definition based on the relative linearity error has been developed. According to this definition, the forces can be estimated with an accuracy of about 10 % and the moments in the range of 20 %.

Since the first stage has proven the applicability of the system to the TBM, the second stage will be dedicated to the validation of the electro-magnetic codes based on a simple structure and the implementation of a more sophisticated setup for the model identification.

The second stage of the experimental program will be conducted with another mock-up, a reduced-sized mock-up of the TBM, which has already been developed and built as well. This will also necessitate a new experimental setup able to generate magnetic fields in order to induce eddy currents in the mock-up as well as the development of a detailed FEM model of the reduced-sized mock-up suitable for the electro-magnetic analysis.

Since the accuracy of the reconstructed forces is mainly dependent on the accuracy of the identified modal parameters, an accuracy below 10 % is very likely to achieve with a more sophisticated equipment for the modal analysis. This includes polyreference curve fitting

methods to increase the consistency in the modal parameters as well as more recently developed methods for modal parameter extraction, as for example the Alias Free Polyreference (AFPOLY) method. The characteristic of this method introduced in the last decade is the ability to eliminate the influence of out of band modes on the estimated modal parameters. This is especially important with regard to the modal analysis on the real TBM in the pre-installation phase.

The third and last stage is dedicated to the adaption of the force reconstruction methods to the final design of the TBM and the installation of the system in ITER.

For the adaption to the final TBM design, it is important to note that the force reconstruction methods developed in this work can be applied to other TBM attachment designs as long as the overall system can be described by a modal model. This is an important feature of the developed methods and procedures since the final design of the attachment system in ITER is not yet defined. This, however, requires a new assessment of the assumptions of the TBM box rigidity, number of considered modes and type of sensors based on the new design.

In the pre-installation phase, the TBM has to be equipped with the necessary number of sensors. Therefore, the eligible sensor technologies will have to be studied in detail in advance, especially with regard to radiation hardness, since the expected level of radiation is unusual for presently available sensors.

In the next step, an experimental modal analysis will have to be conducted on the real TBM or a corresponding mock-up, which necessitates a suitable experimental setup to generate the required excitations.

In the final implementation of the force reconstruction methods in ITER, they could be combined with other methods to estimate forces acting on the TBM in order to validate advanced engineering models and codes. For example, electromagnetic forces can also be estimated measuring the magnetic field and eddy currents on the TBM box. This, indeed, requires an additional effort in developing a method for information fusion that combines the data coming from the different sources.

Finally, the described force reconstruction methods could be further developed to a quasi-online force monitoring system. Up to now, the identification of regularization parameters, which is an important part in the application of the selected force reconstruction algorithms, has been carried out by applying the L-curve method manually. With regard to an online force monitoring system, this method has to be further improved by developing an automatized way that could also incorporate the presented method to detect excitation events.

In addition, the L-curve method, the method to detect excitation events, the method to compensate the time delay in the AKF as well as the MPC algorithm itself require recorded sensor data with a duration of about 20 ms before the algorithms are able to provide the force estimates. In relation to this time span the computation time of the MPC algorithm cannot be neglected, but certainly depends on the available computational power at the time of the implementation of the system.

Bibliography

[1] International Energy Agency (IEA), "World Energy Investment Outlook (Special Report)," 2014.

[2] L. M. Giancarli, M. Abdou, D. J. Campbell, V. A. Chuyanov, M. Y. Ahn, M. Enoeda, C. Pan, Y. Poitevin, E. Rajendra Kumar, I. Ricapito, Y. Strebkov, S. Suzuki, P. C. Wong and M. Zmitko, "Overview of the ITER TBM Program," *Fusion Engineering and Design,* vol. 87, no. 5-6, pp. 395-402, 2012.

[3] H.-S. Bosch, "Nuclear Fusion," in *Plasma Physics*, Berlin Heidelberg, Springer, 2005, pp. 445-460.

[4] R. Aymar, P. Barabaschi and Y. Shimomura, "The ITER design," *Plasma Physics and Controlled Fusion,* vol. 44, pp. 519-565, 2002.

[5] S. Malang, A. R. Raffray, A. Sagara and A. Ying, "Range of blanket concepts from near term solutions to advanced concepts," *Fusion Engineering and Design,* Vols. 61-62, pp. 295-306, 2002.

[6] L. V. Boccaccini, L. Giancarli, G. Janeschitz, S. Hermsmeyer, Y. Poitevin, A. Cardella and E. Diegele, "Materials and design of the European DEMO blankets," *Journal of Nuclear Materials,* Vols. 329-333, pp. 148-155, 2004.

[7] F. Romanelli, P. Barabaschi, D. Borba, G. Federici, L. Horton, R. Neu, D. Stork and H. Zohm, "Fusion Electricity - A roadmap to the realisation of fusion energy," November 2012. [Online]. Available: http://www.efda.org/wpcms/wp-content/uploads/2013/02/JG12.356-web.pdf. [Accessed 24 May 2014].

[8] ITER Organisation. [Online]. Available: http://www.iter.org. [Accessed 23 May 2014].

[9] R. Roccella, L. V. Boccaccini, R. Meyder, S. Raff and M. Roccella, "Assessment of EM loads on the EU HCPB TBM during plasma disruption and normal operating scenario including the ferromagnetic effect," *Fusion Engineering and Design,* vol. 83, no. 7-9, pp. 1212-1216, 2008.

[10] P. Andrew, P. Noll and V. Riccardo, "The relation between halo currents and plasma displacement/deformation in JET," *Fusion Engineering,* vol. 1, pp. 108-111, 1997.

[11] L. V. Boccaccini, A. Aiello, O. Bede, F. Cismondi, L. Kosek, T. Ilkei, J.-F. Salavy, P. Sardain and L. Sedano, "Present status of the conceptual design of the EU test blanket systems," *Fusion Engineering and Design,* vol. 86, no. 5-8, pp. 478-483, 2011.

[12] S. Madeleine, A. Saille, J.-P. Martins, J.-F. Salavy, N. Jonquères, G. Rampal, O. Bede, H. Neuberger, L. V. Boccaccini and L. Doceul, "Engineering studies for integration of the test blanket module (TBM) systems inside an ITER equatorial port plug," *Fusion Engineering and Design,* vol. 84, no. 7-11, pp. 1233-1237, 2009.

[13] F. Cismondi, S. Kecskes, P. Pereslavtsev, E. Magnani and U. Fischer, "Preliminary thermal design and related DEMO relevancy of the EU-HCPB TBM in vertical arrangement," *Fusion Engineering and Design,* vol. 85, no. 10-12, pp. 2040-2044, 2010.

[14] H. Neuberger, X. Jin, L. V. Boccaccini, B. E. Ghidersa and R. Meyder, "Helium loop for the HCPB Test Blanket Module," *Fusion Engineering and Design,* vol. 82, no. 15-24, pp. 2288-2293, 2007.

[15] F. Cismondi, G. Rampal, G. Aiello and A. Li Puma, "Input data, software/models, physical correlations and material properties for HCPB TBM generic box and shield design activities," F4E Reference: 05.6_TBMCA.2009.D1D4.0001_f1.0, 2009.

[16] F. Cismondi, *Internal communication,* 2009.

[17] F. Elio, K. Ioki, M. Yamada, Y. Strebkov, W. Daenner and M. Akiba, "Design and R&D progress of blanket attachments," *Fusion Engineering and Design,* vol. 69, no. 1-4, pp. 321-326, 2003.

[18] A. Alekseev, E. Privalova and M. Sukhanova, *EU/RF collaborative task on the Development of diagnostic systems for the TBM, Intermediate Report, Part 4,* 2007.

[19] A. Heudt, *Thermo-mechanical study of the attachment between a TBM and a shield module in ITER*

environment, 2009.

[20] C. I. Walker, *Technical Specification for the Diagnostic Equatorial Port Plug #01 ITER_D_22FNKA*, 2005.

[21] B. Dolenksy, *CEA-Attachment with links*, 2007.

[22] S. Kecskes, "Shape Optimization of the TBM Attachment System," 2009.

[23] C. Zeile and H. Neuberger, "Design and Analyses of the attachment system - Status Jun 2010," 2010.

[24] C. Zeile and H. Neuberger, "Design and Analyses of the attachment system - Status Dec 2010," 2010.

[25] C. Zeile, H. Neuberger and B. Dolensky, "ITER Port Plug Engineering Trainee Program: Design, manufacturing and integration of structural components (analysis of the attachment)," *Fusion Engineering and Design*, vol. 86, no. 9-11, p. 2029–2032, 2011.

[26] *Design and construction rules for mechanical components of nuclear installations (RCC-MR)*, afcen (association francaise pour les règles de conception, de construction et de surveillance en exploitation des matériels des chaudières électro-nucléaires), 2007.

[27] *STRUCTURAL DESIGN CRITERIA for ITER in-vessel components (SDC-IC)*, 2004.

[28] C. Zeile and H. Neuberger, "Design and Analysis of the attachment system consisting of a hollow cylinder," 2011.

[29] C. Zeile and H. Neuberger, "A revised design approach of the attachment system for the ITER EU-HCPB-TBM based on a central cylindrical connection element," *Fusion Engineering and Design*, vol. 87, no. 5-6, pp. 859-863, 2012.

[30] Norm, *DIN 1319-1 Grundlagen der Messtechnik*, 1995.

[31] M. Klinkov and C.-P. Fritzen, "An Updated Comparison of the Force Reconstruction Methods," *Key Engineering Materials*, vol. 347, pp. 461-466, 2007.

[32] E. Jacquelin, A. Bennani and P. Hamelin, "Force reconstruction: analysis and regularization of a deconvolution problem," *Journal of Sound and Vibration*, vol. 265, pp. 81-107, 2003.

[33] T. Uhl, "The inverse identification problem and its technical application," *Archive of Applied Mechanics*, vol. 77, pp. 325-337, 2007.

[34] A. Kirsch, An Introduction to the Mathematical Theory of Inverse Problems, Springer, 2011.

[35] J. Hadamard, *Lectures on the Cauchy Problem in Linear Partial Differential Equations*, New Haven: Yale University Press, 1923.

[36] D. Simon, Optimal State Estimation, Hoboken, New Jersey: John Wiley & Sons., 2006.

[37] A. D. Steltzner and D. C. Kammer, "Input Force Estimation Using an Inverse Structural Filter," in *17th International Modal Analysis Conference (IMAC XXVII)*, Kissimmee, Florida, 1999.

[38] M. S. Allen and T. G. Carne, "Delayed, multi-step inverse structural filter for robust force identification," *Mechanical Systems and Signal Processing*, vol. 22, pp. 1036-1054, 2008.

[39] T. P. Nordberg and I. Gustafsson, "Dynamic regularization of input estimation problems by explicit block inversion," *Computer Methods in Applied Mechanics and Engineering*, vol. 195, pp. 5877-5890, 2006.

[40] P. E. Hollandsworth and H. R. Busby, "Impact force identification using the general inverse technique," *International Journal of Impact Engineering*, vol. 8, pp. 315-322, 1989.

[41] D. M. Trujillo, "Application of dynamic programming to the general inverse problem," *International Journal for Numerical Methods in Engineering*, vol. 12, pp. 613-624, 1978.

[42] P. C. Hansen, "Analysis of discrete ill-posed problems by means of the L-curve," *SIAM Review*, vol. 34, no. 4, pp. 561-580, 1992.

[43] E. Turco, "A strategy to identify exciting forces acting on structures," *International Journal for Numerical Methods in Engineering*, vol. 64, pp. 1483-1508, 2005.

[44] G. Genaro and D. Alves, "Input Force Identification in the Time Domain," in *16th International*

Modal Analysis Conference (IMAC XVI), California, 1998.

[45] F. Xia, C. Cole and P. Wolfs, "An inverse railway wagon model and its applications," *Vehicle System Dynamics,* vol. 45, no. 6, pp. 583-605, 2007.

[46] D. L. Gregory, T. G. Priddy and D. O. Smallwood, "Experimental Determination of the Dynamic Forces Acting on Non-Rigid Bodies," in *Aerospace Technology Conference and Expostion*, Long Beach, California, 1986.

[47] G. H. James, T. Carne, K. Elliot and B. Wilson, "Estimation of the space shuttle rollout forcing function," in *23rd International Modal Analysis Conference (IMAC XXIII)*, Orlando, Florida, 2005.

[48] T. G. Carne, R. L. Mayes and V. I. Bateman, "Force reconstruction using the sum of weighted accelerations technique- Max-flat procedure," in *12th International Modal Analysis Conference (IMAC XII)*, 1994.

[49] M. S. Allen and T. G. Carne, "Comparison of Inverse Structural Filter (ISF) and Sum of Weigted Acceleration Technique (SWAT)Time Domain Force Identification Methods," in *47th AIAA-ASME ASCE-AHS-ASC Structures, Structural Dynamics, and Materials Conference*, Newport, RI, 2006.

[50] R. J. Hundhausen, D. E. Adams, P. Kukuchek and R. Alloway, "Transient Loads Identification for a Standoff Metallic Thermal Protection System Pane," in *23rd International Modal Analysis Conference (IMAC XXIII)*, Orlando, Florida, 2005.

[51] D. J. Haas and R. Imber, "Identification of helicopter Component Load using Multiple Regression," *Journal of Aircraft,* vol. 31, no. 4, pp. 929-935, 1994.

[52] A. Barr and E. A. Feigenbaum, The Handbook of Artificial Intelligence Volume 1, Los Altos, California: William Kaufmann, Inc., 1981.

[53] A. Böge, „Fuzzy-Regelung,“ in *Handbuch Maschinenbau*, Wiesbaden, Vieweg+Teubner, 2009, pp. 1349-1356.

[54] M. T. Hagan, H. B. Demuth and M. H. Beale, Neural Network Design, PWS Publishing Company, 1996.

[55] P. M. Trivailo and C. L. Carn, "The inverse determination of aerodynamic loading from structural response data using neural networks," *Inverse Problems in Science and Engineering*, vol. 14, no. 4, pp. 379-395, 2006.

[56] R. Kruse, C. Borgelt, F. Klawonn, C. Moewes, M. Steinbrecher and P. Held, "Introduction to Evolutionary Algorithms," in *Computational Intelligence*, London, Springer, 2013, pp. 167-195.

[57] R. Hashemi and M. H. Kargarnovin, "Vibration Based Identification of Impact Force using Genetic Algorithm," *International Journal of Aerospace and Mechanical Engineering,* vol. 1, no. 4, pp. 206-212, 2007.

[58] D. M. Hawkins, “The Problem of Overfitting,” *Journal of Chemical Information and Computer Sciences,* vol. 44, pp. 1-12, 2004.

[59] J. E. Moody, "The Effective Number of Parameters: An Analysis of Generalization and Regularization in Nonlinear Learning Systems," *Advances in Neural Information Processing Systems,* vol. 4, pp. 847-854, 1991.

[60] S. Haykin, Neural Networks - A comprehensive Foundation, Pearson Education, Inc., 1999.

[61] E. Lourens, E. Reynders, G. De Roeck, G. Degrande and G. Lombaert, "An augmented Kalman filter for force identification in structural dynamics," *Mechanical Systems and Signal Processing,* vol. 27, pp. 446-460, 2012.

[62] E. Lourens, C. Papadimitriou, S. Gillijns, E. Reynders, G. De Roeck and G. Lombaert, "Joint input-response estimation for structural systems based on reduced-order models and vibration data from a limited number of sensors," *Mechanical Systems and Signal Processing,* vol. 29, pp. 310-327, 2012.

[63] J. L. Garriga and M. Soroush, "Model Predictive Control Tuning Methods: A Review," *Industrial & Engineering Chemistry Research,* vol. 49, no. 8, pp. 3505-3515, 2010.

[64] A. Bemporad, M. Morari and N. L. Ricker, "Model Predictive Control Toolbox," in *MATLAB User's Guide*, Natick, MA, USA, The MathWorks, Inc., 2012.

[65] L. V. Boccaccini, "Design Description Document for the European Helium Cooled Pebble Bed (HCPB) Test Blanket Modules," 2005.

[66] U. Fischer, D. Große, F. Moro, P. Pereslavtsev, L. Petrizzi, R. Villari and V. Weber, "Integral approach for neutronics analyses of the European test blanket modules," *Fusion Engineering and Design,* vol. 86, no. 9-11, pp. 2176-2179, 2011.

[67] E. Hering and G. Schönfelder, Sensoren in Wissenschaft und Technik, Wiesbaden: Vieweg+Teubner Verlag, 2012.

[68] Vishay PG, Inc., "Special Use Strain Gages - High-Temperature Strain Gages," [Online]. Available: http://www.vishaypg.com/docs/11532/highpat.pdf. [Accessed 9 May 2014].

[69] K. Hoffmann, "An Introduction to Stress Analysis and Tranducer Design using Strain Gauges," 2012. [Online]. Available: http://www.kk-group.ru/help/Strain_Gauge_Measurements_Book_2012_01.pdf. [Accessed 10 May 2014].

[70] Vishay PG, Inc., "Tech Note TN-501-2: Noise Control in Strain Gage Measurements," 9 June 2013. [Online]. Available: http://www.vishaypg.com/docs/11051/tn501.pdf. [Accessed 9 May 2014].

[71] Capacitec, Inc., "High Radiation & Magnetic Field," [Online]. Available: http://www.capacitec.com/Markets/Extreme-Environment/High-Radiation-Magnetic-Field. [Accessed 9 May 2014].

[72] Vishay PG, Inc. , "Special Use Sensors - Magnetic Field Strain Gages," 2 February 2010. [Online]. Available: http://www.vishaypg.com/docs/11517/magfield.pdf. [Accessed 9 May 2014].

[73] RDP Electrosense, "PY Extreme Environment Non-Contact Displacement Transducer," 18 November 2013. [Online]. Available: http://www.rdpe.com/us/py.pdf. [Accessed 12 May 2014].

[74] K. O. Hill and G. Meltz, "Fiber Bragg Grating Technology Fundamentals and Overview," *Journal of Ligtwave Technology,* vol. 15, no. 8, pp. 1263-1276, 1997.

[75] I.-B. Kwon, M.-Y. Choi and H. Moon, "Strain measurement using fiber optic total reflected extrinsic Fabry–Perot interferometric sensor with a digital signal processing algorithm," *Sensors and Actuators A,* vol. 112, pp. 10-17, 2004.

[76] C. R. Liao and D. N. Wang, "Review of Femtosecond Laser Fabricated Fiber Bragg Gratings for High Temperature Sensing," *Photonic Sensors,* vol. 3, no. 2, pp. 97-101, 2013.

[77] T. Reinsch and J. Henninges, "Temperature dependent characterization of optical fibres for distributed temperature sensing in hot geothermal wells," *Measurement Sciene and Technology,* vol. 21, no. 9, 2010.

[78] B. Brichard, A. Fernandez, H. Ooms, F. Berghmans, M. Decréton, A. Tomashuk, S. Klyamkin, M. Zabezhailov, I. Nikolin, V. Bogatyrjov, E. Hodgson, T. Kakuta, T. Shikama, T. Nishitani, A. Costley and G. Vayakis, "Radiation-hardening techniques of dedicated optical fibres used in plasma diagnostic systems in ITER," *Journal of Nuclear Materials,* Vols. 329-333, no. Part B, pp. 1456-1460, 2004.

[79] S. Girard, J. Kuhnhenn, A. Gusarov, B. Brichard, M. Van Uffelen, Y. Ouerdane, A. Boukenter and C. Marcandella, "Radiation Effects on Silica-Based Optical Fibers: Recent Advances and Future Challenges," *IEEE Transactions on nuclear science,* vol. 60, no. 3, pp. 2015-2036, 2013.

[80] B. Brichard, A. L. Tomashuk, H. Ooms, V. A. Bogatyrjov, S. N. Klyamkin, A. F. Fernandez, F. Berghmans and M. Decreton, "Radiation assessment of hydrogen-loaded aluminium-coated pure silica core fibres for ITER plasma diagnostic applications," *Fusion Engineering and Design,* vol. 82, no. 15-24, pp. 2451-2455, 2007.

[81] S. J. Mihailov, "Fiber Bragg Grating Sensors for Harsh Environments," *Sensors,* vol. 12, pp. 1898-1918, 2012.

[82] T.-H. Yi, H.-N. Li and M. Gu, "Optimal Sensor Placement for Health Monitoring of High-Rise

Structure Based on Genetic Algorithm," *Mathematical Problems in Engineering*, vol. 2011, 2011.

[83] R. Sedaghati, Y. Soucy and N. Etienne, "Experimental estimation of effective mass for structural dynamics and vibration applications," in *Proceedings of 21th International Modal Analysis Conference*, Kissimmee, Florida, 2003.

[84] L. J. Nordström and P. T. Nordberg, "A time delay method to solve non-collocated input estimation problems," *Mechanical Systems and Signal Processing*, vol. 18, pp. 1469-1483, 2004.

[85] VDI, *Guideline VDI 2230: Systematische Berechnung hochbeanspruchter Schraubenverbindungen - Mehrschraubenverbindungen*, Düsseldorf, 2011.

[86] Ansys Inc., Documentation for Release 14.5, Canonsburg, PA, 2012.

[87] G. Sannazzaro, "MPQ Load Specifications," ITER reference: ITER_D_222QGL v3.4, 2009.

[88] R. J. Allemang, "The Modal Assurance Criterion - Twenty Years of Use and Abuse," in *20th International Modal Analysis Conference (IMAC)*, Los Angeles, CA, US, 2002.

[89] Guideline, *VDI 2638 Characteristics of force transducers*, 2008.

Appendix

A Tables of cumulative modal effective masses

		Excitation direction					
Mode No.	Eigenfrequency	x	y	z	rx	ry	rz
1	65 Hz	0 %	45 %	0 %	0 %	0 %	37 %
2	91 Hz	0 %	45 %	84 %	62 %	96 %	37 %
3	112 Hz	0 %	45 %	84 %	89 %	96 %	37 %
4	260 Hz	0 %	100 %	84 %	89 %	96 %	38 %
5	286 Hz	98 %	100 %	84 %	89 %	96 %	99 %
6	417 Hz	98 %	100 %	96 %	97 %	99 %	99 %
7	521 Hz	98 %	100 %	100 %	100 %	100 %	99 %
8	602 Hz	98 %	100 %	100 %	100 %	100 %	99 %
9	664 Hz	100 %	100 %	100 %	100 %	100 %	100 %
10	707 Hz	100 %	100 %	100 %	100 %	100 %	100 %

Table A.1: Cumulative fraction of modal effective masses of the total mass (or moment of inertia) for the TBM computed with the FEA software ANSYS for the excitation directions x,y and z and the rotations about the x-axis (rx), y-axis (ry) and z-axis (rz) of the coordinate system. The cumulative fraction for the first six modes sums up to more than 90 % for each excitation direction.

		Excitation direction					
Mode No.	Eigenfrequency	x	y	z	rx	ry	rz
1	109 Hz	0 %	0 %	80 %	11 %	36 %	0 %
2	113 Hz	0 %	91 %	80 %	63 %	36 %	58 %
3	226 Hz	0 %	91 %	80 %	92 %	36 %	58 %
4	377 Hz	0 %	91 %	100 %	95 %	46 %	58 %
5	480 Hz	100 %	91 %	100 %	95 %	100 %	88 %
6	529 Hz	100 %	100 %	100 %	100 %	100 %	100 %
7	1529 Hz	100 %	100 %	100 %	100 %	100 %	100 %
8	1531 Hz	100 %	100 %	100 %	100 %	100 %	100 %
9	1722 Hz	100 %	100 %	100 %	100 %	100 %	100 %
10	1723 Hz	100 %	100 %	100 %	100 %	100 %	100 %

Table A.2: Cumulative fraction of modal effective masses of the total mass (or moment of inertia) for the reduced-sized mock-up computed with the FEA software ANSYS for the excitation directions x,y and z and the rotations about the x-axis (rx), y-axis (ry) and z-axis (rz) of the coordinate system. The cumulative fraction for the first six modes sums up to more than 90 % for each excitation direction.

		Excitation direction					
Mode No.	Eigenfrequency	x	y	z	rx	ry	rz
1	42 Hz	0 %	89 %	0 %	98 %	0 %	0 %
2	52 Hz	93 %	89 %	0 %	98 %	100 %	0 %
3	82 Hz	93 %	89 %	0 %	98 %	100 %	100 %
4	286 Hz	100 %	89 %	0 %	98 %	100 %	100 %
5	306 Hz	100 %	100 %	0 %	100 %	100 %	100 %
6	369 Hz	100 %	100 %	98 %	100 %	100 %	100 %
7	907 Hz	100 %	100 %	100 %	100 %	100 %	100 %
8	980 Hz	100 %	100 %	100 %	100 %	100 %	100 %
9	1318 Hz	100 %	100 %	100 %	100 %	100 %	100 %
10	1322 Hz	100 %	100 %	100 %	100 %	100 %	100 %

Table A.3: Cumulative fraction of modal effective masses of the total mass (or moment of inertia) for the simple pipe mock-up computed with the FEA software ANSYS for the excitation directions x,y and z and the rotations about the x-axis (rx), y-axis (ry) and z-axis (rz) of the coordinate system. The cumulative fraction for the first six modes sums up to more than 90 % for each excitation direction.

B Bolt Pattern Analysis

If the forces acting on a body can be described by their effect on a single reference point, the forces can be distributed analogous to the classical bolt pattern analysis. The effect of a number of forces on a reference point can be described in a Cartesian coordinate system by a 6-component vector $\left[F_x\ F_y\ F_z\ M_x\ M_y\ M_z\right]^T$ containing three forces and three moments. The forces and moments are projected from the reference point to the center of gravity of the n_{fa} force application points. This is illustrated for the two-dimensional case in Figure B.1.

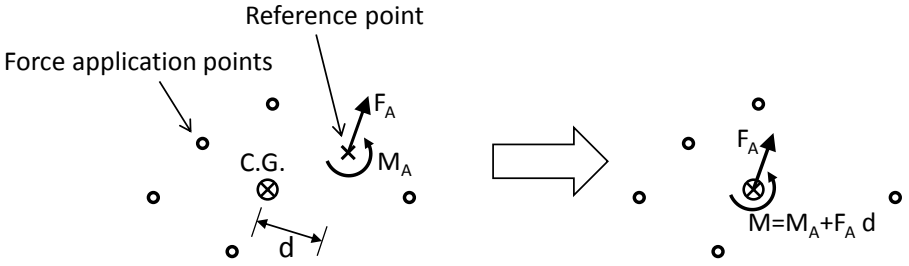

Figure B.1: Classical bolt pattern analysis: Force F_A and moment M_A are represented as an equivalent force F_A and moment M at the center of gravity (C.G.) of the force application points.

The forces are uniformly distributed to the force application points as demonstrated in Figure B.2.

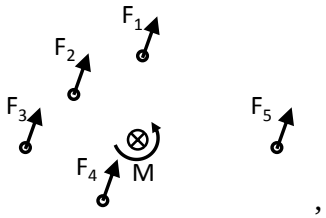

Figure B.2: Classical bolt pattern analysis: The force at the center of gravity is transferred to the force application points.

with the magnitude of the force $|F_i| = \frac{F_A}{n_{fa}}$ at each force application point.

The forces due to the moments M_x, M_y, M_z are assigned to the force application points according to the squared distance d_j^2 from the center of gravity. This is shown for the two-dimensional case in Figure B.3.

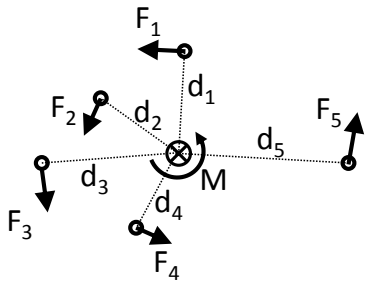

,

Figure B.3: Classical bolt pattern analysis: The moment at the center of gravity is represented by forces at the force application points.

with the magnitude of the force $|F_i| = \frac{M\, d_i}{\sum_{j=1}^{n_{fa}} d_j^2}$ at each force application point.

The corresponding representation in the three-dimensional case assuming that each force application point has three displacement DOF can be seen in Figure B.4.

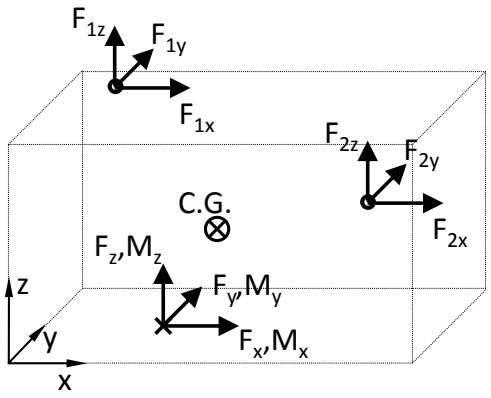

Figure B.4: Classical bolt pattern analysis: Force application points and force component in the three-dimensional case.

The representation of the force vector $\boldsymbol{f}(t)$ in equation (4.3) can now be expressed by the 6-component force function vector $\boldsymbol{p}(t) = \left[F_x(t)\; F_y(t)\; F_z(t)\; M_x(t)\; M_y\;(t) M_z(t)\right]^T$ and the application of a force distribution according to the classical bolt pattern analysis in matrix form as follows:

$$\boldsymbol{f}(t) \approx \boldsymbol{S}_{BP}\, \boldsymbol{p}(t), \tag{B.1}$$

with the force distribution matrix according to the classical bolt pattern analysis $\boldsymbol{S}_{BP} = \begin{bmatrix} \boldsymbol{S}_{BP1} \\ \boldsymbol{0} \\ \vdots \\ \boldsymbol{S}_{BPn} \end{bmatrix}$,

with

$$\boldsymbol{S}_{BPi} = \begin{bmatrix} F_{ix} \\ F_{iy} \\ F_{iz} \end{bmatrix}$$

$$= \begin{bmatrix} \left(\frac{1}{n} + \frac{\Delta x_y\, x_{i,y}}{\Theta_{xy}} + \frac{\Delta x_z\, x_{i,z}}{\Theta_{xz}}\right) & \frac{\Delta x_x\, x_{i,y}}{\Theta_{xy}} & \frac{\Delta x_{x1}\, x_{i,z}}{\Theta_{xz}} & 0 & \frac{x_{i,z}}{\Theta_{xz}} & \frac{-x_{i,y}}{\Theta_{xy}} \\ \frac{-\Delta x_y\, x_{i,x}}{\Theta_{xy}} & \left(\frac{1}{n} - \frac{\Delta x_x\, x_{i,x}}{\Theta_{xy}} + \frac{\Delta x_z\, x_{i,z}}{\Theta_{yz}}\right) & \frac{-\Delta x_y\, x_{i,z}}{\Theta_{yz}} & \frac{-x_{i,z}}{\Theta_{yz}} & 0 & \frac{x_{i,x}}{\Theta_{xy}} \\ \frac{-\Delta x_z\, x_{i,x}}{\Theta_{xz}} & \frac{-\Delta x_z\, x_{i,y}}{\Theta_{yz}} & \left(\frac{1}{n} + \frac{\Delta x_y\, x_{i,y}}{\Theta_{yz}} - \frac{\Delta x_x\, x_{i,x}}{\Theta_{xz}}\right) & \frac{x_{i,y}}{\Theta_{yz}} & \frac{-x_{i,x}}{\Theta_{xz}} & 0 \end{bmatrix},$$

with the magnitude of the force in x,y,z-direction of force application point i, F_{ix}, F_{iy}, F_{iz}, distances from the center of gravity to the reference point $(\Delta x_x, \Delta x_y, \Delta x_z)$, the location of the force application point i relative to the center of gravity $(x_{i,x}, x_{i,y}, x_{i,z})$ and the sum of the squared distances $\Theta_{op} = \sum_{j=1}^{n} x_{j,o}^2 + x_{j,p}^2$. The zero matrices $\mathbf{0}$ correspond to the non-force application points. The arrangement of the matrices $\boldsymbol{S}_{BPi}$ and $\mathbf{0}$ in $\boldsymbol{S}_{BP}$ certainly depends on the order of the degree of freedom in the representation of the model.

C Sensor Placement APMU (Ansys)

The sensor positions that have been used for force reconstruction with simulated strain data are listed according to the number of sensors used in the model in Table C.1. The positions and orientations of the sensors can be determined according to Figure C.1. The origin of the coordinate system is on the cylinder axis at the bottom of the base plate. The measurement direction of the strain gauges is along the long side of the sensor.

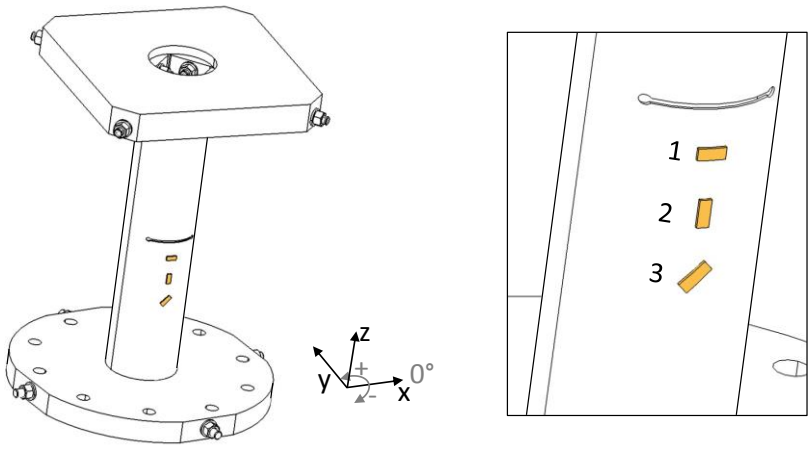

Figure C.1: Sensor Positions: The positions on the cylinder are specified by an angle (positive and negative following the convention in ANSYS) and height on the cylinder with the origin of the coordinate system on the cylinder axis at the bottom of the base plate (left). The orientation of the sensors is indicated by the number 1, 2 and 3 (right).

6 sensors				10 sensors				16 sensors			
No.	Orient.	Angle	Height	No.	Orient.	Angle	Height	No.	Orient.	Angle	Height
1	2	149.7°	280 mm	1	2	-3.5°	56 mm	1	2	0°	408 mm
2	2	-139.0°	412 mm	2	2	-89.1°	51mm	2	2	-178.1°	57 mm
3	2	32.1°	280 mm	3	2	89.1°	41 mm	3	2	89.1°	51 mm
4	2	-153.2°	54 mm	4	2	178.2°	54 mm	4	2	-81.9°	42 mm
5	2	32.1°	177 mm	5	2	89.1°	51 mm	5	2	-178.1°	403 mm
6	3	-89.1°	280 mm	6	3	92.7°	280 mm	6	2	-92.6°	54 mm
				7	2	0°	409 mm	7	3	92.6°	280 mm
				8	2	28.5°	280 mm	8	3	-89.1°	177 mm
				9	3	-89.1°	280 mm	9	2	178.2°	412 mm
				10	2	28.5°	177 mm	10	2	-81.9°	409 mm
								11	3	89.1°	177 mm
								12	2	28.5°	177 mm
								13	2	14.3°	51 mm
								14	3	-89.1°	280 mm
								15	2	92.7°	415 mm
								16	2	178.2°	66 mm

Table C.1: Sensor positions for the simple pipe mock-up with simulated strain data for 6, 10 and 16 sensors.

D Experimental modal analysis

Apart from the eigenfrequencies and damping ratios, the experimental modal analysis is used to determine the modal displacement eigenvectors as well as the strain eigenvectors. For this purpose, at first the strains are linked to the displacements by the strain-displacement matrix. Subsequently, the modal analysis procedure to determine the strain eigenvectors is illustrated. Finally, the sensor and excitation locations are summarized together with the related eigenvectors.

Strain-displacement matrix

The displacement field $\boldsymbol{\psi}$ in Cartesian coordinates is expressed by

$$\boldsymbol{\psi} = \boldsymbol{\psi}(\boldsymbol{x}, t) = \left[\psi_x\ \psi_y\ \psi_z\right]^T , \tag{D.1}$$

with the location of the point $\boldsymbol{x} = \left[x_x\ x_y\ x_z\right]^T$.

The displacement of an arbitrary point in a finite element $\boldsymbol{\psi}_e$ can be expressed by shape functions N_i, which are generally a polynomial function of its spatial coordinates with constant coefficients and the displacements at the nodes $\boldsymbol{\psi}_n$.

$$\boldsymbol{\psi}_e = \boldsymbol{N}\,\boldsymbol{\psi}_n\ , \tag{D.2}$$

where $\boldsymbol{\psi}_e = \left[\psi_{xe}\ \psi_{ye}\ \psi_{ze}\right]^T$, $\boldsymbol{\psi}_n = [\psi_{xn1}\ \psi_{yn1}\ \psi_{zn1}\ \psi_{xn2}\ \psi_{yn2} \cdots]^T \in \mathbb{R}^{3n_{nodes}\times 1}$ and $\boldsymbol{N} = \begin{bmatrix} N_1 & 0 & 0 & N_2 & \cdots \\ 0 & N_1 & 0 & 0 & \cdots \\ 0 & 0 & N_1 & 0 & \cdots \end{bmatrix} \in \mathbb{R}^{3\times 3n_{nodes}}$.

Now the strains for small displacements can be determined with the linear strain-displacement relation $\varepsilon_{ik} = \frac{1}{2}\left[\frac{\partial \psi_i}{\partial x_k} + \frac{\partial \psi_k}{\partial x_i}\right]$ from the nodal displacements $\boldsymbol{\psi}_n$:

$$\boldsymbol{\varepsilon} = \boldsymbol{B}\,\boldsymbol{\psi}_n\,, \tag{D.3}$$

with the elements of the strain tensor $\boldsymbol{\varepsilon} = \left[\varepsilon_{xx}\ \varepsilon_{yy}\ \varepsilon_{zz}\ 2\varepsilon_{xy}\ 2\varepsilon_{yz}\ 2\varepsilon_{zx}\right]^T$ and the strain-displacement matrix $\boldsymbol{B} = \boldsymbol{D}_\varepsilon \boldsymbol{N} = [\boldsymbol{B}_1\ \boldsymbol{B}_2 \cdots]$ with $\boldsymbol{B}_i = \begin{bmatrix} \frac{\partial N_i}{\partial x_x} & 0 & 0 \\ 0 & \frac{\partial N_i}{\partial x_y} & 0 \\ 0 & 0 & \frac{\partial N_i}{\partial x_z} \\ \frac{\partial N_i}{\partial x_y} & \frac{\partial N_i}{\partial x_x} & 0 \\ 0 & \frac{\partial N_i}{\partial x_z} & \frac{\partial N_i}{\partial x_y} \\ \frac{\partial N_i}{\partial x_z} & 0 & \frac{\partial N_i}{\partial x_x} \end{bmatrix}$.

Determination of strain eigenvectors

For the determination of the strain eigenvectors, the modal representation of the system in equation (3.16) is repeated here as equation (D.4):

$$\boldsymbol{I}\ddot{\boldsymbol{\phi}} + \Delta\dot{\boldsymbol{\phi}} + \boldsymbol{W}\boldsymbol{\phi} = \boldsymbol{R}^T\boldsymbol{f}\,. \tag{D.4}$$

Using the back transformation of the displacement vector

$$\boldsymbol{\phi} = \boldsymbol{R}^{-1}\boldsymbol{\psi} \tag{D.5}$$

and applying the Fourier transformation to (D.4) leads to the following expression in modal dimensions with the transform Ψ_i of the coordinate ψ_i:

$$[-\Omega^2\boldsymbol{I} + j\Omega\Delta + \boldsymbol{W}]\boldsymbol{R}^{-1}\boldsymbol{\Psi}(\Omega) = \boldsymbol{R}^T\,\boldsymbol{F}(\Omega), \tag{D.6}$$

with

$$\begin{gathered}\boldsymbol{\Psi}(\Omega) = \boldsymbol{R}[-\Omega^2\boldsymbol{I} + j\Omega\Delta + \boldsymbol{W}]^{-1}\,\boldsymbol{R}^T\,\boldsymbol{F}(\Omega) = \boldsymbol{H}(\Omega)\boldsymbol{F}(\Omega) \\ \rightarrow\ \boldsymbol{H}(\Omega) = \boldsymbol{\Psi}(\Omega)\boldsymbol{F}(\Omega)^{-1}\,.\end{gathered} \tag{D.7}$$

The displacement frequency response function (DFRF) matrix $\boldsymbol{H}(\Omega)$ is given as

$$\boldsymbol{H}(\Omega) = \boldsymbol{R}[-\Omega^2\boldsymbol{I} + j\Omega\Delta + \boldsymbol{W}]^{-1}\,\boldsymbol{R}^T \quad . \tag{D.8}$$

By substituting the displacements in the back transformation (D.5) by the strain-displacement relation (D.3) as follows

$$\boldsymbol{\phi} = \boldsymbol{R}^{-1}\boldsymbol{B}^{-1}\boldsymbol{\varepsilon}, \tag{D.9}$$

subsequently using the back transformation (D.9) in the system of equations (D.4) and finally applying the Fourier transformation, the strain frequency response function (SRFR) matrix $\boldsymbol{H}_\varepsilon(\Omega)$ can be developed:

$$[-\Omega^2\boldsymbol{I} + j\Omega\Delta + \boldsymbol{W}]\boldsymbol{R}^{-1}\boldsymbol{B}^{-1}\mathbf{E}(\Omega) = \boldsymbol{R}^T\,\boldsymbol{F}(\Omega);$$

$$\mathbf{E}(\Omega) = \boldsymbol{B}\boldsymbol{R}[-\Omega^2\boldsymbol{I} + j\Omega\Delta + \boldsymbol{W}]^{-1}\,\boldsymbol{R}^T\,\boldsymbol{F}(\Omega) = \boldsymbol{H}_\varepsilon(\Omega)\boldsymbol{F}(\Omega) \quad \rightarrow \boldsymbol{H}_\varepsilon(\Omega) = \mathbf{E}(\Omega)\boldsymbol{F}(\Omega)^{-1}; \tag{D.10}$$

$$\boldsymbol{H}_\varepsilon(\Omega) = \boldsymbol{B}\boldsymbol{R}[-\Omega^2\boldsymbol{I} + j\Omega\Delta + \boldsymbol{W}]^{-1}\,\boldsymbol{R}^T.$$

The diagonal matrix $[-\Omega^2\boldsymbol{I} + j\Omega\Delta + \boldsymbol{W}]$ can be inverted line by line, which leads to

$$\boldsymbol{\alpha} = [-\Omega^2\boldsymbol{I} + j\Omega\Delta + \boldsymbol{W}]^{-1} = diag\left(\frac{1}{-\Omega^2 + j2\delta_i\Omega + \omega_i^2}\right), \tag{D.11}$$

with the damping coefficient $\delta_i = \frac{1}{2}(\alpha_i + \omega_i^2\beta_i)$.

The DFRF matrix $\boldsymbol{H}(\Omega)$ and the SFRF matrix $\boldsymbol{H}_\varepsilon(\Omega)$ can now be written as:

$$\boldsymbol{H}(\Omega) = \boldsymbol{R}\boldsymbol{\alpha}\boldsymbol{R}^T \quad \text{and} \quad \boldsymbol{H}_\varepsilon(\Omega) = \boldsymbol{R}_\varepsilon\boldsymbol{\alpha}\boldsymbol{R}^T, \tag{D.12}$$

with the strain modal matrix $\boldsymbol{R}_\varepsilon = \boldsymbol{B}\boldsymbol{R}$.

As only the diagonal elements of $\boldsymbol{\alpha}$ are none-zero, the elements of $\boldsymbol{H}(\Omega)$ and $\boldsymbol{H}_\varepsilon(\Omega)$ are given by:

$$h_{ij} = \sum_{k=1}^{N}\alpha_{kk}r_{ik}r_{jk} = \sum_{k=1}^{N}\frac{A_{ij}^{(k)}}{(-\Omega^2 + \omega_k^2) + j2\delta_k\Omega} \tag{D.13}$$

and

$$h_{\varepsilon ij} = \sum_{k=1}^{N}\alpha_{kk}r_{\varepsilon ik}r_{jk} = \sum_{k=1}^{N}\frac{A_{\varepsilon ij}^{(k)}}{(-\Omega^2 + \omega_k^2) + j2\delta_k\Omega} \tag{D.14}$$

and in matrix form:

$$\boldsymbol{H}(\Omega) = \sum_{k=1}^{N}\alpha_k\boldsymbol{r}_k\boldsymbol{r}_k^T = \sum_{k=1}^{N}\alpha_k\boldsymbol{A}_k \tag{D.15}$$

and

$$\boldsymbol{H}_{\varepsilon}(\Omega) = \sum_{k=1}^{N} \alpha_k \boldsymbol{r}_{\varepsilon k} \boldsymbol{r}_k^T = \sum_{k=1}^{N} \alpha_k \boldsymbol{A}_{\varepsilon k}, \tag{D.16}$$

where $A_{ij}^{(k)}$ or $A_{\varepsilon ij}^{(k)}$ are the residues, $\boldsymbol{A}_k$ or $\boldsymbol{A}_{\varepsilon k}$ are the residue matrices and k is the mode number.

Equation (D.16) can be expanded to:

$$\boldsymbol{H}_{\varepsilon}(\Omega) = \sum_{k=1}^{N} \alpha_k \begin{bmatrix} r_{\varepsilon 1k} r_{1k} & r_{\varepsilon 1k} r_{2k} & \cdots & r_{\varepsilon 1k} r_{nk} \\ r_{\varepsilon 2k} r_{1k} & r_{\varepsilon 2k} r_{2k} & \cdots & r_{\varepsilon 2k} r_{nk} \\ \cdots & \cdots & \cdots & \cdots \\ r_{\varepsilon mk} r_{1k} & r_{\varepsilon mk} r_{2k} & \cdots & r_{\varepsilon mk} r_{nk} \end{bmatrix}. \tag{D.17}$$

From the representation of the SFRF matrix $\boldsymbol{H}_{\varepsilon}$ in (D.17) it can easily be seen that it is sufficient to measure any row together with any column to build the entire SFRF matrix $\boldsymbol{H}_{\varepsilon}$. If only certain elements of the strain eigenvector are to be determined, only the element of the displacement eigenvector in the corresponding column has to be known before.

Excitation and measurement points and corresponding eigenvectors

The positions of the strain gauges and the corresponding eigenvectors that are used in the experimental setup are listed in Table D.1. The positions are described by height and angle on the pipe surface and are marked by small blocks in Figure D.1. The origin of the coordinate system is located on the axis of the cylinder at the bottom of the base plate. The sensor orientations are indicated in the same way as described in Figure C.1. The positions of excitation and measurement points are indicated by small circles on the top plate in Figure D.1. In addition, the positions are listed together with the corresponding eigenvectors in Table D.2.

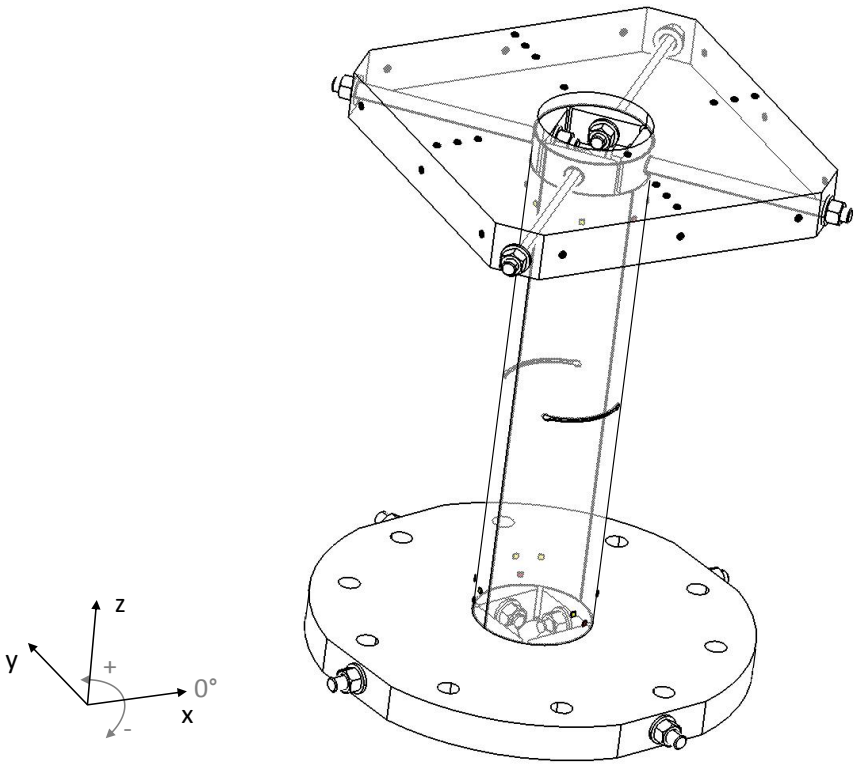

Figure D.1: Excitation and sensor positions on simple pipe mock-up. The origin of the coordinate system is located on the axis of the cylinder at the bottom of the base plate.

Orient.	Angle	Height	Mode 1	Mode 2	Mode 3	Mode 4	Mode 5	Mode 6
2	166.2°	55 mm	-0.007	0.081	0.013	0.073	-0.029	-0.325
3	-72.7°	38 mm	0.015	0.004	0.053	0.070	0.079	-0.020
3	-76.1°	407 mm	0.005	0.009	0.041	0.152	-0.084	-0.039
2	72.7°	55 mm	-0.058	-0.017	-0.012	0.025	-0.207	-0.076
2	3.5°	410 mm	-0.001	-0.012	0.011	0.330	0.048	-0.265
2	-90.0°	55 mm	0.057	-0.008	0.007	0.017	0.193	-0.036
3	152.3°	38 mm	-0.009	0.017	0.058	0.026	-0.114	-0.059
2	176.6°	410 mm	0.000	0.008	-0.007	-0.225	0.041	-0.157
2	-131.5°	410 mm	0.009	0.010	0.027	-0.325	-0.324	-0.218
2	48.5°	55 mm	-0.045	-0.045	-0.025	-0.033	-0.155	-0.131
2	138.5°	55 mm	-0.037	0.052	0.029	0.032	-0.146	-0.201
2	-41.5°	410 mm	0.005	-0.013	-0.031	0.354	-0.345	-0.292
2	48.4°	410 mm	-0.009	-0.010	0.025	0.303	0.341	-0.189
3	65.8°	38 mm	-0.010	-0.016	0.046	-0.078	-0.006	0.000
2	-45.0°	58 mm	0.041	-0.062	0.027	-0.040	0.164	-0.169
2	138.5°	410 mm	-0.007	0.012	-0.026	-0.285	0.313	-0.174

Table D.1: Experimental modal analysis: Positions of strain gauges and corresponding eigenvectors

No.	Pos. X	Pos. Y	Pos. Z	Mode 1	Mode 2	Mode 3	Mode 4	Mode 5	Mode 6
1	-103.5 mm	-150 mm	454 mm	0.174	0.000	-0.149	0.000	0.069	0.000
2	0 mm	-150 mm	454 mm	0.175	0.000	0.002	0.000	0.067	0.000
3	150 mm	-103.5 mm	454 mm	0.000	0.176	0.147	0.051	0.000	0.000
4	150 mm	0 mm	454 mm	0.000	0.172	0.001	0.036	0.000	0.000
5	0 mm	-54.5 mm	474 mm	0.042	0.000	0.000	0.000	-0.117	-0.164
6	103.5 mm	-150 mm	454 mm	0.172	0.000	0.159	0.000	0.046	0.000
7	148.5 mm	103.5 mm	454 mm	0.000	0.177	-0.154	0.040	0.000	0.000
8	0 mm	-139.5 mm	474 mm	0.085	0.000	0.000	0.000	-0.261	-0.171
9	139.5 mm	0 mm	474 mm	0.000	-0.071	0.000	0.291	0.000	-0.170
10	121.5 mm	0 mm	474 mm	0.000	-0.061	0.000	0.208	0.000	-0.160
11	-121.5 mm	0 mm	474 mm	0.000	0.061	0.000	-0.199	0.000	-0.155
12	103.5 mm	0 mm	474 mm	0.000	-0.054	0.000	0.227	0.000	-0.166
13	-103.5 mm	0 mm	474 mm	0.000	0.053	0.000	-0.195	0.000	-0.141
14	0 mm	-121.5 mm	474 mm	0.073	0.000	0.000	0.000	-0.237	-0.161
15	0 mm	121.5 mm	474 mm	-0.077	0.000	0.000	0.000	0.224	-0.210
16	0 mm	103.5 mm	474 mm	-0.066	0.000	0.000	0.000	0.179	-0.213
17	0 mm	-103.5 mm	474 mm	0.066	0.000	0.000	0.000	-0.194	-0.144
18	103.5 mm	150 mm	454 mm	0.175	0.000	0.166	0.000	0.044	0.000
19	0 mm	150 mm	454 mm	0.175	0.000	0.002	0.000	0.067	0.000
20	-150 mm	103.5 mm	454 mm	0.000	0.176	-0.147	0.051	0.000	0.000
21	-150 mm	0 mm	454 mm	0.000	0.176	0.001	0.045	0.000	0.000
22	0 mm	54.5 mm	474 mm	-0.032	0.000	0.000	0.000	0.105	-0.164
23	-103.5 mm	150 mm	454 mm	0.172	0.000	-0.159	0.000	0.046	0.000
24	-150 mm	-103.5 mm	454 mm	0.000	0.177	0.154	0.040	0.000	0.000
25	0 mm	139.5 mm	474 mm	-0.084	0.000	0.000	0.000	0.272	-0.164
26	-139.5 mm	0 mm	474 mm	0.000	0.071	0.000	-0.273	0.000	-0.152

Table D.2: Experimental modal analysis: Excitation and measurement points on the top plate and corresponding eigenvectors

Danksagung

Ich bedanke mich sehr herzlich bei Herrn Professor Dr.-Ing. Robert Stieglitz für die Möglichkeit, am Institut für Neutronenphysik und Reaktortechnologie (INR) zu promovieren, sein ständiges Interesse an der Arbeit sowie die wichtigen Anregungen und Ratschläge.

Ebenso gilt mein Dank Herrn Professor Dr.-Ing. Alexander Fidlin für die Übernahme des Koreferats sowie die interessanten Diskussionen und wertvollen Ratschläge, die zum Gelingen dieser Arbeit beigetragen haben.

Besonders möchte ich mich auch bei Herrn Dr. Lorenzo Virgilio Boccaccini bedanken, dass er es mir ermöglicht hat, im Rahmen meiner Tätigkeit in seiner Gruppe „Design und Analyse nuklearer Komponenten, Fertigung und Qualifizierung“ (DAF) diese Arbeit anzufertigen sowie für seine Hilfsbereitschaft und Unterstützung, die ich immer sehr zu schätzen wusste.

Meinem Kollegen Herrn Dr. Ivan Alessio Maione gilt mein besonderer Dank für die vielen konstruktiven Diskussionen, seiner großen Hilfsbereitschaft sowie aufmerksamen Durchsicht der Arbeit.

Meinen Kollegen der Gruppe DAF danke ich ebenso herzlich für die vielen hilfreichen Gespräche, die ständige Unterstützung sowie die angenehme Arbeitsatmosphäre.